SPATIAL ORGANISATION OF THE SNARE PROTEINS: THE ROLE OF MUNC18-1

Claire Medine
BSc Hons

University of Edinburgh
2008

This dissertation is submitted for the degree of Doctor of Philosophy

ABSTRACT

Regulated exocytosis is a highly conserved process in all eukaryotes that is mediated by conserved protein families. Central to this process are the SNARE (soluble N-ethylmaleimide-sensitive fusion protein (NSF) attachment protein receptor) proteins that are targeted either to the target plasma membrane (t-SNAREs) or to the vesicle membrane (v-SNAREs). The fusion of the two phospholipids bilayers is dependent on the formation of the ternary SNARE complex, in which the plasma membrane-associated SNAP-25 and syntaxin 1a interact with the vesicle-associated membrane protein (VAMP). The formation of this SNARE complex is essential to drive membrane fusion and thus the sites of SNARE complex formation are strictly regulated both temporally and spatially. Many accessory factors have been identified that are essential to control the availability of these proteins to form the ternary SNARE complex. Syntaxin 1a, a component of the SNARE complex in neurons and neuroendocrine cells, is directly regulated by munc18-1, its cognate Sec1/Munc18 (SM) protein, although the cellular functions have remained controversial.

In this study I show using *in vitro* and *in vivo* approaches that in neuroendocrine cells munc18-1 has two modes of binding to syntaxin 1a. I demonstrate that munc18-1 plays a vital role in binding to a closed-form of syntaxin 1a, keeping syntaxin 1a inactive and permitting its trafficking to the plasma membrane. Munc18-1 is also able to bind to an active open form of syntaxin 1a, allowing it to bind to other SNAREs. Using Förster resonance energy transfer (FRET) and fluorescence lifetime imaging microscopy (FLIM) I demonstrate that in the absence of munc18-1, syntaxin 1a and SNAP-25 can readily interact in the Golgi complex, forming reactive SNARE complexes that fail to traffic to the plasma membrane. The exocytotic SNARE proteins are highly promiscuous in their interactions with other SNAREs, and thus it is essential to traffic the exocytotic SNARE proteins through intracellular compartments while avoiding ectopic interactions between non-cognate SNARE proteins. Munc18-1 has a vital regulatory role in preventing the formation of the binary complex between syntaxin 1a and SNAP-25 before the proteins reach their target destination of the plasma membrane. Upon delivery to the plasma membrane

the t-SNAREs have been shown to form cholesterol dependent clusters in several cell types of between 60-750 nm, depending on the imaging approach employed. Recently, it was shown that syntaxin 1a forms dynamic clusters by virtue of self association. However, the factors that regulate SNAP-25 cluster stability are unknown. Here I present evidence to show that once at the plasma membrane syntaxin 1a and SNAP-25 are concentrated in clusters of high local concentration that co-localise in neuroendocrine cells. Interestingly, despite reducing the affinity of SNAP-25 for syntaxin 1a using mutagenesis, these proteins still co-cluster and interact on the plasma membrane. The newly delivered t-SNAREs, less than 48 hours old, can form interaction-heterogeneous clusters with interactions modulated by elevated Ca^{2+} levels. Furthermore, quantitative changes in the lipid microenvironment by cholesterol depletion play a role in cluster integrity. In summary, the pathway for SNARE cluster formation involves munc18-1 regulation of syntaxin 1a, cholesterol association and SNARE protein interactions. Munc18-1 plays a vital role in trafficking syntaxin 1a through the secretory pathway, preventing ectopic interactions between SNARE proteins. This is essential to present syntaxin 1a and SNAP-25 in dynamic clusters at the plasma membrane and represents a mechanism of membrane patterning that is based on favourable local membrane composition and protein-protein interactions. Munc18-1 has spatially and functionally distinct roles that are defined by its binding mode to syntaxin.

DECLARATION

This thesis is the result of my own work and includes nothing which is the outcome of work done in collaboration, except where indicated in the text.

This thesis includes material that has been the outcome of work done in collaboration. The portions of the thesis that were done in collaboration have been explicitly designated within the Acknowledgements. The names of the collaborators and the nature of their contribution have been stated.

The work in this thesis has not been submitted for any other degree or professional qualification.

Claire Medine

TABLE OF CONTENTS

LIST OF FIGURES AND TABLES

ABBREVIATIONS

ADC	Analogue-digital converter
AEBSF	4-(2-Aminoethyl) benzenesulphonyl fluoride
BP	Band pass
BSA	Bovine serum albumin
CCD	Charge coupled device
CFD	Constant fraction discriminator
CLSM	Confocal laser scanning microscopy
CMV	Human cytomegalovirus
DAG	Diacylglycerol
DEPC	Diethyl pyrocarbonate
DRM	Detergent resistant membrane
DsRed	*Discosoma striata* red fluorescent protein
ECFP	Enhanced cyan fluorescent protein
ECL	Enhanced chemiluminescence
EDTA	Ethylenediaminetetraacetate
EGFP	Enhanced green fluorescent protein
ER	Endoplasmic reticulum
EYFP	Enhanced yellow fluorescent protein
FBS	Foetal bovine serum
FITC	Fluorescein isothiocyanate
FLIM	Fluorescence lifetime imaging microscopy
FM	Fei Mao dyes
FP	Fluorescent protein
FRET	Förster resonance energy transfer
FWHM	Full width half maximum
GFP	Green fluorescent protein
GST	Glutathione sepharose transferase
HBSS	Hanks' balanced salt solution
HEK293	Human embryonic kidney 293 cell line
HEPES	N-(2-Hydroxyethyl) piperazine-N'-(2-ethanesulfonic acid)
HRP	Horseradish peroxidase
IPTG	Isopropyl-β-D-thiogalactopyranoside
kb	Kilobase
kDa	Kilodalton
LDCV	Large dense core vesicle
LP	Long pass
mCerulean	Monomeric cerulean fluorescent protein
mCherry	Monomeric cherry fluorescent protein
MβCD	Methyl-β-cyclodextrin
MCS	Multiple cloning site
mRFP	Monomeric red fluorescent protein
N2a	Neuroendocrine 2a cell line
NEM	N-ethylmaleimide
NSF	N-ethylmaleimide sensitive factor
PBS	Phosphate buffered saline

PCR	Polymerase chain reaction
PFA	Paraformaldehyde
PKC	Protein kinase C
PMA	Phorbol-12-myristate-13-acetate
PMT	Photo multiplier tube
PSF	Point spread function
PVDF	Polyvinylidene difluoride
RRP	Readily releasable pool
SDS	Sodium dodecyl sulphate
SDS-PAGE	Sodium dodecyl sulphate polyacrylamide gel electrophoresis
SEM	Standard error of the mean
SM protein	Sec1/munc18 protein
SNAP	Soluble NSF attachment protein (see also NSF)
SNAP-25	Synaptosomal-associated protein of 25 kDa
SNARE	Soluble N-ethylmaleimide-sensitive-factor attachment protein receptor
STED	Stimulated emission deletion
TAC	Time-to-amplitude converter
TCSPC	Time correlated single photon counting
3-D	Three-dimensional
TIRFM	Total internal reflection fluorescence microscopy
TMR	Transmembrane region
TritonX-100	Octylphenyl-nonaoxyethylene
t-SNARE	Target SNARE (see also SNARE)
Tween 20	Polyoxyethylene-sorbitan monolaurate
UV	Ultraviolet
v-SNARE	Vesicle SNARE (see also SNARE)

ACKNOWLEDGEMENTS

I simply wanted to write 'forget everyone else; this was down to me', but that would be a blatant lie. Many people deserve my appreciation for helping me achieve this.

Foremost, I would like to thank my supervisor Dr Rory Duncan - it's been great working for you and thank you for giving me the opportunity to do a PhD. I'm also very grateful to Dr Colin Rickman for always answering my 'quick' questions. Both Rory and Colin deserve my gratitude for their endless help, scientific advice and knowledge throughout this project. Additionally, Colin performed and analysed the syntaxin 1a-munc18-1 binding experiments (Figures 3.3 and 3.8A-C) and imaging (Figures, 3.4 and 3.7). I am also grateful to Dr Carolyn Brechin who performed the MβCD cell viability assay (Figure 6.1B) and David Moulton who performed and analysed the Laurdan staining (Figure 6.1C).

I thank the entire crowd of the old MBG, past and present - it's been fun working with all of you. I'm also grateful to Trudi Gillespie for all her help. I was tempted to individually thank all my friends, but for fear of leaving someone out, I will instead say thank you to them all. You're all simply unique, and always there for the banter and the laughs (you know who you are!). Cheers to Helen and Derek, who I promised I would mention, and I always keep my promises.

A special thank you to my Mum and Dad, you can never be appreciated enough. Gavin I thank you for setting the bar so high, the competition never ends. Finally, but most importantly, I thank the man who has supplied me with wine, and constantly ignored the craziness, Rob. Thanks for always being there.

PUBLICATIONS

The following papers were published during the course of my study for the degree of Doctor of Philosophy. The findings of this thesis are included, in part, in these publications:

- Rickman, C., **Medine, C.N.**, Bergmann, A. and Duncan, R.R. (2007) Functionally and spatially distinct modes of munc18-syntaxin 1 interaction. *J Biol Chem*, **282**, 12097-12103.

- **Medine, C.N.**, Rickman, C., Chamberlain, L.H. and Duncan, R.R. (2007b) Munc18-1 prevents the formation of ectopic SNARE complexes in living cells. *J Cell Sci*, **120**, 4407-4415.

- **Medine, C.N.**, McDonald, A., Bergmann, A. and Duncan, R.R. (2007a) Time-correlated single photon counting FLIM: some considerations for physiologists. *Microsc Res Tech*, **70**, 420-425.

CHAPTER ONE:

INTRODUCTION

1.1 THE SECRETORY PATHWAY

Eukaryotic cells have evolved a secretory pathway that is composed of characteristic membrane bound organelles capable of multiple biochemical processes that can proceed simultaneously and independently of one another. These membranous organelles are capable of communicating with one another and the plasma membrane via the formation, release and merging of membrane bound protein vesicles. Protein trafficking is crucial to their biological function and it occurs via the budding and subsequent fusion of transport vesicles (Jamieson & Palade, 1967; Palade, 1975). Newly synthesised proteins that are destined for secretion to the cell exterior enter the secretion pathway at the endoplasmic reticulum (ER) and are incorporated into the ER lumen where they become packaged into transport vesicles. These vesicles bud from the ER and fuse with the *cis*-Golgi or with each other to form the membrane stacks of the *cis*-Golgi reticulum (Jamieson & Palade, 1967; Palade, 1975). Proteins destined to be secreted move to the *trans* face of the Golgi and then into a complex network of vesicles termed the *trans*-Golgi network. It is only during exit from the last *trans* compartment that newly synthesised proteins are separated according to their final destination (Griffiths & Simons, 1986). Proteins are also packaged into constitutive or regulated secretory vesicles in the *trans* compartment before release into the cytoplasm where they are free to migrate to, and fuse with, the plasma membrane (Griffiths & Simons, 1986; Jahn, 2004; Rothman, 1994b) (Figure 1.1). The fusion of the cargo-containing vesicles with the plasma membrane is known as exocytosis, which allows the release of the vesicular contents to the outside of the cell. Exocytosis is critical to an array of cellular processes and intercellular communication, which is fundamental to the integrity of all eukaryotic cells.

1.2 CONSTITUTIVE AND REGULATED EXOCYTOSIS

Exocytosis is the process by which proteins packaged in vesicles are secreted from a cell. The mis-regulation of this process has been implicated in many disease states, including diabetes (Lam et al, 2005; Nagamatsu et al, 1999; Zhang et al, 2002),

epilepsy (Hinz et al, 2001; Kamphuis et al, 1995) and Alzheimer's disease (Shimohama et al, 1997; Sze et al, 2000). Proteins destined for secretion are sorted in the *trans*-Golgi network into transport vesicles that immediately move to, and fuse with, the plasma membrane, releasing their contents by exocytosis. The process of constitutive secretion occurs in all eukaryotic cells in the absence of any external stimulus, allowing cells to continuously secrete extracellular molecules, such as newly synthesised lipids and proteins for the insertion of new plasma membrane (Burgess & Kelly, 1987; Burgoyne & Morgan, 2003). In contrast, regulated secretion, as its name implies, is a pathway for those proteins that require a stimulus for controlled secretion. These proteins are sorted in the *trans*-Golgi into secretory vesicles that are stored inside the cell awaiting a stimulus for exocytosis (Burgess & Kelly, 1987; Burgoyne & Morgan, 2003; Jahn, 2004; Jahn & Sudhof, 1999). In specialised secretory cell types, including neurons and pancreatic β-cells, secretion is tightly regulated to allow the controlled release of neurotransmitters and hormones only in response to a physiological stimulus, commonly mediated by an elevation in cytosolic Ca^{2+} (Burgess & Kelly, 1987; Burgoyne & Morgan, 2003; Jahn, 2004).

Regulated exocytosis starts with the packaging of neurotransmitters or hormones into vesicles. For example, proinsulin, the precursor of insulin, is packaged into large dense core vesicles (LDCVs) in the *trans*-Golgi network where it is cleaved into mature and active insulin (Dodson & Steiner, 1998). Secretory cells are capable of storing these vesicles within their cytoplasm in the absence of stimulation. It is well established that to allow secretory cells to respond rapidly to stimulation they require a reservoir of vesicles known as the readily releasable pool (RRP) that does not require further maturation steps, and can therefore be secreted in a rapid exocytotic burst by the cell (Burgess & Kelly, 1987; Rizzoli & Betz, 2004). The loaded vesicles are transported to the plasma membrane where they are believed to encounter two pre-fusion steps. Initially, the vesicles undergo docking or tethering to the active zone on the plasma membrane, followed by an ATP-dependent priming reaction that may involve the assembly of the molecular fusion machinery, converting the vesicles into a fusion competent state ready for Ca^{2+} triggered fusion (Burgoyne & Morgan, 2003; Sudhof, 2004). A healthy β-cell for example, contains greater than 10,000

vesicles, of which only 1,000 are docked and only about 100 sit in the primed RRP (Rorsman & Renstrom, 2003). In response to an influx of Ca^{2+} through voltage gated ion channels, the vesicles fuse with the plasma membrane forming fusion pores, and subsequent vesicle secretion ensues (Jahn & Sudhof, 1999; Takahashi et al, 2002). The secretory vesicles can fuse en masse with the plasma membrane, releasing their contents into the extracellular space (Burgoyne & Morgan, 2003; Jahn et al, 2003; Jahn & Sudhof, 1999; Liu et al, 2005). Extensive research has led to the belief that all types of intracellular membrane fusion, from yeast to man share a common mechanism (Bennett & Scheller, 1993; Clary et al, 1990; Ferro-Novick & Jahn, 1994). The fusion of vesicles with the target membrane is accepted in molecular terms to be induced by the pairing of specific proteins on the vesicle membrane with opposing proteins on the target membrane. The key players in this concluding fusion step are the so-called SNARE (soluble N-ethylmaleimide-sensitive fusion protein attachment protein receptors) proteins and their regulatory partners (Sollner et al, 1993a; Sollner et al, 1993b) (Figure 1.1).

1.3 THE SNARE FUSION MACHINERY

1.3.1 FINDING THE FUSION MACHINERY

To understand the molecular mechanisms that govern the delivery of distinct sets of proteins to the numerous subcellular organelles within a cell, initial genetic and biochemical studies focused on intracellular transport between the ER and the Golgi complex. Proteins that are synthesised in the ER are sorted and transported according to their cellular destinations. Secretory proteins pass through the Golgi complex and are subsequently packaged into vesicles destined for fusion with the plasma membrane (Griffiths & Simons, 1986; Jamieson & Palade, 1967; Palade, 1975). In the late 1970s, biochemical studies of membrane trafficking in yeast were conducted by Novick and colleagues (Novick et al, 1981; Novick et al, 1980; Novick & Schekman, 1979) and led to the identification of essential components of the fusion machinery. Extensive studies to screen for secretion deficient or *sec* mutants in *Saccharomyces cerevisiae* resulted in the identification of an array of proteins

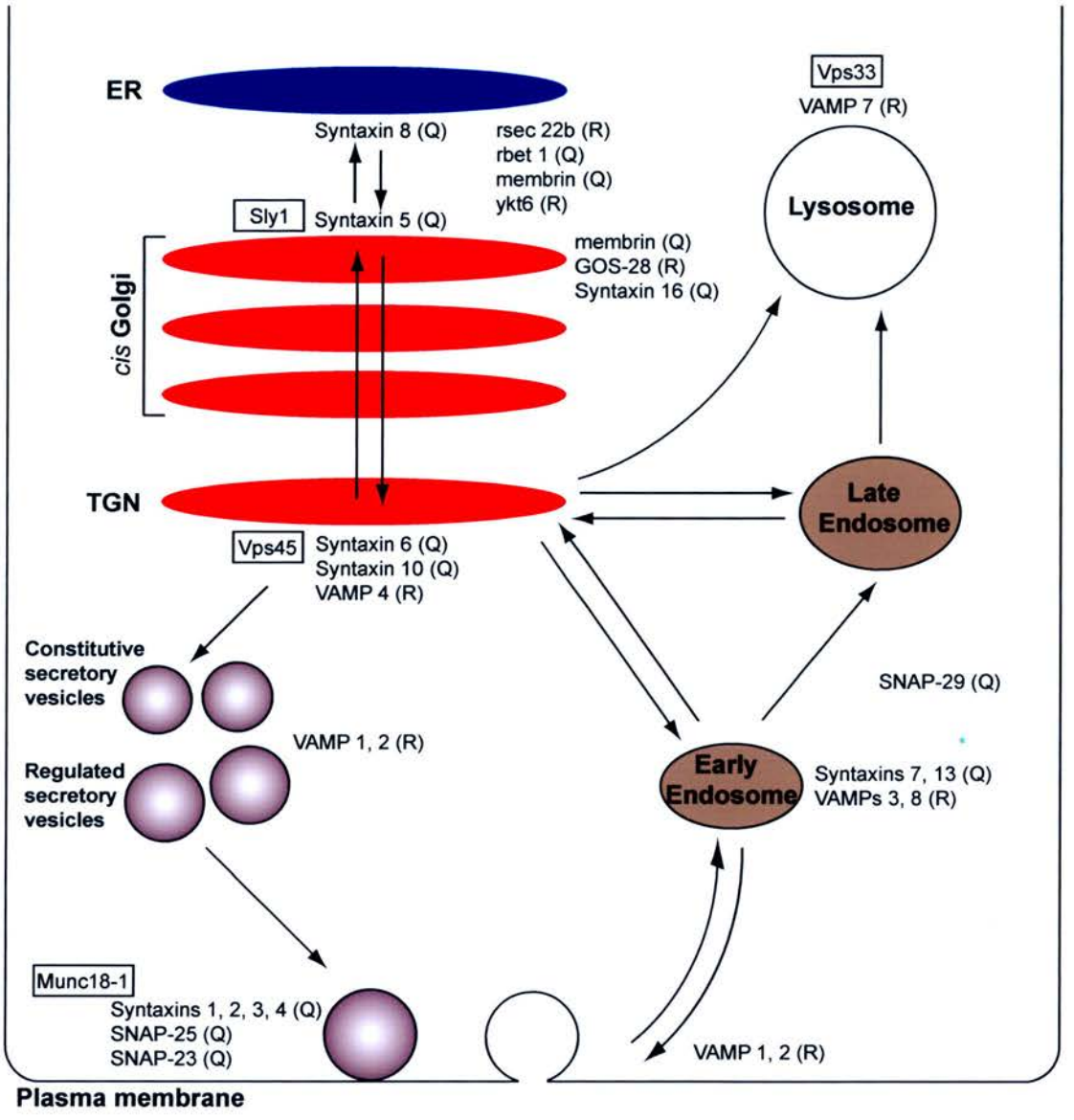

Figure 1.1 Subcellular localisation of the membrane proteins involved in the secretory pathway in mammalian cells.

Eukaryotic cells consist of membrane-bound compartments that communicate with one another via the formation, release and merging of membrane bound protein vesicles. Delivery of different proteins to different destinations relies on protein sorting and targeting. Newly synthesised proteins are assembled in the endoplasmic reticulum (ER) and undergo further assembly in the *cis* Golgi complex. Secretory vesicles form in the *trans*-Golgi network (TGN) for delivery to distinct destinations. The TGN acts as a major branchpoint from which distinct membrane pathways emanate, including constitutive traffic via small vesicles to the plasma membrane, lysosomal biogenesis via the endosomal system and the regulated secretory pathway via secretory vesicles. The Q-SNARE proteins (Q) and R-SNARE proteins (R) and the Sec1/Munc18 proteins (boxed) are involved at different steps of the secretory pathway. (Adapted from Bellen, 1999).

involved in the yeast secretory pathway. Initially, temperature sensitive mutants defective in constitutive secretion of the protein invertase, a component of the yeast cell wall, were subjected to temperature changes. As a result cell surface growth in the secretion mutants was blocked, yet protein synthesis continued, and additionally the mutants failed to secrete invertase and other components of the cell wall (Novick & Schekman, 1979). The identified secretory mutants represented defects in a total of 23 gene products that were involved in the secretory pathway: from the ER to the Golgi complex; from the Golgi complex to the formation of secretory vesicles; or from the transport of secretory vesicles to the cell surface (Novick et al, 1980). This included Sec1 (a Sec1/munc18 protein), Sec4 (a Rab/GTPase), Sec9 (a target membrane SNARE protein), and Sec22 (a vesicle membrane SNARE protein) (Novick et al, 1980).

In subsequent years, Rothman and colleagues developed an experimental system in which the vesicular transport of proteins between successive Golgi compartments was reconstituted *in vitro* (Balch et al, 1984; Rothman & Fries, 1981). The Golgi membranes from a mutant mammalian cell defective in glycosylation were mixed with those from a normal cell, and the transport of vesicular viral glycoproteins between the defective and normal Golgi compartments were detected (Balch et al, 1984; Rothman & Fries, 1981). This cell free assay advanced the field considerably by allowing the isolation of factors that are essential for intracellular transport. Studies showed that the process required ATP and could be inhibited by N-ethylmaleimide (NEM) (Glick & Rothman, 1987). Subsequently, the identification and characterisation of N-ethylmaleimide-sensitive fusion protein (NSF) (Fries & Rothman, 1980; Rothman & Fries, 1981) and soluble NSF attachment proteins (SNAPs) (Clary et al, 1990; Clary & Rothman, 1990) initiated a new understanding of membrane fusion. Future studies identified SNAPs as molecules that were capable of binding with NSF and the action of SNAPs was suggested to be conserved throughout evolution (Clary et al, 1990; Clary & Rothman, 1990). NSF is a trimeric ATPase that is known to be directly involved in membrane fusion and can only bind to Golgi membranes in the presence of SNAPs (Clary et al, 1990; Clary & Rothman, 1990). Therefore, both NSF and SNAPs were recognised as being essential for the

maintenance of intracellular membrane fusion. It transpired that the factors Sec17 and Sec18 originally identified by Novick and colleagues (Novick et al, 1980) were homologous to α-SNAP (Clary et al, 1990) and NSF (Wilson et al, 1989), respectively.

Following the biochemical observations provided by NSF and SNAPs, Rothman and colleagues investigated the membrane receptors of these proteins. It was established that three neuronal SNARE proteins existed and that they were universally involved in membrane fusion in mammalian cells (Sollner et al, 1993b). It must be noted that these three SNARE proteins had been identified previously. Vesicle associated membrane protein (VAMP) (Trimble et al, 1988) or synaptobrevin (Baumert et al, 1989) was first described as one of the components of synaptic vesicles. Syntaxin 1 was first identified using a monoclonal antibody raised against a synaptosomal membrane preparation (Barnstable et al, 1985; Inoue & Akagawa, 1992). Alongside, synaptosome-associated protein of 25 kDa (SNAP-25) was isolated and charactersised (Oyler et al, 1989), and found to be associated with the presynaptic plasma membrane via its palmitoyl chains (Hess et al, 1992). However, the work by Rothman and colleagues was the first to conclude that the SNARE proteins interacted to form a SNARE core complex that localised to membranes destined to fuse (Sollner et al, 1993a; Sollner et al, 1993b).

Subsequent studies confirmed that the SNARE proteins were involved in all intracellular transport processes and that they were highly conserved throughout the eukaryotic kingdom (Bennett & Scheller, 1993; Ferro-Novick & Jahn, 1994; Jahn & Sudhof, 1999; Sudhof et al, 1989). Therefore, the initial identification of SNARE proteins in the yeast secretory pathway established the basis and fundamental importance of the SNARE proteins in membrane fusion. These findings have since led to major advances in our understanding of the molecular mechanisms of the SNARE proteins and their regulation of membrane fusion.

1.3.2 THE SNARE PROTEINS

At a molecular level, secretory vesicle exocytosis is a highly regulated cascade that proceeds through an orchestrated sequence of protein-protein interactions, coupled with elevated calcium levels, resulting in the fusion of docked vesicles with the plasma membrane (Burgoyne & Morgan, 2003; Jahn & Sudhof, 1999). The molecules involved in exocytosis are well defined, but the location and timings of their actions remain largely unknown. The conserved family of SNARE proteins and their regulatory partners mediate intracellular membrane fusion events throughout the eukaryotic kingdom (Bennett & Scheller, 1993; Ferro-Novick & Jahn, 1994). Although SNARE proteins are present in neurons, their identification in pancreatic β-cells suggested that they may play a role in other forms of exocytosis (Jacobsson et al, 1994; Kuliawat et al, 2004; Wheeler et al, 1996). This model of the exocytotic process has been supported by studies of decreased SNARE expression in diabetic models (Gaisano et al, 2002; Nagamatsu et al, 1999; Zhang et al, 2002).

SNARES are a superfamily of small, abundant membrane-anchored or membrane-associated proteins. In neuronal and hormonal cells these consist of synaptobrevins, syntaxins, and synaptosomal-associated protein of 25 kDa (SNAP-25s) (Chen & Scheller, 2001; Jahn, 2004; Jahn & Sudhof, 1999). Traditionally, SNAREs were classified in relation to their membrane localisation, suggesting two types of SNAREs, v-(vesicle) SNAREs and t-(target membrane) SNAREs (Sollner et al, 1993a). These localisations led to the SNARE hypothesis that vesicle docking and subsequent fusion was determined by the specificity of v-SNARE and t-SNARE interactions (Rothman, 1994a; Rothman, 1994b; Sollner et al, 1993a). In addition, a second classification was proposed, depending on the presence of a single key residue in their SNARE binding motif, arginine (R-SNAREs) or glutamine (Q-SNAREs) (Fasshauer et al, 1998) (Figure 1.2). The SNARE proteins are defined by a heptad repeat sequence of 60-70 amino acids, known as the SNARE motif, which is characterised by a high potential coiled-coil formation (Jahn & Sudhof, 1999; Weimbs et al, 1997). Both syntaxin and synaptobrevin contain a single SNARE motif adjacent to a C-terminal transmembrane domain (Fasshauer, 2003) (Figure 1.2A). Additionally, syntaxin contains an

independently folded three-helical N-terminal domain, called the Habc domain (Fernandez et al, 1998). In contrast, SNAP-25 is composed of two SNARE motifs present at the C-terminus and N-terminus, which are connected by a flexible cysteine-rich central domain (Gerst, 1999; Salaun et al, 2004) (Figure 1.2A). As SNAP-25 lacks a transmembrane region, it is anchored to the plasma membrane via the attachment of fatty acids to the cysteine residues of the linker region, known as palmitoylation (Gonzalo et al, 1999; Loranger & Linder, 2002; Veit et al, 1996). The SNARE motifs from syntaxin, synaptobrevin and SNAP-25 can all interact to form a stable ternary complex, known as the core complex, which bridges opposing membranes preceding membrane fusion (Sollner et al, 1993a).

1.3.3 SNARE CORE COMPLEX ASSEMBLY

Biochemical studies have revealed binary interactions between all three SNARE proteins, yet these studies relied primarily on western blotting techniques (Chapman et al, 1994; Hayashi et al, 1994; Pevsner et al, 1994a), and the only stable binary complex is formed between syntaxin and SNAP-25 (Rickman et al, 2004). This binary complex was difficult to characterise and the isolation of a 2:1 syntaxin/SNAP-25 binary complex represented a dead end complex (Fasshauer et al, 1997). It is now known that the syntaxin/SNAP-25 binary complex exhibits 1:1 stoichiometry and represents a dynamic acceptor for synaptobrevin binding (Rickman et al, 2004; Weninger et al, 2008).

An overwhelming body of evidence has established that the SNARE proteins are essential for intracellular membrane fusion, mediated by a core complex composed of all three SNARE proteins (Gerst, 2003; Jahn & Sudhof, 1999; Sollner et al, 1993a; Sudhof, 2004). In neuronal and neuroendocrine cells, vesicle fusion at the plasma membrane is mediated by the vesicular protein synaptobrevin, and the plasma membrane proteins, syntaxin 1a and SNAP-25. These three proteins undergo a large structural rearrangement to form a trimeric four helical complex, bringing together opposing membranes (Hu et al, 2002; Parlati et al, 1999; Sutton et al, 1998; Weber et

al, 1998) (Figure 1.2A). By virtue of their SNARE motifs, synaptobrevin, syntaxin 1a and SNAP-25 interact to form a highly stable, *trans* core complex with 1:1:1 stoichiometry (Jahn, 2004). The SNARE motifs assemble spontaneously and in parallel to form an elongated coiled four-helix bundle, with the N-termini at one end of the bundle and the C-termini at the membrane anchor end (Jahn & Sudhof, 1999; Sutton et al, 1998) (Figure 1.2A).

The crystalline structure of the complex was obtained by x-ray crystallography, and not only revealed the four helical structure but in addition, the important hydrophobic and ionic interactions between the four α-helices (Sutton et al, 1998). The core complex is a twisted four helical bundle with an overall length of 12 nm (Sutton et al, 1998). The centre of the SNARE core complex consists of 16 layers of hydrophobic interactions, stacked perpendicular to the axis of the helical bundle (Sutton et al, 1998). In the centre of the helical bundle is a central ionic layer formed from one glutamine amino acid on each helix of syntaxin (Q226) and SNAP-25 (Q53 and Q174) and an arginine residue (R56) from synaptobrevin (Fasshauer et al, 1998) (Figure 1.2B). It was predicted that the trans SNARE complex forms in sequential steps as the four helices 'zipper up' starting with the folding N-terminal tips of SNAP-25 and syntaxin 1a helices, progressing towards the membrane C-terminal regions that anchor the proteins to the membrane (Fasshauer, 2003; Zhang et al, 2005). This would bring the membranes into close proximity to one another, and therefore is essential for SNARE complex formation and membrane fusion (Fasshauer, 2003; Zhang et al, 2005) (Figure 1.2C).

1.3.4 THE SNARE HYPOTHESIS

The discovery that the three SNARE proteins interact to form the SNARE core complex led Sollner and colleagues (Sollner et al, 1993a; Sollner et al, 1993b) to speculate how specificity was achieved during membrane trafficking and the SNARE

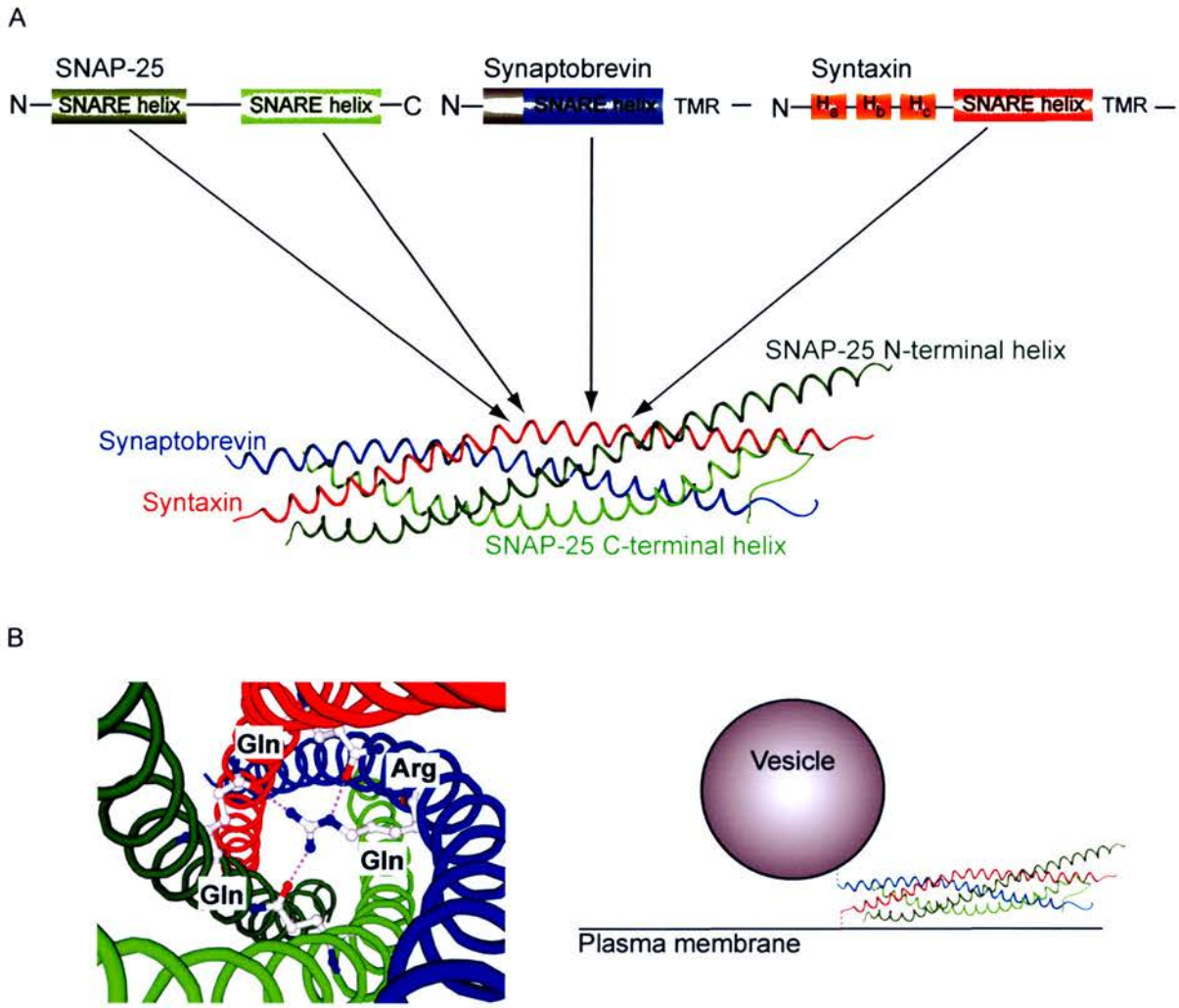

Figure 1.2 Model of the neuronal SNAREs assembled into the SNARE core complex

(A) SNAP-25 contains two SNARE helices joined by a central palmitoylated linker region. Syntaxin contains one SNARE helix between the C-terminal transmembrane region (TMR) and the N-terminal Habc domain. Synatobrevin has one SNARE helix adjacent to its TMR. The SNARE proteins are largely monomeric in their unreactive state and undergo a large structural rearrangement to form the ternary SNARE complex. The SNARE helices from the SNARE proteins form a four helical SNARE core complex and are shown as a ribbon diagram. Colour scale as follows: SNAP-25, green; Synaptobrevin, blue; Syntaxin, red. (Protein Data Bank number: 1SFC (Sutton et al., 1998)). **(B)** The central ionic layer of the SNARE core complex (left panel). The protein backbone is shown as a ribbon diagram with the colour scale corresponding to above. This layer is composed of one glutamine residue (Gln) from syntaxin (Q-SNARE) and two from SNAP-25 (Q-SNARE). The R-SNARE synaptobrevin contributes one arginine (Arg) residue to the ionic layer. The SNARE core complex forms between the plasma membrane and vesicle membrane SNAREs (right panel). This pulls the two opposing bilayers together, driving membrane fusion.

hypothesis emerged. The two major theories of the SNARE hypothesis were that NSF and α-SNAP would bind to the SNARE complex, and ATP hydrolysis by NSF was vital to provide the energy to merge the two opposing bilayers (Sollner et al, 1993a; Sollner et al, 1993b). It was also hypothesised that the donor membranes contained unique v-SNAREs, which would bind cognate t-SNAREs on the acceptor membranes. Therefore, the SNARE hypothesis provided a molecular explanation for the specific targeting of vesicles to the correct membrane compartments.

However, the SNARE hypothesis was later revised when it was discovered that the complex containing syntaxin, SNAP-25, synaptobrevin, NSF and α-SNAP was involved in the final fusion step, and ATP hydrolysis by NSF appeared to be the driving force in membrane fusion (Rothman, 1994a; Rothman, 1994b). Rothman and colleagues also showed that SNARE proteins can only interact productively with their cognate partners if they are in the correct orientation (Rothman, 1994a; Rothman, 1994b). It then became clear that the function of NSF and SNAP was not only to drive membrane fusion but also to open up or disassemble the SNARE complex, allowing recycling for the next round of fusion (Nichols et al, 1997; Ungermann et al, 1998). Furthermore, it was hypothesised that the formation of the stable core complex generated the energy to overcome the energy barrier separating the two membranes and drive fusion (Sutton et al, 1998). After the final fusion step the SNARE complexes adopt a *cis*-configuration, with their energy spent, ready for recycling by NSF induced ATP hydrolysis, and re-localisation to act as fusion catalysts for the next round of membrane fusion (Hanson et al, 1995; Jahn, 2004; Jahn & Sudhof, 1999; Littleton et al, 2001).

It was originally thought that there may be enough v- and t-SNAREs to allow each SNARE to act in only one transport step. However, it is now evident that a limited subset of SNAREs exists, therefore indicating that these are not sufficient to specifically label all the different cell compartments for membrane fusion. Biochemical studies have demonstrated that various SNAREs can interact to form multiple combinations of complexes with similar stabilities (Fasshauer et al, 1999;

Yang et al, 1999). It does however, remain clear that the SNARE proteins play a central role in membrane fusion, yet it is unknown if they provide all the specificity and control leading up to SNARE complex assembly. A wide variety of SNARE interacting proteins have been identified and implicated in the regulation of SNARE protein function, including munc13-1, which has been allocated a role in vesicle priming (Ashery et al, 2000; Gerst, 2003; Sheu et al, 2003), while others such as munc18-1 and Rab proteins are suggested to control vesicle trafficking, docking and exocytosis (Dulubova et al, 1999; Dulubova et al, 2003; Fischer von Mollard et al, 1994; Sogaard et al, 1994).

So, although parts of the SNARE hypothesis have been disproved, its core proposal has survived, that the SNARE proteins are the driving force of membrane fusion through the formation of the SNARE complex. However, the proteins responsible for specificity remain controversial with an array of candidates currently being investigated.

1.4 Regulation of SNARE complex formation

1.4.1 Sec1/munc18 (SM) proteins

A vital regulatory function in membrane fusion is the prevention of active fusion between membranes without control. Secretory cells can achieve this by limiting the participation of the SNARE proteins in the core complex. Central to this is the ability of the SNARE proteins to switch from inactive to active structural conformations, which is suggested to be under the control of the Sec1/Munc18 (SM) proteins that operate throughout the secretory pathway (Dulubova et al, 1999; Dulubova et al, 2003). The SM proteins are present throughout the eukaryotic kingdom and regulate SNARE function by interacting with their cognate syntaxins, thus regulating both temporally and spatially the formation of the SNARE complex (Dulubova et al, 2003; Gundelfinger et al, 2003).

SM protein mutations are characterised by severe disruption of general secretion or neurotransmitter release, indicating a central role for SM proteins in intracellular trafficking (Harrison et al, 1994; Novick & Schekman, 1979; Verhage et al, 2000). Early genetic screens in *S.cerevisiae* for secretion mutants revealed that many more proteins than just the SNAREs were essential for membrane fusion (Novick et al, 1981; Novick et al, 1980; Novick & Schekman, 1979). One such regulatory factor, named Sec1p, was found to play an essential role in *S.cerevisiae* intracellular pathways, and work in yeast subsequently identified several gene products that participate in exocytosis. Sec1 homologues were identified in *Caenorhabditis elegans* (Brenner, 1974) and *Drosophila melanogaster* (Salzberg et al, 1993). In mutant screens of *C.elegans*, a Sec1 homologue was independently found and termed unc-18 (uncoordinated-18) (Brenner, 1974). The importance of unc-18 was highlighted by mutations which resulted in motor defects due to an impairment of presynaptic function. This phenotype was also observed in *D.melanogaster* for the Sec1 homologue Rop (Ras opposite) (Salzberg et al, 1993).

The mammalian SM protein munc18-1 was first identified biochemically in rat brain based on its ability to bind to syntaxin with high affinity (Hata et al, 1993). It was later cloned based on its similarity to *D.melanogaster* Rop and *C.elegans* unc-18 (Garcia et al, 1994; Pevsner et al, 1994b). Munc18-1 is also known as n-Sec1 and rbSec1, which led to the confusion in the nomenclature of this protein, and thereby resulted in the Sec1p homologues all being grouped into the SM protein family. Grouping all the Sec1p homologues into the same protein family suggested a common mechanism throughout the eukaryotes; however, this is not supported by the available biochemical and genetic evidence.

The mammalian SM protein munc18-1 binds to the monomeric form of its cognate syntaxin, syntaxin 1, and studies using recombinant SNARE protein fragments and munc18-1 suggested that this rendered the t-SNARE unable to form the ternary SNARE complex (Pevsner et al, 1994b; Yang et al, 2000). Munc18-1 is a large cytosolic protein found predominantly in neurons and neuroendocrine cells (Hata et al, 1993; Pevsner et al, 1994a) that needs to bind to syntaxin to localise to the plasma

membrane (Dulubova et al, 1999; Dulubova et al, 2003). Initial interpretations all centred around the idea that munc18-1 acted to inhibit syntaxin, preventing SNARE complex formation. However, the SM proteins appear to have disparate binding specificities, and the specificity of munc18-1 for the monomeric form of syntaxin is in sharp contrast to that of its yeast homologue Sly1p which binds to the N-terminal of its cognate syntaxin, Sed5p, when in the ternary SNARE complex (Bracher & Weissenhorn, 2002) (Figure 1.3). Another yeast SM protein, Vps45p, binds to Tlg2p, its cognate syntaxin, both in the monomeric state and in the ternary SNARE complex (Bryant & James, 2001). This apparent discrepancy in binding modes suggested differences in the binding sites and recognition motifs of the SM proteins and their syntaxin partners.

To date, the crystal structures of both munc18-1 and Sly1p, in complex with their cognate syntaxins, have been solved (Bracher & Weissenhorn, 2002; Misura et al, 2000b). Sly1p formed a similar arch like structure to munc18-1, composed of three distinct domains. However, comparison of the binding sites of syntaxin and Sed5p revealed two separate modes of interaction with their respective SM protein. Bracher and Weissenhorn (2002) showed that Sed5p bound solely to the N-terminal domain of Slylp on the surface of the protein (Figure 1.3B). In contrast, syntaxin binds to domains 1 and 3 of munc18-1 and occupies most of the space of the arch of munc18-1 (Misura et al, 2000b) (Figure 1.3A). These differences in the binding specificity have resulted in controversy over the role of SM proteins.

1.4.2 SYNTAXIN AT THE CENTRE STAGE OF REGULATION

The syntaxin proteins are membrane-integrated Q-SNARE proteins that are crucial components of the SNARE fusion machinery, vital for intracellular vesicle trafficking and membrane fusion. At present the syntaxin family consists of 15 members in mammals, and 7 syntaxin-like genes in the yeast *Saccharomyces cerevisiae* (Teng et al, 2001). Syntaxin was first described as two 35 kDa proteins, which are now known as syntaxin 1a and 1b, sharing an overall sequence identity of

84% and interacting with the synaptic-vesicle protein synaptotagmin (Bennett et al, 1992; Bennett et al, 1993). The domain structure of syntaxin 1a was the first to be identified and is shown in Figure 1.2A (Weimbs et al, 1997). Syntaxins possess a single C-terminal transmembrane domain, a conserved central SNARE helix domain that provides one α-helix to the SNARE core complex (Weimbs et al, 1997), and in addition an N-terminal Habc domain that serves as a vital regulatory domain (Bracher & Weissenhorn, 2004; Lerman et al, 2000; Weimbs et al, 1997). This domain is conserved among syntaxin isoforms that are operating at the plasma membrane, including syntaxin 2, 3 and 4, and the yeast isoforms Sso1p and Sso2p (Fernandez et al, 1998). The sequence conservation would suggest that the N-terminal domain of syntaxin may have a specific function for exocytosis. The three dimensional structure of the N-terminal domain was first determined by Fernandez and colleagues using nuclear magnetic resonance spectroscopy (Fernandez et al, 1998). The domain was found to consist of a three helical bundle, and the third helix bound to the other two helices to form a groove between the second and third helix (Hb and Hc) (Fernandez et al, 1998). The amino acid residues within this groove were highly conserved, and it was suggested that it may serve as an interaction surface for another α-helix, in particular a SNARE α-helix (Fernandez et al, 1998).

Subsequently, it became clear that the N-terminal domain of syntaxin was capable of binding to several proteins that are suggested to be essential for synaptic vesicle exocytosis, including munc18-1 (Hata et al, 1993; Kee et al, 1995), and munc13-1 (Betz et al, 1997). Further experiments also revealed that the N-terminal Habc domain of syntaxin fulfilled an important regulatory function, allowing syntaxin to adopt two different conformations (Dulubova et al, 1999; Munson & Hughson, 2002; Nicholson et al, 1998). Crystallisation of syntaxin 1a in complex with munc18-1 revealed the existence of a closed conformation (Misura et al, 2000b), however, it must be noted that in this structural study the first 29 amino acid residues of the N-terminus of syntaxin 1a were unresolved. Reanalysis of this data has since demonstrated that the N-terminus of syntaxin 1a is bound to munc18-1 (Burkhardt et al., 2008). In the closed conformation, the N-terminal Habc domain formed by three α-helices is folded over the SNARE helix obstructing its interaction with cognate

SNAREs, thereby preventing SNARE complex assembly (Bracher & Weissenhorn, 2004; Dulubova et al, 1999; Fasshauer, 2003; Misura et al, 2000b; Toonen, 2003). In comparison, an open or reactive conformation is also possible in which the SNARE helix is free and SNARE core complex formation is permitted (Dulubova et al, 1999; Fasshauer, 2003; Salaun et al, 2004; Toonen, 2003; Toonen & Verhage, 2007). Therefore, the three dimensional structures of syntaxin 1a in the core complex and in complex with munc18-1 may be snapshots of potential intermediates in membrane fusion. The interaction of the N-terminal domain and the SNARE helix of syntaxin may have evolved to fulfil special regulatory requirements of membrane fusion. It may be possible that this interaction is controlled by other proteins such as munc18-1 or munc13-1, proving to be essential to SNARE regulation.

1.4.3 THE SYNTAXIN 1A – MUNC18-1 INTERACTION

It is generally accepted that munc18-1 has a close inter-relationship with its cognate syntaxin and that munc18-1 plays a vital regulatory role in SNARE function. In the closed conformation, the N-terminal Habc domain interacts with the SNARE helix obstructing its interaction with cognate SNAREs and thus SNARE complex assembly (Bracher & Weissenhorn, 2004; Dulubova et al, 1999; Misura et al, 2000b). Munc18-1 binds with high affinity to this closed conformation preventing syntaxin from entering the SNARE complex, acting as a negative regulator of membrane fusion (Dulubova et al, 1999). In contrast, in the open conformation, the SNARE helix does not interact with the N-terminal domain and this conformation was previously shown not to interact with munc18-1 (Dulubova et al, 1999). This was supported by *in vitro* studies, where removal of the Habc domain and open mutations such as L165A/E166A were used to disrupt munc18-1 binding to syntaxin (Dulubova et al, 1999). It was hypothesised that to initiate SNARE core complex assembly, the dissociation of the syntaxin 1a-munc18-1 complex was necessary to allow a conformational change in syntaxin 1a, essentially "opening" the molecule and exposing the SNARE helix to initiate SNAP-25 and synaptobrevin binding to permit SNARE complex assembly (Dulubova et al, 1999) (Figure 1.3A).

In contrast, the yeast homologues Sec1 and Sly1p suggest a positive regulatory role for SM proteins in SNARE mediated membrane fusion, remaining bound to their cognate syntaxin during SNARE complex formation, and therefore acting as chaperones (Bracher & Weissenhorn, 2002; Carr et al, 1999; Dulubova et al, 2003; Misura et al, 2000b). The binding of Sly1p to the N-terminal region of its cognate Sed5p is compatible with SNARE complex assembly (Figure 1.3B). With the apparent divergence in binding modes between members of the SM protein family, recent studies have focused on the interaction of munc18-1 with the N-terminal domain of syntaxin. The interaction between munc18-1 and the N-terminal domain of syntaxin could be maintained throughout the formation of the binary and ternary SNARE complex, something not previously realised (Burkhardt et al, 2008; Dulubova et al, 2007; Rickman et al, 2007; Shen et al, 2007).

1.4.4 Regulating the syntaxin 1a-munc18-1 interaction

Munc18-1 binds tightly to syntaxin holding it in a closed conformation that prevents SNARE complex assembly (Bracher & Weissenhorn, 2004; Dulubova et al, 1999; Misura et al, 2000). In some as yet undefined way, syntaxin switches to an open conformation that permits its interaction with cognate SNARE proteins. Therefore, the munc18-1-syntaxin 1a interaction provides an important mechanism for the regulation of membrane fusion. A number or factors have been implicated in the regulation of the munc18-1-syntaxin 1a complex.

Increased protein phosphorylation has been shown to enhance exocytosis in most secretory cell types, including neurons and neuroendocrine cells (Gillis et al, 1996; Hille et al, 1999; Majewski & Iannazzo, 1998). However, the molecular mechanisms and the protein targets remain unclear. Importantly, munc18-1 is known to be phosphorylated by protein kinase C (PKC) *in vitro* at the serine amino acid residue at position 313 (Craig et al, 2003). A recent report highlighted that the phosphorylation

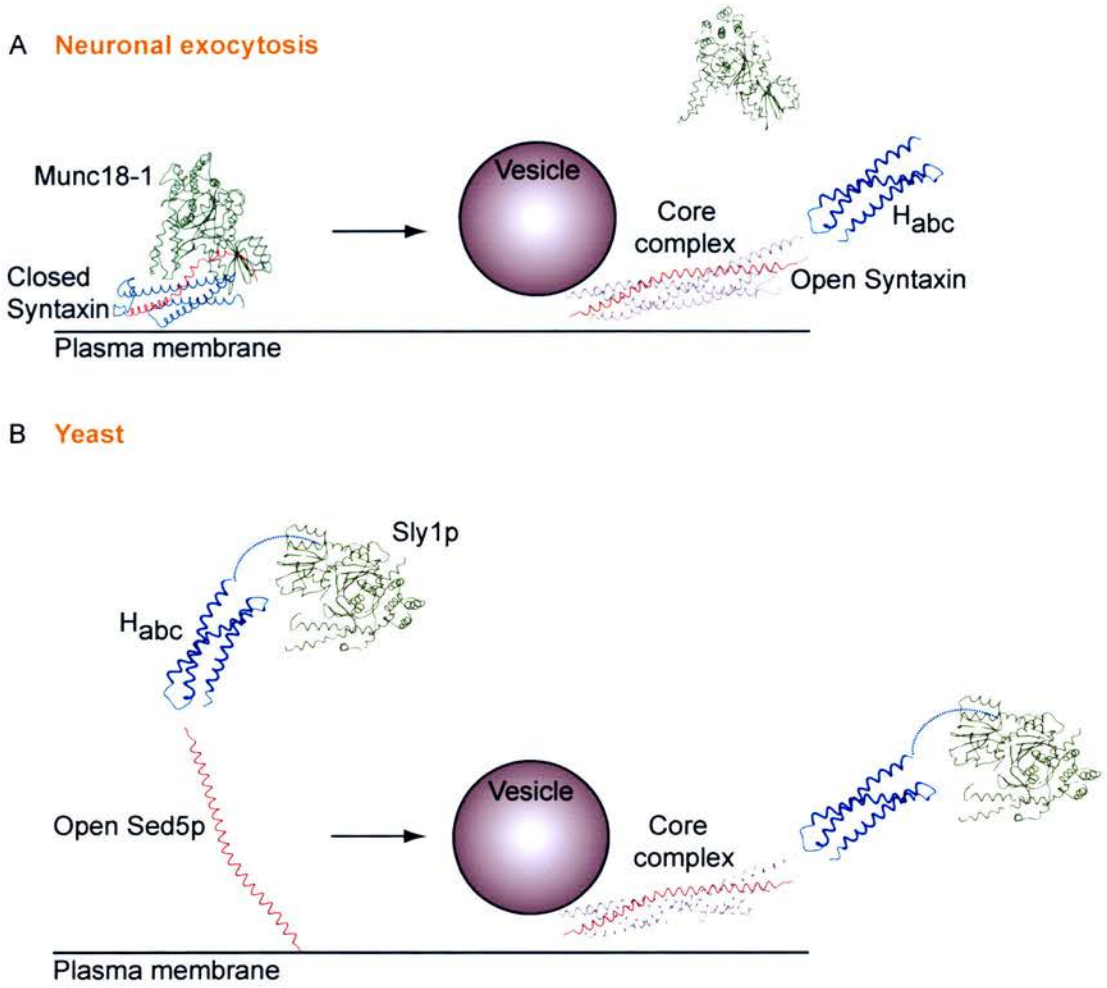

Figure 1.3 Different modes of syntaxin and SM protein coupling.
(A) In neuronal exocytosis munc18-1 (green) interacts with the closed conformation of syntaxin (SNARE helix, red, N-terminal H_{abc} domain, blue) (Protein Data Bank number: 3C98 (Burkhardt et al., 2008)) and prevents the assembly of the SNARE core complex. Munc18-1 was suggested to dissociate from syntaxin, allowing it to adopt the open conformation and enter into the SNARE core complex (Protein Data Bank number: 1SFC (Sutton et al., 1998)). Syntaxin N-terminal H_{abc} domain (Protein Data Bank number: 1BR0 (Fernandez et al., 1998)). **(B)** In yeast, the munc18-1 homologue Sly1p (green) (Protein Data Bank number: 1MQS (Bracher and Weissenhorn, 2002)) binds to the N-terminus of the syntaxin homologue, Sed5p, when it is in the open conformation and allows the formation of the SNARE core complex. Sly1p remains bound to the N-terminus of Sed5p upon SNARE core complex assembly (Protein Data Bank number: 1SFC (Sutton et al., 1998)).

of munc18-1 is essential for the regulation of exocytotic release kinetics by PKC (Barclay et al, 2003), suggesting that Ser-313 phosphorylation is functionally significant. Additionally, it has been reported that munc18-1 phosphorylation by PKC reduces the affinity of munc18-1 for closed syntaxin 1a (Fujita et al, 1996; Toonen & Verhage, 2007). Furthermore, munc18-1 phosphorylation by cyclin-dependent kinase 5 (Cdk5) resulted in the dissociation of the munc18-1-syntaxin 1a complex (Fletcher et al, 1999) thereby suggesting that Cdk5 acts to regulate munc18-1 interaction with syntaxin 1a. However, both the PKC and Cdk5 phosphorylation sites are buried at the centre of the munc18-1-syntaxin 1a complex, indicating that PKC and Cdk5 phosphorylation can only occur when munc18-1 is free from syntaxin 1a. This argues against a direct disruption of the munc18-1-syntaxin 1a complex. The phosphorylation of munc18-1 may therefore regulate the number of munc18-1-syntaxin 1a complexes available, and thus represent a potential regulatory mechanism underlying membrane fusion.

Another candidate for the regulation of the munc18-1-syntaxin 1a complex is the munc13 protein family. Munc13 proteins consist of a family of three highly homologous synaptic molecules (munc13-1, munc13-2, munc13-3), and munc13-1 has been shown to bind to free syntaxin 1 through the same binding site as munc18-1 (Betz et al, 1997). Munc13-1 has been identified as a priming factor by accelerating the maturation of docked vesicles to a pool of releasable, competent, primed vesicles (Ashery et al, 2000). The domain structure of munc13 with one diacylglycerol (DAG) binding domain and two Ca^{2+} binding domains is homologous to protein kinase C (PKC), indicating a possible calcium and DAG-dependent regulatory role for munc13 (Shen et al, 2005). Because munc13 proteins have C_1 domains that bind DAG, they may be subject to activation by the DAG second messenger pathway and PKC activators leading to membrane translocation and enhanced priming activity (Betz et al, 2001; Sheu et al, 2003; Stevens et al, 2005). The suggestion that munc13-1 plays a regulatory role in exocytosis is also supported by its interaction with the core complex by binding directly to syntaxin 1a and potentially switching on the exocytotic machinery (Betz et al, 1997). Therefore, munc13-1 priming activity possibly involves its regulation of the conformation of syntaxin 1a (Stevens et al,

2005), and it may stabilise an intermediate form of the core complex (Betz et al, 1997).

While these factors may regulate the pools of free munc18-1 and syntaxin 1a, additional factors may be responsible for the actual disruption of the munc18-1 interaction with the closed conformation of syntaxin 1a. Recent studies have identified that membrane fatty acids may play a role in regulating the conformational states of syntaxin 1a to permit SNARE complex assembly (Connell et al, 2007; Darios & Davletov, 2006; Rickman & Davletov, 2005). It has been shown that munc18-1 inhibition of neuronal syntaxin 1 can be overcome by arachidonic acid (Rickman & Davletov, 2005), which suggested that arachidonic acid acts to disrupt the munc18-1-syntaxin 1 interaction. Furthermore, it has been reported that arachidonic acid does not dissociate munc18-1 from syntaxin 1 but instead allows a conformational change in syntaxin 1, permitting the munc18-1-syntaxin 1 complex to interact with SNAP-25 (Connell et al, 2007). Additionally, the polyunsaturated fatty acids omega-3 and omega-6 have been suggested to change the conformational state of syntaxin 3 to permit an interaction with other SNAREs (Darios & Davletov, 2006). Together, these findings indicate that fatty acids may have a role in regulating the conformational status of syntaxin and thus SNARE complex formation.

Therefore, syntaxin appears to be a key player in the regulation of membrane fusion and its interaction with its regulatory partners, munc18-1 and munc13-1, or the action of phosphorylation or fatty acids on the munc18-1-syntaxin 1a complex may provide limiting steps in the secretory pathway. The ability of syntaxin to adopt two conformations may be vital in regulating the formation of the SNARE complex and subsequent membrane fusion. To date, the conformational states of the SNARE proteins, and the complexity of their interactions with one another and their regulatory partners is at the forefront of membrane fusion studies.

1.5 Optical approaches for investigating protein function in living cells

The credit for the first compound microscope is given to Zacharias Janssen in 1590. This compound microscope consisted merely of a tube with lenses at either end, with a magnifying power ranging from approximately 3 to 9. In 1648, it was Antonie van Leeuwenhoek who was the first person to actually build the first simple microscope. This microscope consisted simply of a magnifying glass mounted on a small stand that was capable of magnifying objects to a power of 3. Leeuwenhoek made good use of this microscope and he was the first to describe blood specimens, bacteria (from teeth scrapings), and protozoans (from pond water), the biological discoveries for which he is now famous. Leeuwenhoek's discoveries of protozoans in a drop of water were re-confirmed by Robert Hooke who made a copy of Leeuwenhoek's light microscope and improved on his design. However, it wasn't until the middle of the 19^{th} century that giant strides were made to improve the quality and capability of microscopes to gain instruments similar to today's microscopes. The biomedical sciences have been transformed by technological advances in microscopy that now allow dynamic investigations into living cells and tissues. A vast assortment of optical tools are currently being explored to understand the array of protein interactions involved in secretion, protein localisation, and the formation of protein complexes within cells.

The discovery of fluorescent proteins and the great technological advances in confocal microscopy in the 20^{th} century have also propelled microscopy to the forefront of biomedical research. Fluorophores that span the entire visible light spectrum are now commonly used as fusion partners to proteins to monitor their expression, distribution, co-localisation and dynamics within a cell (Day & Schaufele, 2005; Tsien, 1998; Tsien & Miyawaki, 1998; Wouters et al, 2001). The application of a wide range of new synthetic and naturally occurring fluorophores have made it possible to identify cells and sub-microscopic cellular components with a high degree of specificity. To date, investigations of exocytosis and the molecular machinery involved are readily accomplished with advanced fluorescent microscopy.

1.5.1 PRINCIPLES OF FLUORESCENCE

The term fluorescence was first introduced by George Stokes in 1852, based on his ability to illuminate a quinine solution using the ultraviolet region of the solar spectrum. It was these observations that led to the principle that fluorescence occurred at longer wavelengths than the exciting light, and this displacement was subsequently termed the Stokes shift. In addition to the Stokes shift, the phenomenon of fluorescence displays a number of general characteristics.

During fluorescence, a photon is supplied by an external light source (such as a laser) and absorbed by the fluorophore, which is therefore raised to an energetically excited state. The molecule stays in this excited state for a short period of time, typically 1-10 nanoseconds, losing energy before it relaxes back to the low energy ground state emitting a photon (Lakowicz, 2006; Lakowicz et al, 1992; Müller, 2002) (Figure 1.5A). Due to the energy dissipation during the excited state lifetime, the energy of this photon is lower, and therefore of a longer wavelength than the excitation photon (Pawley, 2006). This difference in energy or wavelength is known as the Stokes shift. The excess energy can be dissipated in many ways, the most common simply being to increase the atomic vibrations within the molecule, or to the surrounding environment (Lakowicz, 2006; Müller, 2002). When a molecule falls back to the ground state energy can be transferred to a second molecule via resonance energy transfer, which raises the second molecule to its excited state (Eftink, 1991; Förster, 1946) (see section 1.5.8).

Fluorescence data are usually presented as emission spectra. In a typical emission spectrum, the excitation wavelength is fixed, and the fluorescence intensity versus the wavelength is obtained. Emission spectra vary widely and are dependent upon the chemical structure of the fluorophore and the solvent in which it is dissolved (Lakowicz, 2006; Müller, 2002). However, perhaps the most important characteristics of a fluorophore are the fluorescence lifetime and the quantum yield. The fluorescence of a molecule is not only characterised by the emission spectrum, but it also possesses a distinctive fluorescence lifetime (Lakowicz et al, 1992). The

fluorescence lifetime of a molecule is defined as the average length of time that the molecule remains in the excited state before it falls back down to the ground state (Lakowicz et al, 1992). Another important parameter is the efficiency of fluorescence which is defined by the quantum yield. The quantum yield of fluorescence is the ratio of emitted photons to absorbed photons. Therefore, the quantum yield gives the probability of the excited state being deactivated by fluorescence rather than by another non-radiative mechanism (Lakowicz, 2006; Müller, 2002).

The principles of fluorescence are used every day in a variety of different technologies and industrial applications, from lighting to biomedical science. At present, fluorescence illumination and observation is now one of the most rapidly expanding microscopy techniques employed by the scientific community.

1.5.2 GREEN FLUORESCENT PROTEIN (GFP)

The discovery of genetically encoded fluorescent proteins (FPs) has sparked a revolution in fluorescence imaging, allowing the direct visualisation and quantification of individual proteins and protein complexes moving within and between cells. The discovery of green fluorescent protein (GFP), a naturally occurring fluorescent protein, is credited to the 2008 Nobel prize winner Osamu Shimomura, who isolated and purified GFP (Shimomura et al, 1962) from Pacific jellyfish *Aequorea victoria* and studied its properties. In *A.victoria*, GFP fluorescence occurs when the protein aequorin interacts with Ca^{2+} ions, inducing bursts of blue light and some of this luminescent energy is transferred to GFP, shifting the overall colour towards green (Morise et al, 1974). The molecular cloning of GFP cDNA (Prasher et al, 1992) and the ability to express GFP as a functional transgene (Chalfie et al, 1994) by the 2008 Nobel prize winner Martin Chalfie has revolutionised the biomedical sciences. Fluorescent GFP has since been successfully expressed in bacteria (Chalfie et al, 1994), yeast (Kahana et al, 1995), plants (Casper & Holt, 1996; Epel et al, 1996), drosophila (Wang & Hazelrigg, 1994), zebrafish

(Amsterdam et al, 1996) and mammalian cells (Kaether & Gerdes, 1995; Ludin et al, 1996).

The primary structure of GFP was initially deduced from the cDNA sequence (Prasher et al, 1992) and the crystal structure was later solved by Yang and colleagues (Yang et al, 1996). GFP is comprised of 238 amino acid residues and has a molecular weight of 27 kDa. Its structure consists of 11 antiparallel β-strands, wound into a 3D cylindrical barrel-like structure approximately 2.4 by 4.2 nm, and these hydrogen-bonded polypeptide β-sheets surround and protect a central α-helix containing the fluorophore, at the heart of the protein (Ormo et al, 1996; Prasher et al, 1992; Shimomura, 1979; Yang et al, 1996). The principal fluorophore (also known as the chromophore) is a tripeptide consisting of the amino acid residues serine, tyrosine and glycine at positions 65-67 in the sequence (Cody et al, 1993; Ormo et al, 1996; Shimomura, 1979; Yang et al, 1996). The maturation step of the fluorophore occurs within the specialised environment provided by the central interior of the β-barrel structure created by the folded protein. This modification involves a rapid cyclisation between the residues serine 65 and glycine 67 to form an imidazolin-5-one intermediate which is subsequently followed by a slower rate limiting oxygenation of the tyrosine 66 side chain (Heim et al, 1994; Ormo et al, 1996; Shimomura, 1979; Yang et al, 1996).

The excitation spectrum of wild-type GFP from *A.victoria* has two excitation maximum peaks, its biggest absorbance peak is at 395 nm (in the long UV range) with a smaller one at 475 nm (blue) (Chalfie, 1995). The fluorescence emission spectrum (green) peaks at 509 nm, but it also has a small emission peak at 540 nm (Chalfie, 1995). The recombinant *A.victoria* GFP generated in *E.coli* also has the same spectral properties (Chalfie et al, 1994). Initially, a problem for the use of GFP in fluorescent microscopy was the excitation and emission spectrum of the fluorophore. For wild-type GFP, exciting the protein at 395 nm led to rapid quenching of the fluorescence and 488 nm excitation was a more commonly available excitation source (Heim et al, 1995; Tsien, 1998). For these reasons, wild-type GFP has been significantly modified to improve its qualities as a fluorescent

reporter (Tsien, 1998). The work of 2008 Nobel prize winner Roger Tsien, led to spectral changes exerted by substitutions in amino acids from the GFP fluorophore, expanding the fluorescence behaviour of GFP, and ultimately provided an array of GFP variants for use in fluorescence microscopy.

Green fluorescent proteins were quickly found to exist in a variety of coelenterates, including hydrozoa such as *Aequorea*, *Obelia*, and *Phialidium*, and anthozoa such as the sea pansy *Renilla* (Morin & Hastings, 1971; Ward & Cormier, 1979). A variety of marine organisms have now been the source of greater than 100 fluorescent proteins and their analogues (Verkhusha & Lukyanov, 2004). An explosion in the use of fluorescent proteins has also resulted in numerous fluorescent protein genetic variants being produced, featuring fluorescence emission spectral profiles spanning almost the entire visible light spectrum, thereby making it possible for biologists to examine the expression, distribution, co-localisation and dynamics of specific proteins in cells (Tsien, 1998; Tsien & Miyawaki, 1998). Extensive mutagenesis of the original *A.victoria* fluorophore has resulted in an array of colour mutants, including blue fluorescent protein (BFP) (Heim et al, 1994), cyan fluorescent protein (CFP) (Heim et al, 1994), yellow fluorescent protein (YFP) (Ormo et al, 1996) and red or orange fluorescent proteins (Campbell et al, 2002; Tsien, 1998).

1.5.3 GFP VARIANTS

Yellow fluorescent protein (YFP) is one of the most versatile genetically encoded GFP variants yet developed, and it was engineered immediately after the crystal structure of GFP was resolved (Ormo et al, 1996; Tsien, 1998). The crystal structure of GFP revealed that the threonine residue at position 203 was positioned very close to the chromophore, thereby allowing Ormo and colleagues to hypothesise that it exhibited the potential to alter the spectral properties (Ormo et al, 1996). YFP was engineered by substitution of the threonine residue at position 203 with tyrosine or histidine in the GFP chromophore (Ormo et al, 1996; Tsien, 1998). This subsequently resulted in a 20 nm shift in the spectral profile, with longer

wavelengths for both the excitation and emission of the fluorophore detected (Ormo et al, 1996). However, in order to improve the performance of YFP in Förster or fluorescence resonance energy transfer (FRET) experiments, further sequence refinements were undertaken and led to the development of the enhanced yellow fluorescent protein (EYFP). This variant was produced by the substitution of glutamine by lysine at position 69 (Q69K) (Ormo et al, 1996; Tsien, 1998). At present, EYFP is one of the brightest and most widely utilised fluorescent proteins and when coupled with enhanced cyan fluorescent protein (ECFP) they provide a desirable FRET pair.

The first fluorescent proteins emitting in the cyan spectral region, from approximately 450 to 500 nm, were identified simultaneously with BFP during site directed mutagenesis studies (Heim et al, 1994; Tsien, 1998). Substitution of the tyrosine amino acid at position 66 in the GFP chromophore with tryptophan or histidine resulted in blue-green or cyan emission (Heim et al, 1994; Tsien, 1998). The largest change was evident for the histidine mutation, in which the excitation and emission peaks shifted 14 nm and 60 nm respectively, from that of wild-type GFP (Heim et al, 1994). The tryptophan mutation on the other hand resulted in excitation and emission wavelengths between that of wild-type GFP and the histidine mutation, and the fluorophore showed weak fluorescence (Heim et al, 1994). Further sequence refinements were therefore necessary to improve the fluorescence and photostability of the cyan fluorescent proteins, and consisted of the F64L (Cormack et al, 1996) and S65T (Heim et al, 1995) mutations. This resulted in the production of an enhanced version (ECFP) which exhibited both increased brightness and photostability (Cormack et al, 1996; Heim et al, 1995; Tsien, 1998).

Through the modification of existing fluorophores and the cloning of new colour variants, fluorescent proteins are now used as unique probes throughout the biomedical sciences. Overall, the array of genetically encoded fluorescent proteins now available, combined with advanced imaging techniques, have become revolutionary tools for labelling organelles and other subcellular compartments,

tracking the dynamic behaviour, co-localisation and spatial relationships between proteins in living cells.

1.5.4 CONFOCAL LASER SCANNING MICROSCOPY (CLSM)

The basic concept of confocal microscopy was originally developed and patented by Marvin Minsky in the mid-1950s, yet it wasn't until the late 1970s and 1980s that advances in computer and laser technology, coupled with new algorithms for digital manipulation of images led to a growing interest in confocal microscopy (Amos & White, 2003; Müller, 2002; Pawley, 1995). During the 1990s, large advances in optics and electronics allowed more stable and powerful lasers, high efficiency scanning mirror units, high throughput fibre optics and detectors with reduced noise characteristics to be developed (Amos & White, 2003; Diaspro, 2002; Müller, 2002; Pawley, 1995).

Confocal microscopy offers several advantages over conventional widefield optical microscopy, including the ability to control depth of field, elimination or reduction of background information away from the focal plane, and the ability to obtain serial optical sections from thick specimens (Diaspro, 2002; Müller, 2002; Pawley, 1995; Schatten & Pawley, 1988). The most powerful advantage of confocal microscopy over conventional microscopy is the ability to reject out-of-focus background light. This is achieved by an adjustable pinhole positioned in front of the detector, resulting in an improvement in the spatial resolution (Diaspro, 2002; Müller, 2002; Pawley, 1995). As a direct result only the light within the focal plane can pass through the pinhole for detection (Müller, 2002; Pawley, 1995; Pawley, 2006). To achieve point illumination the laser beam is focused to a diffraction limited spot, which illuminates only a point of the object at a time. It is possible to image a thin optical slice out of a thick specimen, a method known as optical sectioning. This allows a series of thin (0.1 to 1.5 μm) optical sections to be recorded at different planes of the specimen (Müller, 2002; Pawley, 1995). Therefore, the primary advantage of confocal microscopy is to create a three-dimensional (3-D) data set which makes it possible to

build 3-D renditions of the specimen. Furthermore, optical sectioning eliminates artefacts that occur during physical sectioning and fluorescent staining of tissue specimens for traditional forms of microscopy (Müller, 2002; Pawley, 1995).

The introduction of lasers in the 1960s provided an excitation source powerful enough that the fluorescent signal from a fluorophore was still usable after rejection by the pinhole, paving the way for the first laser scanning microscope in the early 1980s (Müller, 2002; Pawley, 1995; Pawley, 2006). Importantly, these advances in confocal microscopy allowed multi-dimensional views of living cells and tissues, which include image formation in the x, y and z dimensions as a function of time and multi-spectral detection using two or more fluorophores (Müller, 2002; Pawley, 1995). To date, an array of technological advances have made laser scanning microscopy an ideal choice for steady state fluorescence imaging permitting an increasingly accurate portrayal of the specimen under investigation (Day & Piston, 1999; Dumas et al, 2004; Schatten & Pawley, 1988). The developments that are relevant here include multi-photon excitation and techniques used to minimise image degradation caused by diffraction and noise.

1.5.5 TWO-PHOTON EXCITATION MICROSCOPY

A fast-growing technique that is directly related to confocal microscopy is multi-photon microscopy, which is used in this thesis in a two-photon configuration. The basic principles of two-photon excitation were first described by Maria Göppert-Mayer in 1931 (Göppert-Mayer, 1931), however, the hypothesis wasn't confirmed experimentally until the development of laser sources due to the high light intensity that is required to generate two-photon excitation (Berns, 1976; Denk et al, 1990; Kaiser & Garrett, 1961).

Two-photon microscopy is a powerful optical tool that combines the advanced optical techniques of laser scanning microscopy with long wavelength two-photon fluorescence excitation to capture high-resolution images to a depth of one millimetre with reduced phototoxicity (Denk et al, 1990; Helmchen & Denk, 2005;

Theer et al, 2003). Two-photon excitation works on the principle that at high photon densities, two photons can be almost simultaneously absorbed whose total energy equals that required for one-photon excitation (Callis, 1997; Denk et al, 1990; Denk & Svoboda, 1997). The high intensity illumination, at twice the excitation wavelength, is provided by pulsed lasers (such as a Titanium:Sapphire laser) that deliver a burst of photons to the same focal region in a short period of time (Denk et al, 1990; Diaspro, 2002; Duncan et al, 2004; Rubart, 2004). After the arrival of the first photon, the electron is raised from the ground state and to prevent the rapid loss of this excess energy a second photon must arrive within < 0.1 femtoseconds so that together they reach the energy threshold for excitation (Callis, 1997; Denk & Svoboda, 1997; Diaspro et al, 2006; Esposito et al, 2004; Rubart, 2004). For this reason, two-photon excitation requires a high density of photons, and a high energy pulsed laser.

Two-photon excitation gives rise to several advantages over commonly used single-photon confocal microscopy (Denk et al, 1990; Diaspro, 2002; Diaspro et al, 2006). Limiting fluorescence to the focal volume allows two-photon excitation to address the fundamental weakness of confocal laser scanning microscopy: that the laser beam also excites the specimen above and below the focal plane (Denk et al, 1990; Diaspro, 2002). The photons emitted from these regions will be rejected by the pinhole and therefore this information will be lost in traditional confocal microscopy (Denk et al, 1990; Denk & Svoboda, 1997; Diaspro, 2002; Rubart, 2004). In two-photon excitation, illumination is only achieved within the focal volume, so out-of-focus fluorescence is never generated (Denk et al, 1990). As excitation is limited to the focal plane there is no pinhole required in the microscope detection path, resulting in increased fluorescence collection efficiency (Denk et al, 1990; Diaspro et al, 2006; Rubart, 2004). The fluorophore excitation is therefore localised to the region immediately surrounding the focal point, as it is here that the photon density is at its highest, and this represents a thin optical section of the entire specimen (Diaspro, 2002; Diaspro et al, 2006; Rubart, 2004). This arises from the principle that when photons from the pulsed laser source are focused by a high numerical aperture objective, they become more crowded, thereby increasing the probability that two or

more will interact simultaneously (Denk et al, 1990; Diaspro, 2002; Rubart, 2004). Two-photon excitation ultimately results in higher image contrast due to the non-linear excitation (Centonze & White, 1998; Denk et al, 1990; Oheim et al, 2001). As other regions of the specimen are effectively not excited, they neither emit fluorescence nor are subject to photobleaching or photodamage, making two-photon excitation particularly favourable for live cell imaging.

Another advantage of two-photon excitation is that the penetration depth of the excitation beam is increased (Denk et al, 1990; Denk & Svoboda, 1997; Rubart, 2004). Observations on a variety of biological specimens have demonstrated that two-photon microscopy can increase penetration depth by at least two-fold in comparison to confocal imaging (Centonze & White, 1998; Oheim et al, 2001; Theer et al, 2003). There are a variety of reasons why penetration depth is increased in two-photon excitation. First, the longer wavelengths that are necessary for two-photon excitation are scattered considerably less than the shorter wavelengths used in standard confocal microscopy, and thus deeper penetration of the specimen is possible (Denk et al, 1990). Second, in standard confocal microscopy the scattered light emitted from the fluorophore is discarded by the pinhole and does not contribute to the final image. In direct contrast, in two-photon excitation, the scattered and non-scattered emitted light are both used to generate the final two-photon image, thereby increasing both fluorescence collection efficiency and signal intensity (Denk et al, 1990). Together these advantages of two-photon excitation have enabled specimens as diverse as brain (Denk & Svoboda, 1997; Helmchen & Denk, 2002), heart (Rubart, 2004), kidney (Molitoris & Sandoval, 2005), skin (Laiho et al, 2005) and lymphatic organs (Bousso & Robey, 2004; Cahalan et al, 2003) to be investigated. Therefore, in combination, improved specimen penetration depth, a limitation of fluorophore excitation to the focal plane, and a reduction in photobleaching have all allowed two-photon microscopy to become an invaluable tool in fluorescence microscopy.

1.5.6 LIGHT BEHAVIOUR IN THE MICROSCOPE

The ultimate purpose of the illumination path in microscopy is to produce a diffraction-limited illuminating spot at a plane within the biological specimen, and maintain the spot's integrity during the scanning process. However, microscope images are characterised by a number of microscope-specific parameters such as the numerical aperture (NA), magnification and resolution, and additional parameters that are dependent upon the specimen, including signal-to-noise, contrast and dynamic range (Inoué, 1995; Pawley, 1995; Pawley, 2006).

The microscope image is essentially formed by the scattering of light (diffraction) by the biological specimen, and by the collection of this diffracted light by the lens, to create the image (Pawley, 1995; Pawley, 2006). Every specimen detail that is uniformly illuminated by a circular aperture within a microscope does not produce a single point of light, but instead it appears as a diffuse circular disk. This is produced by spherical waves exiting the rear aperture of the objective and converging on the focal point (Diaspro, 2002; Inoué, 1995; Müller, 2002; Pawley, 1995). These diffraction disks are called Airy disks after their discovery by George Airy in 1827. The disks appear as a central circular point of maximum intensity surrounded by alternating bright and dark rings whose intensity decreases rapidly as the distance increases (Inoué, 1995; Pawley, 1995). This example of light diffraction is of great importance as the width of the Airy disk is used to define the theoretical maximum resolution of an optical system, and if the diameter of the Airy disks central peak becomes large relative to the pixel size it can begin to have a visual impact on the image (Pawley, 1995; Pawley, 2006). Alternatively, if two Airy disks become any closer than half their width they are also no longer resolvable (Müller, 2002; Pawley, 1995; Pawley, 2006).

The resolution of a microscope is defined as the distance between two light sources at which they can be distinguished as two separate points rather than a single point, typically around 200 nm (Pawley, 2006) (see also Chapter 2, Figure 2.4). The resolution is determined essentially by the illuminating light, the wavelength and the

numerical aperture (NA) of the objective (Inoué, 1995; Pawley, 1995). Therefore, one of the most important features of the microscope is the NA as it determines the proportion of emitted light that reaches the microscope detector (Pawley, 1995; Pawley, 2006). The NA is dependent upon the angle of collection light emitted from the specimen, and the refractive index of the medium between the lens and the specimen coverslip, which together affect the ability to distinguish between two adjacent punctate light sources (Bolte & Cordelieres, 2006). Therefore, higher values of NA allow increasingly oblique rays to enter the objective front lens, thereby improving the brightness and resolving power in both the vertical (z) and the lateral (x-y) focal plane (Pawley, 1995; Pawley, 2006).

In CLSM, optical sectioning is used to collect a 3-D data set that represents the 3-D volume of the biological specimen. As a consequence the diffraction or distribution of light in the focal region is considered as 3-D information, and this is defined by the point spread function (PSF) (Pawley, 2006). The PSF of an optical device is described as the 3-D light distribution of a single point, and as the PSF describes how a single point is distributed in 3-D, it also describes the distribution of every light source of a specimen measured by a fluorescence microscope (Inoué, 1995; Müller, 2002; Pawley, 2006). For these reasons, the image formation theory of a microscope is ultimately described by the PSF, which is the main element that builds up the acquired image (Inoué, 1995; Müller, 2002; Pawley, 1995). The entire image is built up by all the contributions from the original light sources, each generating a PSF, and the image is therefore computed as a summed contribution of PSFs, each shifted to the location and scaled according to the intensity of the corresponding point (Pawley, 1995; Pawley, 2006).

During the process of image acquisition by the microscope some information is degraded as a direct result of out-of-focus light, axial distortion and noise degradation, resulting in a decrease in image quality (Inoué, 1995; Pawley, 1995; Pawley, 2006). This degree of spreading or blurring is defined mathematically by the convolution of the PSF and is a direct measure of the microscope's ability to transform contrast from the specimen to the intermediate image plane at a specific

resolution (Pawley, 2006). The dimensions of the PSF can vary between fluorophores, refractive indices, and microscope systems, and the degree of blurring is indicative of the quality of the microscope (Müller, 2002; Pawley, 2006). So as the PSF can be used to characterise the image formation process in any specimen, knowledge of the PSF of an optical system acts as a useful tool to undo the degradations commonly introduced by the imaging process.

1.5.7 IMAGE RESTORATION THROUGH DECONVOLUTION

Although there are many advantages to using three-dimensional fluorescence microscopy, it also has its limitations, mainly the presence of electronic noise, and blurring due to the finite resolving power of the optical system. The diffraction of light and the variations in the refractive indices of the cells, tissue and surrounding structures in the region of interest can lead to a loss in intensity and distortion in the optical response of the system (Diaspro, 2002; Müller, 2002; Pawley, 2006). Therefore, image processing is required to deal with these problems, subsequently leading to improved image quality. A common image restoration process employed is deconvolution. This is a computationally intensive technique that works by reversing the optical distortion that occurs in the microscope to improve the contrast and resolution of the image (McNally et al, 1999; Pawley, 2006; Wallace et al, 2001).

The process of deconvolution employs the dimensions of the PSF and the microscope parameters along with deconvolution algorithms, which allows the out-of-focus fluorescence and background signals to be redistributed to restore the original signal (McNally et al, 1999; Pawley, 2006; Sibarita, 2005; Wallace et al, 2001). As a 3D image arises from the summed contributions of several PSFs, deconvolution works to deduce the original distribution of these point sources of light in the specimen to give rise to a more resolved image (McNally et al, 1999; Pawley, 2006; Sibarita, 2005; Wallace et al, 2001). Therefore, an accurate PSF is vital for deconvolution, and it is possible to experimentally measure the PSF in a

microscope system by recording the image of a sub-resolution spherical bead. However, due to the technical difficulties in directly measuring a PSF, theoretical PSFs are commonly used. Image restoration techniques such as deconvolution can be applied to 3D images from any microscope to further improve image quality. The importance of deconvolution has also been implicated in image analysis techniques such as co-localisation (Bolte & Cordelieres, 2006).

1.5.8 FÖRSTER RESONANCE ENERGY TRANSFER (FRET)

When and where proteins or other molecules interact with one another in living cells is a vital question to unravel their functions. GFP and related proteins have become important research tools that are commonly used as fluorescent fusions to proteins to report numerous biological events. To study protein-protein interactions high resolution is necessary, yet the optical resolution of light microscopy is restricted to approximately 200 nm (Müller, 2002; Pawley, 2006). Using Förster resonance energy transfer (FRET), the relative proximity of molecules can be reported beyond the optical resolution of light microscopy, allowing the identification of protein interactions and conformational changes inside living cells (Sekar & Periasamy, 2003; Stryer, 1978; Stryer & Haugland, 1967; Wouters et al, 2001). Traditionally, these interactions have been described using biophysical or biochemical techniques such as affinity chromatography or co-immunoprecipitation; however, these methods do not allow direct access to the protein interactions in their natural environment inside the living cell. In comparison, FRET microscopy allows this information to be obtained from living cells at nanometre resolution (Stryer, 1978; Stryer & Haugland, 1967).

FRET involves the direct non-radiative transfer of energy from a donor fluorophore to a neighbouring acceptor fluorophore through long range dipole-dipole interactions over short distances (Förster, 1965; Stryer, 1978; Stryer & Haugland, 1967; Wu & Brand, 1994). FRET imaging is therefore useful in reporting the ratio of fluorescence between the fluorophores indicating the degree of physiological association between

the labelled proteins (Sekar & Periasamy, 2003; van Roessel & Brand, 2002). This technique is based on the theories of Theodor Förster who in the 1940s proposed that electronic excitation energy can be efficiently transferred through dipole-dipole interactions from a donor fluorophore to an acceptor fluorophore in a distance dependent manner (Förster, 1946; Förster, 1965). However, a set of specific conditions must be established first for efficient energy transfer to occur (Figure 1.4). First, the distance between the donor and acceptor fluorophores must not exceed 10 nm (Figure 1.4A). Efficient fluorescence energy transfer from a donor molecule to an acceptor molecule decreases with the sixth power of the distance and thus is apparent only at distances shorter than 10 nm (Stryer, 1978; Stryer & Haugland, 1967). Second, the FRET signal can be reduced if the relative orientation of the donor emission dipole moment and the acceptor absorption dipole moment in 3D space is not favourable (Centonze et al, 2003; Sekar & Periasamy, 2003; Wu & Brand, 1994) (Figure 1.4A). Third, there must be a high degree of spectral overlap between the emission spectra of one fluorophore (the donor) and the absorption spectra of another fluorophore (the acceptor) (Centonze et al, 2003; Elangovan et al, 2002; Sekar & Periasamy, 2003) (Figure 1.4B). Finally, the donor and acceptor pair chosen must have a high quantum yield, so there is a high probability of energy transfer (Lakowicz, 2006).

The most promising use of ECFP became its coupling with EYFP to form a FRET pair, however, problems arose as the brightness levels obtained from ECFP were only about 33% of that shown by enhanced GFP (Rizzo et al, 2004). Additional problems were also identified, including limitations in the fluorophore properties that restricted measurements to a small dynamic range, and the potential to form dimers at high concentrations when confined to two dimensions (Zacharias et al, 2002). To overcome the dimerisation problems, Zacharias and colleagues replaced hydrophobic residues at the crystallographic interface of the dimer with positively charged amino acids (A206K, L1221K or F223R) in both ECFP and EYFP to produce monomeric forms of the fluorophores (Zacharias et al, 2002). The mutations did not alter the spectral properties of the fluorophores and further analysis by analytical ultracentrifugation confirmed that dimerisation was essentially limited in these

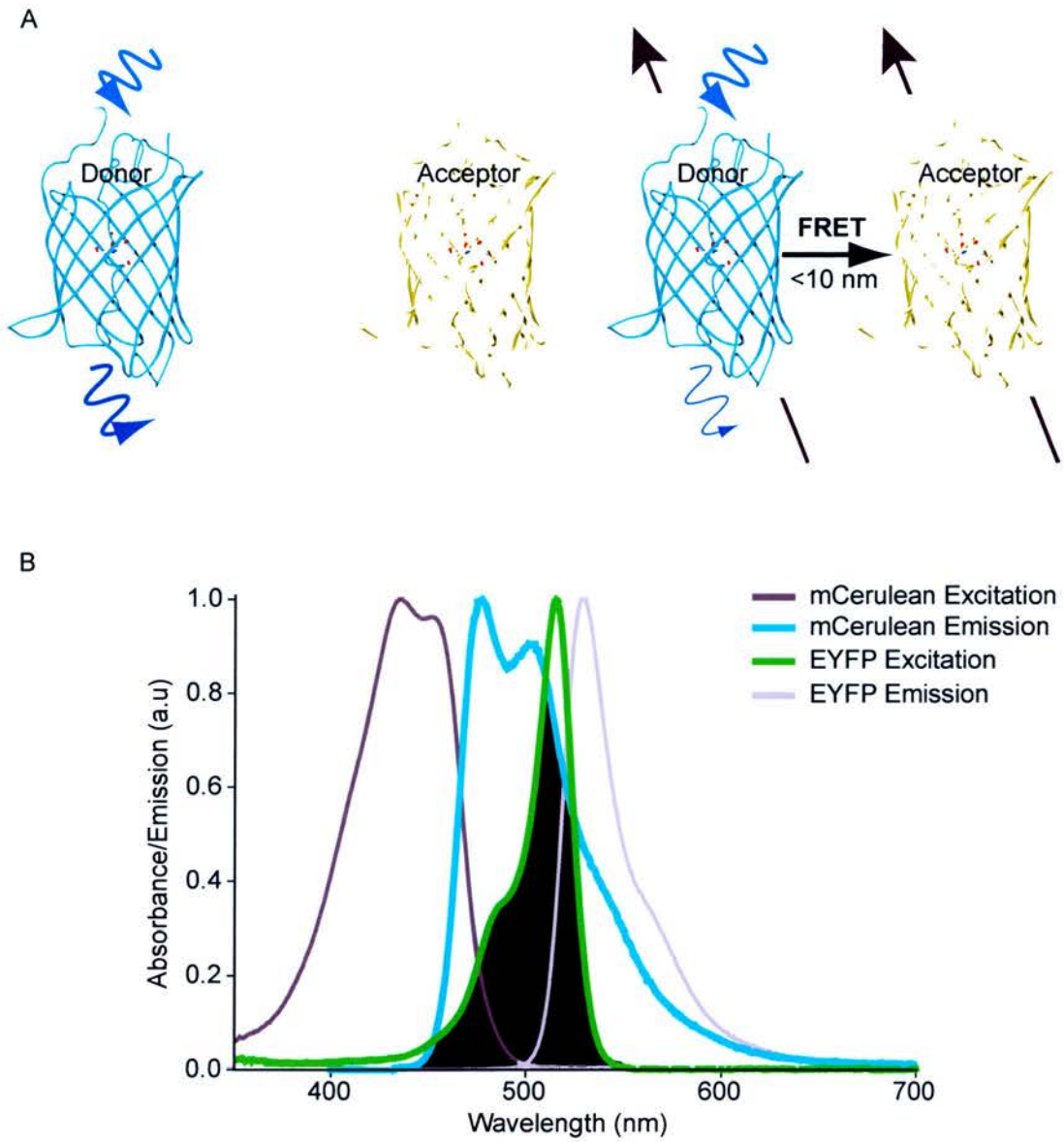

Figure 1.4 Factors affecting FRET measurements.
(A) A number of conditions must be met for FRET detection to be possible. A donor and an acceptor fluorophore must be <10 nm apart to undergo non-radiative energy transfer through a dipole-dipole interaction. The FRET signal can be reduced if the relative orientation of the donor and acceptor dipoles is not favourable. If the donor and acceptor dipoles are aligned parallel to each other, the FRET efficiency will be higher than if they were perpendicular. If the donor is excited, the excess energy may be lost via the emission of fluorescence or via energy transfer to the nearby acceptor. **(B)** Excitation and emission spectra overlap integral of mCerulean and EYFP. The donor fluorescence emission spectrum and the acceptor absorption spectrum must have a substantial overlap region, shown in black. The rate of energy transfer depends on the extent of spectral overlap between the donor emission and acceptor absorption.

monomeric forms (Zacharias et al, 2002). These mutations can therefore be applied to any GFP variant in order to generate a monomeric form to increase FRET efficiency levels between fluorophores (Zacharias et al, 2002).

Despite these advances in ECFP, problems still existed in using ECFP coupled with EYFP in FRET experiments, namely a low quantum yield, dim fluorescence and the fluorescent lifetime (see section 1.5.9) of ECFP was best fit to a double exponential decay function suggesting possible multiple excited states (Duncan et al, 2004; Rizzo et al, 2004). A "cerulean" fluorescent probe was engineered by Rizzo and colleagues (Rizzo et al, 2004) to improve the quantum yield of ECFP and to produce a CFP with a single exponential fluorescence lifetime. Mutation of the histidine residue at position 148 to aspartate provided a cerulean fluorophore that was over 2-fold brighter than ECFP in living cells and its fluorescence lifetime was best fit with a single exponential (Rizzo et al, 2004). The cerulean fluorophore was also found to have a similar spectral profile to ECFP, with only a slight reduction in the 505 nm emission peak observed (Rizzo et al, 2004). Together these improvements, and monomerisation, have greatly improved the use of cerulean as a FRET donor when coupled with yellow emitting fluorescent proteins such as EYFP in FRET investigations (Rizzo et al, 2006; Rizzo et al, 2004; Tsien, 1998). Common examples of widely used FRET pairs include, mCerulean-EYFP, CFP-YFP, FITC-Rhodamine and EBFP-EYFP. Multi-colour imaging of two or more proteins, each labelled with a different fluorophore therefore provides a valuable tool to determine the distribution of proteins and direct protein interactions within living cells.

1.5.9 Fluorescence lifetime imaging microscopy (FLIM)

To detect and quantify protein interactions, fluorescent lifetime imaging microscopy (FLIM) coupled with multi-photon excitation and FRET, has become a commonly used technique. This approach relies on measurements of the length of time a fluorophore remains in the excited state (Bastiaens & Squire, 1999; Becker et al, 2001; Lakowicz et al, 1992; Periasamy et al, 2002). Importantly, fluorescent

molecules possess a distinctive fluorescence lifetime, and including this lifetime in the imaging process provides a direct approach to detect changes in the fluorophores surrounding environment.

Fluorescence refers to the ability of molecule to absorb a photon of given energy and then release a photon of a diminished energy (a longer wavelength) (Lakowicz, 2006; Müller, 2002). When a fluorophore absorbs a photon it elevates the electrons into a short lived excited state. The electrons stay in this higher energy state for a period of time, typically 1-10 nanoseconds, before releasing a photon as they fall back to the lower energy or ground state (Eftink, 1991; Lakowicz, 2006) (Figure 1.5A). The fluorescence lifetime is the exponential decay in emission after the excitation of a fluorescent molecule (Lakowicz et al, 1992). In other words, the fluorescence lifetime of a fluorophore is the mean time that it spends in the high energy excited state, usually a few nanoseconds, and FLIM aims to measure this time (Bastiaens & Squire, 1999; Lakowicz, 2006; Lakowicz et al, 1992). Fluorescent molecules possess a characteristic fluorescence lifetime (Lakowicz et al, 1992). This fluorescence lifetime is affected by micro-environmental factors; including hydrophobic properties, oxygen concentration, pH, molecular binding, and molecular interactions by energy transfer (Becker, 2005; Lakowicz, 2006). Any transfer of energy between an excited molecule and its environment leads to a change in this fluorescence lifetime, therefore providing a direct approach to probe the local environment parameters of a fluorophore via lifetime changes (Bastiaens & Squire, 1999; Dumas & Stoltz, 2005; Duncan et al, 2004; Lakowicz et al, 1992; Verveer et al, 2001).

1.5.10 METHODOLOGIES FOR MEASURING FLUORESCENCE LIFETIME

Two methods of measuring fluorescence lifetimes with high spatial accuracy are currently in use: the frequency domain approach (Bastiaens & Squire, 1999; Lakowicz et al, 1992) and the time domain approach (Becker, 2005; Cole et al, 2001). In the frequency domain approach the specimen is excited with a modulated light source, and the emission is forced to respond with a similar modulating

frequency. Frequency domain techniques record the amplitude and the phase of the signal as a function of frequency (Bastiaens & Squire, 1999; Lakowicz et al, 1992). The lifetime of the fluorophore causes the emission to be delayed in time relative to the excitation, which is evident as a phase shift, and it is this offset that is measured and used to determine the fluorescence lifetime (Bastiaens & Squire, 1999; Lakowicz, 2006; Lakowicz et al, 1992). The primary advantage of this approach is that a scanning light source is not required and this method can be applied to wide-field microscopes as essentially any oscillating light source can be employed. However, this method suffers from the major disadvantage that it depends on the depth of modulation of the excitation light and the way the detector signal is modulated (Becker, 2005; Lakowicz et al, 1992). Furthermore, frequency domain approaches have low sensitivity and low spatial resolution (Becker, 2005).

The alternative method in operation is the time domain approach that makes use of ultra fast laser excitation pulses and records the fluorescence decay function directly (Becker, 2005; Cole et al, 2001; Lakowicz, 2006). In the time domain approach the sample is excited with a pulsed light source, and the signal intensity is recorded directly into a large number of time channels (Becker, 2005; Cole et al, 2001). Fluorescence lifetime imaging in the time domain can be achieved by two different techniques, including multi-gated photon counting and time-correlated single photon counting (TCSPC). In multi-gated photon counting the detected photons are counted within a small number of subsequent time windows by several parallel counters (Becker, 2005; Becker et al, 2004; Becker et al, 2001; Lakowicz, 2006). The efficiency of this technique is dependent upon the number and the width of the pulsed time gates (Becker, 2005; Lakowicz, 2006). Therefore, multi-gated scanning involves a narrow time gate being scanned over the signal waveform, resulting in a poor efficiency due to the majority of the signal photons being rejected.

In direct comparison, TCSPC is based on the detection of single photons using periodic low energy light with femtosecond resolution, and the measurement of the detection times of a number of individual photons, enabling the reconstruction of the decay function from all the individual time measurements (Becker, 2005; Becker et

al, 2004; Becker et al, 2001) (Figure 1.5B). The introduction of multi-dimensional TCSPC by Wolfgang Becker increased the recording speed, and allowed the photon distribution to be recorded versus time in the fluorescence decay, and also in scan co-ordinates and wavelength (Becker, 2005). It works on the basis that for high repetition rate signals the light intensity is so low that the probability of detecting one photon in one signal period is far less than one, the detection rate being typically one photon per 100 excitation pulses (Becker et al, 2004; Becker et al, 2002; Becker et al, 2001). The detector signal is a series of randomly distributed pulses that corresponds to the detection of individual photons with high temporal accuracy. Once a photon is detected, the time of the detector pulse in the signal period is measured, and numerous events are collected in a memory location which allows a distribution of the average photon times to be built up (Becker, 2005) (Figure 1.5B). For these reasons, TCSPC attempts to count and record every light signal with a high spatial resolution and a near ideal efficiency (Becker, 2005; Duncan et al, 2004), making it a more accurate time domain technique for detecting fluorescent lifetimes.

1.5.11 TCSPC-FLIM TO QUANTIFY FRET

FRET measurement has become an important tool in cell biology (Bastiaens & Squire, 1999; Day & Piston, 1999; Hink et al, 2002; Periasamy & Day, 1999; Voss et al, 2005). It is commonly used to verify whether labelled proteins physically interact by measuring FRET "efficiency" at distances measured on a nanometre scale. In order to calculate the distance between the fluorophores it is necessary to determine the efficiency of FRET. This can be accomplished by intensity-based FRET approaches that compare the intensity of the donor in the presence of the acceptor (Gordon et al, 1998; Liu et al, 2004; Xia & Liu, 2001). However, a common difficulty in intensity based FRET measurements is that the concentrations of the donor and acceptor are variable and unknown, and a further complication is that only a fraction of the donor molecules interact with an acceptor molecule. For these reasons, the effects are hard to distinguish in intensity based FRET measurements, yet a variety of FRET techniques based on intensity imaging have been developed

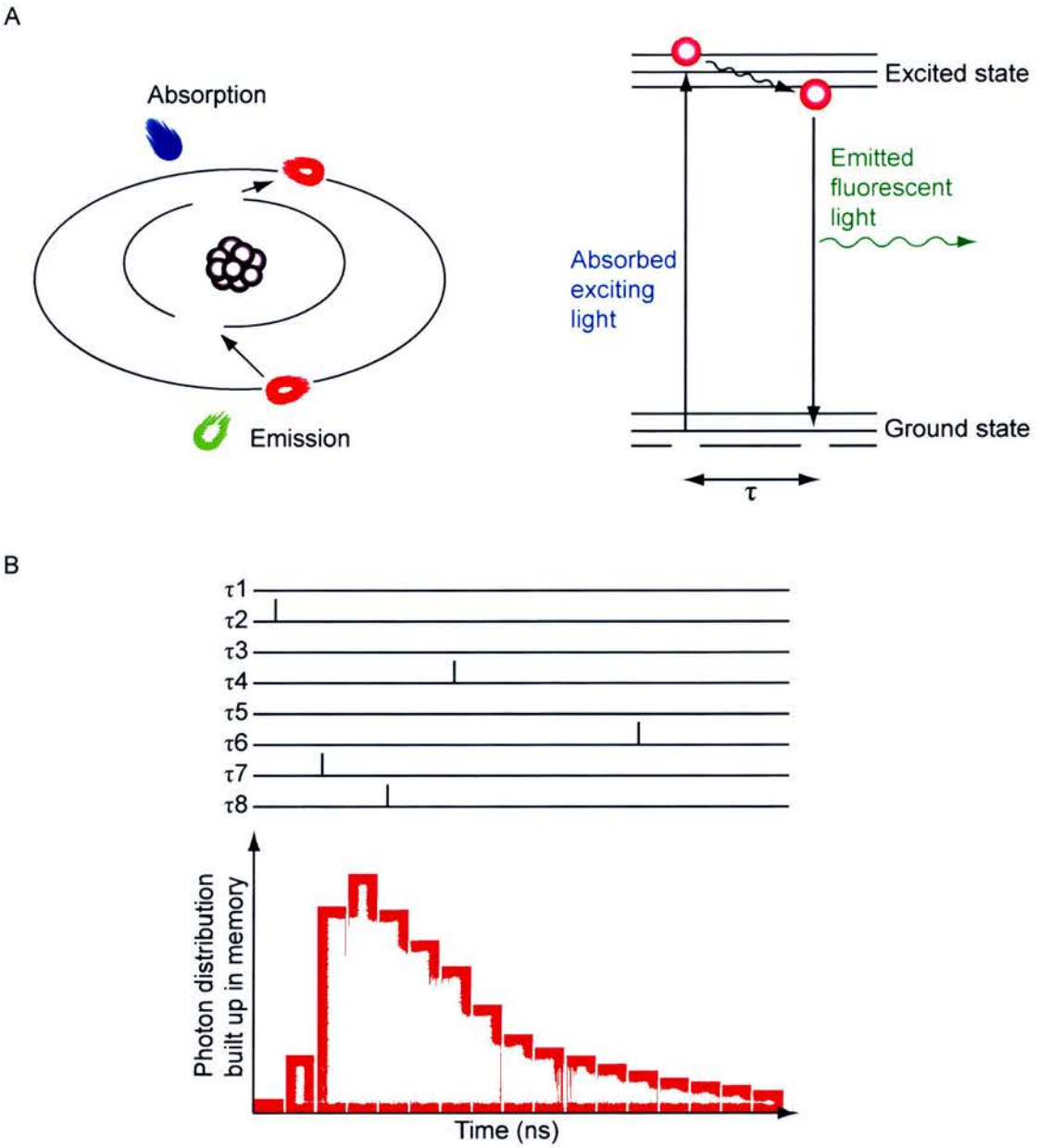

Figure 1.5 General principle of time correlated single-photon counting (TCSPC) and fluorescence lifetime imaging microscopy (FLIM).

(A) Prior to excitation, the fluorophore is in the ground state. Upon absorption of a photon of excitation light, electrons are raised into a higher energy exited state, where they spend a short period of time before they fall back to the lower energy ground state When the electrons fall back to the ground state they may lose energy as emitted fluorescent light. The fluorescence lifetime (τ) is defined as the average time that a molecule remains in the excited state before returning to the ground state (left panel). Fluorescence activity is illustrated in a Jablonski diagram (right panel), to describe absorption and emission of light. **(B)** The TCSPC-FLIM technique makes use of the fact that for low-level, high repetition rate signals, the probability of detecting one photon in one signal period is far less than one. Instead of attempting to detect several photons in one signal period, many signal periods are employed to record the photons, measure their fluorescent lifetimes (τ) in the signal period and build up a histogram of the average photon lifetime. (Adapted from Becker, 2005)

(Gordon et al, 1998; Gu et al, 2004; Periasamy & Day, 1999; Xia & Liu, 2001). Techniques that combine FRET with fluorescence lifetime measurements have been developed to overcome the problems associated with intensity based FRET approaches.

TCSPC-FLIM is a particularly attractive technique when coupled with FRET. As the fluorescence lifetime of a fluorophore is sensitive to environmental conditions that influence the excited state, the FLIM approach can provide a quantitative measure of the fraction of molecules undergoing FRET (Chen et al, 2003; Duncan et al, 2004). As the donor molecule can either emit a photon or transfer the energy to an acceptor molecule the observed time that the donor molecule spends in the excited state is decreased (Bastiaens & Squire, 1999; Becker, 2005; Duncan et al, 2004; Lakowicz et al, 1992). Importantly, in the presence of FRET, the donor fluorescence lifetime is quenched and consequently the fluorescence lifetime is shortened, indicating a protein interaction (Bastiaens & Squire, 1999; Chen et al, 2003; Duncan et al, 2004; Elangovan et al, 2002; Lakowicz et al, 1992). For FLIM-FRET measurements, the presence of an acceptor molecule shifts the mean fluorescence lifetime of the donor molecule to shorter lifetimes because resonance energy transfer dissipates the donor excited-state energy (Becker, 2005). Furthermore, fluorescent lifetime measurements are not affected by photobleaching, and they are independent of donor or acceptor concentrations as only the donor molecule decay function is analysed, thus eliminating corrections for spectral bleed through (Becker et al, 2004; Becker et al, 2002; Becker et al, 2001). Therefore, FLIM provides a direct method to quantify FRET between fluorophores and can be used in protein interaction studies to characterise the spatial distribution of fluorescent lifetimes within fixed and living cells.

1.6 IMAGING THE SECRETORY PATHWAY

Advanced imaging approaches and fluorescent microscopy have been applied to numerous studies of the secretory pathway (Betz & Bewick, 1992; Clayton &

Cousin, 2008; Cochilla et al, 1999; Cousin & Robinson, 1999; Duncan et al, 2004; Duncan et al, 2003; Fix et al, 2004; Granseth et al, 2007; Lagnado et al, 1996; Lang et al, 2001; Lang et al, 1997; Liu et al, 2004; Ma et al, 2004; Medine et al, 2007b; Ohara-Imaizumi et al, 2004a; Ohara-Imaizumi et al, 2004b; Rickman et al, 2007; Rizzoli & Betz, 2004; Straub et al, 2000). In the last 20 years the arrival of molecular biology and fluorescent fusions has propelled fluorescent microscopy to the forefront of science. With the discovery of GFP and its variants and technological advances in confocal microscopy, live cell imaging has become an important experimental approach. In conjunction with biochemical and genetic approaches, imaging techniques now play a pivotal role in unravelling the process of membrane trafficking and the associated regulatory machinery in the secretory pathway.

Rapid advances in confocal microscopy have led to the development of a number of highly advanced fluorescent imaging approaches that have permitted the visualisation and quantification of protein interactions within cells. Multi-photon excitation has enabled the average absorbed excitation energy to be lower than in conventional laser scanning microscopy, and more diverse specimens to be investigated due to deeper penetration of specimens (Callis, 1997; Denk et al, 1990; Theer et al, 2003). Multi-photon excitation also led to the development of powerful techniques such as FLIM (Becker et al, 2001; Lakowicz et al, 1992), which is fast becoming a popular technique to report protein interactions within living cells. Particular emphasis is now focused on individual protein behaviour and protein-protein interactions using the up and coming technology of imaging techniques such as FLIM and FRET. As FRET is sensitive to the exact distance between fluorophores, it has become an ideal method to analyse the close proximity of fluorescent fusion proteins. Incorporating FLIM into the equation has also provided a sensitive tool to detect FRET between fluorophores, and has allowed further insight into the protein interactions underlying membrane fusion. Using this technology, investigations of FRET between secretory pathway proteins and their regulators have been undertaken. There are reports of FRET being used to detect an interaction between synaptobrevin and SNAP-25 in neurons (Xia et al., 2001), and the same group have also shown FRET between SNAP-25 and syntaxin on the plasma

membrane of PC12 cells (Xia & Liu, 2001). FRET has also been employed to examine the protein interaction between munc18-1 and syntaxin in CHO and MDCK cells (Yerrapureddy et al, 2005). Several FRET techniques are now in existence based on widefield, confocal and two-photon microscopy as well as FRET/FLIM approaches, that each possesses their own advantages and disadvantages.

Therefore, the development and use of fluorescent sensors based on the genetically encoded variants of green fluorescent protein have facilitated the observation of biochemistry on a microscopic scale within living cells. Protein activities and interactions can now be imaged and localised within a single cell, allowing greater insight into the molecular machinery that controls cellular homeostasis.

1.7 AIMS OF THIS WORK

The aim of this thesis was to determine the molecular mechanisms that modulate the conformational states of syntaxin 1a in neuroendocrine cells, by combining cell and molecular biology techniques with advanced fluorescent imaging approaches such as TCSPC-FLIM and FRET, to track co-localisation and interactions of specific protein partners together with protein structural conformations in living cells. The protein interaction cascade mediating regulated exocytosis has been investigated in numerous studies. However, whilst the protein participants have been well characterised, the spatial and temporal regulation of the interactions within living cells remains largely unknown. The exocytotic SNARE proteins are also known to be highly promiscuous in their interactions with other non-cognate SNAREs, so it is a vital cellular requirement that SNAREs are trafficked through the ER and Golgi complex while avoiding ectopic interactions between the SNARE proteins.

Syntaxin appears to be at the centre stage of regulation (Calakos et al, 1994; Dulubova et al, 1999; Hanson et al, 1995). The closed form of syntaxin competes with SNARE core complex assembly, because only in the open conformation can syntaxin bind to SNAP-25 then synaptobrevin to become part of the SNARE

complex. The precise functional role of these conformations and the interaction of syntaxin 1a with its regulatory partner munc18-1 remain unclear. Does munc18-1 control the correct assembly of core complexes for SNARE dependent fusion or does it act as a direct component of the fusion machinery itself? This thesis will test the hypothesis that the interactions of syntaxin 1a (and the regulation of its conformations) are essential for the control of SNARE complex formation and membrane fusion. Using biochemical studies coupled with FRET and TCSPC-FLIM analysis, the intracellular localisation of syntaxin 1a and its interaction with its binding partners, munc18-1 and SNAP-25, will be investigated. FRET studies will also be employed to examine the conformational states of syntaxin 1a, and the spatial and temporal regulation of their interactions with munc18-1 and SNAP-25 in living cells.

In specialised secretory cells, exocytosis is restricted to specially equipped areas of the plasma membrane demanding specific interactions and conformational states of exocytotic proteins at these sites. Upon arrival at the plasma membrane syntaxin and SNAP-25 have been shown to form cholesterol-dependent clusters, but the molecular mechanisms underlying this are unknown. This thesis will examine if t-SNARE interactions in these clusters are spatially regulated and examine the factors that regulate cluster stability. If the t-SNAREs are arranged in clusters on the plasma membrane they may contain differential functional conformations at the molecular level.

In summary, many accessory factors have been identified that are essential to control the availability of the SNARE proteins to form the ternary SNARE complex in neurons and neuroendocrine cells. Munc18-1 appears to play a vital role in trafficking syntaxin through the secretory pathway and this thesis will examine how it regulates the conformational status of syntaxin at the plasma membrane and thus SNARE complex formation.

TCSPC-FLIM is a particularly attractive technique when coupled with FRET. As the fluorescence lifetime of a fluorophore is sensitive to environmental conditions that influence the excited state, the FLIM approach can provide a quantitative measure of the fraction of molecules undergoing FRET (Chen et al, 2003; Duncan et al, 2004). As the donor molecule can either emit a photon or transfer the energy to an acceptor molecule the observed time that the donor molecule spends in the excited state is decreased (Bastiaens & Squire, 1999; Becker, 2005; Duncan et al, 2004; Lakowicz et al, 1992). Importantly, in the presence of FRET, the donor fluorescence lifetime is quenched and consequently the fluorescence lifetime is shortened, indicating a protein interaction (Bastiaens & Squire, 1999; Chen et al, 2003; Duncan et al, 2004; Elangovan et al, 2002; Lakowicz et al, 1992). For FLIM-FRET measurements, the presence of an acceptor molecule shifts the mean fluorescence lifetime of the donor molecule to shorter lifetimes because resonance energy transfer dissipates the donor excited-state energy (Becker, 2005). Furthermore, fluorescent lifetime measurements are not affected by photobleaching, and they are independent of donor or acceptor concentrations as only the donor molecule decay function is analysed, thus eliminating corrections for spectral bleed through (Becker et al, 2004; Becker et al, 2002; Becker et al, 2001). Therefore, FLIM provides a direct method to quantify FRET between fluorophores and can be used in protein interaction studies to characterise the spatial distribution of fluorescent lifetimes within fixed and living cells.

1.6 IMAGING THE SECRETORY PATHWAY

Advanced imaging approaches and fluorescent microscopy have been applied to numerous studies of the secretory pathway (Betz & Bewick, 1992; Clayton & Cousin, 2008; Cochilla et al, 1999; Cousin & Robinson, 1999; Duncan et al, 2004; Duncan et al, 2003; Fix et al, 2004; Granseth et al, 2007; Lagnado et al, 1996; Lang et al, 2001; Lang et al, 1997; Liu et al, 2004; Ma et al, 2004; Medine et al, 2007b; Ohara-Imaizumi et al, 2004a; Ohara-Imaizumi et al, 2004b; Rickman et al, 2007; Rizzoli & Betz, 2004; Straub et al, 2000). In the last 20 years the arrival of molecular

biology and fluorescent fusions has propelled fluorescent microscopy to the forefront of science. With the discovery of GFP and its variants and technological advances in confocal microscopy, live cell imaging has become an important experimental approach. In conjunction with biochemical and genetic approaches, imaging techniques now play a pivotal role in unravelling the process of membrane trafficking and the associated regulatory machinery in the secretory pathway.

Rapid advances in confocal microscopy have led to the development of a number of highly advanced fluorescent imaging approaches that have permitted the visualisation and quantification of protein interactions within cells. Multi-photon excitation has enabled the average absorbed excitation energy to be lower than in conventional laser scanning microscopy, and more diverse specimens to be investigated due to deeper penetration of specimens (Callis, 1997; Denk et al, 1990; Theer et al, 2003). Multi-photon excitation also led to the development of powerful techniques such as FLIM (Becker et al, 2001; Lakowicz et al, 1992), which is fast becoming a popular technique to report protein interactions within living cells. Particular emphasis is now focused on individual protein behaviour and protein-protein interactions using the up and coming technology of imaging techniques such as FLIM and FRET. As FRET is sensitive to the exact distance between fluorophores, it has become an ideal method to analyse the close proximity of fluorescent fusion proteins. Incorporating FLIM into the equation has also provided a sensitive tool to detect FRET between fluorophores, and has allowed further insight into the protein interactions underlying membrane fusion. Using this technology, investigations of FRET between secretory pathway proteins and their regulators have been undertaken. There are reports of FRET being used to detect an interaction between synaptobrevin and SNAP-25 in neurons (Xia et al., 2001), and the same group have also shown FRET between SNAP-25 and syntaxin on the plasma membrane of PC12 cells (Xia & Liu, 2001). FRET has also been employed to examine the protein interaction between munc18-1 and syntaxin in CHO and MDCK cells (Yerrapureddy et al, 2005). Several FRET techniques are now in existence based on widefield, confocal and two-photon microscopy as well as FRET/FLIM approaches, that each possesses their own advantages and disadvantages.

Therefore, the development and use of fluorescent sensors based on the genetically encoded variants of green fluorescent protein have facilitated the observation of biochemistry on a microscopic scale within living cells. Protein activities and interactions can now be imaged and localised within a single cell, allowing greater insight into the molecular machinery that controls cellular homeostasis.

1.7 AIMS OF THIS WORK

The aim of this thesis was to determine the molecular mechanisms that modulate the conformational states of syntaxin 1a in neuroendocrine cells, by combining cell and molecular biology techniques with advanced fluorescent imaging approaches such as TCSPC-FLIM and FRET, to track co-localisation and interactions of specific protein partners together with protein structural conformations in living cells. The protein interaction cascade mediating regulated exocytosis has been investigated in numerous studies. However, whilst the protein participants have been well characterised, the spatial and temporal regulation of the interactions within living cells remains largely unknown. The exocytotic SNARE proteins are also known to be highly promiscuous in their interactions with other non-cognate SNAREs, so it is a vital cellular requirement that SNAREs are trafficked through the ER and Golgi complex while avoiding ectopic interactions between the SNARE proteins.

Syntaxin appears to be at the centre stage of regulation (Calakos et al, 1994; Dulubova et al, 1999; Hanson et al, 1995). The closed form of syntaxin competes with SNARE core complex assembly, because only in the open conformation can syntaxin bind to SNAP-25 then synaptobrevin to become part of the SNARE complex. The precise functional role of these conformations and the interaction of syntaxin 1a with its regulatory partner munc18-1 remain unclear. Does munc18-1 control the correct assembly of core complexes for SNARE dependent fusion or does it act as a direct component of the fusion machinery itself? This thesis will test the hypothesis that the interactions of syntaxin 1a (and the regulation of its

conformations) are essential for the control of SNARE complex formation and membrane fusion. Using biochemical studies coupled with FRET and TCSPC-FLIM analysis, the intracellular localisation of syntaxin 1a and its interaction with its binding partners, munc18-1 and SNAP-25, will be investigated. FRET studies will also be employed to examine the conformational states of syntaxin 1a, and the spatial and temporal regulation of their interactions with munc18-1 and SNAP-25 in living cells.

In specialised secretory cells, exocytosis is restricted to specially equipped areas of the plasma membrane demanding specific interactions and conformational states of exocytotic proteins at these sites. Upon arrival at the plasma membrane syntaxin and SNAP-25 have been shown to form cholesterol-dependent clusters, but the molecular mechanisms underlying this are unknown. This thesis will examine if t-SNARE interactions in these clusters are spatially regulated and examine the factors that regulate cluster stability. If the t-SNAREs are arranged in clusters on the plasma membrane they may contain differential functional conformations at the molecular level.

In summary, many accessory factors have been identified that are essential to control the availability of the SNARE proteins to form the ternary SNARE complex in neurons and neuroendocrine cells. Munc18-1 appears to play a vital role in trafficking syntaxin through the secretory pathway and this thesis will examine how it regulates the conformational status of syntaxin at the plasma membrane and thus SNARE complex formation.

CHAPTER TWO:

MATERIALS AND METHODS

2.1. MATERIALS AND SOLUTIONS

2.1.1. GROWTH MEDIA AND SOLUTIONS

All chemicals were supplied by Sigma Aldrich, UK, unless otherwise stated.

LB media:	1% (w/v) Yeast Extract 1% (w/v) Bacto-tryptone 86 mM NaCl
2x TY media:	1% (w/v) Yeast Extract 1.6% (w/v) Bacto-tryptone 172 mM NaCl
SDS-PAGE Sample Buffer (4x):	6.4% (w/v)SDS 200 mM Tris-HCl, pH 6.8 5 mM EDTA 16% (v/v) Glycerol A few grains of Bromphenol blue
SDS-PAGE Running Buffer:	25 mM Tris 0.2 M Glycine 0.1% (w/v) SDS
Western Transfer Buffer:	25 mM Tris 0.2 M Glycine 20% (v/v) Methanol
1 x PBS	0.01 M Phosphate Buffer (pH 7.0) 0.0027 M Potassium chloride 0.137 M Sodium chloride
PBS Tween:	1 x PBS 0.05% (v/v) Tween-20
Coomassie Stain:	10% (v/v) Methanol 20% (v/v) Acetic Acid 200 mg/L Coomassie R-250
Orange G Loading Dye (10x conc.):	50% (v/v) Glycerol 5 mg/ml Orange G
Buffer A (GST-tagged proteins):	20 mM HEPES (pH 7.4) 100 mM NaCl 1 mM EDTA 0.1% (v/v) Triton X-100

Buffer B (His_6-tagged proteins): 20 mM HEPES (pH 7.4)
100 mM NaCl
20 mM Imidazole
0.1% (v/v) Triton X-100

2.1.2. ESCHERICHIA COLI (E.COLI) STRAINS

The following *E.coli* strains were used for DNA amplification and protein expression (Table 2.1). XL10-Gold ultracompetent cells were used for the transformation of DNA with high efficiency. BL21 (DE3) competent cells were used for the transformation and expression of GST tagged proteins. M15 (pREP4) competent cells were used for the transformation and expression of His_6 tagged proteins.

Table 2.1. *E.coli* strains

E.coli Host Strain	Usage	Source
XL10-Gold	DNA amplification	Stratagene, Europe
BL21 (DE3)	GST tagged protein expression	Stratagene, Europe
M15 (pREP4)	His_6 tagged protein expression	Qiagen, UK

2.1.3 DNA PLASMIDS

The following table shows DNA plasmids that were gifts and those from commercial suppliers used in direct and non-directional cloning with cDNAs of interest.

Table 2.2. DNA plasmids.

Plasmid	Antibiotic resistance	Fusion Tag	Promoter(s)	Source
pEGFP-C2	Kanamycin	EGFP	CMV	Clontech, UK
pEYFP-N1	Kanamycin	EYFP	CMV	Clontech, UK
pmCerulean-C1	Kanamycin	mCerulean	CMV	Dr D. Piston*
pGEM-T-Easy	Ampicillin	-	T7, SP6	Promega, UK
pGEX-KG	Ampicillin	GST	Lac Iq	(Guan & Dixon, 1991)
pQE-30	Ampicillin	His_6	T5	Qiagen, UK

pCI	Ampicillin	-	CMV	Promega, UK
pmCherry-GRASP65	Kanamycin	mCherry	CMV	Dr J. Lane**
pcDNA3-EYFP-Munc18-1	Ampicillin	EYFP	-	Dr D. Apps***
pEGFP-N1-SNAP-25	Kanamycin	EGFP	CMV	Dr M. Linder†

* Kind gift of Dr D. Piston, Vanderbilt Kennedy Center for Research on Human Development, Nashville, USA.
** Kind gift of Dr J. Lane, Department of Biochemistry, University of Bristol, UK.
*** Kind gift of Dr D. Apps, Centre for Integrative Physiology, The University of Edinburgh, UK.
† Kind gift of Dr M. Linder, Department of Cell Biology and Physiology, Washington University, St. Louis, USA.

2.1.4 BACTERIAL PROTEIN EXPRESSION PLASMIDS

The following proteins were expressed in *Escherichia coli* BL21 (section 2.3.7) or M15 (pREP4) cells (section 2.3.8) depending on the purification tag (Table 2.3).

Table 2.3. Bacterial protein expression plasmids.

Protein + Protein Fragment	Purification Tag	Parent Vector	Source
Syntaxin 1a (1-261)*	GST	pGEX-KG	Constructed for this study
Syntaxin 1a (7-261)*	GST	pGEX-KG	Constructed for this study
Syntaxin 1a (13-261)*	GST	pGEX-KG	Constructed for this study
Syntaxin 1a (22-261)*	GST	pGEX-KG	Constructed for this study
SNAP-25 (1-206)	GST	pGEX-KG	Constructed for this study
SNAP-25 (1-206) [G43D]	GST	pGEX-KG	Constructed for this study
SNAP-25 (1-206)	His_6	pQE-30	Constructed for this study
SNAP-25 (1-206) [G43D]	His_6	pQE-30	Constructed for this study
Munc18-1	His_6	pQE-30	Professor R. Burgoyne**

* In the absence and presence of the open mutation L165A/E166A.
** Kind gift of Professor R. Burgoyne, The Physiological Department, University of Liverpool, UK.

2.1.5. ANTIBODIES

The following antibodies were used for western immunoblotting and direct immunofluorescent confocal imaging.

Table 2.4. Antibodies used for direct immunofluorescence (IF) and western immunoblotting (WB).

Antibody	Host	Clone	Dilution for IF	Dilution for WB	Source
anti-syntaxin	Rabbit		1:500	1:5000	Dr B. Davletov*
anti-syntaxin	Mouse	HPC-1	1:500	1:5000	Sigma Aldrich, UK
anti-SNAP-25	Mouse	SMI81	1:500	1:5000	Sternberger, UK
anti-SNAP-25	Mouse	71.2	1:500	1:5000	Synaptic Systems, Germany
anti-munc18-1	Mouse		1:500	1:5000	BD Bioscience, UK
anti-synaptobrevin	Mouse	69.1	1:500	1:5000	Synaptic Systems, Germany
anti-rabbit alexa 488	Donkey		1:1000	-	Invitrogen, UK
anti-mouse alexa 488	Goat		1:1000	-	Invitrogen, UK
anti-mouse alexa 647	Goat		1:1000	-	Invitrogen, UK
anti-mouse alexa 568	Goat		1:1000	-	Invitrogen, UK
anti-rabbit alexa 488 (Fab Fragment)	Goat		1:1000	-	Invitrogen, UK
anti-mouse alexa 488 (Fab Fragment)	Goat		1:1000	-	Invitrogen, UK
anti-mouse alexa 568 (Fab Fragment)	Goat		1:1000	-	Invitrogen, UK
anti-mouse HRP conjugated	Goat		-	1:5000	Pierce, UK
anti-rabbit HRP conjugated	Goat		-	1:5000	Pierce, UK

* Kind gift of Dr B. Davletov, MRC Laboratory of Molecular Biology, Cambridge, UK.

2.1.6 OLIGONUCLEOTIDES

All custom designed oligonucleotides for cloning were purchased from Sigma Genosys, Sigma-Aldrich, UK.

2.2 MOLECULAR TECHNIQUES

2.2.1. POLYMERASE CHAIN REACTION (PCR)

All PCR was performed using a Gene Amp PCR System 9700 (Applied Biosystems). For the routine amplification of large DNA fragments from template DNA, the Expand High Fidelity PCR System (Roche, UK) was used. Custom oligonucleotides (Sigma Genosys, Sigma-Aldrich, UK) were designed and used to amplify the DNA fragment of interest.

The following standard reaction was used:

DNA template (50 ng/ml)	1 µl
Nucleotide mix (10 mM of each dNTP)	1 µl
Oligonucleotide 1 (10 pmol/µl)	1 µl
Oligonucleotide 2 (10 pmol/µl)	1 µl
Expand High Fidelity Buffer (10X conc.)	5 µl
Expand High Fidelity enzyme mix	1 µl
Sterile double distilled water	Up to a final volume of 50 µl

The PCR cycle parameters were as stated in the manufacturer's instructions. The Expand High Fidelity enzyme mix was added to the reaction at 95 °C. The polymerase enzyme mix (*Taq* DNA polymerase and *Tgo* DNA polymerase) acts by extending the annealed oligonucleotides to synthesise DNA from 3' end of the oligonucleotide. This process of denaturation, annealing and synthesis is repeated numerous times, with each newly synthesised DNA acting as a template for the next reaction. Agarose gel electrophoresis (section 2.2.3) was used to ensure that a PCR product was visible. The PCR product was subsequently ligated into the plasmid of interest (section 2.2.7) and transformed into XL-10 Gold ultra-competent *E. coli* cells (section 2.2.8).

2.2.2 SITE-DIRECTED MUTAGENESIS

The QuickChange XL Site-Directed Mutagenesis Kit (Stratagene, UK) was used to make defined mutations *in vitro* to cloned DNA, as per the manufacturer's

instructions. The control reaction included the DNA vector containing the insert of interest and two complementary oligonucleotide primers (Sigma Genosys, Sigma-Aldrich, UK), both containing the desired mutation flanked by unmodified nucleotide sequence.

The standard reaction was as follows:

10X Reaction Buffer	5 µl
DNA template	5 ng/µl of plasmid DNA
Oligonucleotide 1	100 ng/µl
Oligonucleotide 2	100 ng/µl
Nucleotide mix (10 mM of each dNTP)	1 µl
Quiksolution	3 µl
Pfu Ultra DNA polymerase	2.5 U/µl
Sterile double distilled water	Up to a final volume of 50 µl

The PCR cycle parameters were as stated in the manufacturer's instructions, with an extension time of 1 min per kb of plasmid. Agarose gel electrophoresis (section 2.2.3) was used to confirm that a PCR product had been produced. *Dpn*I (1 µl) restriction enzyme was added directly to each amplification reaction and the reaction immediately incubated at 37 °C for 1 hour to digest the parental supercoiled dsDNA. The PCR product was subsequently transformed into XL-10 Gold ultra-competent *E. coli* cells (section 2.2.8).

2.2.3 AGAROSE GEL ELECTROPHORESIS

Agarose gel electrophoresis was used for the analytical or preparatory separation of DNA. A 1% (w/v) agarose gel solution in 1 x Tris/Borate/EDTA (TBE) buffer was prepared and the solution brought to the boil. Once the solution had cooled, SYBR Safe (Invitrogen, Paisley, UK) was added at a dilution of 1:10,000 and the mixture poured into the gel rack containing the appropriate gel comb. Orange G loading dye of the appropriate volume was added to the DNA sample and the DNA samples loaded, with a 1 Kb plus DNA marker (Invitrogen, Paisley, UK) alongside. DNA gels were run at 100 V in 1 x TBE buffer, and imaged using a UV light source.

2.2.4 RESTRICTION ENDONUCLEASE DIGESTS

Restriction endonucleases (Promega, UK) were employed to check that plasmid DNA contained inserts of the correct orientation and for directional cloning to cut plasmid DNA and remove DNA inserts of interest. In addition, restriction enzyme digests were commonly used to cut out and swap fluorophores between DNA plasmids. Double digests were used if restriction enzymes showed buffer compatibility, and if buffers were incompatible then digests were done sequentially. A typical double restriction enzyme digest reaction was as follows:

Plasmid DNA	1 µg plasmid DNA
Restriction enzyme 1	0.5 µl (enzymes 1/10 final volume)
Restriction enzyme 2	0.5 µl
10 X Enzyme Buffer	1 µl
BSA (10 mg/ml)*	1 µl
Sterile double distilled H_2O	Up to a final volume of 10 µl

* Depends on the commercial restriction endonuclease buffer as some buffers contain BSA

For a typical double restriction digest the reagent mixture was incubated for 1 hour at 37 °C, and for sequential digests each separate enzyme mixture was incubated for 1 hour at 37 °C. After digestion with both restriction enzymes, DNA was separated using agarose gel electrophoresis (section 2.2.3). Subsequently, the DNA of interest was purified using a QIAquick gel extraction kit (Qiagen, UK) (section 2.2.5).

cDNA encoding fluorescent proteins were commonly cut out of vectors using *Age*I/*Bsr*GI sites for ligation into other vectors.

2.2.5 DNA EXTRACTION

To extract and purify DNA from agarose gels, a QIAquick gel extraction kit (Qiagen, UK) was used and the manufacturer's instructions followed.

2.2.6 LIGATION OF INSERT DNA AND VECTOR DNA

The ligation of insert DNA and vector DNA was performed with T4 DNA LigaFast (Promega, UK). The ligation reaction was optimised using different ratios for each individual reaction, typically a molar mass ratio of 1:1 or 1:3 (vector:insert) was used. The ligation reaction was set up in a 10 µl reagent mixture as follows:

Vector DNA	1 µl
Insert DNA	1 or 3 µl
Rapid Ligation Buffer	5 µl
T4 DNA Ligase	1 µl
Sterile double distilled water	Up to a final volume of 10 µl

The ligation reaction was performed according to the manufacturer's instructions. The reagent mixture was incubated at room temperature for 1 hour.

2.2.7 TRANSFORMATION OF E.COLI BY PLASMID DNA

For protein expression, BL21 (DE3) or M15 (pREP4) (Table 2.1) competent cells were used. XL-10 Gold ultracompetent cells (Table 2.1) were used for the transformation of ligated and large DNA molecules with high efficiency. On ice 1 µg of DNA or 10 µl of ligation product was added to 45 µl of competent cells in a pre-chilled tube. The suspension was incubated for 10 mins on ice, swirling gently every 2 min before being subjected to a heat shock in a 42 °C water bath for 30 seconds, and returned to ice for 2 min. Following the heat shock, 0.5 ml preheated Luria Bertani (LB) media was added to the tubes and incubated at 37 °C for 1 hour with shaking at 200 rpm. Following transformation, 10 and 100 µl samples of the culture were plated on LB agar plates containing 0.1 mg/ml of the appropriate antibiotic and incubated at 37 °C overnight.

2.2.8 SMALL SCALE PLASMID DNA PURIFICATION

The isolation and purification of small scale plasmid DNA was carried out with a QIAprep Miniprep Kit (Qiagen, UK) according to the manufacturer's instructions. Briefly, a single colony of transformed *E.coli* containing the DNA plasmid of interest was picked and used to inoculate a culture of 5 ml of LB medium, containing the appropriate antibiotic. The culture was incubated overnight at 37 ºC with shaking at 200 rpm.

The bacterial cells were harvested in 15 ml tubes by centrifugation at 5000 x*g* in a swinging bucket conventional table top centrifuge for 5 min at 4 ºC. The pelleted bacterial cells were re-suspended in 250 µl of Buffer P1 and transferred to a micro-centrifuge tube. 250 µl of Buffer P2 was added and the tube inverted 4-6 times, followed by the addition of 350 µl of Buffer N3 and again the tube was inverted 4-6 times. The solution was centrifuged at 13,000 x*g* in a micro-centrifuge for 10 min at room temperature. The supernatant was applied to a QIAprep spin column by pipetting and centrifuged for 30-60 sec, discarding the flow through. The QIA prep spin column was washed by the addition of 0.5 ml of Buffer PB and centrifuged for 30-60 sec, and again the flow through was discarded. The QIAprep spin column was further washed with 0.75 ml of Buffer PE and centrifuged for 30-60 sec, and the flow through discarded. To elute the DNA, the QIAprep column was placed in a clean microcentrifuge tube and 50 µl of Buffer EB added to the centre of the column. The column was allowed to stand for 1 min, followed by centrifugation for 1 min.

2.2.9 LARGE SCALE PLASMID DNA PURIFICATION

The isolation and purification of large scale plasmid DNA purification was completed using a HiPure Maxiprep Kit (Invitrogen, Paisley UK). The manufacturer's instructions were followed with some alteration. Briefly, a single colony of transformed *E.coli* containing the DNA plasmid of interest was picked and used to inoculate a culture of 5 ml of LB medium, containing the appropriate antibiotic. The

culture was incubated for 6 hours at 37 °C with shaking at 200 rpm. The starter culture was used to inoculate 250 ml of LB medium and the culture incubated overnight at 37 °C with shaking at 200 rpm.

The bacterial cells were harvested in 250 ml centrifuge bottles by centrifugation at 5,000 x*g* for 10 min at 4 °C. The pelleted bacterial cells were re-suspended in 10 ml of re-suspension buffer containing RNase A. Ten millilitres of lysis buffer was added and the solution gently mixed by inverting the bottle 5 times. The solution was incubated at room temperature for 5 mins before the addition of 10 ml of precipitation buffer. The solution was mixed immediately by inverting the tube 5 times. The solution was loaded into a funnel containing filter paper (Whatman, UK) and allowed to drain by gravity flow onto a PureLink HiPure Maxi equilibrated column. The column was washed with 60 ml of wash buffer and allowed to drain by gravity flow. To elute the DNA, a clean 50 ml falcon tube containing 10 ml of isopropanol was placed under the column. Fifteen millilitres of elution buffer was added to the column and allowed to drain by gravity flow. The DNA-isopropanol mix was transferred to a glass tube and centrifuged at 15,000 x*g* for 30 min at 4 °C. The supernatant was carefully removed and discarded. The DNA pellet was washed in 10 ml of 70% ethanol and centrifuged at 15,000 x*g* for 5 min at 4 °C. The supernatant was carefully removed and discarded, and the DNA pellet was dried at 37 °C for 10-20 min. The DNA pellet was re-suspended in 0.5 ml of 0.5% DEPC distilled H_2O and the concentration measured.

2.2.10 DNA QUANTIFICATION

The concentration of plasmid DNA was determined using spectrophotometry, by absorption at 260 nm. DNA was diluted 1:200 with 0.5% DEPC H_2O in balanced Hellma 6040-UV 10 mm Quartz cuvettes and measured using a Thermo Electron Corporation, Biomate 3 UV-Vis spectrophotometer.

2.2.11 DNA SEQUENCING

The coding sequences for all constructs were verified by sequencing. All plasmid DNA sequencing was conducted by Cogenics, UK, using standard or custom designed oligonucleotides of 18-25 nucleotides in length. DNA sequences were analysed with Invitrogen Vector NTI software using the basic alignment tool.

2.3 PROTEIN BIOCHEMISTRY TECHNIQUES

2.3.1 SDS-POLYACRYLAMIDE GEL ELECTROPHORESIS (SDS-PAGE)

SDS-Polyacrylamide gel electrophoresis (SDS-PAGE) was used for the separation of proteins. The Mini-PROTEAN 3 electrophoresis apparatus (Biorad, UK) was used with Ready Gel 12% Tris-HCl pre-cast polyacrylamide gels (Biorad, UK). The samples were denatured at 100 °C for 5 min in 1 x SDS sample buffer (section 2.1.1). Once the gel was fitted in the chamber, the tank was filled with SDS running buffer (section 2.1.1), and the samples loaded, including a Precision Plus Protein Standards All Blue protein marker (Biorad, UK). A potential of 120 V was applied and the samples were run until the dye front reached the bottom of the gel.

2.3.2 WESTERN IMMUNOBLOTTING

2.3.2.1 WESTERN TRANSFER

To detect a specific protein in a given sample, western blotting was utilised. Proteins separated via SDS-PAGE, were transferred from a polyacrylamide gel to Polyvinylidene fluoride (PVDF) membrane (Millipore, UK) where they were probed with antibodies specific to the target protein. A stack was put together in the following order from cathode to anode: sponge; filter paper soaked in transfer buffer; SDS-PAGE gel; PVDF membrane pre-soaked in methanol and then transfer buffer on top of the gel; filter paper soaked in transfer buffer; sponge. It is important that the membrane is positioned between the gel and the anode as the samples and current

will be moving in that direction. The stack was sandwiched in a Mini-Trans Blot Cell cassette (Biorad, UK) and the tank filled with pre-chilled Western transfer buffer (section 2.1.1). A constant current of 250 mA was applied for 90 min.

2.3.2.2 IMMUNOBLOTTING

Following transfer of the proteins, the PVDF membrane was blocked to prevent spurious antibody binding. The membrane was blocked in 10 ml of 5% (w/v) dried milk in 0.05% (v/v) PBS Tween (PBST) for 30 min with gentle agitation. The primary antibody was added to the milk + PBST at the appropriate dilution for the antibody (typically 1:5000) and incubated for 1 hour with gentle agitation. Unbound antibody was removed by three 5-min washes with 20 ml of PBST. A horseradish peroxidase (HRP) -conjugated secondary antibody was diluted in 10 ml of 5% dried milk in 0.05% PBST at a dilution of 1:5000, and incubated for 30 mins with gentle agitation. Again unbound antibody was removed by three 5-min washes with 20 ml PBST.

2.3.2.3 ENHANCED CHEMILUMINESCENCE (ECL)

To detect the proteins of interest via the secondary HRP conjugated antibody, enhanced chemiluminescence (ECL) was applied to the membrane. Protein bands were visualised using a West Dura enhanced chemiluminescence reagent kit (Pierce, UK). Briefly, 0.5 ml of Peroxide Buffer + 0.5 ml of Luminol/Enhancer Solution was mixed and spotted on to the membrane, ensuring it was evenly spread over the entire membrane. In a dark room, the membrane was exposed to Kodak chemiluminescence BioMax light x-ray film for the appropriate length of time, typically 1-10 min. The film was then immersed in Kodak GBX developer for 1-5 min, and immersed in water before being fixed in Kodak GBX fixer for 1-5 min. Finally, the film was rinsed in water before being dried using a photo film drier.

2.3.3 COOMASSIE BLUE STAINING

Following separation by SDS-PAGE, proteins were visualised by Coomassie Brilliant Blue R-250 staining. The SDS-PAGE gel was placed in a glass container containing Coomassie stain (section 2.1.1) (approximately 1 cm depth) and brought to the boil for 30 seconds in a microwave oven. The gel was allowed to stain on a rocker for 10 min, and then the Coomassie stain was replaced with deionised water to de-stain the gel. As many water changes were used as necessary to reduce the background staining on the gel to zero. The gel was then dried using a GelAir Drying System (Biorad, UK).

2.3.4 SYPRO RED STAINING

SYPRO Red protein gel stains were also used in conjunction with Coomassie brilliant blue due to higher sensitivity. Following separation by SDS-PAGE, the proteins were visualised by SYPRO Red protein gel stains (Invitrogen, Paisley, UK). The staining solution was prepared by diluting the stock SYPRO Red reagent 1:5000 in 7.5% (v/v) acetic acid and mixing vigorously. The staining solution was poured into a small plastic dish with the gel, using about 50 ml of staining solution for one standard mini gel. The container was covered with aluminium foil to protect the dye from bright light. The gel was gently agitated at room temperature for 45 min. Excess stain was removed by rinsing the gel briefly in 7.5% (v/v) acetic acid. Gels were imaged using a Typhoon 9200 Variable Mode Imager (Amersham Pharmacia Biotech).

2.3.5 PROTEIN QUANTIFICATION

All protein was quantified against a BSA gradient using a BCA Protein Assay Kit (Pierce, UK). The manufacturer's protocol was followed.

2.3.6 Recombinant protein Growth/expression conditions

All SNARE proteins used in this study were expressed under standard conditions. Fifty millilitres of 2x TY media + 0.1 mg/ml ampicillin or kanamycin was inoculated with a single colony of BL21 (DE3) or M15 (pREP4) cells carrying the relevant expression plasmid. The culture was grown for 6 hours at 37 °C with shaking at 200 rpm and then used to inoculate 0.5 l of 2x TY media + 0.1 mg/ml ampicillin or kanamycin in a 2 l flask. After 2 hours of growth at 37 °C with shaking at 200 rpm, IPTG was added at a final concentration of 1 mM to induce expression of the fusion protein. Following the addition of IPTG, the temperature was reduced to 19 °C and the bacteria grown overnight (~16 hours) with shaking at 200 rpm before harvesting.

2.3.7 Purification of GST-tagged proteins

2.3.7.1 Preparation of bacterial lysates

The 0.5 l bacterial cultures containing glutathione S-transferase (GST) fusion proteins encoded by pGEX-KG vectors were centrifuged at 3,000 x*g* for 10 min at 4 °C, and the supernatant discarded. All further work was carried out at 4 °C and using cold solutions. The bacterial pellet was re-suspended in 5 ml of chilled buffer A (section 2.1.1) + EDTA free protease inhibitor tablets (Roche, UK) and transferred to a 50 ml tube. Cells were lysed by sonication for 30 seconds and incubated at 4 °C for 20 min with rotation. Triton X-100 was added to a final concentration of 2% (v/v). The mixture was transferred to a centrifuge tube and insoluble material was pelleted by centrifugation at 15,000 x*g*, for 20 min at 4 °C.

2.3.7.2 Isolation of GST-tagged proteins

GST fusion proteins were purified using sepharose beads coated with glutathione. Glutathione sepharose beads (0.5 ml) (GE Healthcare, UK) were transferred to a 15 ml falcon tube and washed once with buffer A by centrifugation and the buffer

carefully removed leaving the beads. The lysed bacterial supernatant (section 2.3.7.1) was transferred to the tube containing the glutathione sepharose bead slurry and incubated at 4 °C with rotation for 1.5 hours. The GST-fusion protein glutathione complex was washed by centrifugation at 200 x*g* with 3 x 1 min washes with buffer A (20 mM HEPES, 1 M NaCl, 1 mM EDTA, 0.1% (v/v) TX-100), followed by 3 x 1 min washes with buffer A. After the final wash the beads were re-suspended in 7.5 ml of buffer A. SDS-polyacrylamide gel electrophoresis (section 2.3.1) was used to analyse 30 µl of the GST-fusion protein glutathione complex bead slurry. Glycerol was added to the bead slurry to a final volume of 15 ml with sufficient mixing, and stored at -20 °C.

2.3.7.3 Elution of GST-tagged proteins

Bound GST fusion proteins were eluted via cleavage by thrombin. The GST-fusion protein glutathione complex was washed once with buffer A (section 2.1.1). The complex was re-suspended in 1 ml buffer A + 10 U/ml of thrombin. The complex + thrombin were incubated at 37 °C for 1 hour with shaking at 200 rpm. Glutathione was removed by ultracentrifugation. Eluted protein and beads were separated using 0.45 µm filters (Spin X, Corning Costar, UK). The protein eluate was collected and 1 µM AEBSF ((4-(2-Aminoethyl) benzenesulphonyl fluoride)) added to inhibit thrombin. Eluted protein samples were then solubilised in sample buffer and monitored by SDS-polyacrylamide gel electrophoresis (section 2.3.1).

2.3.8 Purification of HIS_6-tagged proteins

2.3.8.1 Preparation of bacterial lysates

Bacterial cultures containing His_6 fusion proteins encoded by pQE-30 vectors were prepared as for section 2.3.7.1 but instead using buffer B (section 2.1.1).

2.3.8.2 ISOLATION OF His_6-TAGGED PROTEINS

His_6 fusion proteins were purified by immobilised Ni^{2+} affinity chromatography. One millilitre of Profinity Ni-charged resin (Biorad, UK) was transferred to a 15 ml falcon tube and washed once with buffer B (section 2.1.1) by centrifugation and the buffer carefully removed leaving the resin. The lysed bacterial supernatant from above was transferred to the tube containing the resin slurry and incubated at 4 °C with rotation for 1.5 hours. The His_6-fusion protein resin complex was washed by centrifugation at 200 x*g*, with 3 x 1 min washes with buffer B (section 2.1.1). After the final wash the complex was re-suspended in 7.5 ml buffer B and 7.5 ml glycerol added, the solution was mixed and stored at -20 °C. Before the addition of glycerol, 30 µl of the His_6-fusion protein resin complex slurry was analysed by SDS-polyacrylamide gel electrophoresis (section 2.3.1).

2.3.8.3 ELUTION OF HIS_6-TAGGED PROTEINS

Bound His_6 fusion proteins were eluted from Ni^{2+} charged resin using buffer containing the competitor ligand imidazole. Using ultracentrifugation, samples were transferred to 0.45 µm filter columns (Spin X, Corning Costar, UK) and washed with buffer B and the eluate discarded. The protein was eluted with 4 washes with a buffer containing excess imidazole (20 mM HEPES (pH 7.4), 100 mM NaCl, 300 mM imidazole, 0.1% (v/v) TX-100). The protein eluate for each wash was collected in a separate tube. Eluted protein samples were solubilised in sample buffer and monitored by SDS- polyacrylamide gel electrophoresis (section 2.3.1). As most of the protein was eluted in the second and third fraction, eluates were combined for protein dialysis.

2.3.8.4 DIALYSIS OF HIS_6-TAGGED PROTEINS

Proteins were dialysed to remove excess NaCl following affinity chromatography. Firstly, the protein was injected into a Slide-a-lyzer dialysis cassette (Pierce, UK) and the remaining air in the cavity drawn out. A flotation buoy was attached to the cassette and the cassette placed in 1 l of dialysis buffer (20 mM HEPES (pH 7.4), 100 mM NaCl, 0.1% (v/v) TX-100). All proteins were dialysed against two changes of 1 l of dialysis buffer at 4 °C with gentle stirring. To remove the protein after dialysis, the cassette chamber was injected with air and the protein sample removed.

2.3.9 PREPARATION OF RAT BRAIN LYSATES

All preparation and reactions were performed at 4 °C using cold solutions. Adult rats were culled according to Home Office regulations under schedule 1. Adult rat brain lysates were prepared by homogenising whole rat brains in 6 ml of buffer A (section 2.1.1) using a glass homogeniser. The lysate was then transferred to a 15 ml tube and buffer A (section 2.1.1) added to a final volume of 10 ml. Triton X-100 was added to a final concentration of 2% (v/v) before incubation for 20 min at 4 °C with rotation. Cell debris was removed by centrifugation at 100,000 x*g* using a Beckman TLA-100 rotor for 40 min at 4 °C. The rat brain lysate was then used fresh or stored at -70 °C for future use.

2.4 PROTEIN INTERACTIONS

2.4.1 SATURATION BINDING ASSAYS

Glutathione S-transferase (GST) fusion proteins encoded by pGEX vectors were expressed in *E. coli* using standard methods (section 2.3.7). Eluted proteins or rat brain lysates were incubated with immobilised GST-SNAP-25 or GST-Syntaxin 1a. Incubations were for 1 hour at 4 °C with rotation following which the beads were recovered by centrifugation in a table top micro-centrifuge at 13,000 x*g*. Beads were

washed 4 times in 1 ml of buffer A (section 2.1.1) prior to solubilisation in sample buffer for SDS-polyacrylamide gel electrophoresis. Electrophoresed samples were transferred to PVDF membranes for immunoblotting with the appropriate antibodies (section 2.3.2).

2.4.2 EQUILIBRIUM BINDING EXPERIMENTS

To investigate the binding affinities or equilibrium dissociation constant (K_d) of wild-type syntaxin 1a and mutants for munc18-1, or wild-type SNAP-25 and mutants for syntaxin 1a, binding equilibrium experiments were employed.

GST-syntaxin 1a or mutants and GST-munc18-1 were expressed in E. coli BL21, and purified using standard methods (section 2.3.7). SNAP-25 and SNAP-25 [G43D] fusion proteins encoded by pQE-30 vectors were expressed in *E. coli* M15 (pREP4), purified and eluted using standard methods (section 2.3.8). Glutathione Sepharose bead immobilised syntaxin 1a or mutants were incubated with a concentration gradient of SNAP25 or munc18-1 in a reaction volume of 0.5 ml. Proteins were incubated for 2 hours at 21 ºC, with shaking at 200 rpm to reach equilibrium. As a very small amount of GST-syntaxin 1a was used in each reaction and the reaction volume was sufficiently large, it can be assumed that the original SNAP-25 or munc18-1 concentration will equal the free concentration at equilibrium. To separate bound and free SNAP-25 or munc18-1, centrifugation by rapid filtration was employed. Samples were filtered at 4 ºC using 0.45 µm filters (Spin X, Corning Costar, UK), followed by two washes with 0.25 ml of ice cold buffer A. Samples were eluted and solubilised in sample buffer for SDS-polyacrylamide gel electrophoresis (section 2.3.1). Bound protein was analysed by western immunoblotting (section 2.3.2) using a mouse monoclonal antibody for SNAP-25 (clone 71.2) (section 2.1.5) or a mouse monoclonal antibody for munc18-1 (section 2.1.5). The ECL signal (section 2.3.2.3) was detected using a Gene Gnome bio imaging instrument (Syngene, UK) that contains a cooled charge coupled device (CCD), which has a far greater linear dynamic range than photographic film.

Immunoblots were quantified using NIH ImageJ software (http://rsb.info.nih.gov/ij/), by calculating protein band densities. Binding data was analysed by fitting the pooled data from each triplicate experiment to a variable slope dose response relationship using Prism 3.0 software from GraphPad (GraphPad Software, CA, USA).

2.4.3 Protein structural data

Protein structural data was obtained from the RCSB Protein Data Bank archive (http://www.rcsb.org/pdb/home/home.do). All protein structure illustrations were generated using Swiss-Pdb Viewer 3.7 (SP5) software (http://www.expasy.org/spdbv/).

2.5 Mammalian Cell Culture

All cell culture reagents were Gibco branded products supplied by Invitrogen (Paisley, UK) unless otherwise stated. All plasticware was Greiner branded products (Greiner, UK).

2.5.1 Routine mammalian cell culture

All mammalian cells were routinely cultured in the appropriate growth medium and supplemented with 5 or 10% (v/v) foetal bovine serum (FBS), and any additional supplements specified by the cell type (Table 2.5). Human Embryonic Kidney (HEK293) and Neuroblastoma 2a (N2a) cells were maintained at 37 ºC in 5% (v/v) CO_2, 95% (v/v) air. PC12 cells were maintained at 37 ºC in 7.5% (v/v) CO_2, 92.5% (v/v) air. To passage HEK293 cells, medium was removed and discarded, and the cells washed with 1 ml of versene (0.53 mM EDTA in PBS, pH 7.4). The cells were

passaged by applying 1 ml/75 cm^2 flask of trypsin-EDTA to the cell layer and incubated for 1-5 min at 37 °C. The cells were washed off the flask surface with the appropriate medium and re-suspended. To passage N2a cells, media was removed and discarded. The N2a cells were passaged by applying new medium to the flask and trituration was employed to wash the cells off the flask surface and re-suspend the cells. All cells were re-seeded into flasks, typically at a 1:3 or a 1:5 dilution. The cells were re-seeded every 3-4 days or when confluency was high. To passage PC12 cells, medium was removed and discarded, and the cells rinsed off the plastic using 5 ml of versene. The cell suspension was diluted with 50 ml medium and centrifuged at 500 x*g* for 5 min at room temperature. Medium was removed and the cells re-suspended in 3 ml media. The PC12 cells were re-seeded into collagen-coated flasks, typically at a 1:3 dilution. For microscopic or assay purposes, all cells were re-suspended in the appropriate medium at a density of approximately 10^6 cells/ml before being seeded onto glass coverslips in 6 well plates or 60 mm dishes.

Table 2.5. Routine mammalian cell culture conditions

Cell Line	Growth Medium	Media Supplements	Re-seed dilution	Supplier
HEK293	Dulbecco's modified Eagle's medium (D-MEM)	10% (v/v) Foetal bovine serum (FBS) 50 units of penicillin 50 µg/ml streptomycin 1% (v/v) L-Glutamine	1:5	ATCC*
N2a	Dulbecco's modified Eagle's medium (D-MEM)	10% (v/v) FBS 50 units of penicillin 50 µg/ml streptomycin	1:5	ATCC*
PC12	Advanced RPMI 1640	5% (v/v) FBS** 10% Horse serum** 1% Glutamax 50 µg/ml Gentamicin	1:3	ATCC*

* American Tissue Culture Company, Middlesex, UK.
** Hyclone, UK.

2.5.2 CLEANING OF GLASS COVERSLIPS

To prevent foreign material on coverslips interfering with imaging experiments, all coverslips were cleaned before poly-D-lysine coating or plating with cells. Firstly, coverslips were washed once with 100 mM NaOH + 0.1% (v/v) Decon- 90 detergent in a sonicator bath for 10 sec. Following sonication, the coverslips were washed 4 times with double distilled H_2O and washed once with 100% ethanol. Finally, the coverslips were washed with 100% acetone and allowed to air dry before use.

2.5.3 COATING COVERSLIPS FOR MICROSCOPY

To improve the ability of weakly adherent cell lines to attach to the glass surface, coverslips were coated with poly-D-lysine. Coating of coverslips was also essential for TIRF microscopy (section 2.7.2) to ensure a large surface area adhered to the glass surface. Poly-D-lysine was prepared in sterile double distilled water to a final concentration of 50 µg/ml. Glass coverslips (30 mm or 40 mm) were immersed in poly-D-lysine for 30 min before being washed with sterile distilled water and allowed to air dry under a UV light source. Alternatively, where required, Cell Tak (BD Biosciences, UK) was used to coat coverslips as per the manufacturer's instructions.

2.5.4 MAMMALIAN CELL TRANSFECTIONS

For the delivery of plasmid DNA into mammalian cells, cell transfections were performed using ExGen500 (Fermentas, UK) reagent for HEK293 and N2a cells or Lipofectamine 2000 (Invitrogen, UK) for PC12 cells. Twenty four hours prior to transfection, cells were seeded onto 30 mm or 40 mm glass coverslips at a density of approximately 10^6 cells/ml and maintained at 37 °C in 5% (v/v) CO_2, 95% (v/v) air. Before transfection the cells were allowed to reach 60-70% confluency. For HEK293 and N2a cell transfection samples, 5 µg DNA was diluted in 200 µl of 150 mM NaCl and mixed gently. For each sample, 16.5 µl ExGen500 was added and the solution

mixed gently. The optimal ratio of ExGen500 (µl) to nucleic acid (µg) is in the range of 3.3 to 1. After 10 min incubation at room temperature, 200 µl (1/10 of the total volume of the culture medium) of the reaction complex was added to the cells. The cells were incubated at 37 °C in 5% (v/v) CO_2, 95% (v/v) air for 48 hours prior to imaging. Lipofectamine 2000 (Invitrogen, UK) was used for PC12 cell transfections as per the manufacturer's instructions.

2.6 SAMPLE PREPARATION FOR MICROSCOPY

2.6.1 CELL FIXATION WITH PARAFORMALDEHYDE

For immunofluorescence, cells were fixed with 4% (w/v) paraformaldehyde (PFA). PFA was prepared by adding PFA powder (4 g) to double distilled sterile water (50 ml), heated to 60 °C, and cleared by the addition of 1 M NaOH. This stock solution was diluted with phosphate buffered saline (2 x PBS) (50 ml). The culture medium was removed and the cells were gently washed twice with 1 x PBS (section 2.1.1), and then fixed with 4% (w/v) PFA for 20 min. The fixative was removed by aspiration and the cells were washed twice with 1 x PBS and subsequently incubated with 50 mM ammonium chloride for 10 min, to quench autofluorescence. The cells were washed twice with 1 x PBS, before immunofluorescence staining.

2.6.2 DIRECT IMMUNOFLUORESCENCE

After fixation with 4% (w/v) paraformaldehyde, cells were immunostained using the appropriate antibodies. To permeabilise the cell membranes, the cells were incubated in 0.5% (v/v) Triton X-100 detergent diluted in 1 x PBS (section 2.1.1) for 4 min and then washed twice with 1 x PBS. The cells were incubated in the primary antibody (typically 1:500 dilution), diluted in 1 x PBS supplemented with 0.5% (w/v) fish skin gelatine for 3 hours at room temperature. The fish skin gelatine acts as a non-specific protein that blocks spurious antibody binding. The cells were washed at least 3 times with 0.5% (w/v) fish skin gelatine diluted in 1 x PBS. The cells were stained with the

conjugated secondary antibody (1:1000 dilution) diluted in 1 x PBS supplemented with 0.5% (w/v) fish skin gelatine for 1 hour at room temperature. The secondary antibody was removed and the cells washed 5 times with 1 x PBS and mounted on microscopic slides with mowiol anti-fade medium (Calbiochem, UK).

2.6.3 MAINTENANCE OF CELLS FOR LIVE CELL IMAGING

On the microscopic stage, cells were imaged in a POC-chamber-system (La Con, Germany). To control temperature and CO_2 levels, all live cell imaging was conducted on a heated stage at 37 °C, and cells were at 5% (v/v) CO_2, 95% (v/v) air, before and during imaging.

2.6.4 PLASMA MEMBRANE LABELLING

FM4-64 (N-(3-triethylammoniumpropyl)-4-(6-(4-(diethylamino)phenyl)hexatrienyl) pyridinium dibromide) (Invitrogen, Paisley, UK) was used as a plasma membrane marker. FM1-43 and its derivatives such as FM4-64 are used as probes for membrane trafficking as they are polar molecules that reversibly insert into a lipid bilayer membrane. These dyes are membrane-impermeant and are more fluorescent when bound to membranes than when in solution, and for these reasons are commonly used to study exocytosis and endocytosis of synaptic vesicles from central neurones (Betz & Bewick, 1992). The styryl dye FM4-64 was added to the medium at a final concentration of 5 μg/ml on the microscope stage. Cells were imaged immediately and FM4-64 was excited with an argon laser line at 515 nm.

2.6.5 CHOLESTEROL DEPLETION ASSAY

To study the effect of cholesterol depletion on SNARE protein localisation, cholesterol was sequestered using methyl-β-cyclodextrin (MβCD). Cells were

incubated with 10 mM MβCD in serum free medium at 37 °C in 5% (v/v) CO_2, 95% (v/v) air, for 30 min immediately before fixation and immunofluorescence, or live cell imaging.

2.6.6 CELL VIABILITY ASSAY USING CALCEIN-AM AND PROPIDIUM IODIDE

Calcein-AM (3', 6'-Di(O-acetyl)-2', 7'-bis[N, N bis(carboxymethyl)aminomethyl] fluoresceintetraacetoxymethyl ester) is a molecule that crosses the plasma membrane and is converted to a green-fluorescent calcein moiety after acetoxymethyl ester hydrolysis by intracellular esterases. Propidium iodide is a red-fluorescent nuclear and chromosome counterstain that is not permeant to live cells and thus can only stain dead cells. Both molecules are used to assay for living and dead cells, respectively. To assess cell viability following cholesterol depletion, both propidium iodide (Molecular Probes, Invitrogen, UK) and calcein-AM (Molecular Probes, Invitrogen, UK) were added to the cells at a final concentration of 3 μM for both dyes. Cells were incubated for 5 minutes on a heated stage at 37 °C in a chamber containing 5% (v/v) CO_2, 95% (v/v) air, and imaged immediately. Propidium iodide was excited with a helium/neon laser line at 543 nm. Calcein-AM was excited with an argon laser line at 488 nm.

2.6.7 LAURDAN STAINING

One hour prior to imaging, the cells medium was replaced with phenol red-deficient DMEM and Laurdan (6-dodecanoyl-2-dimethylamine-naphthalene) at a final concentration of 5 μM. By imaging time, the Laurdan had spread throughout the cell so that transient transfer in overall intensities between internal and plasma membranes was no longer noticeable. The coverslip and 1 ml of the colourless medium was transferred to the imaging chamber and incubated on a heated stage at 37 °C with 5% (v/v) CO_2, 95% (v/v) air during imaging. The same Laurdan-containing medium was used to maintain the equilibrium between partitioned and

non-partitioned Laurdan that had been set up in the previous hour. Laurdan fluorescence was collected in a blue channel (390-465 nm) and a red channel (480-520 nm).

The spectral shifts in the fluorescence emission of Laurdan can be quantified by calculating the generalised polarisation (GP) values for each pixel in the image. To enable quantitative comparison, the GP was skewed by a degree set by a factor, G. In accordance with the methodology of Gaus and colleagues (Gaus et al, 2003), G is defined as the multiplier necessary to obtain a GP of 0.207 for 0.1 mM Laurdan in DMSO with the same PMT gain settings. Our (corrected) GP values were given by the following equation:

$$GP = \frac{I_B - GI_R}{I_B + GI_R}$$

Where I_B = intensity of the blue channel, and I_R = intensity of the red channel.

2.6.8 CELL STIMULATION

In stimulation experiments, for imaging the medium was replaced with Krebs-Ringer bicarbonate buffer (115 mM NaCl, 5 mM KCl, 24 mM $NaHCO_3$, 2.5 mM $CaCl_2$, 1 mM $MgCl_2$, 10 mM HEPES (pH 7.4) and 0.1% (w/v) BSA; adjusted to 320 mOsm) . To elicit calcium influx, cells were stimulated with 55 mM KCl or 100 nM ionomycin and incubated for 20 min on a heated stage at 37 °C in a chamber containing 5% (v/v) CO_2, 95% (v/v) air, and imaged immediately or after 20 min.

2.7 MICROSCOPY TECHNIQUES

2.7.1 CONFOCAL LASER SCANNING MICROSCOPY (CLSM)

Confocal laser scanning microscopy (CLSM) microscopy is a technique that allows the acquisition of high resolution images from thin optical sections in a thick specimen. CLSM uses light from one or more lasers to focus on a single point on the defined focal plane to excite fluorescence. A computer controlled scanning mirror allows the laser beam to be rapidly scanned in lines across the specimen in the x-y direction at the focal plane to illuminate and record the entire field. A mixture of both emitted fluorescent light from the specimen and reflected laser light is recollected by the objective. The light then passes through a beam splitter that separates the light, allowing laser light through, and fluorescent light is instead reflected through a pinhole into the detection apparatus. The fluorescence detected at each point on the specimen is measured via a highly sensitive photomultiplier tube (PMT) (Figure 2.1). During the scanning, the PMT readings are recorded and an image is built up. In this study data was collected from fixed or live cells that had been labelled with single, double or triple fluorescent probes. Data image processing techniques of sequences of images were used to generate 3D representations of specimens.

All confocal images were acquired on a Zeiss LSM510 Axiovert confocal laser scanning inverted microscope fitted with an LSM510 scanning head, and equipped with four lasers, an Argon laser tuneable to 458 nm, 477 nm, 488 nm and 514 nm, a 543 nm He-Ne1 laser, a 633 nm He-Ne2 laser, and a MIRA 900 Ti:Sapphire femto-second pulsed laser at 800 nm. Band pass (BP) and long pass (LP) emission filters were used to allow frequencies within a given range through and reject those out with the given range. PMT detector gain and laser power were set to balance image brightness versus noise. Laser intensity and laser scanning was kept to a minimum to reduce phototoxic and bleaching effects. Digital scan zoom was set to acquire at Nyquist sampling rates (section 2.8.1) to improve resolution dependent upon the chosen objective. Using the multi-track approach or dual laser excitation, separate fluorescence emission channels were collected. Data acquisition was performed

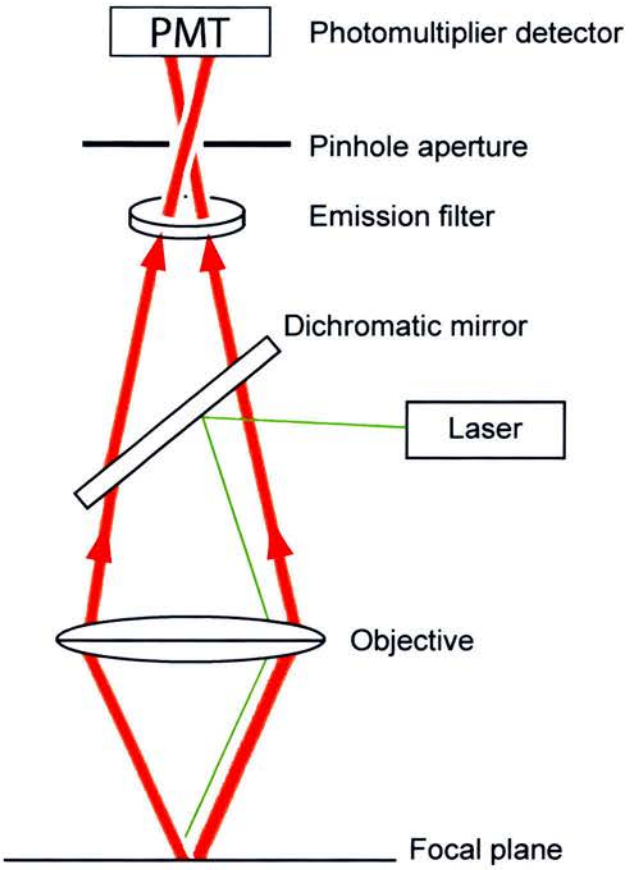

Figure 2.1 Confocal laser scanning microscopy (CLSM)
A schematic diagram of the optical pathway and principal components in the confocal laser scanning microscope system. The light source is a laser that produces high intensity, coherent light of a defined wavelength. The light is mirrored into the objective by the dichromatic mirror. The objective projects this laser beam on to the focal plane within the specimen. If you excite a fluorophore, light passes back through the dichromatic mirror and is focused at the detector pinhole aperture. While the laser light is focused on the focal plane considerable fluorescence is emitted above and below the focal plane as well, which results in blurring of the final image if this reaches the detector. A pinhole is introduced between the detector and the specimen to remove this light.

using a 1024 X 1024 pixel image size, using a Zeiss Plan NeoFLUAR 1.4 numerical aperture (NA) 63x oil immersion objective lens. All imaging was performed using fixed cells or live cells maintained at 37 °C in 5% (v/v) CO_2, 95% (v/v) air. Images were processed using Huygens Professional Software for image deconvolution (section 2.8.1) and Image J software for image data analysis.

2.7.2 Total Internal Reflection Fluorescence Microscopy (TIRFM)

TIRFM is a technique that exploits the unique properties of an induced evanescent wave or field in a limited region of the specimen immediately adjacent to the interface between two media possessing different refractive indices. The evanescent waves selectively illuminate and excite the fluorophores in the region of the specimen adjacent to the glass-medium interface (Figure 2.2). The half-maximal penetration depth of the evanescent wave is approximately 150 nm into the sample medium and thus only fluorophores adjacent to the surface will be excited and fluoresce. Therefore, this feature of TIRFM permits the selective visualisation of surface regions of a cell, such as the plasma membrane. This allows the visualisation of features and events on the plasma membrane, such as the identification of membrane proteins and their response to a stimulus, single protein trafficking, vesicles undergoing exocytosis, and vesicle movements close to the plasma membrane.

All TIRFM was undertaken on an Olympus total internal reflection system with minor modifications. Light from a 488 nm laser or a 561 nm laser was introduced into a motorised inverted epifluorescence microscope (IX81, Olympus, UK) through separate condensers. A micrometer screw in the illuminator changes the position of the laser beam in order to reach the critical angle for TIRF illumination and to adjust the depth of field. When in non-TIRF mode the laser beam was able to penetrate the specimen and allowed widefield illumination. The laser beam travelling through the objective exits the front lens at a high incident angle limited by the numerical aperture. Living cells have a refractive index between 1.33 and 1.38, so to achieve total internal reflection such a specimen was illuminated with a numerical aperture

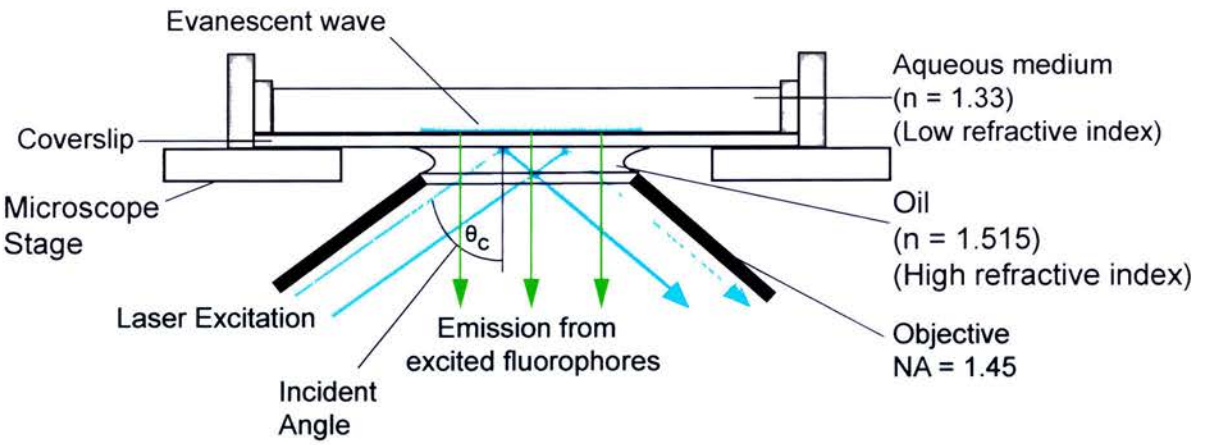

Figure 2.2 Illustration of total internal reflection fluorescence microscopy (TIRFM)

A schematic diagram of total internal reflection fluorescence microscopy. TIRF is a microscope technique that can be used to observe fluorescent events occuring at the interface between two media of different refractive indices. Laser illumination of a selected wavelength is introduced at a high incident angle through the glass coverslip, to which the specimen is adhered to. Refractive index differences between the glass and aqueous phases regulates how light is refracted or reflected at this interface as a function of the indicent angle. At a critical angle (θ_c) the light undergoes total internal reflection generating an evanescent wave in the aqueous medium. The evanescent wave excites fluorescent molecules immediately adjacent to the specimen-glass interface, typically within a few hundred nanometres, while those further afield are not excited.

greater then 1.38 to induce the evanescent wave that excites the fluorophores near the interface. The objective then recaptured the beam and redirected it back into the microscope. The system was equipped with excitation and emission filters allowing rapid sequential imaging of red and green fluorescent emission. Data acquisition was performed using a 512 x 512 pixel image size, using an Olympus 1.45 NA 60x oil immersion objective lens. TIRFM images were acquired on a Hamamatsu Electron Multiplier CCD (EM-CCD) digital camera. For TIRFM imaging, all cells were plated on coverslips coated with poly-D-lysine (section 2.5.3). All imaging was performed using live cells maintained at 37 ºC in 5% (v/v) CO_2, 95% (v/v) air or cells fixed with 4% (w/v) paraformaldehyde and subsequently immunostained and imaged in PBS.

2.7.3 TIME CORRELATED SINGLE-PHOTON COUNTING FLUORESCENCE LIFETIME IMAGING MICROSCOPY (TCSPC-FLIM)

In this study, to quantify protein interactions, time correlated single-photon counting (TCSPC) fluorescence lifetime imaging microscopy (FLIM) was used. This is a technique used to perform fluorescence lifetime imaging with a laser scanning microscope. The fluorescence of molecules is characterised by both the emission intensity and the emission spectrum, but in addition it also has a characteristic lifetime. If a photon excites a fluorophore, electrons are raised to an excited state. The electrons stay in this excited state for a period of time before releasing a photon as they drop back to the ground state. It is the time from excitation of the fluorophore to emission of a photon that is the fluorescence lifetime. The interaction of an excited molecule with its surrounding micro-environment can change the fluorescence lifetime (For theory see Chapter 1: Introduction) (Figure 1.5).

In this study, all imaging experiments were performed using a Zeiss LSM510 Axiovert confocal laser scanning microscope, equipped with a pulsed excitation source (MIRA 900 Ti:Sapphire femto-second pulsed laser coupled with a VERDI 10W pump laser (Coherent)) capable of delivering pulses of photons at a repetition rate of 80 MHz (Duncan et al, 2004) (Figure 2.3). TCSPC measurements were made

under 800-820 nm TPE (two-photon excitation), which efficiently excited monomeric Cerulean (mCerulean), without any detectable excitation or emission from EYFP, using a fast photomultiplier tube (H7422; Hamamatsu Photonics UK) coupled directly to the rear port of the Axiovert microscope and protected from room light using a Uniblitz shutter. The non-descanned detector (NDD) feeds the detected light into the photomultiplier tube. Two constant fraction discriminators (CFD) receive the single photon pulses and a time-to-amplitude converter (TAC) measures the time from the detection of a photon to the next laser pulse. The time after each laser pulse, when a single photon hits the detectors, is measured and the stop pulse for the time measurement is obtained from the laser. This 'reversed start-stop' principle is vital to the processing of the high laser repetition rates. The TAC output voltage is converted by the 8-bit analog-digital converter (ADC) into 256 time bins. The scanning interface is a system of counters that receives the scan control pulses from the Zeiss LSM510 microscope and determines the current position of the laser in the scanning area. Once a photon is detected, the device determines the time, t, within the decay curve and the precise location of the laser spot with the scanning area, x and y. Our system records data from a single point at a time as the confocal scans across the field of view. In the memory, the photon distribution versus t, x and y, builds up and the result can be shown as an array of pixels containing a complete fluorescent decay function. The recording is synchronised with the scanning via the pixel clock, line clock, and the frame clock signals from the microscope control box. Band pass (BP) and long pass (LP) filters were used to allow spectral separation of the donor and acceptor fluorophores. TCSPC recordings were acquired routinely for between 10 s and 60 s, and mean photon counts were between $10^5 - 10^6$ counts per second. Images were recorded at 256 x 256 pixels from a 1024 x 1024 image scan (because of a 4 x 4 bin) with 256 time bins over a 12 ns period, using a Zeiss Plan NeoFLUAR 1.4 NA 63x oil immersion objective lens. The number of photons given off by the sample decreasing over time results in a decay curve which can be fit to provide a measure of the lifetime of the fluorophore.

TCSPC-FLIM becomes really useful when looking at Förster Resonance Energy Transfer (FRET) between fluorescent protein partners. FRET involves the direct

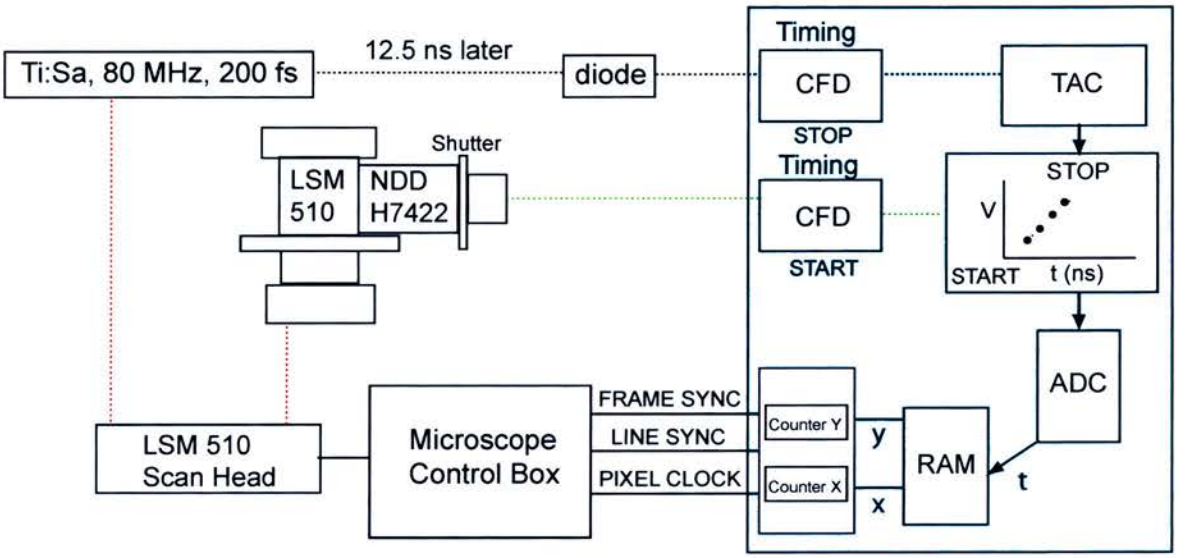

Figure 2.3 Setup of the time correlated single-photon counting (TCSPC)-fluorescence lifetime imaging microscopy (FLIM) system.
For a detailed explanation of the theory of TCSPC-FLIM and its implementation see Chapter 1: Introduction (sections 1.5.5, 1.5.9 and 1.5.10) and section 2.7.3 respectively. Adapted from Becker and Hickl, 2005.

transfer of non-radiative energy between a donor and an acceptor molecule and this can be used to report protein interactions. TCSPC-FLIM provides quantitative data to measure the fraction of molecules undergoing FRET which is observed as a shortening or quenching of the donor fluorescence lifetime. This effect was quantified directly in each pixel of an image and used to show that molecules were within 10 nm of each other by nature of the transfer of energy. In this study, mCerulean, a fluorescent protein with a mono-exponential fluorescence decay, was fused to the C-terminus of syntaxin 1a (donor). mCerulean has a single fluorescence lifetime (Rizzo et al, 2004) but in the presence of an acceptor molecule such as an EYFP fusion protein with which FRET can occur, a second, quenched donor lifetime was detected.

2.8 IMAGE PROCESSING AND ANALYSIS

2.8.1 IMAGE DECONVOLUTION AND NYQUIST SAMPLING RATES

All confocal microscopy three-dimensional (3D) image stacks were subject to deconvolution to improve the contrast and resolution. Deconvolution is a computational method that works by reversing the optical distortion that occurs in a microscope. This was necessary to reassign out-of-focus fluorescence, and background signals, thereby improving the contrast and resolution of the image (Figures 2.4 and 2.5). During the process of image acquisition by the microscope information is degraded as a result of out-of-focus light, axial distortion and electronic noise degrading the image quality. This blurring and electronic noise from the PMT is defined mathematically by the point spread function (PSF). The PSF describes the 3D light distribution of a single point, and therefore describes the distribution of every light source of a sample measured by a fluorescence microscope. The dimensions of the PSF vary between fluorophores, refractive indices, and microscope systems. The process of image deconvolution employs the PSF and the microscope parameters, along with an iterative algorithm to reassign the out-of-focus light and thus restore the original image. It is possible to experimentally measure the PSF in the microscope by recording the image of a sub-resolution

spherical bead, however, due to the technical difficulties in directly measuring a PSF, theoretical PSFs are commonly used (Figure 2.4).

It is vital for the quality of deconvolution that all the information gathered by the optics of the microscope is captured optimally. Thus when sampling a signal or converting an analog signal to a digital signal, the sampling rate interval in the x, y and z direction should be set at 2.3 times that of the resolvable spatial frequency which conforms to the Nyquist sampling theorem (Pawley, 2006). The Nyquist sampling frequency is therefore the minimal sampling at which a sample must be recorded to ensure that all the information present in the real signal is represented in the samples. This enables the reconstruction of the original image from the sampled version. In confocal microscopy, the Nyquist sampling rate depends on various factors, including the excitation wavelength, the numerical aperture of the objective, and the refractive indices of the immersion and mounting medium. Image data acquired at Nyquist sampling rates were deconvolved using Huygens software (Scientific Volume Imaging, The Netherlands), using a theoretical PSF calculated from the microscope parameters, and the resulting images were analysed using NIH Image J software (http://rsb.info.nih.gov/ij/) (Figure 2.5).

2.8.2 QUANTIFICATION OF PROTEIN CO-LOCALISATION

Co-localisation can be defined as the presence of two or more distinct fluorescent molecules in the same non-resolvable volume. Quantitative co-localisation analysis was performed to determine the spatial localisation of two or more proteins in the cytoplasm or at the plasma membrane. The proteins were either fluorescently tagged via molecular cloning or are fluorescent through direct immunofluorescence staining. If they co-localise then the colours emitted by them will occupy the same voxel in the image. All image co-localisation analysis was conducted after image data deconvolution (section 2.8.1). Using the NIH Image J software (http://rsb.info.nih.gov/ij/) co-localisation threshold plugin a number of measurements were generated (Figure 2.6).

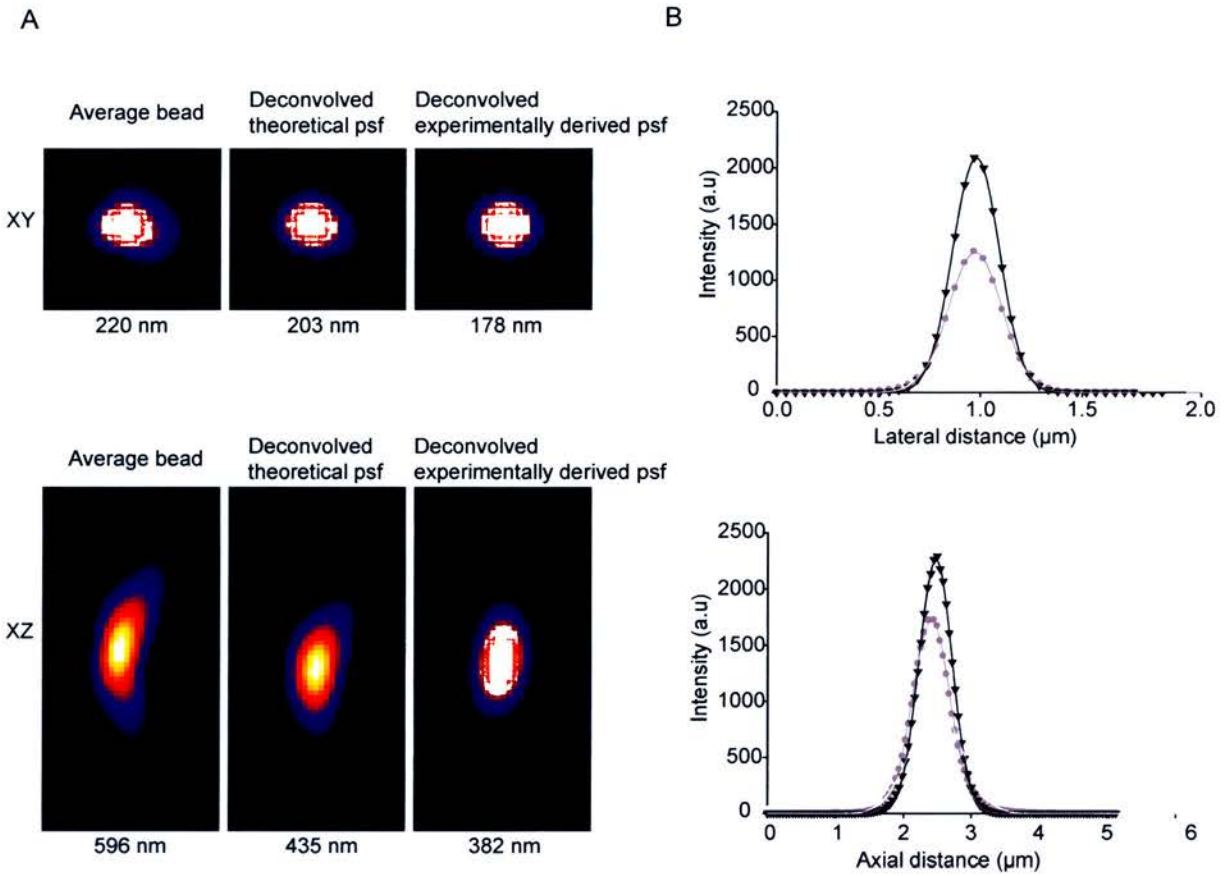

Figure 2.4. Using fluorescent beads to determine the PSF of the microscope system.

Fluorescent beads, 0.175 μm in diameter were immobilised using Cell Tak on glass coverslips and imaged in aqeuous media by CLSM. Confocal stacks were analysed using Huygens Professional software to generate an average bead using automatic object recognition (n = 20). **(A)** The average bead was deconvolved using Huygens Essential software using a theoretical PSF calculated from the microscopic parameters and using an experimentally derived PSF. The raw image and the resulting deconvolved images were analysed using NIH Image J software. XY profiles and XZ profiles of the average bead are shown. Note that in both the XY and XZ projections after deconvolution out of focus fluorescence is re-assigned and thus the images are sharper. **(B)** The lateral and axial profiles of the raw data image (light grey circles ( )), the theoretical PSF deconvolution image (dark grey circles (•)), and the experimentally derived PSF deconvolution image (black triangles (▾)), were plotted to determine the resolution of the confocal microscope.

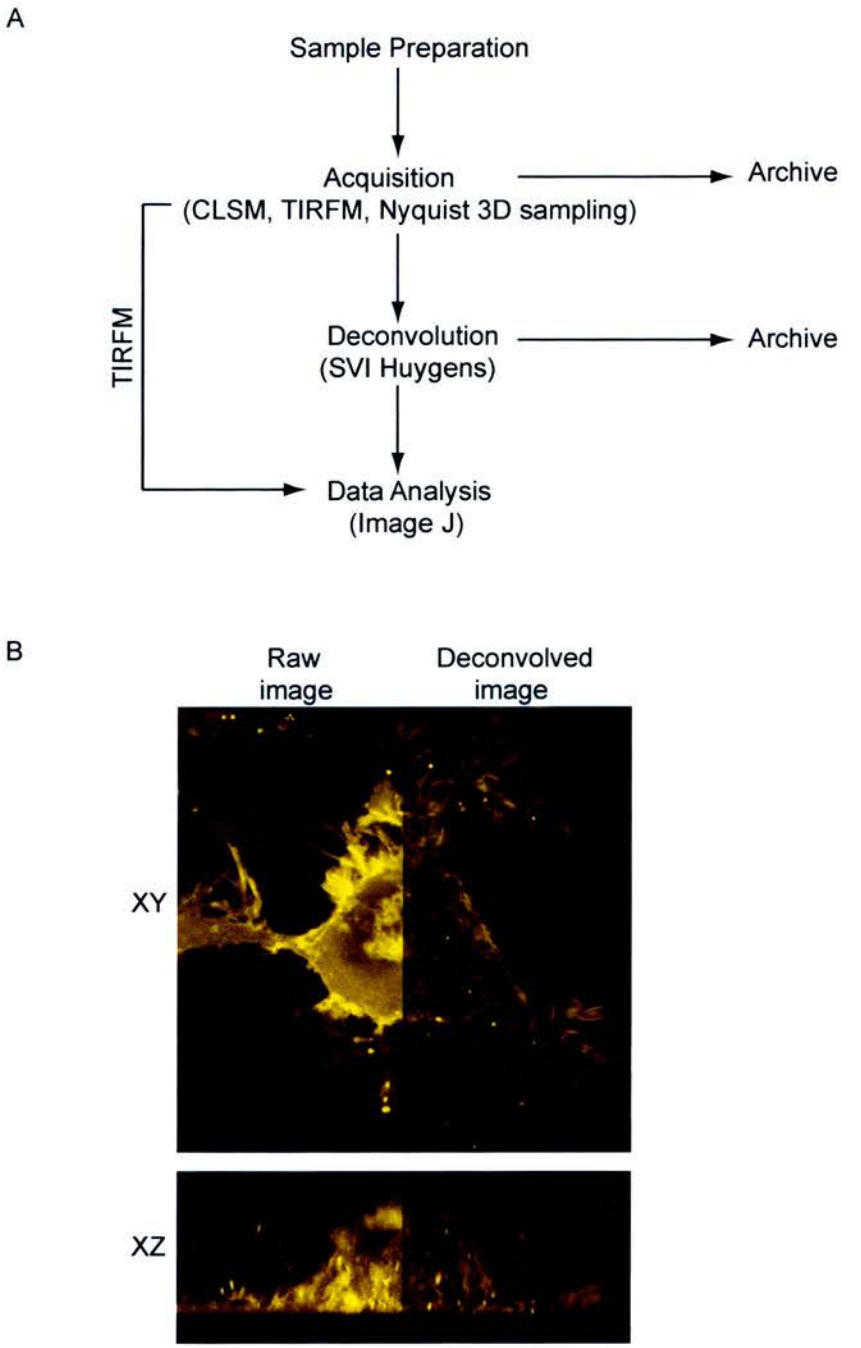

Figure 2.5 Data acquisition and deconvolution.
(A) A flowchart representing microscopy image workflow from sample preparation through to image quantification. **(B)** Raw and processed images of a live N2a cell expressing EYFP-SNAP25A$_{1\text{-}206}$ and imaged by CLSM. The processed image was deconvolved using Huygens Software (Scientific Volume Imaging, The Netherlands), using a theoretical PSF calculated from the microscopic parameters. The raw image and the resulting deconvolved image were analysed using NIH Image J (http://rsbweb.nih.gov/ij/). The raw image before deconvolution was merged with the deconvolved image. Note that noise is reduced, data is re-assigned and resolution in axial and lateral dimensions is increased.

The degree of co-localisation cannot be judged by simple visualisation with the naked eye even when it seems obvious and therefore more reliable statistically rigorous quantitative methods are necessary for comparing images. In this study two alternative methods were used to quantify the overlap or co-localisation between two separate channels. Pearson's correlation coefficient and Mander's overlap coefficient were employed.

Pearson correlation coefficient (R) measures the intensity-dependent correlation between two channels and provides a value ranging from -1 to 1. This value reflects the degree of linear relationship between the two variables, R= 1 represents perfect co-localisation, R= 0 shows there is no co-localisation whatsoever, and R= -1 represents perfect negative co-localisation, however, the latter is theoretically impossible in fluorescence microscopy. The Pearson's correlation coefficient was computed for 2 channels of an image, yielding a measure for the degree of co-localisation of the proteins.

Mander's overlap coefficient represents the fraction of total red signal that is co-localised with green signal and the fraction of total green signal that is co-localised with red signal to show a percentage overlap (Manders et al, 1993). It may be the case that in some examples all the red pixels overlap with the green pixels, yet in other regions, many green pixels are alone where no red signal is detected. Manders overlap coefficient for two channels in an image yields a value between 0 and 1, with 0 being low coincidence and 1 being high coincidence.

Co-localisation was displayed in a qualitative manner by merging the two channels resulting in yellow hues representing overlapping pixels or areas of coincidence (Figure 2.6). The relationship between the red and green pixels in an image was displayed in a quantitative manner by generating a frequency histogram of red versus green pixels (Figure 2.6). A perfect correlation results in a pixel distribution along a straight line whose slope depended on the fluorescence intensity ratio between the two channels. Deviation from this line (the residual for each voxel) could then be calculated to produce a residual map that corresponded to covariance between the

two channels in an image (Figure 2.6). A residual map is a method of graphically representing the degree of correlation throughout the cell. The residual maps were generated by calculating the residual of each voxel from the linear regression fit to the intensities of each channel from all voxels. The co-localisation threshold plugin from Image J software (http://rsb.info.nih.gov/ij) was used to calculate the linear regression equation of best fit ($y = mx + b$). The x axis channel (green) was used to generate a predicted y axis channel (red) using the line of best fit. The difference between the observed y axis channel and the predicted y axis channel was then calculated using the following equation:

$$\text{Residual} = \frac{\text{Observed - Predicted}}{\text{Observed + Predicted}}$$

This equation was applied to constrain the residual values to a range of -1 to 1. For display, the residual was shown on a Hue Saturation Brightness (HSB) colour scale, where Hue was defined by the residual, Brightness was the combined intensities of channels 1 and 2, and Saturation was the maximum value of 255. The resulting residual maps are displayed on a colour scale from -1 to 1, with cyan representing a zero residual or perfect intensity covariance between the channels.

2.8.3 FLIM DATA ANALYSIS AND FRET CALCULATIONS

TCSPC-FLIM data analysis used pixel-based fitting software (SPCImage, Becker & Hickl) that was able to import the data generated from the FLIM module. The data was fit to a mono-exponential or a bi-exponential decay using the minimum number of components to minimise the residuals. In addition, an adaptive offset-correction was performed. This constant offset takes into consideration the time-independent baseline due to the dark noise of the detector and the background caused by room light, calculated from the average number of photons per channel preceding the rising part of the fluorescence trace. To fit the parameters of the multi-exponential decay to the fluorescence decay trace measured by the system, a convolution with the

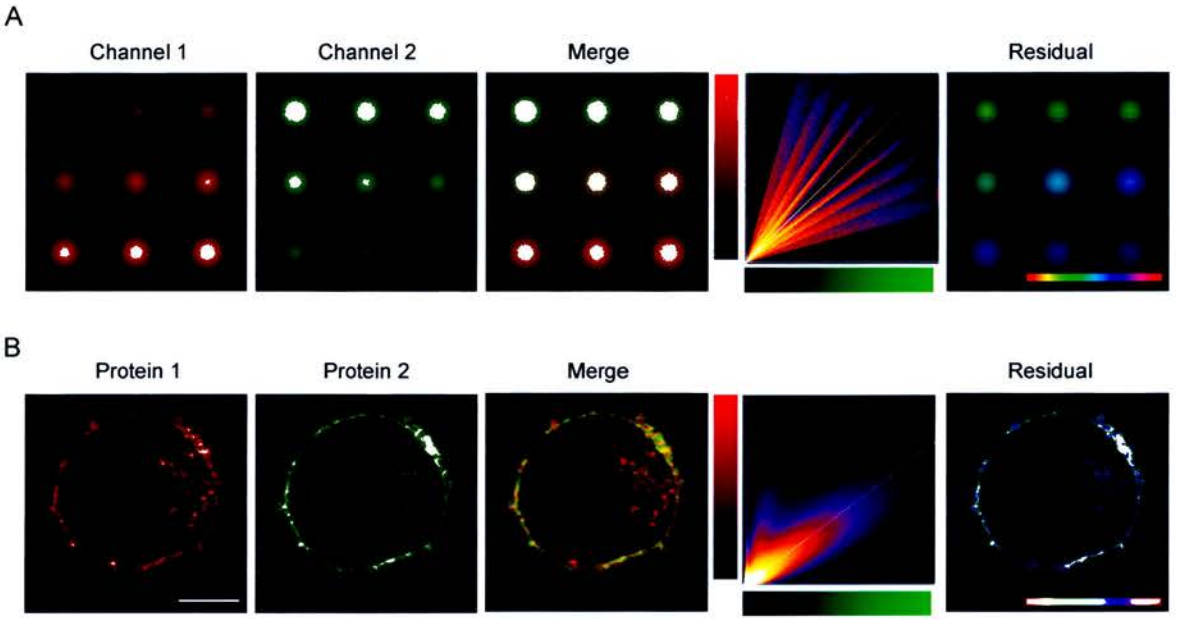

Figure 2.6 Quantitative analysis of co-localisation and covariance of fluorescently labelled proteins in living cells.
(A) Synthetic data analysed in a qualitative and quantitative manner. Two arrays of dual colour spheres of varying intensity (red and green channels) can be analysed in a qualitative manner by merging the two channels resulting in yellow hues which represent areas of coincidence or co-localisation. The relationship between the red and green pixels in an image can be displayed in a quantitative manner by generating a frequency histogram of channel 1 and channel 2 intensity in each pixel for all pixels in the dataset. A perfect correlation results in a pixel distribution along a straight line whose slope will depend on the fluorescence ratio between the two channels and whose spread is quantified by the Pearson's correlation coefficient. Deviation from this line (the residual for each pixel) can then be calculated to produce a residual map that corresponds to covariance between the channels. The hue is from -1 to 1 with *cyan* corresponding to a zero residual or perfect covariance. **(B)** Application of quantitative analysis of co-localisation and covariance in N2a live cells. Two fluorescently labelled proteins thought to interact with a defined stoichiometry were co-expressed in live cells and imaged by CLSM in 3D. The channels were analysed by merging (co-localisation) and residual mapping (covariance) as described for the synthetic data in (A).The merged image shows areas of coincidence in yellow hues on the plasma membrane and the two dimensional histogram represents the intensity of each channel in each voxel with a colour scale representing frequency and shows that the intensities of the two proteins appear to correlate. Residual mapping indicates that the proteins show low residuals on the plasma membrane and in some intracellular compartments. Scale bar, 5 μm.

instrumental response function was carried out. The optimisation of the fit parameters was performed by using the Levenberg-Marquardt algorithm, minimising the weighted chi-square quantity. This approach can be used to separate the interacting from the non-interacting donor fraction in our FRET systems. The long lifetime component $\tau 2$ was determined by control assays with cerulean alone, or expressed with (non-interacting) EYFP. This value was subsequently used as a fixed $\tau 2$ lifetime for all other experiments.

2.8.4 ANALYSIS OF t-SNARE CLUSTERS

All image analysis was carried out after image data deconvolution (section 2.8.1). For the analysis of syntaxin 1a and SNAP-25 cluster sizes from 3D confocal image stacks, the full width at half maximum intensity (FWHM) approach was employed as this does not require the edge of the cluster to be defined. Regions of interest were obtained from the plasma membrane. The plasma membrane was determined by plotting the z-axis profile of the confocal stack and taking the z slice at half the maximum intensity (illustrated in Figure 5.1A). Using Image J software (http://rsb.info.nih.gov/ij/), two perpendicular lines were drawn through the centre of the cluster, ensuring that they bisect the brightest point. To quantify the FWHM of individual clusters, the intensity profile along a row of pixels was used. Gaussian statistics were applied to calculate the FWHM which is directly proportional to the standard deviation. The FWHM value was calculated by multiplying the standard deviation of the individual cluster value (obtained from the Gaussian fit of the line plot) by 2.35 (illustrated in Figure 5.5B).

CHAPTER THREE:

MODES OF SYNTAXIN1A AND MUNC18-1 INTERACTION

3.1 INTRODUCTION

Syntaxin has the ability to act as a molecular switch by adopting two structurally distinct forms; a closed conformation that is incapable of forming the SNARE complex, and an 'open' or apparently reactive conformation, allowing SNARE complex formation (Dulubova et al, 1999; Fasshauer, 2003; Munson & Hughson, 2002; Salaun et al, 2004; Toonen, 2003). In the open conformation, the SNARE helix is free to interact with cognate SNARE proteins and in this conformational state syntaxin was previously shown not to interact with munc18-1 (Dulubova et al, 1999). In contrast, in the closed conformation the N-terminal Habc domain of syntaxin binds to the SNARE helix of syntaxin obstructing its interaction with cognate SNAREs, and thus SNARE complex assembly (Bracher & Weissenhorn, 2004; Dulubova et al, 1999; Misura et al, 2000b; Munson & Hughson, 2002). Munc18-1 has been shown to bind with high affinity to this closed conformation preventing syntaxin entering the SNARE complex, and therefore acting as a negative regulator of membrane fusion (Pevsner et al, 1994a; Pevsner et al, 1994b; Yang et al, 2000). This was supported by *in vitro* studies of an open mutation (L165A/E166A) of syntaxin (Dulubova et al, 1999). This mutant was said to represent an open conformation of syntaxin which disrupted its ability to bind munc18-1, thereby permitting rapid acceleration of SNARE complex formation (Dulubova et al, 1999). To initiate SNARE core complex assembly it was thought that the dissociation of the syntaxin 1a-munc18-1 complex was necessary to allow an open conformation of syntaxin 1a, exposing the SNARE helix to initiate an interaction with SNAP-25 and synaptobrevin to form the SNARE complex (Dulubova et al, 1999). In contrast, the yeast homologues Sec1p and Sly1p suggest a positive regulatory role in SNARE mediated membrane fusion, remaining bound to their syntaxin homologue during SNARE complex formation and for this reason are believed to act as chaperones (Bracher & Weissenhorn, 2002; Carr et al, 1999; Dulubova et al, 2003; Misura et al, 2000b).

At the inception of this work the interaction of munc18-1 with syntaxin 1a was in sharp contrast to the specificity of its yeast homologues Sec1p and Sly1p which both bind to the N-terminus of their cognate syntaxins and remain bound during SNARE

complex formation. As the yeast and mammalian SM proteins possess different binding mechanisms and regulatory effects, the precise functional role of the syntaxin 1a-munc18-1 interaction remains unclear. In this chapter, the questions arose whether munc18-1 can in fact bind to the N-terminus of its cognate syntaxin 1a, and if munc18-1 can remain associated with syntaxin 1a throughout core complex assembly as seen with yeast homologues.

In this investigation, the syntaxin 1a-munc18-1 interaction was analysed using wild-type syntaxin 1a, N-terminal truncations and an "open" (L165A/E166A) mutation in which syntaxin 1a adopts the open conformation (Dulubova et al, 1999). I show that munc18-1 adopts two binding modes with syntaxin 1a. Using quantitative co-localisation and TCSPC-FLIM I demonstrate that these two binding modes are spatially segregated within living cells. Furthermore, I demonstrate that munc18-1 can readily bind to the N-terminal of an "open" mutation of syntaxin 1a allowing both binary and ternary SNARE complex formation as seen in other eukaryotic species.

3.2 Evolutionarily distant syntaxin homologues show high degrees of structural conservation

Throughout evolution the SM proteins show remarkable structural conservation which would suggest a common binding mechanism and function. However, in different species disparate modes of binding between SM proteins and their cognate syntaxins exist. For this reason, I investigated whether it was possible, despite previous reports, that mammalian munc18-1 could remain bound to the N-terminus of syntaxin 1a during ternary SNARE complex formation.

A structural alignment of the yeast SM protein Sly1p bound to the N-terminus of the peptide Sed5p with munc18-1 bound to syntaxin 1a clearly shows that munc18-1 and Sly1p demonstrate highly conserved topology despite an overall sequence identity of only 18% (Figure 3.1A, left panel). Sed5p displays N-terminal binding to Sly1p, yet in contrast munc18-1 binds to the closed conformation of syntaxin 1a and this has

long been accepted as the principal mode of interaction. However, due to the highly conserved topology between munc18-1 and Sly1p it would be expected that syntaxin 1a interacts with munc18-1 through its N-terminus. Therefore, it is possible that an open mutation of syntaxin 1a could still support an interaction with munc18-1. Figure 3.1A (right panel) shows a structural diagram of munc18-1 bound to syntaxin 1a (Burkhardt et al, 2008) showing the position of the syntaxin 1a open mutation (L165A, E166A) that is used throughout this thesis.

Initially, the conservation of amino acids in a variety of syntaxin homologues from evolutionarily distant species, including Sed5p from *S.cerevisiae*, were examined (Figure 3.1B). Sequence analysis of the syntaxin homologues revealed a high degree of similarity throughout the sequence, corresponding to the SNARE helix and the head domain of syntaxin. It was also evident that there was a high degree of similarity in the first 15 amino acids corresponding to the N-terminus of syntaxin. Close inspection of the amino acids contained within the N-terminal region of the syntaxin homologues revealed a high degree of conservation (Figure 3.1C), with an aspartate-arginine (K/R DR) motif conserved in both Sed5p and the syntaxin homologues. Therefore, to determine whether the N-terminal region of syntaxin 1a was capable of interacting with munc18-1, as seen in yeast homologues, a series of N-terminal truncations of syntaxin 1a were constructed which can preferentially adopt the closed or open conformational states.

3.3 CONSTRUCTION OF SYNTAXIN 1A AND MUTANT FUSION PLASMIDS

To investigate the interaction between munc18-1 and syntaxin 1a, *in vitro* studies were coupled with genetically encoded fluorescent fusion protein studies in mammalian neuroendocrine cells. A variety of syntaxin 1a mCerulean fusion proteins were constructed (Figure 3.2). In order to accomplish this, the N-terminal pmCerulean-C1-syntaxin 1a ($Syx1a_{1\text{-}288}$) fusion plasmid encoding syntaxin 1a and a mCerulean fluorescent region was constructed. The ECFP region from pECFP-C1-syntaxin 1a (Table 2.2) was excised and substituted for mCerulean from the vector

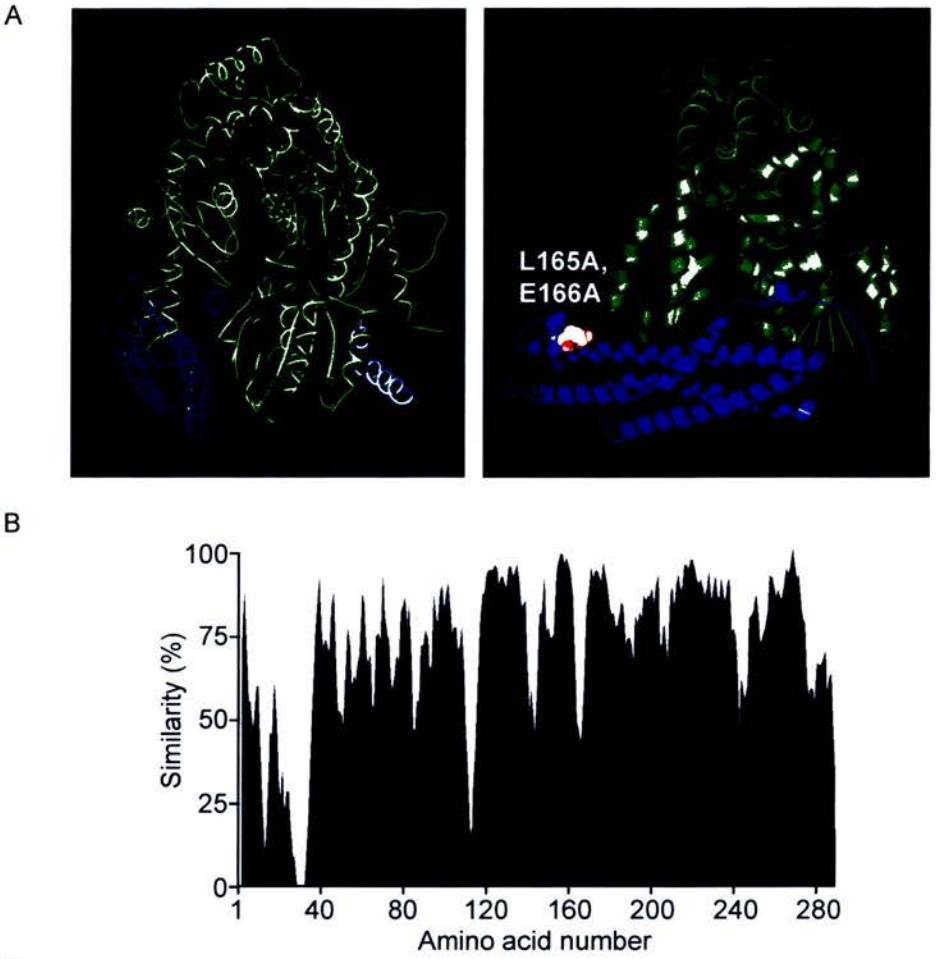

Figure 3.1 Sequence and structural conservation in syntaxin/SM protein interactions.

(A) Structural alignment of yeast SM protein Sly1p ( ) bound to an N-terminal peptide of Sed5p ( ) and mammalian SM protein munc18-1 ( ) bound to syntaxin 1a ( ) (left panel) (Protein Data Bank number: IMQS (Bracher and Weissenhorn, 2002) and 3C98 (Burkhardt et al., 2008) respectively). Both munc18-1 and Sly1p show highly conserved topology despite an overall sequence conservation of only 18%. Ribbon diagram of munc18-1 ( ) bound to syntaxin 1a ( ) (Protein Data Bank number: 3C98 (Burkhardt et al., 2008)) showing the open mutation (L165A/E166A) (right panel). **(B)** Sequence alignment of syntaxin homologues with similarity scored at each position. **(C)** The highly conserved N-terminal region (amino acids 1-28) of syntaxin homologues and Sed5p are shown on a colour-coded scale (yellow, identical; cyan, conserved; green, similar).

pmCerulean-C1 (Table 2.2) at *Nhe*I and *Bsr*GI sites using standard molecular techniques (see Chapter 2: Materials and Methods).

The generation of N-terminal truncations of pmCerulean-C1-syntaxin 1a was performed by standard PCR techniques using the following primers: $Syx1a_{1-288}$ forward primer, 5'–CAA GCT TCG GCT ATG AAG GAC CGA ACC CAG GAG- 3', $Syx1a_{7-288}$ (Δ6) forward primer, 5' –CAA GCT TCG GCT GCC GCA GCG GCG CTC CGC ACG GCC AAG GAC AG- 3', Syx1a reverse primer, 5' –CGG TAC CGT TCC AAA GAT GCC CCC GAT GGT GGA GGC G- 3'. Syntaxin 1a cDNA was amplified using standard PCR practices (see Chapter 2: Materials and Methods) and the resultant amplified product ligated into *Hin*dIII/*Kpn*I sites of pmCerulean-C1.

The generation of N-terminal truncations of GST fusion proteins of syntaxin 1a were performed by standard PCR techniques using the following primers that were designed to incorporate restriction sites flanking the cDNA region of interest: $Syx1a_{7-261}$ (Δ6), 5' - TCT AGA CGC AGA AGC GGA GCT CCG CAC GGC CAA GGC CAG C- 3', $Syx1a_{13-261}$ (Δ 12), 5' – TCT AGA CGC AGA AGC GGA CAG CGA TGA CGA TGA TGT CAC- 3', $Syx1a_{22-261}$ (Δ21), 5' – TCT AGA CGC AGA AGC GGT CAC TGT GGA CCG AGA CCG CTT CAT GG- 3', $Syx1a_{1-261}$ reverse primer, 5' - AAG CTT ATG CCT TTG CTC TGG TAC TTG ACG GCC TTC- 3'. Syntaxin 1a cDNA was amplified using standard PCR practices (see Chapter 2: Materials and Methods) and the resultant amplified product ligated into *Hin*dIII/*Xba*I sites of pGEX-KG. The distance between the fusion protein and syntaxin 1a was maintained in all constructs.

The L165A/E166A [Open] mutation was introduced into pmCerulean-syntaxin 1a and pGEX-KG-syntaxin 1a constructs by site-directed mutagenesis (see Chapter 2: Materials and Methods) using the following oligonucleotide primers: 5' - GAC CAC GAC CAG TGA GGA AGC GGC AGA CAT GCT GGA GAG TG - 3' and 5' – CAC TCT CCA GCA TGT CTG CCG CTT CCT CAC TGG TCG TGG TC – 3'.

To generate an unfused munc18-1 expression vector, a Munc18-1 insert was generated for sub-cloning into pGEM-T-Easy vector by PCR amplification (see Chapter 2: Materials and Methods). The following primers were used that contain a restriction site at the 5' ends (the restriction sites are underlined): primer 1 (*Xho* I), 5'-TCT CGA GCT ATG GCC CCC ATT GGC CTC AAG -3', and primer 2 (*Kpn* I), 5'-GGT ACC TTA ACT GCT TAT TTC TTC GTC TGT TTT ATT C-3'. Subsequently, the munc18-1 insert was ligated into pCI vector (Table 2.2).

The integrity of all the constructs was verified by DNA sequencing. The plasmid construct maps for all the constructs used in this study are shown in the Appendix. Figure 3.2 shows schematic diagrams of all the syntaxin 1a constructs and the naming system adopted throughout this study.

3.4 MUNC18-1 INTERACTS WITH THE N-TERMINUS OF SYNTAXIN 1A *in vitro*

To establish whether munc18-1 can bind to syntaxin 1a via N-terminal binding, a series of N-terminal truncations in both GST fused syntaxin 1a (GST-Syx1a$_{1\text{-}261}$) and an open syntaxin 1a mutant (GST- Syx1a$_{1\text{-}261}$ [Open]) were immobilised on glutathione sepharose beads and incubated with bacterial extract containing expressed recombinant His$_6$ munc18-1 for 30 minutes at 4 °C. It was found that munc18-1 purified via its His tag was unstable, however, it was stable in the bacterial extract. Following standard washing procedures (see Chapter 2:Materials and Methods), bound material was analysed by SDS-PAGE and subsequent Coomassie blue staining (see Chapter 2: Materials and Methods) (Figure 3.3A). Wild-type and N-terminal truncations of syntaxin 1a which can adopt the closed conformation had no effect on munc18-1 binding, and munc18-1 was capable of binding to them all at similar levels. In addition, the open mutation of syntaxin 1a was also able to bind to munc18-1 at a similar level. However, if both modes of binding were severely disrupted by combining the open mutant of syntaxin 1a with N-terminal truncations, the ability of munc18-1 to bind to syntaxin 1a was noticeably reduced.

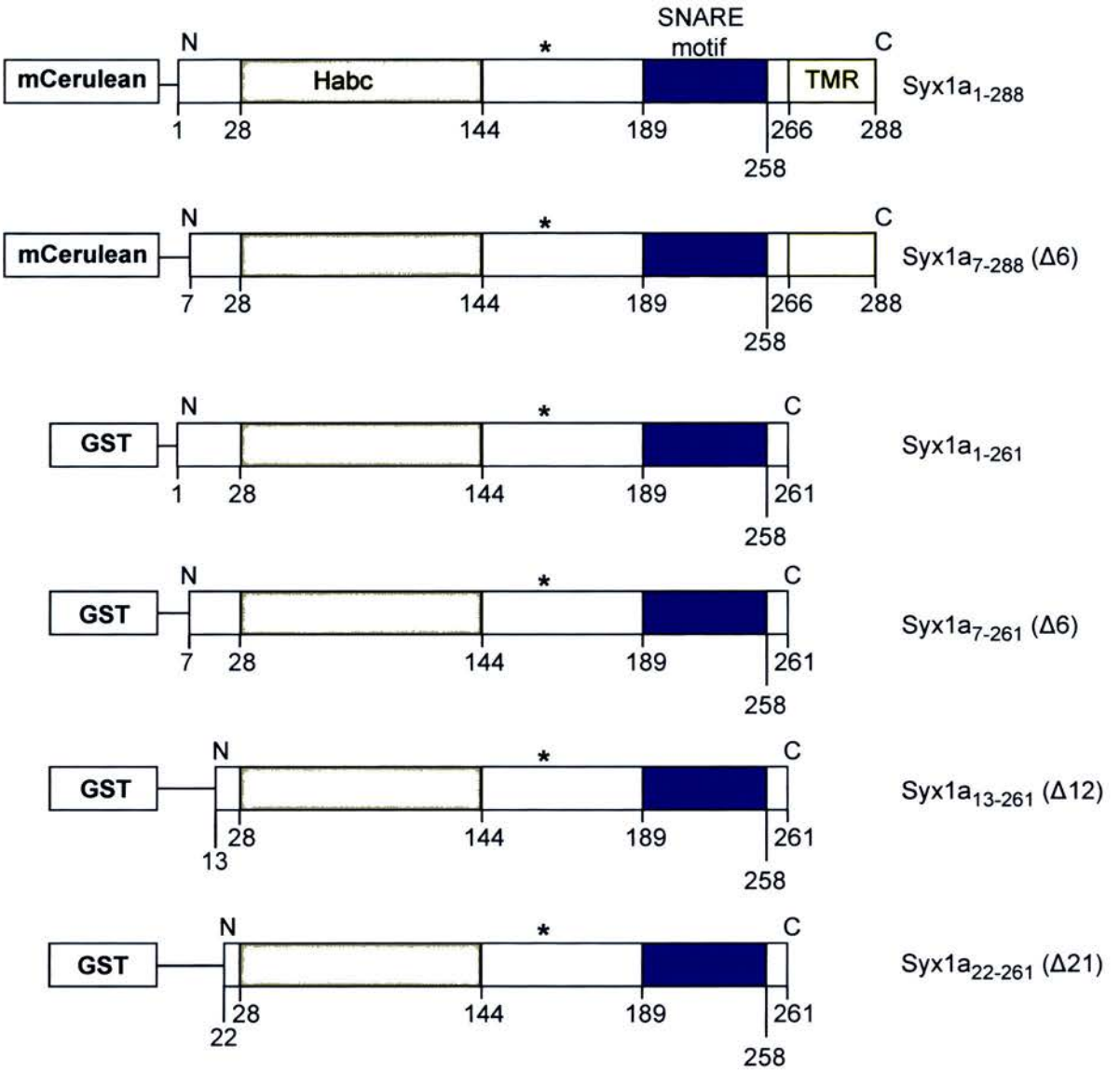

Figure 3.2 Domain structure of syntaxin 1a constructs used in this study.
Schematic diagrams of the syntaxin 1a constructs or fusions used in this study with the naming system used on the right hand side. Numbers below the diagrams correspond to amino acid residues in syntaxin 1a. The Habc domain is indicated in grey. The C-terminal SNARE motif involved in core complex formation is shown in blue. The TMR (yellow) designates the transmembrane region. The fluorescent protein mCerulean or purification tag are shown fused to the N-terminus. The "open" L165A/E166A [Open] mutation, which disrupts the closed conformation of syntaxin 1a is shown by an asterisk (*). Not to scale.

As binding reactions are largely dependent on the relative concentrations of the proteins involved, to further characterise the syntaxin 1a-munc18-1 interaction, the equilibrium dissociation constant (K_d) was measured (Figure 3.3B). To calculate the binding affinities of munc18-1 for syntaxin 1a and mutant forms, the concentration of syntaxin 1a was kept constant while the concentration of munc18-1 was varied. GST-Syx1a$_{1-261}$, GST- Syx1a$_{7-261}$ (Δ6), GST-Syx1a$_{1-261}$ [Open], and GST-Syx1a$_{7-261}$ [Open] (Δ6) were immobilised on glutathione sepharose beads and incubated in the presence of increasing concentrations of free munc18-1 for 2 hours at 21 °C. Following standard washes of the beads (see Chapter 2: Materials and Methods), bound material was analysed using SDS-PAGE, followed by western immunoblotting (see Chapter 2: Materials and Methods) using a monoclonal munc18-1 antibody (clone 31) and enhanced chemiluminescence. Luminescence data were detected using a cooled CCD camera, quantified and these data fit with a variable slope dose response relationship yielding a dissociation constant (K_d) for each set of data (Figure 3.3B). Syx1a$_{1-261}$ (K_d = 5 nM), Syx1a$_{7-261}$ (Δ6) (K_d = 6 nM), and Syx1a$_{1-261}$ [Open] (K_d = 5 nM) all showed similar binding affinities for munc18-1 (Figure 3.3B). In agreement with the saturation binding studies, it was only when the open mutation of syntaxin 1a was combined with an N-terminal truncation that a significant reduction in the binding affinity of munc18-1 for syntaxin 1a (K_d = 44 nM) was detected. These *in vitro* data confirm that syntaxin 1a can indeed interact with munc18-1 through its N-terminus, and therefore verifies that two modes of binding for munc18-1 and syntaxin 1a exist. However, it is still unclear how these two binding modes are employed in a cellular context.

3.5 MUNC18-1 CO-LOCALISATION WITH SYNTAXIN 1A IS DEPENDENT ON EITHER CLOSED FORM BINDING OR N-TERMINAL BINDING IN LIVING CELLS

To investigate the two distinct binding mechanisms between munc18-1 and syntaxin 1a in a cellular context, a quantitative approach was used to examine co-localisation between the two proteins in neuroendocrine cells. To address this issue, fluorescent fusions of wild-type syntaxin 1a or mutant forms which disrupt the two binding

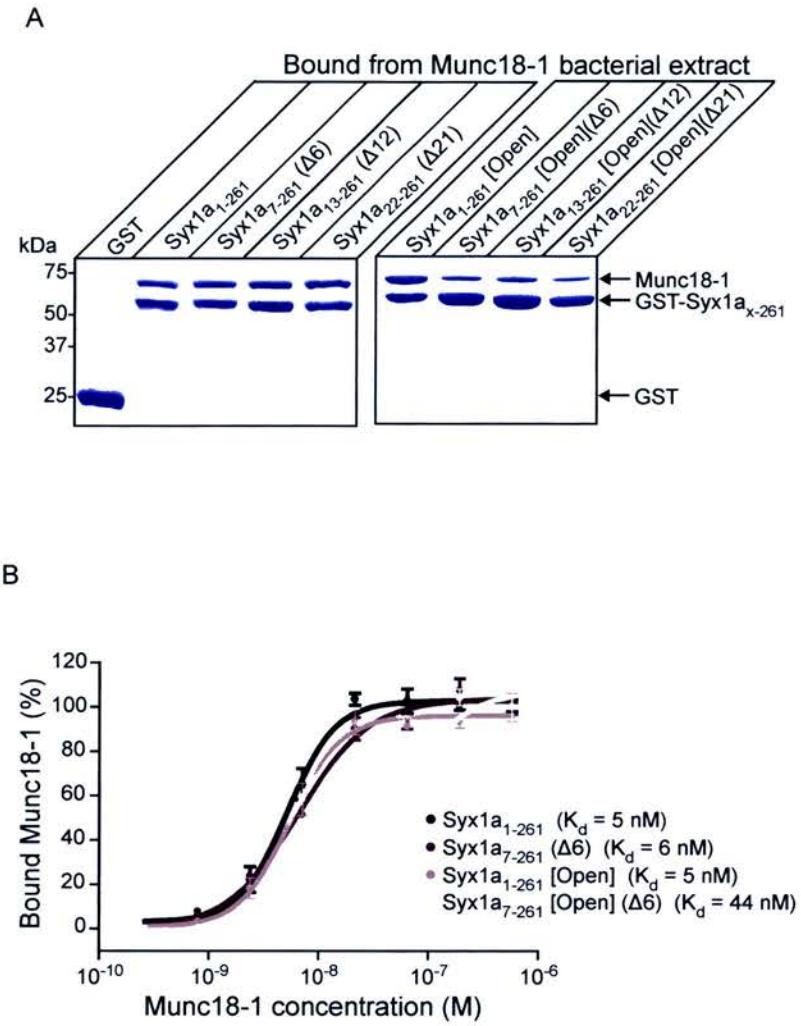

Figure 3.3 Syntaxin 1a interacts with munc18-1 through its N-terminus *in vitro*. **(A)** N-terminal truncations of GST-Syx1a and GST-Syx1a [Open] were immobilised on glutathione-sepharose beads and incubated with His_6-munc18-1 containing bacterial lysate. Following standard washes of the beads, bound material was analysed by SDS-PAGE and Coomassie Blue staining. Truncation of the N-terminus of $Syx1a_{1-261}$ [Open] reduces its ability to bind munc18-1. **(B)** To calculate the equilibrium dissociation constant for the syntaxin1a-munc18-1 complex, the concentration of syntaxin was kept constant while the free concentration of munc18-1 was varied. GST-$Syx1a_{1-261}$, GST-$Syx1a_{7-261}$ (Δ6), GST-$Syx1a_{1-261}$ [Open] or GST-$Syx1a_{7-261}$ [Open] (Δ6) were immobilised on glutathione-sepharose beads and incubated in the presence of varying concentrations of munc18-1. Following standard washes of the beads, bound material was analysed by Western immunoblotting using an anti-munc18-1 monoclonal antibody (clone 31) and enhanced chemiluminescence. Luminescence data were quantified, and the data fit with a variable slope dose response relationship yielding a dissociation constant (K_d), SEM shown, n = 3 experiments.

modes were co-expressed with a fluorescent fusion of munc18-1. Intact, live N2a cells were analysed to avoid fixation which could affect the cellular distribution of the SNARE proteins. N2a cells expressing mCerulean-fused Syx1a$_{1\text{-}288}$, Syx1a$_{7\text{-}288}$ (Δ6), Syx1a$_{1\text{-}288}$ [Open] or Syx1a$_{7\text{-}288}$ [Open] (Δ6) were co-expressed with EYFP fused munc18-1 and imaged by CLSM (Figure 3.4). As a negative control for random co-localisation, EYFP and unfused munc18-1 were co-expressed with mCerulean fused Syx1a$_{1\text{-}288}$.

A quantitative approach was used to investigate co-localisation between the two proteins (see Chapter 2: Materials and Methods). A merged image of both fluorescent channels was used to show areas of high coincidence in yellow hues. To look at the correlation of both channel intensities, the intensity of each voxel was plotted as a two-dimensional histogram showing a colour scale representing frequency. From the linear fit of the histogram, deviation from this fit (the residual for each voxel) was calculated to produce a "residual" map that corresponded to covariance between the two channels. By measuring the residual or deviation from this relationship it is possible to measure not only if the green and red fluorescence exists in the same region but also whether the intensities are covariant. This is evident in the residual map with regions that correlate well coloured in cyan, and any deviation from this fit appears towards either end of the spectrum. Figure 3.4 indicates that disruption of munc18-1 closed conformation binding (Syx1a$_{1\text{-}288}$ [Open]) or munc18-1 N-terminal binding (Syx1a$_{7\text{-}288}$ (Δ6)) to syntaxin 1a had no effect on the co-localisation or covariance of syntaxin 1a and munc18-1. Both syntaxin 1a and munc18-1 clearly trafficked to the plasma membrane, and showed high degrees of co-localisation at the cell surface and in intracellular membranes (Figure 3.4). It must be noted that munc18-1 is a cytoplasmic protein which relies on binding with syntaxin to traffic it to the cell surface, yet upon arrival at the plasma membrane munc18-1 itself is not membrane anchored. Importantly, when the syntaxin 1a N-terminal truncation and open mutation were combined (Syx1a$_{7\text{-}288}$ [Open] (Δ6)), thus disrupting both munc18-1 binding modes, syntaxin 1a no longer co-localised with munc18-1 (Figure 3.4). Munc18-1 remained cytosolic with a large change in co-localisation between the two proteins, indicating that munc18-1 relies

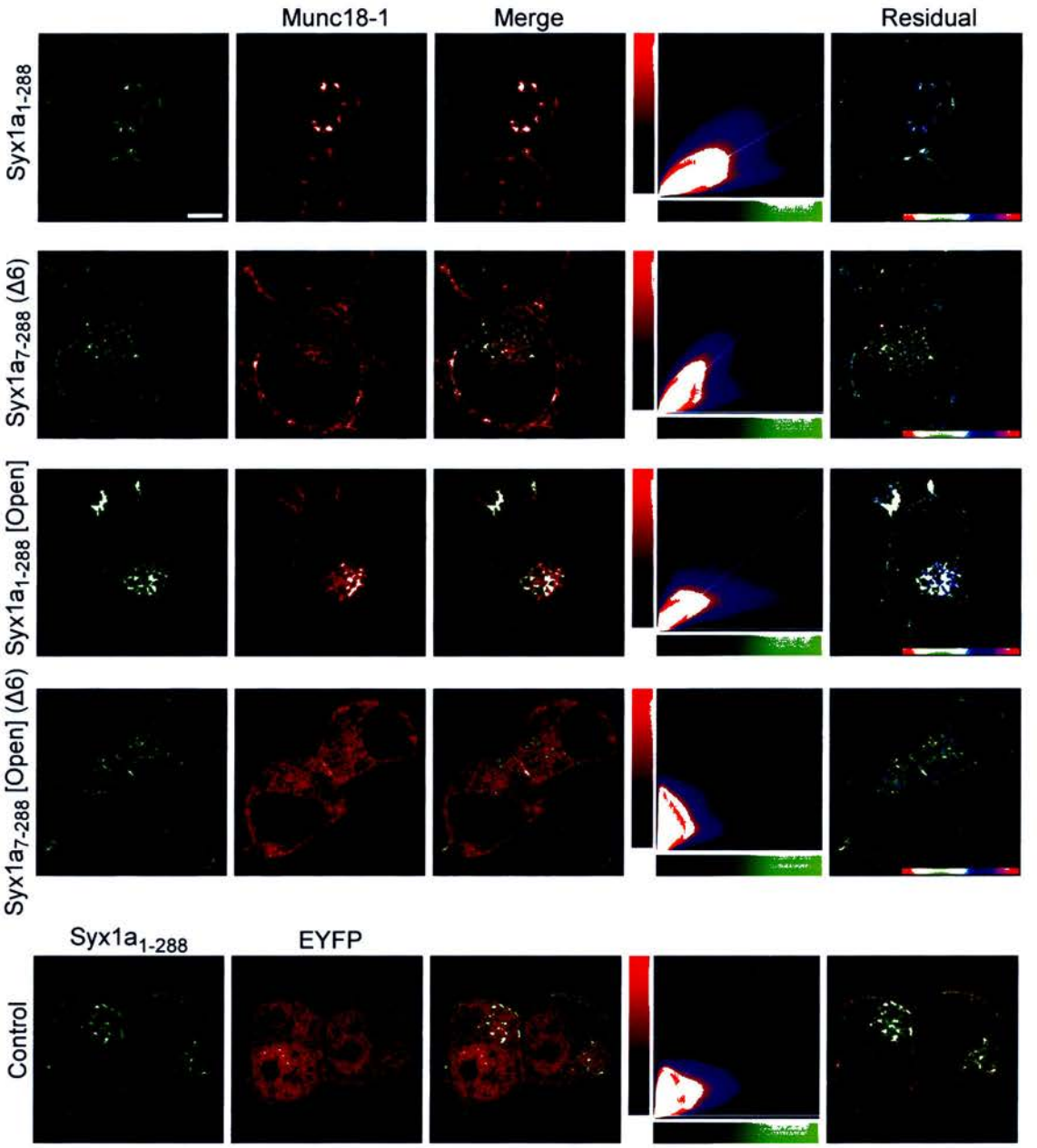

Figure 3.4 Munc18-1 co-localisation with syntaxin 1a in live cells is dependent on either closed form binding or N-terminal binding.

N2a cells expressing mCerulean tagged $Syx1a_{1-288}$, $Syx1a_{1-288}$ [Open], $Syx1a_{7-288}$ (Δ6), or $Syx1a_{7-288}$ [Open] (Δ6) were co-expressed with EYFP tagged munc18-1 and imaged by CLSM. The merged image shows areas of coincidence in yellow hues. The two-dimensional histogram represents the intensity of each channel in each voxel, with a colour scale representing frequency. The residual map corresponds to weighted residuals derived from the linear regression of the histogram, indicating fluorescent channel covariance. The hue is from -1 to 1, with cyan corresponding to a zero residual. EYFP and unfused munc18-1 were used as a control. Shown are representative equatorial sections; $n > 4$. Scale bar, 2 µm.

on its association with syntaxin 1a for membrane localisation. It has been suggested that the open mutation of syntaxin 1a can also spend time in the closed state (Fasshauer & Margittai, 2004). Therefore, it may be possible that munc18-1 can bind to this closed state to traffic syntaxin 1a to the plasma membrane, yet once at the cell surface the disruption of both binding modes causes munc18-1 to dissociate from syntaxin 1a and it remains cytosolic.

These data were quantified for wild-type or mutants of syntaxin 1a and munc18-1 in N2a cells and expressed as Pearson's correlation coefficient (R) values. Notably, there was no significant difference between the high correlation of $Syx1a_{1\text{-}288}$ (R= 0.84 ± 0.01, mean ± SEM, n = 9), $Syx1a_{7\text{-}288}$ (Δ6) (R= 0.78 ± 0.03, mean ± SEM, n = 5), $Syx1a_{1\text{-}288}$ [Open] (R= 0.79 ± 0.02, mean ± SEM, n = 4) and munc18-1. However, when the N-terminal and open mutation were combined ($Syx1a_{7\text{-}288}$ [Open] (Δ6)) there was a significant reduction in the correlation of syntaxin 1a with munc18-1 (R = 0.66 ± 0.04, mean ± SEM, n = 5, t-test, $p < 0.0007$) when compared to wild-type syntaxin 1a. As a negative control for random co-localisation, unfused munc18-1 and EYFP were co-expressed with mCerulean-syntaxin 1a (Figure 3.4). The combined N-terminal deletion and open mutation of syntaxin 1a ($Syx1a_{7\text{-}288}$ [Open] (Δ6)) resulted in a large decrease in correlation to a level not significantly different from the negative control (R = 0.55 ± 0.07, mean ± SEM, n = 5, t-test, p = 0.14). Taken together, these data from living N2a cells support the previous *in vitro* analysis that munc18-1 appears to interact with syntaxin 1a through two distinct modes of binding.

However, co-localisation data are limited by the resolution of the microscope, maximally 178 nm (Figure 2.4) laterally in our system and do not directly indicate an interaction between the two proteins. Therefore, it was essential that these co-localisation data were combined with studies of TCSPC-FLIM and FRET to quantify regions of interest in the cells where both proteins interact.

3.6 DIFFERENT BINDING MODES OF MUNC18-1/SYNTAXIN 1A INTERACTION OCCUR AT SPATIALLY DISTINCT CELLULAR LOCATIONS

It has been shown that munc18-1 has two very distinct modes of binding to syntaxin 1a, and to gain a greater understanding of the function of these binding modes in a cellular context, TCPSC-FLIM (see Chapter 2: Materials and Methods) was employed. In both these modes of binding, do munc18-1 and syntaxin 1a interact and if so, is this regulated spatially?

FLIM quantifies the fluorescence lifetime of a fluorophore, the duration of which is sensitive to the microenvironment which it inhabits (Duncan et al, 2004; Medine et al, 2007a). One of the factors that can influence the fluorescence lifetime of a fluorescent molecule (donor) is the presence of a second fluorophore (acceptor) with the appropriate spectral properties to allow the absorption of energy from the first molecule, or donor, through FRET. Thus, a quenching of the donor fluorescence lifetime is observed and can be used to measure a FRET interaction with the acceptor fluorophore. This affect can be quantified directly in every pixel of an image and allows the fraction of non-interacting and interacting donor fluorescence lifetimes in each pixel to be resolved (see Chapter 1: Introduction and Chapter 2: Materials and Methods). FLIM data analysis uses pixel-based fitting software that generates an array of pixels, and a histogram that shows the number of photons recorded at each pixel for each time interval spanning the lifetime of the fluorescence decay. Thus, FLIM analysis generates images based on separate fluorescence decay curves for each pixel within an image, allowing not only fluorescence lifetime values to be measured but also spatially resolved within a cell. Therefore, variations in the level of protein-protein interactions throughout a cell can be exposed.

To increase the understanding of wild-type syntaxin 1a binding to munc18-1, TCSPC-FLIM was employed to investigate if the two proteins were indeed interacting at the plasma membrane. Figure 3.5 shows a representative FLIM image and histogram for live N2a cells expressing mCerulean fused Syx1a$_{1\text{-}288}$ and unfused munc18-1. Therefore, these non-FRET data were recorded for a sample expressing

only the donor, mCerulean fused to Syx1a$_{1\text{-}288}$, in the absence of the EYFP energy acceptor. The mCerulean donor fluorescence followed a mono-exponential decay function, and the FLIM map showed a uniform, single exponential fluorescence lifetime within cells of 2369 ± 95 ps, mean ± SD; n = approximately 65000 data points from 1 representative cell from a set of at least 10 independent experiments (Figure 3.5A and B). If these data were plotted as a frequency distribution histogram, a long single fluorescence lifetime was evident (Figure 3.5C). In direct contrast, the fluorescence lifetime recorded for the same donor, mCerulean fused to Syx1a$_{1\text{-}288}$, in the presence of the acceptor EYFP fused to munc18-1, could no longer be fitted by a mono-exponential decay function (Figure 3.6). These FRET data were fit instead by a bi-exponential decay function (Figure 3.6A). FLIM data acquired from N2a cells co-expressing both mCerulean fused to Syx1a$_{1\text{-}288}$ and EYFP fused to munc18-1 were treated in the same way. The FLIM map reveals a shorter quenched donor fluorescence lifetime at the opposite end of the colour scale gradient (Figure 3.6B). The colours represent the weighted mean of the two fluorescence lifetimes for each pixel, one similar to the non-FRET lifetime previously detected (2328 ± 111 ps) and a shorter fluorescence lifetime (578 ± 89 ps, mean ± SD; n = approximately 65000 data points from 1 representative cell from at least 10 independent experiments). If the FRET data were plotted as a frequency distribution histogram, a broad distribution was seen indicating the presence of more than one fluorescence lifetime (Figure 3.6C, left panel). However, if these data were plotted as two separate lifetimes, a long lifetime similar to the non-FRET data was observed and a second quenched fluorescent lifetime was also reported (Figure 3.6C, right panel). This enabled the non-FRET and the FRET components, contained within each pixel of an image of a cell to be determined. The lifetime distributions represent the proportions of the FRET and non-FRET components of the donor, and the amplitude of each distribution represents the relative amount of each component. These parameters show the fraction of bound munc18-1 in complex with syntaxin 1a versus unbound munc18-1. Therefore, these data revealed that munc18-1 can remain bound to the closed conformation of syntaxin 1a at the plasma membrane.

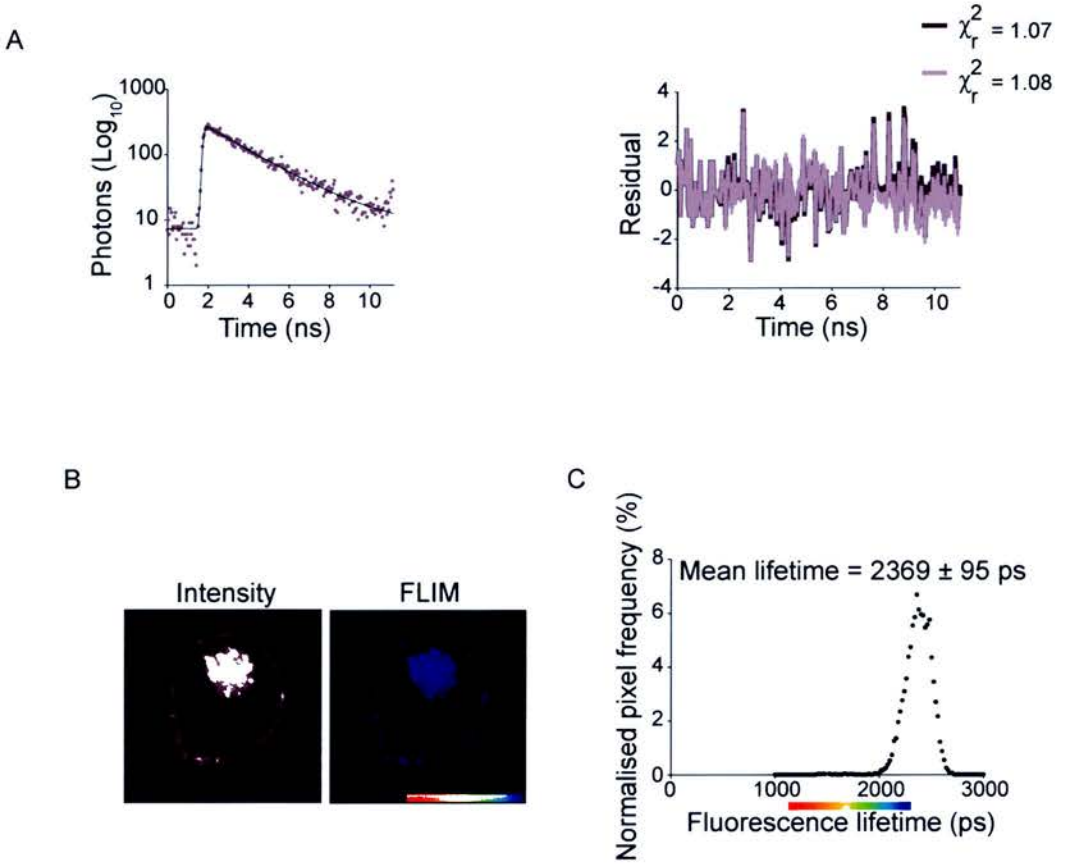

Figure 3.5 Representative fluorescence lifetime images and distribution histograms for the donor mCerulean-fused syntaxin 1a alone.

Offline FLIM data analysis uses pixel based fitting software that provides separate fluorescence decay curves for each pixel in an image enabling FLIM values to be measured but also spatially resolved within a cell. A pixel by pixel map of variations of FLIM with the cell is generated. To extract the fluorescence lifetime of each pixel, the decay trace in the pixel is fit with either a single exponential or a sum of exponential terms and amplitudes. **(A)** Representative single-pixel fluorescence lifetime decay recorded from an mCerulean-Syx1a$_{1\text{-}288}$ expressing N2a cell. These non-FRET data were recorded for a sample not expressing the acceptor EYFP and follow a mono-exponential decay (left panel). Reduced chi-squared residual analysis revealed that there was no advantage to introducing a second exponential into the fitting algorithm (mono-exponential (—), bi-exponential (—)) (right panel). **(B)** The FLIM map shows a single fluorescence lifetime of 2369 ± 95 ps, mean ± SD, n = approximately 65000 data points from 1 representative cell from at least 10 independent experiments . The colour scale represents the weighted mean fluorescence lifetimes for each pixel (from 1250 (red) to 2250 ps (blue)) in a continuous colour gradient. **(C)** These representative data are plotted as a frequency distribution histogram showing a long single fluorescence lifetime of 2369 ± 95 ps.

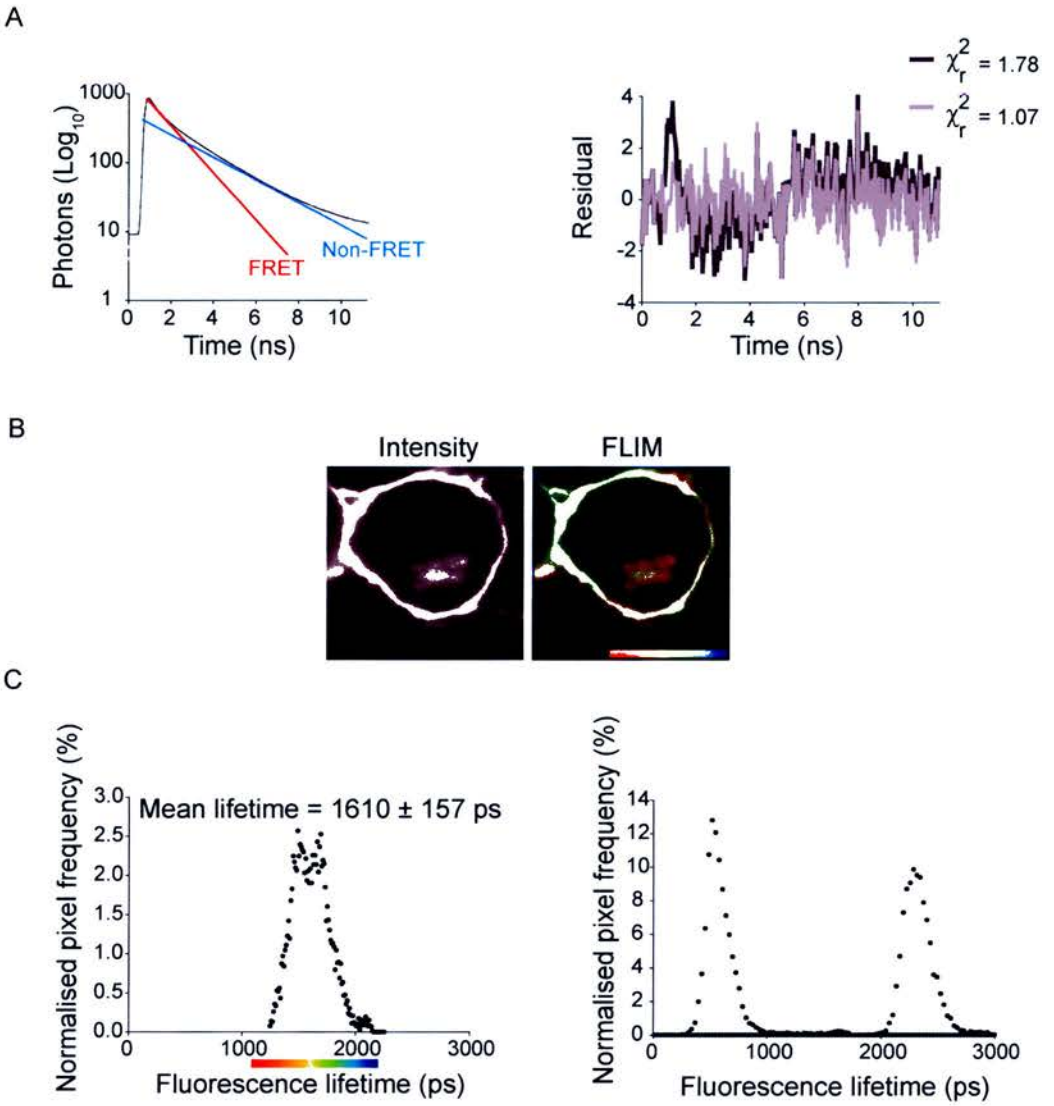

Figure 3.6 Representative fluorescence lifetime images and distribution histograms for the donor mCerulean-fused syntaxin 1a in the presence of the acceptor EYFP-fused munc18-1.

(A) Representative single-pixel fluorescence lifetime decay recorded for the donor, mCerulean fused to $Syx1a_{1-288}$, in the presence of the acceptor EYFP fused to munc18-1. The donor fluorescence lifetime no longer fits to a mono-exponential decay function as seen for the non-FRET control in Figure 3.5 (left panel). Reduced chi-squared residual analysis revealed that this data fit better to a bi-exponential decay function (mono-exponential (—), bi-exponential (—)) (right panel). **(B)** The FLIM map reveals a quenched fluorescence lifetime (right panel). The colour scale represents the weighted mean fluorescence lifetimes for each pixel (from 1250 (red) to 2250 ps (blue)) in a continuous colour gradient. The colours represent the weighted mean of the two fluorescence lifetimes for each pixel, one similar to the non-FRET lifetime (2328 ± 111 ps) and a shorter one (578 ± 89 ps, mean ± SD, n = approximately 65000 data points from 1 representative cell from at least 10 independent experiments). **(C)** These data are plotted as the weighted mean (left panel) and show a broad distribution indicating the presence of more than one lifetime. If these data are plotted as two separate lifetimes, a long lifetime similar to the donor-alone lifetime is reported and a second, quenched lifetime is present (right panel). This represents the non-FRET and the FRET component contained in each pixel.

To understand the function of the two modes of munc18-1 binding to syntaxin 1a in a cellular context TCSPC-FLIM was again employed (Figure 3.7). Live N2a cells expressing EYFP fused munc18-1 and wild-type syntaxin 1a ($Syx1a_{1-288}$) or mutant forms previously used that disrupt the closed or N-terminal modes of munc18-1 binding to syntaxin 1a were utilised. The approaches described above were applied to wild-type syntaxin 1a and each mutant, and in addition the ratio of FRET:non-FRET amplitudes in each pixel were calculated. The mean fluorescence lifetime is a convolution of the two lifetimes (FRET and non-FRET) and their associated amplitude components. To simplify presentation, the values of the two lifetimes were ignored and the amplitudes of the FRET and non-FRET components shown as a ratio (Figure 3.7). The amplitude ratio colour scale displays values of zero or no FRET component as grayscale, 0.1 to 0.66 as red, 0.66 to 1.33 as green and areas with high ratio values of 1.33 to 2.5 as blue. Figure 3.7 demonstrates that fewer $Syx1a_{1-288}$ and munc18-1 molecules interact on the plasma membrane compared with intracellular locations (Mann Whitney, $p < 0.007$, $n = 18$). This confirmed that syntaxin 1a closed form binding with munc18-1 occurred predominantly inside the cell. In direct comparison $Syx1a_{1-288}$ [Open] and munc18-1 showed reduced FRET (donor fluorescence lifetime and amplitude ratios) inside cells when compared with wild-type syntaxin 1a and munc18-1 ($p < 0.001$, $n = 8$), yet cell surface interactions were maintained. $Syx1a_{7-288}$ ($\Delta 6$) that is capable of adopting the closed conformation showed no decrease in intracellular interaction with munc18-1 but a large reduction in FRET at the plasma membrane ($p < 0.001$, $n = 8$). Furthermore, $Syx1a_{7-288}$ [Open] ($\Delta 6$) that disrupts both modes of munc18-1 binding showed decreased FRET both intracellularly and at the plasma membrane, in agreement with the co-variance data shown in Figure 3.4. Syntaxin 1a N-terminal deletion affects plasma membrane interactions between the proteins and disruption of closed form binding affects predominantly intracellular interactions. Therefore, these findings provide evidence that the two binding modes of munc18-1 and syntaxin 1a are spatially distinct within a living cell.

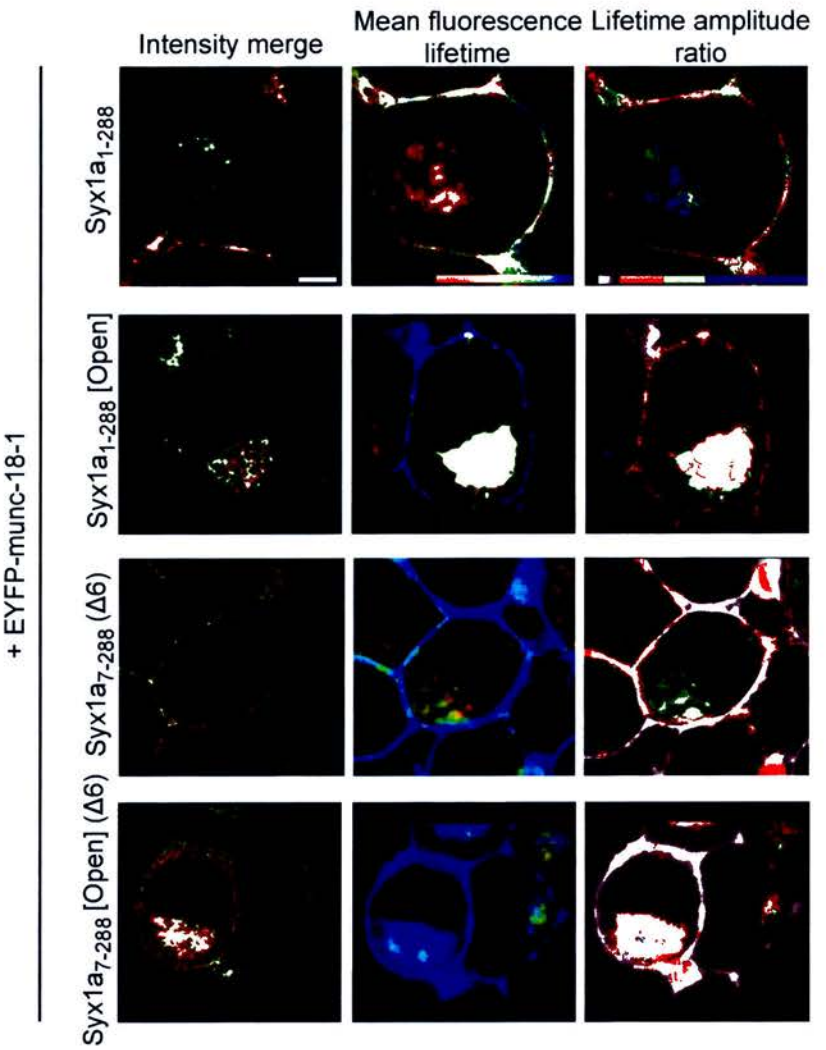

Figure 3.7 Different binding modes of munc18-1 and syntaxin 1a are spatially distinct.

The approaches described in Figure 3.5 were applied to each syntaxin 1a mutant, in addition calculating the lifetime amplitude ratio of FRET:non-FRET amplitudes in each pixel of the images. N2a cells expressing $Syx1a_{1-288}$, $Syx1a_{1-288}$ [Open], $Syx1a_{7-288}$ (Δ6) or $Syx1a_{7-288}$ [Open] (Δ6) co-expressed with EYFP-munc18-1 were analysed. Mean fluorescence lifetime values are shown on a colour scale from 1250 ps (red) to 2250 ps (blue). Lifetime amplitude ratio maps show pixels containing only non-FRET values in grayscale. The amplitude ratio scale: zero to 0.1 (no FRET component, grayscale), 0.1 to 0.66 (red), 0.66 to 1.33 (green), 1.33 to 2.5 (blue). The two binding modes of munc18-1 and syntaxin 1a are spatially distinct with syntaxin 1a N-terminal deletion affecting plasma membrane interactions and abolition of syntaxin 1a closed conformation binding affecting intracellular complexes. Scale bar, 2 μm.

3.7 MUNC18-1 MAY REMAIN ASSOCIATED WITH SYNTAXIN 1A THROUGHOUT THE SNARE ASSEMBLY PATHWAY

It has now been shown both *in vitro* and in living cells that N-terminal binding to munc18-1 is utilised when syntaxin 1a is in the open conformation and unable to bind via the closed conformation. The previous data led to the hypothesis that open syntaxin 1a can remain bound to munc18-1 and permit syntaxin 1a to bind to its cognate SNAREs simultaneously.

The next step was to probe the effect of N-terminal truncation and the open mutation on progression of syntaxin 1a through the SNARE assembly pathway. Purified complexes of munc18-1 with wild-type Syx1a$_{1\text{-}261}$, the open mutant (Syx1a$_{1\text{-}261}$ [Open]) or an N-terminal truncation of syntaxin 1a (Syx1a$_{7\text{-}261}$ (Δ6)) were incubated with SNAP-25 in the presence or absence of synaptobrevin. Purified bacterial detergent extracts containing GST-Syx1a$_{1\text{-}261}$, GST-Syx1a$_{7\text{-}261}$ (Δ6) or GST-Syx1a$_{1\text{-}261}$ [Open] and His$_6$–munc18-1 (see Chapter 2: Materials and Methods) were mixed. The resulting complex was purified sequentially on glutathione sepharose resin (eluted through thrombin cleavage to remove the GST tag) and Profinity IMAC resin. The purity of the resulting complex was assessed using Sypro Red in-gel staining (see Chapter 2: Materials and Methods) to confirm an equimolar stoichiometric ratio. The purified syntaxin 1a-munc18-1 complex was incubated with GST-SNAP-25A$_{1\text{-}206}$ immobilised on glutathione sepharose beads, in the presence or absence of synaptobrevin for 30 minutes at 4 °C. Following standard washing procedures (see Chapter 2: Materials and Methods), the bound material was analysed by SDS-PAGE and subsequent Coomassie blue staining (see Chapter 2: Materials and Methods) (Figure 3.8A-C). Incubation of wild-type Syx1a$_{1\text{-}261}$ and munc18-1, that is capable of adopting the closed formation, showed that in this form syntaxin 1a was incapable of binding to SNAP-25 or synaptobrevin, thus it could not engage in the binary or ternary SNARE complex (Figure 3.8A). The N-terminal truncation of syntaxin 1a (Syx1a$_{7\text{-}261}$ (Δ6)) and munc18-1 was also unable to enter into the binary or ternary complex and showed no binding of either SNAP-25 or synaptobrevin (Figure 3.8B). In direct comparison, the open mutation of syntaxin 1a (Syx1a$_{1\text{-}261}$ [Open]) when bound to munc18-1, demonstrated binding to SNAP-25 and

synaptobrevin forming both the binary and ternary SNARE complex (Figure 3.8C). These findings indicated that munc18-1 remains bound to the N-terminus of syntaxin 1a through the SNARE complex assembly pathway (Figure 3.8D). Therefore, the open conformation of syntaxin 1a bound to munc18-1 via N-terminal binding permits the assembly of both the binary and ternary SNARE complexes, and this syntaxin conformation may be essential at the plasma membrane for this reason.

3.8 MUNC18-1 FACILITATES SYNTAXIN 1A TRAFFICKING TO THE PLASMA MEMBRANE IN LIVING CELLS

A number of studies have shown that the binding of syntaxin to munc18-1 is critical for the efficient trafficking of syntaxin to the plasma membrane in non-specialised cells (Arunachalam et al, 2008; Martinez-Arca et al, 2003; Rowe et al, 2001). However, other studies have demonstrated that syntaxin can traffic to the plasma membrane (albeit inefficiently) in the absence of munc18-1 in a variety of different cell types (Schutz et al, 2005; Toonen et al, 2005). Similar studies using a munc18-1 null mouse have also demonstrated that syntaxin can traffic to the cell surface, but in this system syntaxin levels are reduced by 70% and other munc18 isoforms still exist (Toonen et al, 2005). In PC12 cells, it has been shown that syntaxin exists in excess over munc18-1 (Schutz et al, 2005) and this has been used to argue against a role for munc18-1 in syntaxin trafficking.

However, it still remained to be identified convincingly, whether a SNARE trafficking function for munc18-1 existed in specialised secretory cells such as neuroendocrine cell lines. To address this issue, initial experiments involved the expression of mCerulean-fused syntaxin 1a in live HEK293 or N2a cells, both in isolation or in conjunction with EYFP-fused munc18-1 and imaged by CLSM (Figure 3.9). For both cell types, the expression levels were similar and only cells with the lowest detectable expression levels were selected. HEK293 cells were also employed as they do not contain endogenous munc18-1 (Rowe et al, 2001). In both live HEK293 and N2a cells, full length syntaxin 1a ($Syx1a_{1\text{-}288}$) was not observed

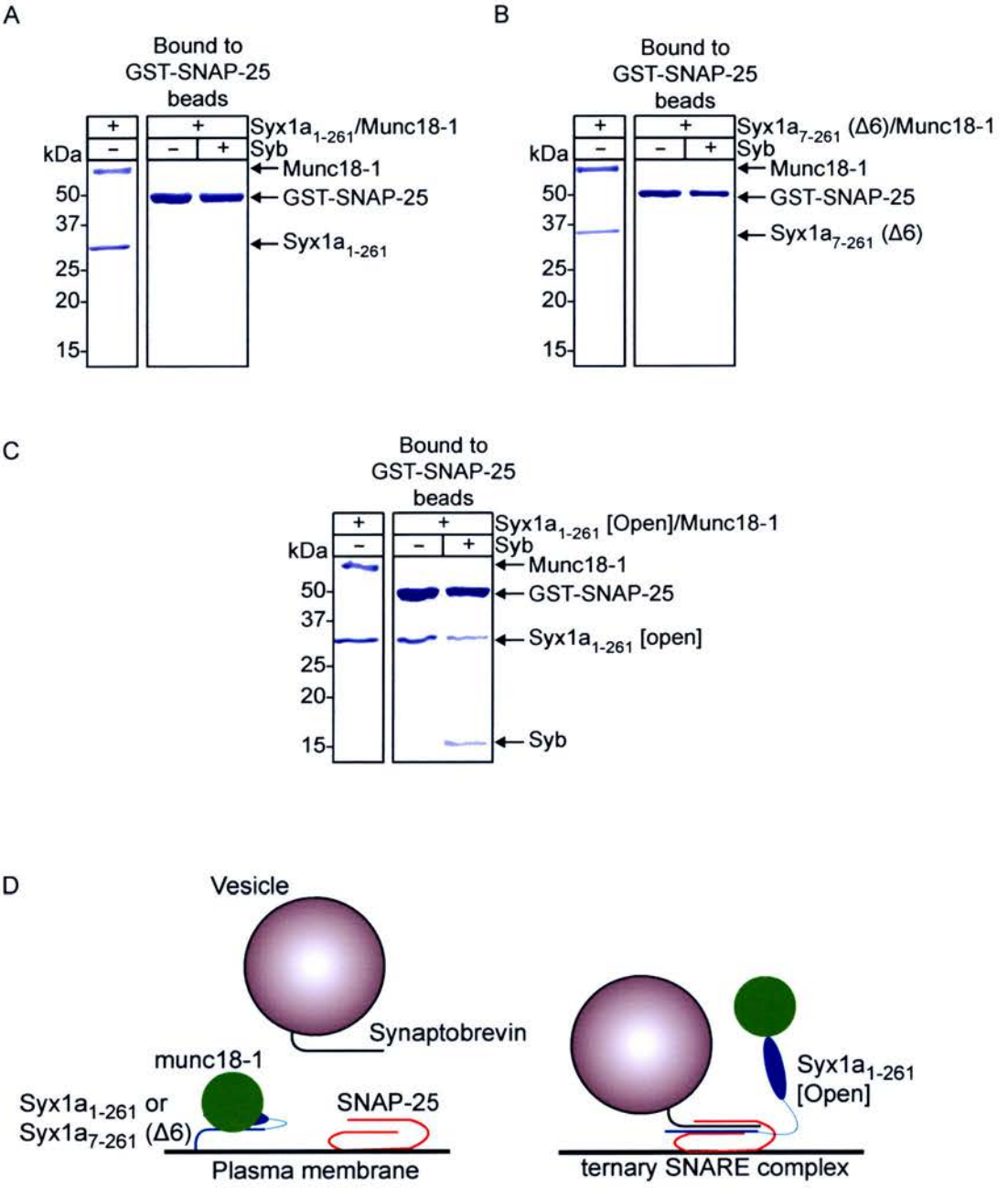

Figure 3.8 Munc18-1 can remain associated with syntaxin 1a through the SNARE assembly pathway.

Munc18-1 in complex with $Syx1a_{1-261}$ **(A)**, $Syx1a_{7-261}$ (Δ6) **(B)** or $Syx1a_{1-261}$ [Open] **(C)** was incubated with immobilised GST-SNAP-25 attached to glutathione sepharose beads, in the presence or absence of synaptobrevin (Syb). Following standard washes of the beads, bound material was analysed by SDS-PAGE and Coomassie Blue staining. $Syx1a_{1-261}$ and $Syx1a_{7-261}$ (Δ6) munc18-1 complexes were unable to interact with GST-SNAP-25. The $Syx1a_{1-261}$ [Open]/munc18-1 complex can bind to GST-SNAP-25 and thus form the ternary SNARE complex. **(D)** Schematic representation of the role of syntaxin 1a conformations in the SNARE complex assembly pathway.

to traffic to the plasma membrane in the absence of co-expressed munc18-1 and remained trapped in intracellular membranes (Figure 3.9). However, upon co-expression with munc18-1, Syx1a$_{1\text{-}288}$ revealed a dramatic change in localisation in both cell types and was visible as a distinct ring of fluorescence at the plasma membrane. The notable fluorescence of syntaxin 1a at the plasma membrane region demonstrated that munc18-1 facilitated the targeting of high levels of syntaxin 1a to the plasma membrane. Figure 3.9 thus demonstrates that in N2a and HEK293 cells munc18-1 plays a critical role in trafficking syntaxin 1a to the plasma membrane.

One argument against the role of munc18-1 as a chaperone for syntaxin 1a would be the ability of a mutant of syntaxin 1a, spending more time in the 'open' conformation (L165A, E166A; Syx1a$_{1\text{-}288}$ [Open]) (Dulubova et al, 1999), to traffic to the plasma membrane. Although munc18-1 has been shown to interact with this open mutant through an alternative N-terminal binding site, the ability of the open mutant to form SNARE complexes while bound to munc18-1 would argue against a 'protective' role for munc18-1. To assess this, I performed similar experiments in HEK293 and N2a cells in which I expressed Syx1a$_{1\text{-}288}$ [Open] either alone or in the presence of EYFP-fused munc18-1 and imaged using CLSM (Figure 3.9). Similar to wild-type syntaxin 1a, in the absence of munc18-1, Syx1a$_{1\text{-}288}$ [Open] failed to traffic to the plasma membrane in HEK293 and N2a cells and became trapped in intracellular membranes (Figure 3.9). However, when co-expressed with munc18-1, Syx1a$_{1\text{-}288}$ [Open] trafficked efficiently to the cell surface demonstrating plasma membrane localisation in both HEK293 and N2a cells (Figure 3.9). Both Syx1a$_{1\text{-}288}$ and Syx1a$_{1\text{-}288}$ [Open] interact with munc18-1 in intracellular membranes and on the cell surface. While these findings may argue against munc18-1 acting as a chaperone for syntaxin 1a, it must be noted that Syx1a$_{1\text{-}288}$ [Open] is not constitutively open as first thought and it does spend time in the closed state (Fasshauer & Margittai, 2004). It has also been shown here that this mutant has an affinity for munc18-1 identical to that of wild-type Syx1a$_{1\text{-}288}$ (K_d = 5 nM) (Figure 3.3), and abolition of the N-terminal motif still allows this 'open' syntaxin to bind to munc18-1 with high affinity (K_d = 44 nM) indicating that it can adopt the closed conformation.

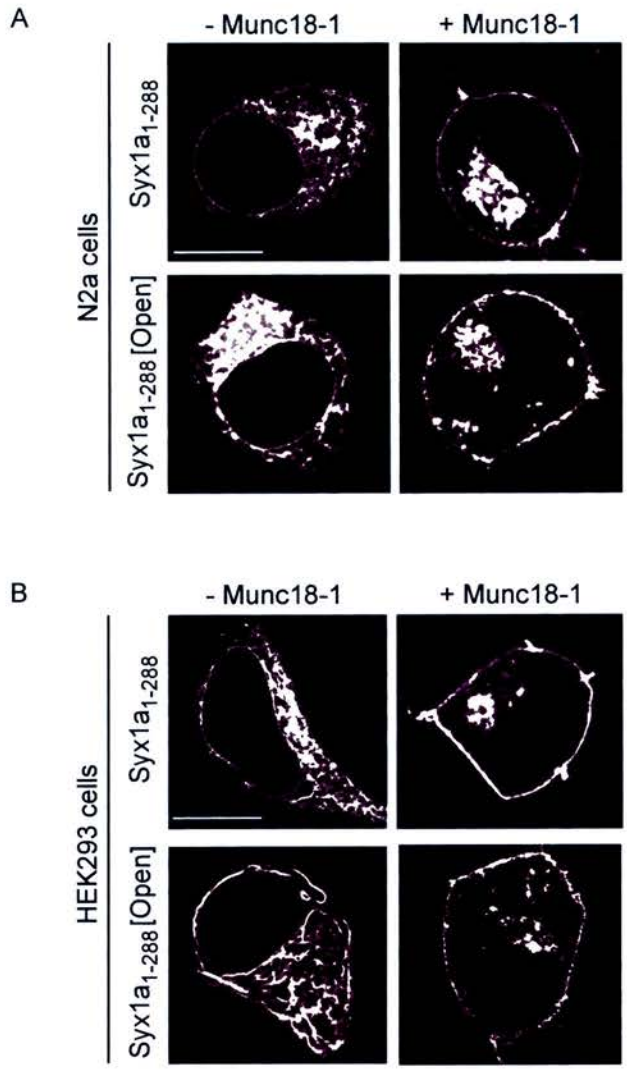

Figure 3.9 Munc18-1 facilitates syntaxin 1a trafficking to the plasma membrane in living cells.
(A) Live N2a cells expressing $Syx1a_{1-288}$ or $Syx1a_{1-288}$ [Open] in the presence or absence of EYFP-munc18-1 and imaged by CLSM. **(B)** Live HEK293 cells expressing $Syx1a_{1-288}$ or $Syx1a_{1-288}$ [Open] in the presence or absence of EYFP-munc18-1 and imaged by CLSM. Scale bars, 5 µm.

To eliminate the possibility that the requirement for munc18-1 in trafficking syntaxin 1a to the plasma membrane was not specific to N2a and HEK293 cells, these experiments were repeated in PC12 cells. Some studies have reported that syntaxin can traffic to the plasma membrane in the absence of munc18-1 in several different cell types (Schutz et al, 2005; Toonen et al, 2005). In live PC12 cells, mCerulean fused $Syx1a_{1-288}$ or $Syx1a_{1-288}$ [Open] were expressed alone or in the presence of EYFP fused munc18-1 and imaged by CLSM. These experiments used cells expressing heterologous proteins at the same levels as those used for FLIM and co-localisation studies. Fields of PC12 cells were then scored for syntaxin 1a trafficking to the plasma membrane and the mean percentage of cells with surface syntaxin 1a was plotted. Figure 3.10 shows that syntaxin 1a was seen to traffic to the plasma membrane, but in a minority of cells (19 ± 2%, mean ± SEM, n = 153 cells from at least 4 experiments), yet when co-expressed with munc18-1 this increased significantly to 93 ± 5% (mean ± SEM, n = 122, t-test $p < 0.001$) of cells with both proteins on the cell surface. This was also evident for the open mutation of syntaxin 1a, in which syntaxin 1a alone was only seen to traffic in 11 ± 4% (mean ± SEM, n = 135) of cells, yet in the presence of munc18-1 this increased significantly to 37 ± 6% (mean ± SEM, n = 100, t-test $p < 0.001$) of cells with syntaxin 1a on the cell surface. In the presence of munc18-1, the mean percentage of $Syx1a_{1-288}$ [Open] on the plasma membrane was significantly lower than that observed for wild-type $Syx1a_{1-288}$ (t-test, $p < 0.001$). These findings therefore confirm that munc18-1 does play a pivotal role in the membrane localisation of syntaxin 1a in living cells.

3.9 Syntaxin 1a overlaps with FM4-64 plasma membrane marker in the presence of munc18-1

To evaluate the extent of wild-type syntaxin 1a or mutant forms to traffic to the cell surface in the presence or absence of munc18-1, a quantitative approach was used to report overlap with the FM4-64 plasma membrane marker.

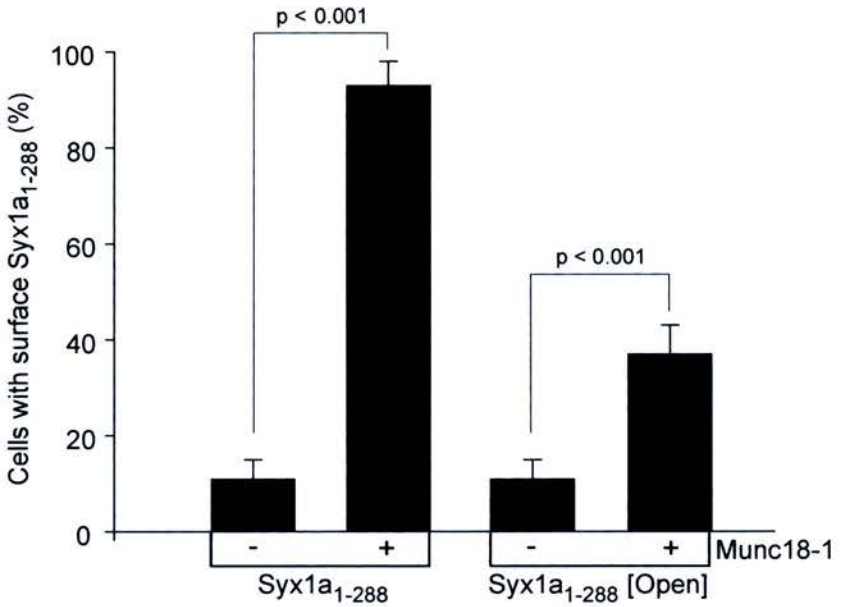

Figure 3.10 Munc18-1 facilitates syntaxin 1a trafficking to the cell surface in PC12 cells.

Live PC12 cells expressing $Syx1a_{1-288}$ or $Syx1a_{1-288}$ [Open] in the presence or absence of EYFP-munc18-1 were imaged by CLSM. Fields of PC12 cells were scored for syntaxin 1a trafficking to the cell surface and the percentage of cells with surface syntaxin 1a was plotted. SEM for n>100, *t* test, $p < 0.001$. Munc18-1 facilitated $Syx1a_{1-288}$ and $Syx1a_{1-288}$ [Open] trafficking to the plasma membrane

For all experiments, HEK293 cells were plated on to glass coverslips and transfected with mCerulean fused Syx1a$_{1\text{-}288}$, Syx1a$_{1\text{-}288}$ [Open], Syx1a$_{7\text{-}288}$ (Δ6) or Syx1a$_{7\text{-}288}$ [Open] (Δ6) in the presence or absence of EYFP fused munc18-1. HEK293 cells were employed as they do not contain endogenous munc18-1 (Rowe et al, 2001). Live HEK293 cells were stained with FM4-64 (final concentration 5 μg/ml) and imaged immediately by CLSM to avoid FM4-64 internalisation (Figures 3.11 and 3.12). FM4-64 was employed as it is a red-emitting lipid marker that is spectrally distinct from mCerulean and EYFP. A quantitative approach was used to investigate overlap between the syntaxin 1a and FM4-64 channels. Pearson's correlation coefficient analysis is inappropriate in this case as the relative intensities would not be expected to be dependent upon each other.

The distribution of syntaxin 1a is shown in red, and the plasma membrane labelled by the styryl dye FM4-64 shown in green (Figures 3.11 and 3.12). A merged image highlights areas of overlap between these two channels in yellow hues (Figures 3.11 and 3.12). In the absence of munc18-1 there was little overlap between wild type Syx1a$_{1\text{-}288}$, Syx1a$_{1\text{-}288}$ [Open], Syx1a$_{7\text{-}288}$ (Δ6) and Syx1a$_{7\text{-}288}$ [Open] (Δ6) with FM4-64. FM4-64 staining was clearly visible on the surface of the membrane of living HEK293 cells and in the absence of munc18-1 wild-type syntaxin 1a and the mutant forms failed to traffic to the plasma membrane and staining was visible in intracellular membranes (Figure 3.11). However, upon co-expression of munc18-1, an increase in the overlap between FM4-64 and wild-type Syx1a$_{1\text{-}288}$, Syx1a$_{1\text{-}288}$ [Open] and Syx1a$_{7\text{-}288}$ (Δ6) was evident (Figure 3.12). Wild-type Syx1a$_{1\text{-}288}$, Syx1a$_{1\text{-}288}$ [Open] and Syx1a$_{7\text{-}288}$ (Δ6) are clearly seen to traffic sufficiently to the cell surface where they show overlap with the membrane marker FM4-64, shown as areas of coincidence in yellow hues in the merged image. Syx1a$_{7\text{-}288}$ [Open] (Δ6) was unable to traffic to the plasma membrane even in the presence of heterologous munc18-1. This may be due to the absence of endogenous munc18-1 in HEK293 cells.

To quantify the overlap between wild-type syntaxin 1a and mutants with FM4-64, a section of the plasma membrane was analysed from 3 experiments for each data set

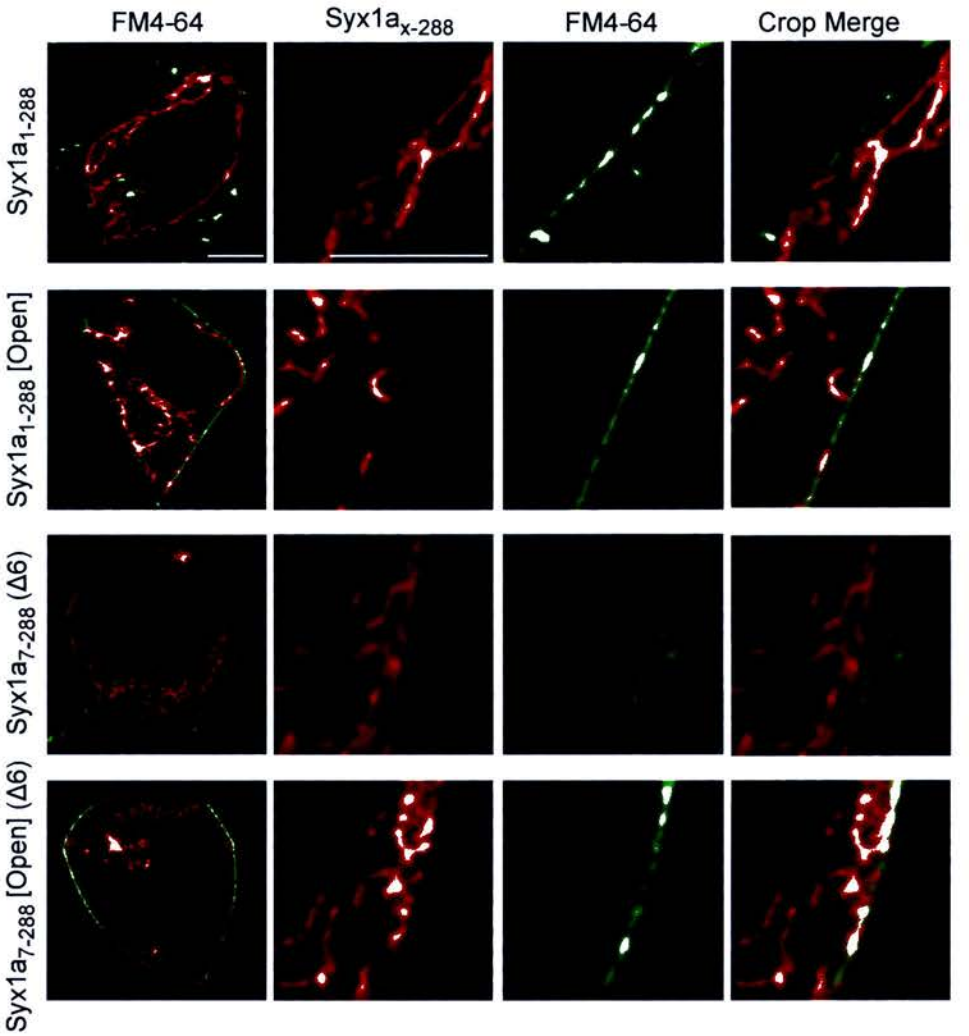

Figure 3.11 Syntaxin 1a becomes trapped in intracellular membranes in the absence of munc18-1.

Syntaxin 1a becomes trapped intracellularly in the absence of munc18-1. Live HEK293 cells expressing mCerulean fused to Syx1a$_{1-288}$, Syx1a$_{1-288}$ [Open], Syx1a$_{7-288}$ (Δ6) or Syx1a$_{7-288}$ [Open] (Δ6) are shown. Immediately before imaging by CLSM, the styryl dye FM4-64 was added to the media on the microscope stage to a final concentration of 5 µg/ml . Wildtype Syx1a$_{1-288}$ and mutants, in the absence of munc18-1 are shown in red and FM4-64 dye is shown in green. The cropped merged image of both channels shows areas of coincidence in yellow hues. Representative equatorial sections are shown (n = 3). Scale bars, 5 µm.

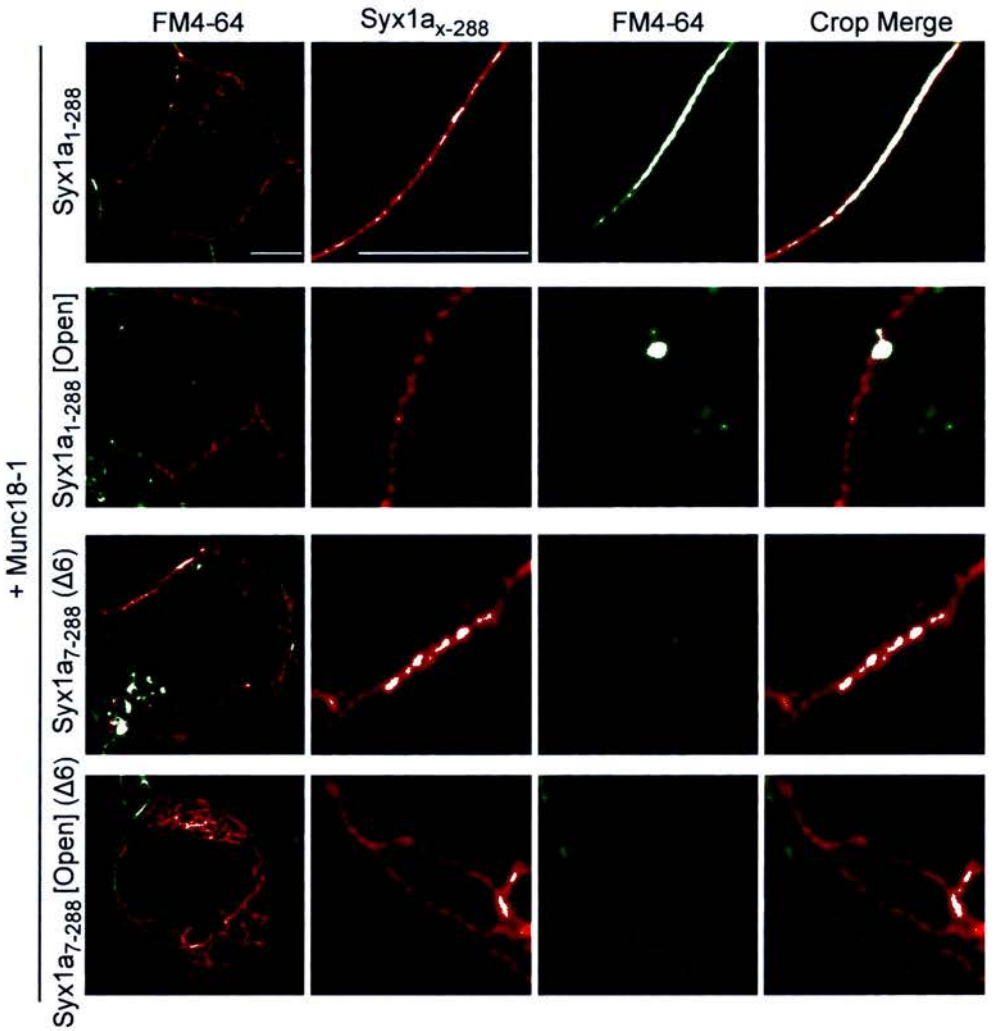

Figure 3.12 Syntaxin 1a traffics to the plasma membrane in the presence of munc18-1.

In HEK293 cells, syntaxin 1a can traffic to the plasma membrane in the closed form and via N-terminal binding to munc18-1. In HEK293 cells if both binding modes are abolished syntaxin1a remains trapped intracellularly. Live HEK293 cells expressing mCerulean fused to Syx1a$_{1-288}$, Syx1a$_{1-288}$ [Open], Syx1a$_{7-288}$ (Δ6) or Syx1a$_{7-288}$ [Open] (Δ6) co-expressed with munc18-1 are shown. Before imaging by CLSM, FM4-64 was added to the media on the microscope stage to a final concentration of 5 µg/ml. Wildtype Syx1a$_{1-288}$ and mutants in the presence of munc18-1 are shown in red and FM4-64 dye is shown in green. The cropped merged image of both channels shows areas of coincidence in yellow hues. Representative equatorial sections are shown (n = 3). Scale bar, 5 µm.

and the percentage of overlap with FM4-64 calculated. Measurements are shown in Figure 3.13 and are expressed as the mean percentage of syntaxin 1a overlapping with FM4-64 in the presence or absence of munc18-1. In the presence of munc18-1, wild-type syntaxin 1a showed high levels of overlap with FM4-64 (61 ± 1%, mean ± SEM, n = 3), and this value was significantly higher than in the absence of munc18-1 (34 ± 5%, mean ± SEM, n = 3, t-test, p <0.006). In the case of $Syx1a_{1-288}$ [Open], overlap between syntaxin 1a and FM4-64 increased significantly (46 ± 3%, mean ± SEM; n = 3, t-test p <0.026) as a result of trafficking of syntaxin 1a, whereas previously in the absence of munc18-1 there was less overlap (32 ± 2%, mean ± SEM, n = 3). In addition, a significant increase in overlap was observed for $Syx1a_{7-288}$ (Δ6) and FM4-64 (29 ± 0.4% to 61 ± 3%, mean ± SEM; n = 3, t-test p <0.001) to reflect trafficking of syntaxin 1a to the plasma membrane when munc18-1 was present. However, $Syx1a_{7-288}$ [Open] (Δ6) failed to show any significant increase in overlap with FM4-64 (33 ± 2% to 30 ± 4%, mean ± SEM; n = 3) in the presence of munc18-1 (Figure 3.13). These findings support the previous data that the syntaxin 1a-munc18-1 complex in the closed form and via N-terminal binding can traffic to the plasma membrane. Disruption of both modes of binding inhibits syntaxin 1a trafficking and it remains trapped intracellularly allowing less efficient membrane localisation.

3.10 Conclusion

Using biochemistry and confocal imaging techniques, it has been shown that munc18-1 can interact with syntaxin 1a through two discrete modes of binding that are spatially distinct within neuroendocrine cells. This study shows that the closed form of binding to munc18-1 plays a role in trafficking syntaxin 1a to the plasma membrane as previously reported (Arunachalam et al, 2008; Martinez-Arca et al, 2003; Rowe et al, 2001). Furthermore, using equilibrium binding experiments coupled with FLIM analysis (Figure 3.7) it is clear that munc18-1 has a high binding affinity (K_d = 5 nM) for this conformation of syntaxin 1a (Figure 3.3B) and that this mode of binding occurs predominantly within intracellular membranes. One possible

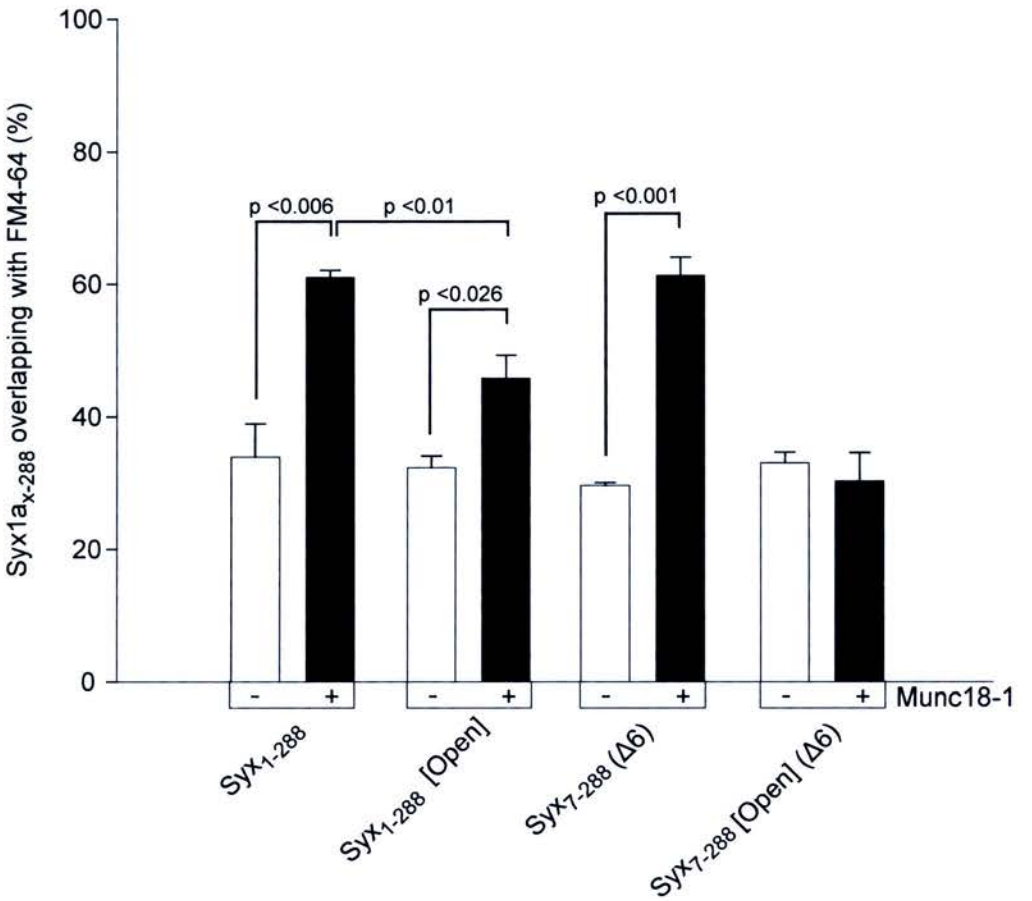

Figure 3.13 Syntaxin 1a traffics via the closed conformation and N-terminal binding to the plasma membrane and overlaps with FM4-64.

Data from live HEK293 cells expressing Cerulean fused Syx1a$_{1-288}$, Syx1a$_{1-288}$ [Open], Syx1a$_{7-288}$ (Δ6), Syx1a$_{7-288}$ [Open] (Δ6) in the presence or absence of munc18-1 and the addition of FM4-64 prior to CLSM were quantified and expressed as the percentage of Syx1a$_{x-288}$ overlapping with FM4-64. These data show that in the presence of munc18-1, Syx1a$_{1-288}$, Syx1a$_{1-288}$ [Open], and Syx1a$_{7-288}$ (Δ6) overlap with FM4-64. In the presence of munc18-1 the percentage of overlap was significantly higher, t test, $p < 0.026$. Data are expressed as the mean ± SEM, n = 3.

function of this closed form interaction may be to keep syntaxin 1a in an inactive state, possibly preventing interactions with cognate SNARE proteins and thus permitting the trafficking of syntaxin 1a through the ER and the Golgi complex to the plasma membrane.

In addition to the closed mode of binding, I have demonstrated in this chapter that syntaxin 1a and munc18-1 can also interact via N-terminal binding as seen with yeast homologues. In this study munc18-1 was found to readily bind to an open mutant of syntaxin 1a with high affinity (K_d = 5 nM) (Figure 3.3B) and there was no reduction in affinity when compared to wild-type syntaxin 1a and munc18-1 binding. A reduction in the binding affinity of munc18-1 for syntaxin 1a was only observed when both the closed and N-terminal modes of binding were disrupted (K_d = 44 nM) (Figure 3.3B), and this was coupled with a disruption in syntaxin 1a and munc18-1 trafficking to the plasma membrane. The open mutation of syntaxin 1a was also shown to bind to SNAP-25 and synaptobrevin suggesting that syntaxin 1a N-terminal binding still permits syntaxin 1a to proceed through the SNARE assembly pathway (Figure 3.8). This is in contrast to previous studies in which it was concluded that munc18-1 was unable to interact with the N-terminus of syntaxin 1a, yet it must be noted that an early clone of syntaxin 1a that has been used widely to report protein-protein interactions lacks a conserved N-terminal region (Calakos et al, 1994).

From these findings and given the high affinity that munc18-1 has for syntaxin 1a in both the closed and open conformational states, it is clear that munc18-1 has two functionally and spatially distinct modes of binding to syntaxin 1a. Munc18-1 has been shown to interact with an open mutation of syntaxin 1a through an alternative N-terminal binding site, and furthermore this open form of syntaxin 1a possesses the ability to form SNARE complexes while remaining bound to munc18-1, which would ultimately argue against a 'protective role' for munc18-1. These findings provide a molecular explanation for the multiple and spatially distinct roles of munc18-1, however, it remains to be established what the functional significance of the two different modes of binding in the SNARE trafficking life cycle are. The presence of an inactive form of syntaxin 1a may be vital in intracellular membranes

to prevent syntaxin 1a from interacting with cognate SNAREs, thereby preventing the formation of misplaced SNARE complexes. Upon delivery to the plasma membrane, syntaxin 1a may switch to its open active form to initiate SNARE core complex assembly and subsequent membrane fusion.

CHAPTER FOUR:

MUNC18-1 PREVENTS THE FORMATION OF ECTOPIC SNARE COMPLEXES

4.1 INTRODUCTION

Membrane trafficking in eukaryotic cells must be fast, properly timed and strictly regulated both temporally and spatially. A sufficient number of vesicles need to be loaded, fusion-ready and adequately replenished at a rapid rate. At the plasma membrane the exocytotic SNARE proteins are essential for this reason. In addition the SNARE proteins are known to be highly promiscuous in their interactions with other non-cognate SNARE proteins. The ER and Golgi complex is a SNARE protein driven cascade of fusion events. It is therefore a vital cellular requirement to traffic these exocytotic SNARE proteins through the ER and Golgi complex while avoiding ectopic interactions between the SNARE proteins before they reach their target destination of the plasma membrane. Although the minimal machinery for membrane fusion is accepted to be the three SNARE proteins, it is clear that other accessory or regulatory factors such as munc18-1 are necessary for efficient controlled exocytosis.

Previous studies have implied that the binding of munc18-1 to syntaxin is required for the efficient trafficking of syntaxin to the plasma membrane (Arunachalam et al, 2008; Rowe et al, 2001; Rowe et al, 1999). In contrast, others have reported that syntaxin can traffic independently to the cell surface in the absence of munc18-1 in a variety of cell types (Schutz et al, 2005; Toonen et al, 2005). This is supported by studies using a munc18-1-null mouse in which syntaxin can be detected at the cell surface (Toonen et al, 2005; Verhage et al, 2000). However, in this system total cellular syntaxin levels are shown to be reduced by >70% and other munc18-1 isoforms are still present, which may play a role in trafficking syntaxin (Toonen et al, 2005). Furthermore, the regulatory protein munc18-1 is suggested to be a docking factor based on observations using the same munc18-1 null mouse (Voets et al, 2001). More recently, however, this same group have suggested that docking is instead syntaxin dependent. The importance of munc18-1 in regulating SNARE protein function has been further strengthened by the observation that SNARE complexes containing munc18-1 bound to 'open' syntaxin 1 are essential for exocytosis (Gerber et al, 2008). Taken together, these observations highlight that the functional significance of munc18-1 in SNARE protein regulation is still a matter of

debate. I hypothesised that the role of munc18-1 in trafficking syntaxin 1a might be dependent upon spatio-temporal factors. If munc18-1 is not present to bind to the closed conformation of syntaxin 1a, inactivating it, then syntaxin 1a may interact with intracellular SNARE proteins and become trapped intracellularly.

In this chapter, I show that syntaxin 1a is able to traffic in an inactive form to the plasma membrane, requiring a closed-form interaction, but not N-terminal binding, with munc18-1. To examine the importance of trafficking exocytotic SNARE proteins through the ER and Golgi complex I employed quantitative imaging approaches including co-localisation and FLIM. I show that syntaxin 1a forms stable intracellular SNARE complexes with SNAP-25 if the proteins encounter one another before munc18-1 binding to closed form syntaxin 1a. The formation of these ectopic SNARE complexes occurs in the Golgi complex, trapping both t-SNAREs so they are unable to traffic to the plasma membrane. Such findings confirm that munc18-1 has two disparate modes of binding with syntaxin 1a which play very different roles in the SNARE trafficking life cycle.

4.2 CONSTRUCTION OF SNAP-25 AND MUTANT FLUORESCENT FUSION PLASMIDS

To investigate the interaction between syntaxin 1a and SNAP-25 by expression in cultured mammalian cells, fluorescent fusions of wild-type SNAP-25 (SNAP-25A_{1-206}) and a truncated SNAP-25 mutant (SNAP-25A_{1-121}) were constructed and the naming system shown in Figure 4.1A adopted in this study.

In order to accomplish this, an EYFP-SNAP-25 fusion was generated by ligation of SNAP-25A_{1-206} (from SNAP-25A_{1-206} in pEGFP-N1 (Table 2.2)) into *Bam*HI/*Eco*RI sites of pEGFP-C2 (Table 2.2), followed by replacement of EGFP with EYFP using standard molecular techniques (see Chapter 2: Materials and Methods). The truncated or D121 STOP mutation (named SNAP-25A_{1-121} throughout this thesis) consists of only the SN1 motif and palmitoylated linker region of SNAP-25A_{1-206}

(Figure 4.1A). The generation of the D121 STOP truncated SNAP-25 mutant was performed by site-directed mutagenesis on pEYFP-C2-SNAP-25A$_{1-206}$ (see Chapter 2: Materials and Methods). An aspartic acid residue at position 121 was changed to a stop codon using the following PCR oligonucleotide primers: primer 1, 5' –GCC AGC CTG CCC GTG TGG TGT AGG AAC GGG AGC AGA TGG- 3'; and primer 2, 5' –CCA TCT GCT CCC GTT CCT ACA CCA CAC GGG CAG GCT GGC- 3'. The plasmid construct maps are shown in the Appendix.

4.3 SNAP-25 TRAFFICS INDEPENDENTLY TO THE PLASMA MEMBRANE

Previous studies have reported that SNAP-25 can traffic independently to the cell surface in NG108-15 and PC12 cells, and is thereby not reliant on the presence of specialised factors (Loranger and Linder, 2002). To confirm that SNAP-25 can traffic in an independent manner to the plasma membrane in the absence of a regulatory protein such as munc18-1, EYFP fused to the N-terminal of wild-type SNAP-25A$_{1-206}$ or a truncated mutant, SNAP-25A$_{1-121}$ were expressed in isolation in live N2a and HEK293 cells and imaged by CLSM. Figure 4.1B demonstrates that in both N2a and HEK293 cells, wild-type SNAP-25A$_{1-206}$ and SNAP-25A$_{1-121}$ were able to traffic independently to the cell surface in the absence of a chaperone protein. Both wild-type SNAP-25A$_{1-206}$ and SNAP-25A$_{1-121}$ were clearly visible as enrichment around the plasma membrane in N2a and HEK293 cells. This therefore supports the hypothesis that SNAP-25 does not require munc18-1 or the presence of any specialised protein and can traffic to the plasma membrane by a syntaxin independent mechanism as previously reported (Loranger & Linder, 2002).

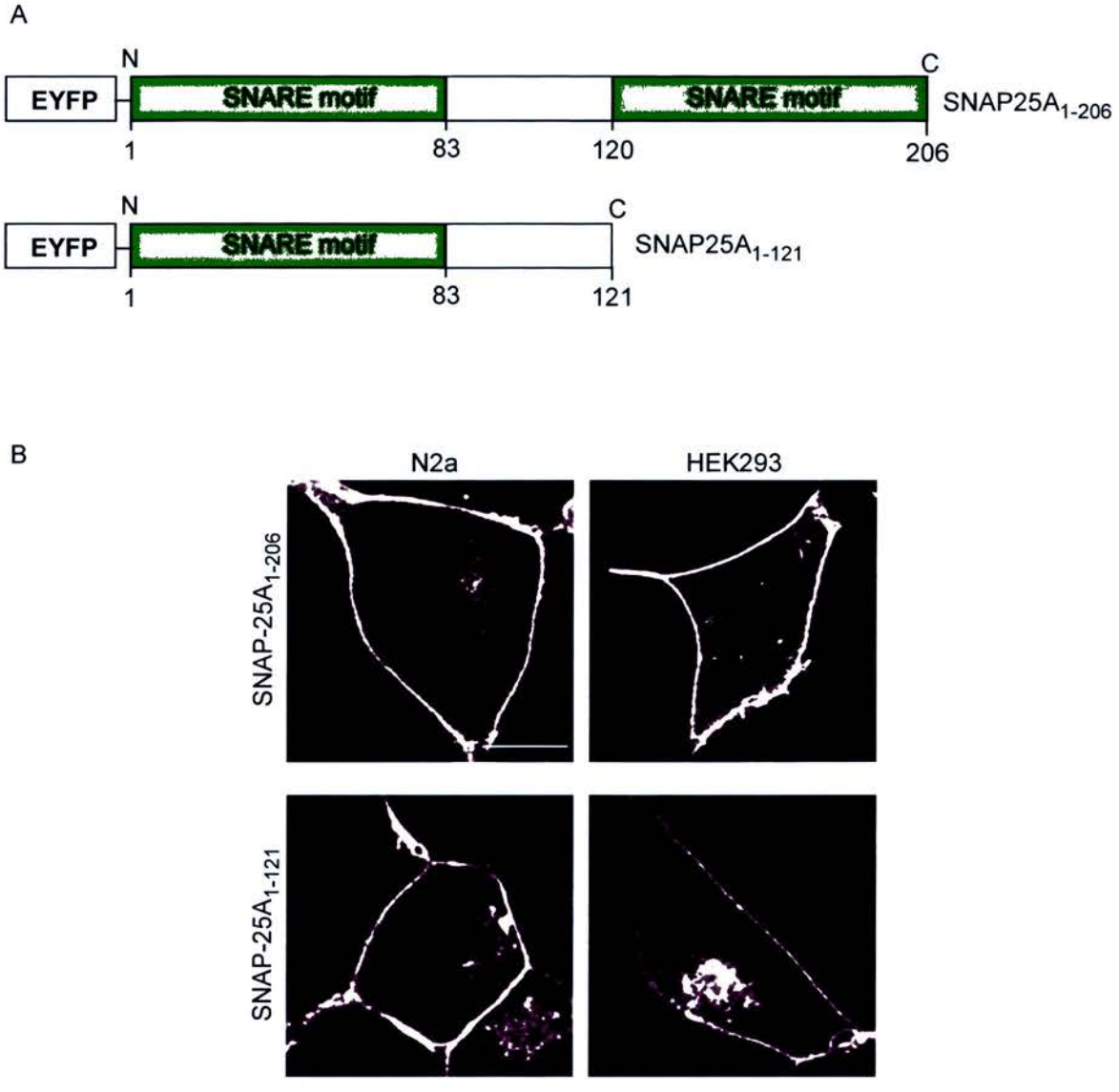

Figure 4.1 SNAP-25 traffics independently to the plasma membrane in living cells.

(A) Schematic diagrams of the EYFP-SNAP-25 fusion proteins are shown. The fusion protein EYFP is attached to the N-terminus. Numbers below the diagrams correspond to amino acid residues in SNAP-25. The SNARE motifs involved in core complex formation are illustrated in green. The D121 STOP mutation that consists of the SN1 motif and the palmitoylated linker region is shown. The naming system adopted in this study is displayed on the right hand side. Not to scale. **(B)** Live N2a or HEK293 cells expressing wildtype EYFP-SNAP-25A_{1-206} or truncated EYFP-SNAP-25A_{1-121} were imaged by CLSM. Shown are representative equatorial sections from 10 independent experiments. Wild-type SNAP-25 and the truncated mutant containing only the first helix are both able to traffic to the plasma membrane independently in living cells. Scale bar, 10 µm.

4.4 SYNTAXIN 1A AND SNAP-25 CO-LOCALISE IN INTRACELLULAR MEMBRANES IN THE ABSENCE OF MUNC18-1

It is not known whether the t-SNAREs are reactive in intracellular membranes and what the functional significance is of munc18-1 binding to the closed conformation of syntaxin 1a in intracellular membranes. To examine whether the role of munc18-1 in trafficking syntaxin 1a might be dependent on spatio-temporal factors, mCerulean-fused Syx1a$_{1\text{-}288}$ and EYFP-fused SNAP-25A$_{1\text{-}206}$ or truncated SNAP-25A$_{1\text{-}121}$ were co-expressed in live N2a and HEK293 cells in the absence of heterologous munc18-1. In addition to N2a cells, HEK293 cells were used as they do not contain endogenous munc18-1 thus eliminating any potential impact from endogenous munc18-1 (Rowe et al, 2001). These experiments were designed to test the ability of syntaxin 1a to form complexes with SNAP-25 and thus address the issue, are the SNAREs reactive or non-reactive in intracellular membranes.

Using CLSM, Z axis stacks were captured, and only weakly expressing cells were analysed. Representative equatorial sections are shown but at no time did syntaxin 1a traffic to the plasma membrane in the absence of heterologous munc18-1 in N2a or HEK293 cells (Figure 4.2). Quantitative co-localisation studies (see Chapter 2: Materials and Methods) indicated that neither t-SNARE trafficked efficiently to the cell surface, even in the presence of endogenous munc18-1 in N2a cells (Figure 4.2). As shown in these images, mislocalised syntaxin 1a and SNAP-25A exhibited a high degree of coincidence and covariance in perinuclear membranes.

Similar co-localisation results were obtained for both N2a and HEK293 cells expressing Syx1a$_{1\text{-}288}$ and the truncated mutant SNAP-25A$_{1\text{-}121}$. Some SNAP-25 was able to traffic to the cell surface in both N2a and HEK293 cells, but most of it still remained co-localised with Syx1a$_{1\text{-}288}$ trapped in intracellular membranes (Figure 4.2). This indicates that the SN1 motif of SNAP-25 may be sufficient to interact with syntaxin 1a, reducing localisation of SNAP-25 to the plasma membrane. In the absence of munc18-1 both t-SNAREs showed a reduction in membrane localisation and appeared to become trapped in intracellular membranes as seen with wild-type SNAP-25, even in the presence of endogenous munc18-1 within N2a cells. Taken

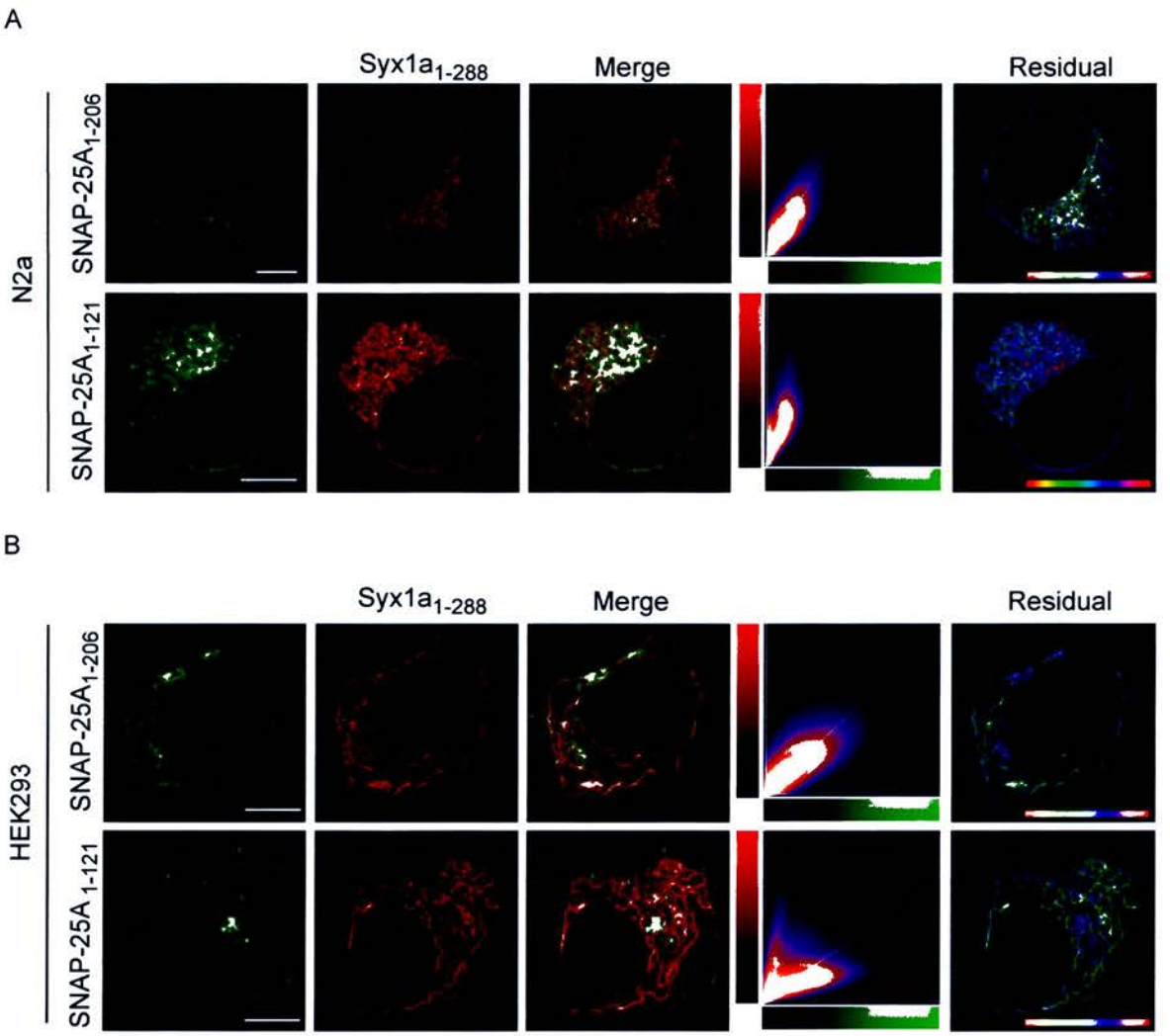

Figure 4.2 Syntaxin 1a and SNAP-25 remain trapped in intracellular membranes if co-expressed in the absence of munc18-1 in living cells.

(A) In the absence of munc18-1, syntaxin 1a and SNAP-25 remain trapped intracellularly and localisation to the plasma membrane is reduced. Wild-type SNAP-25A_{1-206} or truncated SNAP-25A_{1-121} (green) and Syx1a_{1-288} (red) were co-expressed in live N2a cells and imaged by CLSM. The merged image shows areas of coincidence in yellow hues. The two-dimensional histogram represents the intensity of each channel in each voxel, with a colour scale representing frequency. The residual map corresponds to weighted residuals from the linear regression of the histogram, thus indicating fluorescent channel covariance. The hue is from -1 to 1, with cyan corresponding to a zero residual. **(B)** Wild-type SNAP-25A_{1-206} or truncated SNAP-25A_{1-121} (green) and Syx1a_{1-288} (red) were co-expressed in live HEK293 cells and imaged by CLSM. Shown are representative equatorial sections from 10 experiments. All scale bars, 5 µm.

together, these data provide evidence to support the hypothesis that the endogenous t-SNAREs are constitutively active and can readily form SNARE complexes with heterologously added t-SNAREs (Lang et al, 2002). Therefore, another spatially and temporally localised factor must be required to prevent them from forming SNARE complexes within intracellular membranes. Munc18-1 binding to the closed form of syntaxin 1a may have a role in keeping syntaxin 1a in an inactive state until arrival at the cell surface, and this function may be vital in preventing intracellular SNARE complex formation.

4.5 SYNTAXIN 1A AND SNAP-25 COMPLEXES FORM IN THE GOLGI COMPLEX

I have demonstrated that in N2a cells, SNAP-25A$_{1-206}$ alone can traffic independently to the plasma membrane, yet when co-expressed with Syx1a$_{1-288}$ in the absence of munc18-1, both t-SNAREs accumulate and co-localise in intracellular membranes (Figure 4.2A). Therefore, it was necessary to identify this intracellular localisation. I performed similar experiments as before, where I co-expressed N-terminal fluorescent fusions to the t-SNARE proteins, mCerulean-Syx1a$_{1-288}$ and EYFP-SNAP-25A$_{1-206}$ in live N2a cells, but in this instance I also expressed a marker for the *cis*-Golgi, GRASP-65 protein (Table 2.2). The protein GRASP-65 is a Golgi membrane protein involved in establishing the stacking structure of Golgi cisternae and forms a complex with a putative Golgi matrix membrane protein and vesicle docking receptor, GM130 (Barr et al, 1998; Barr et al, 1997). This GRASP-65-GM130 complex is tightly bound to the Golgi membranes and it is for this reason that GRASP-65 is an ideal Golgi marker for this study. The mCherry-GRASP65 protein (Table 2.2) used was spectrally distinct from both mCerulean-Syx1a$_{1-288}$ and EYFP-SNAP-25A$_{1-206}$.

As noted previously, mislocalised Syx1a$_{1-288}$ and SNAP-25A$_{1-206}$ exhibited a high degree of coincidence and covariance in intracellular membranes reminiscent of the Golgi complex (Figure 4.3A). Perinuclear enrichment was observed in the staining with the red-fluorescent (mCherry) protein fusion to GRASP-65 localising to the *cis*-

Golgi (Figure 4.3B). Quantitative co-localisation analysis of GRASP-65 with both the t-SNAREs confirmed that the site of greatest t-SNARE co-localisation was the Golgi complex. By measuring the residual or deviation from this relationship we measure not only whether green and red fluorescence exists in the same region but whether the intensities are covariant. This is shown in the residual map where regions that correlate well are cyan in colour and deviation from this fit appears towards either end of the spectrum. A residual map corresponding to weighted residuals indicated fluorescent covariance between the t-SNAREs (Figure 4.3A). The residuals corresponding to the Golgi were extracted using the mCherry GRASP-65 staining as a mask (Figures 4.3B). The weighted residuals of $Syx1a_{1\text{-}288}$ and $SNAP\text{-}25A_{1\text{-}206}$ contained within the Golgi complex, as defined by a mCherry-GRASP-65 mask, alongside residual values from other areas of the cell were plotted as frequency distribution histograms, verifying that the weighed residuals centered around zero (ie. the highest covariance) were present in the Golgi complex (Figure 4.3C). Therefore, these data indicate that the t-SNAREs are highly reactive in intracellular membranes and in the absence of the correct levels of munc18-1 the trafficking of both syntaxin 1a and SNAP-25 from the Golgi complex to the plasma membrane is severely perturbed.

4.6 Syntaxin 1a and SNAP-25 reactive complexes form in the Golgi complex in the absence of munc18-1

The quantitative co-localisation analysis of mutant proteins in living cells has strengthened the idea that the t-SNAREs are indeed highly reactive and can interact in intracellular membranes in the absence of regulatory factors such as munc18-1. However, it must be noted that the previous co-localisation data is limited by the resolution of the microscope (maximally 178 nm) (Figure 2.4) and although the t-SNAREs may be in the same physical vicinity, this does not directly indicate an interaction between the proteins.

Therefore, to further investigate if the trapped t-SNAREs, syntaxin 1a and SNAP-25 can interact in intracellular membranes or the Golgi complex, I employed

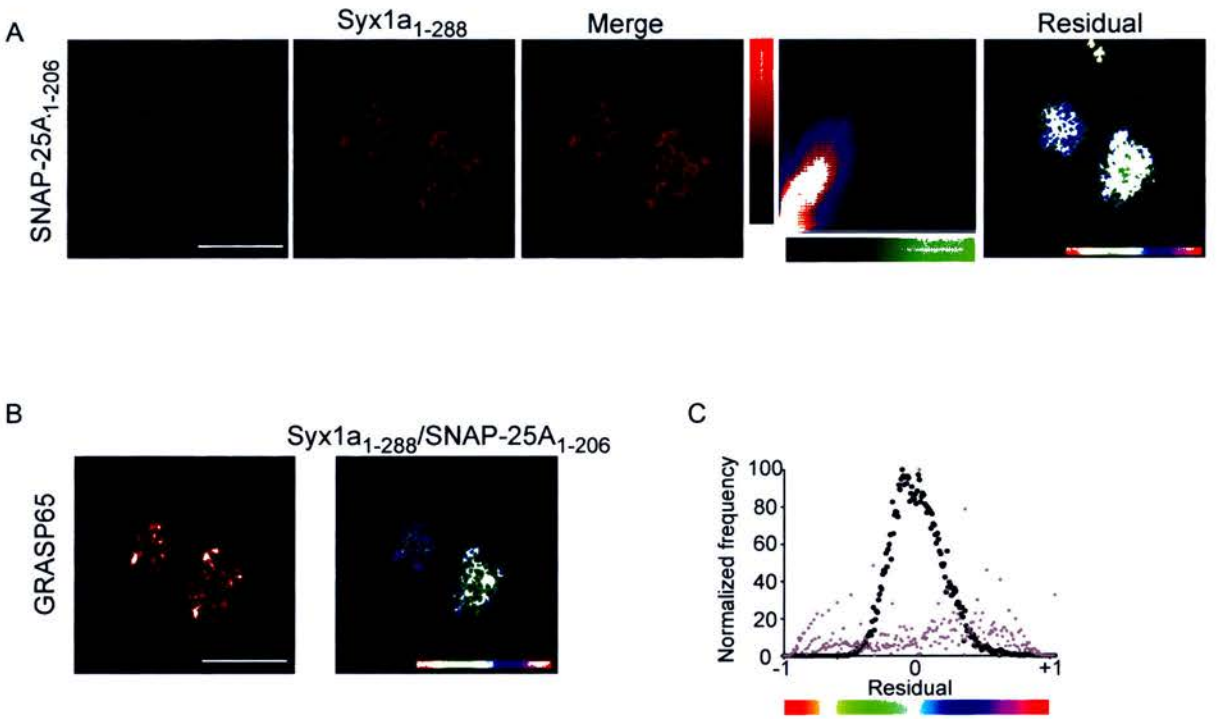

Figure 4.3 Syntaxin 1a and SNAP-25 co-localise in the Golgi complex in living cells in the absence of munc18-1.

(A) Wildtype EYFP-SNAP-25A$_{1-206}$ (green), mCerulean-Syx1a$_{1-288}$ (red) and the Golgi complex marker, GRASP65-mCherry were co-expressed in live N2a cells and imaged by CLSM. The merged image shows areas of coincidence in yellow hues between Syx1a$_{1-288}$ and SNAP-25A$_{1-206}$. The two-dimensional histogram represents the intensity of each channel in each voxel with a colour scale representing frequency. The residual map corresponds to weighted residuals from the linear regression of the histogram, indicating fluorescent channel covariance. The hue is from -1 to 1 with cyan corresponding to a zero residual. Representative equatorial sections from 8 experiments. Scale bar, 10 µm. **(B)** The Golgi complex marker, GRASP65-mCherry, was co-expressed in live N2a cells and imaged by CLSM (left panel). Residual map of Syx1a$_{1-288}$ and SNAP-25A$_{1-206}$ covariance in the Golgi complex (right panel), as defined by a GRASP65-mCherry mask. Scale bar, 10 µm. **(C)** The weighted residuals of Syx1a$_{1-288}$ and SNAP-25A$_{1-206}$ contained within the Golgi complex, as defined by GRASP65-mCherry mask (•), alongside residual values from elsewhere in the cell minus the Golgi complex (•), were plotted as a frequency distribution histogram (right panel). In the absence of munc18-1, syntaxin 1a and SNAP-25 become trapped and co-localise in the Golgi complex in neuroendocrine cells.

fluorescence lifetime imaging microscopy (FLIM) to detect and quantify directly Förster Resonance Energy Transfer (FRET). As co-localisation data can only tell us if the proteins reside in the same region, FLIM analysis was performed to detect FRET between mCerulean fused Syx1a$_{1-288}$ used as the donor and EYFP fused SNAP-25A$_{1-206}$ used as the acceptor in live N2a cells (Figure 4.4A). In the absence of EYFP-SNAP-25A$_{1-206}$ (the acceptor), mCerulean-Syx1a$_{1-288}$ (the donor) fluorescence exhibited an intracellular distribution (Figure 4.4B). By taking all the pixels in the image, the fluorescence lifetimes were displayed on a colour scale in the FLIM map from 1900 picoseconds (red) to 2400 picoseconds (blue), and mCerulean-Syx1a$_{1-288}$ exhibited a single fluorescence lifetime throughout the cell. FLIM analysis of N2a cells expressing the donor mCerulean-Syx1a$_{1-288}$ alone revealed a mono-exponential fluorescence lifetime decay of 2388 ± 47 ps (mean ± SEM; n = 5) (Figure 4.4B), in agreement with previous studies of mCerulean and of mCerulean-Syx1a$_{1-288}$ (Rickman et al, 2007; Rizzo et al, 2004).

In contrast, when I co-expressed the FRET acceptor EYFP fused to SNAP-25A$_{1-206}$ with mCerulean-Syx1a$_{1-288}$ in N2a cells the donor fluorescence decay was very different. The fluorescence lifetime of the donor, mCerulean-Syx1a$_{1-288}$ was shortened significantly to 2176 ± 134 ps (mean ± SEM; n = 5, Mann Whitney Rank Sum test, $p < 0.01$) in the perinuclear Golgi region (Figure 4.4C). If we compare the excited state fluorescence decay of mCerulean-Syx1a$_{1-288}$ in the absence of an energy acceptor, it followed a mono-exponential decay, and in the presence of an energy acceptor, in this case EYFP-SNAP-25A$_{1-206}$, the fluorescence decay of mCerulean-Syx1a$_{1-288}$ was fit by a bi-exponential decay function (Figure 4.4B, right panel). These data are presented as intensity images, frequency distribution histograms and as FLIM maps. FLIM maps represent the measured mean fluorescence lifetime in each pixel of an image as a false-color to reveal the intracellular locations of non-FRET and FRET components. In the presence of the acceptor, the donor fluorescence lifetime was significantly quenched and displayed on a colour scale showed the molecules undergoing FRET with a shortened lifetime and molecules not undergoing FRET with the same lifetime as observed for the donor mCerulean-Syx1a$_{1-288}$ alone (Figure 4.4C).

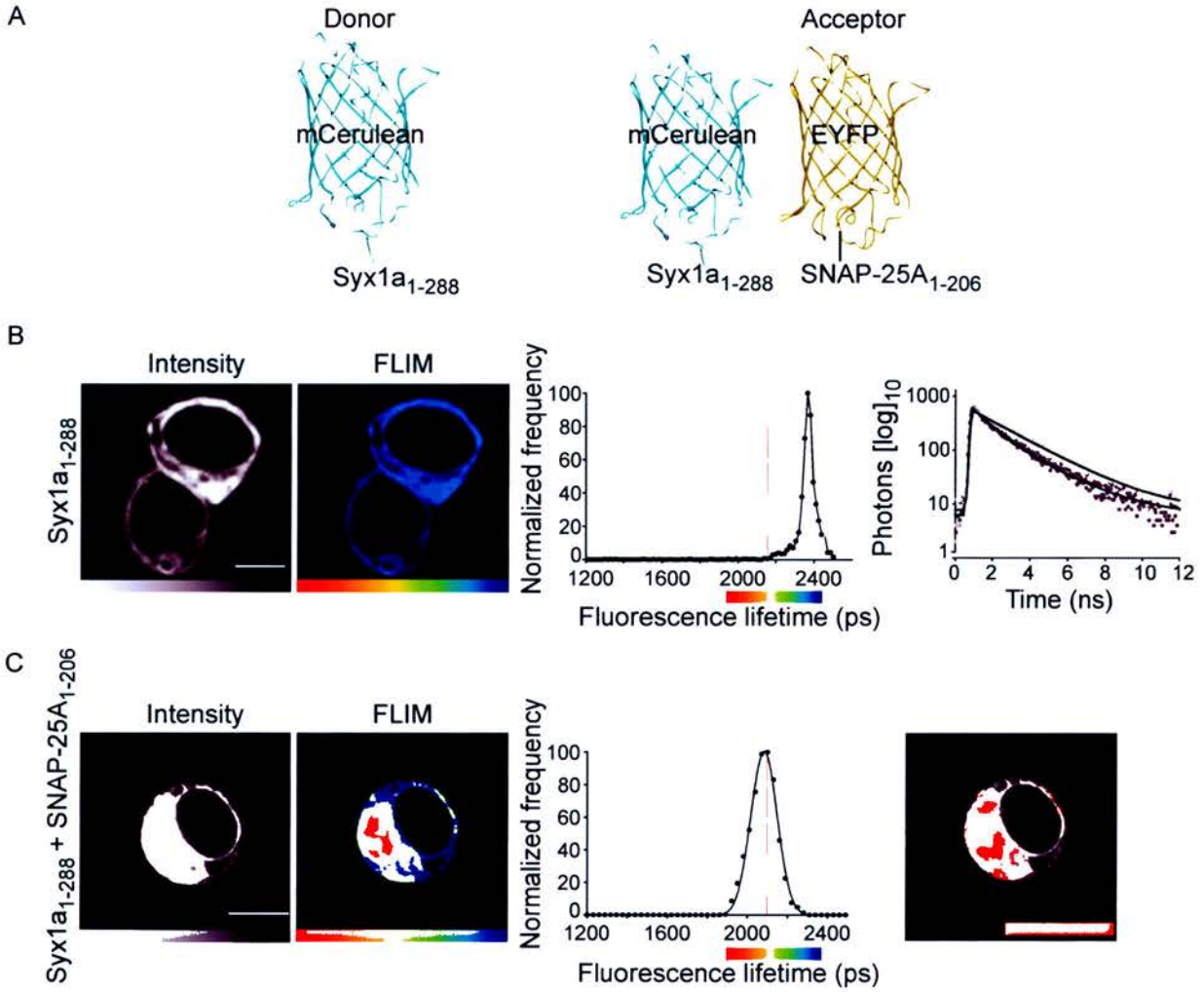

Figure 4.4 Syntaxin 1a and SNAP-25 reactive complexes form in the Golgi apparatus and prevent trafficking of both t-SNAREs.
(A) mCerulean fused $Syx1a_{1-288}$ was used as the donor and EYFP fused $SNAP\text{-}25A_{1-206}$ as the acceptor. $Syx1a_{1-288}$ was expressed alone or co-expressed with $SNAP\text{-}25A_{1-206}$ in live N2a cells and imaged by TCSPC-FLIM. **(B)** mCerulean-$Syx1a_{1-288}$ (donor) fluorescence in the absence of EYFP-$SNAP\text{-}25A_{1-206}$ (acceptor) exhibited an intracellular distribution . Taking all the pixels in the image, the fluorescence lifetimes can be displayed on a colour scale. The colour scale in the FLIM map represents the fluorescence lifetime [1900 ps (red) - 2400 ps (blue)]. The fluorescence lifetime values were plotted as a frequency distribution histogram, showing 99 % confidence interval of the $Syx1a_{1-288}$ fluorescence lifetime distribution (red line). $Syx1a_{1-288}$ alone has a single fluorescence lifetime of 2388 ± 47 ps. The excited state fluorescence decay of $Syx1a_{1-288}$ in the absence of an energy acceptor followed a mono-exponential decay (light grey circles) and in the presence of an energy acceptor, the fluorescence decay of $Syx1a_{1-288}$ was fit to a bi-exponential decay function (dark grey circles) (right panel). **(C)** mCerulean-$Syx1a_{1-288}$ (donor) fluorescence in the presence of EYFP-$SNAP\text{-}25A_{1-206}$ (acceptor) exhibited an intracellular distribution. Again the colour scale in the FLIM map represents the fluorescence lifetime. The fluorescence lifetime values were plotted as a frequency distribution histogram, showing the 99% confidence interval of the $Syx1a_{1-288}$ fluorescence lifetime distribution (non-FRET; red line). The fluorescence lifetime of mCerulean-$Syx1a_{1-288}$ was shortened significantly to 2176 ± 134 ps (Mann-Whitney, $n = 5$, $p < 0.01$) when co-expressed with EYFP-$SNAP\text{-}25A_{1-206}$. $Syx1a_{1-288}$ (donor) fluorescence in the presence of $SNAP\text{-}25A_{1-206}$ (acceptor) showing in red, pixels containing donor fluorescence lifetimes below the 99% confidence interval (right panel). Data are expressed as the mean ± SEM, $n = 5$.

Importantly, from this analysis we know the fractions of molecules undergoing FRET in each pixel. In this instance, statistically significant donor fluorescence lifetime quenching was observed in the perinuclear Golgi region where the t-SNAREs were previously shown to co-localise. This is consistent with the conclusion that the t-SNAREs are therefore reactive in the absence of the correct levels of munc18-1 in the appropriate intracellular location. Thus, syntaxin 1a and SNAP-25 reactive complexes can form in the Golgi complex preventing the trafficking of either t-SNARE.

4.7 MUNC18-1 BINDS TO SYNTAXIN 1A IN INTRACELLULAR MEMBRANES, PREVENTING THE FORMATION OF ECTOPIC SNARE COMPLEXES AND PERMITTING t-SNARE TRAFFICKING

The previous data confirmed that in the absence of munc18-1, both syntaxin 1a and SNAP-25 are reactive and can interact in the Golgi complex. If my hypothesis is correct that munc18-1 can act as a regulatory factor at different intracellular locations and thus prevent syntaxin 1a from entering into ectopic SNARE complexes, then co-expressing munc18-1 with both t-SNAREs should permit the efficient trafficking of both syntaxin 1a and SNAP-25 to the plasma membrane. To elucidate the role for munc18-1 in preventing the trapping and interaction of syntaxin 1a and SNAP-25 in the perinuclear Golgi region, I conducted studies in which munc18-1 was introduced into live cells using munc18-1 expression constructs.

To examine this concept in living cells, I employed HEK293 cells expressing EYFP fused SNAP-25A_{1-206} and mCerulean fused Syx1a_{1-288}, Syx1a_{7-288} (Δ6), Syx1a_{1-288} [Open] or Syx1a_{7-288} [Open] (Δ6) in the presence or absence of munc18-1. Again HEK293 cells were used in this study as they do not express any endogenous munc18-1 (Rowe et al, 2001), thus eliminating the effects of endogenous munc18-1. A quantitative approach was used to analyse covariance between the t-SNAREs (see Chapter 2: Materials and Methods). In the absence of munc18-1, the co-expression of Syx1a_{1-288} or mutants of Syx1a_{1-288} that lack the ability to bind munc18-1 via closed form or N-terminal binding, all remain trapped with SNAP-25A_{1-206} intracellularly in

live HEK293 cells as expected in the absence of both endogenous and heterologous munc18-1. Quantitative co-localisation studies revealed that neither t-SNARE was able to traffic to the plasma membrane and remained co-localised in intracellular membranes (Figure 4.5). Both wild-type and mutants of $Syx1a_{1-288}$ exhibited high degrees of coincidence and covariance with $SNAP\text{-}25A_{1-206}$ in intracellular membranes in the absence of munc18-1.

As hypothesised, syntaxin 1a and SNAP-25 mislocalisation was rescued by the presence of munc18-1 in live N2a cells and HEK293 cells. The co-expression of $Syx1a_{1-288}$, or the mutant $Syx1a_{1-288}$ ($\Delta 6$) that lacks the ability to bind munc18-1 via its N-terminus, with $SNAP\text{-}25A_{1-206}$ and munc18-1, resulted in the trafficking of both t-SNAREs to the plasma membrane where they showed high degrees of co-localisation and covariance in HEK293 cells (Figure 4.6). In contrast, when $Syx1a_{1-288}$ [Open] or $Syx1a_{7-288}$ [Open] ($\Delta 6$) was co-expressed with $SNAP\text{-}25A_{1-206}$ and munc18-1 in HEK293 cells both t-SNAREs failed to traffic to the cell surface and remained co-localised in intracellular membranes (Figure 4.6) where they showed high degrees of co-localisation and covariance. Therefore, the trafficking of both t-SNAREs was severely perturbed indicating that even in the presence of munc18-1 an open conformation of syntaxin 1a may interact ectopically with SNAP-25 preventing the trafficking of both t-SNAREs.

This covariance data for syntaxin 1a and SNAP-25 from HEK293 cells in the presence or absence of munc18-1 was quantified and expressed as Pearson's correlation coefficient values (R) (see Chapter 2: Materials and Methods) (Figure 4.7). These data show that there was no significant difference between the high levels of covariance of the t-SNAREs in the presence or absence of munc18-1. This suggests that munc18-1 binds to the closed conformation of syntaxin 1a, locking syntaxin 1a in an inactive state, enabling the efficient trafficking of both proteins to the plasma membrane. The presence of munc18-1 would prevent syntaxin 1a from interacting with SNAP-25 to form binary complexes until at active sites on the plasma membrane.

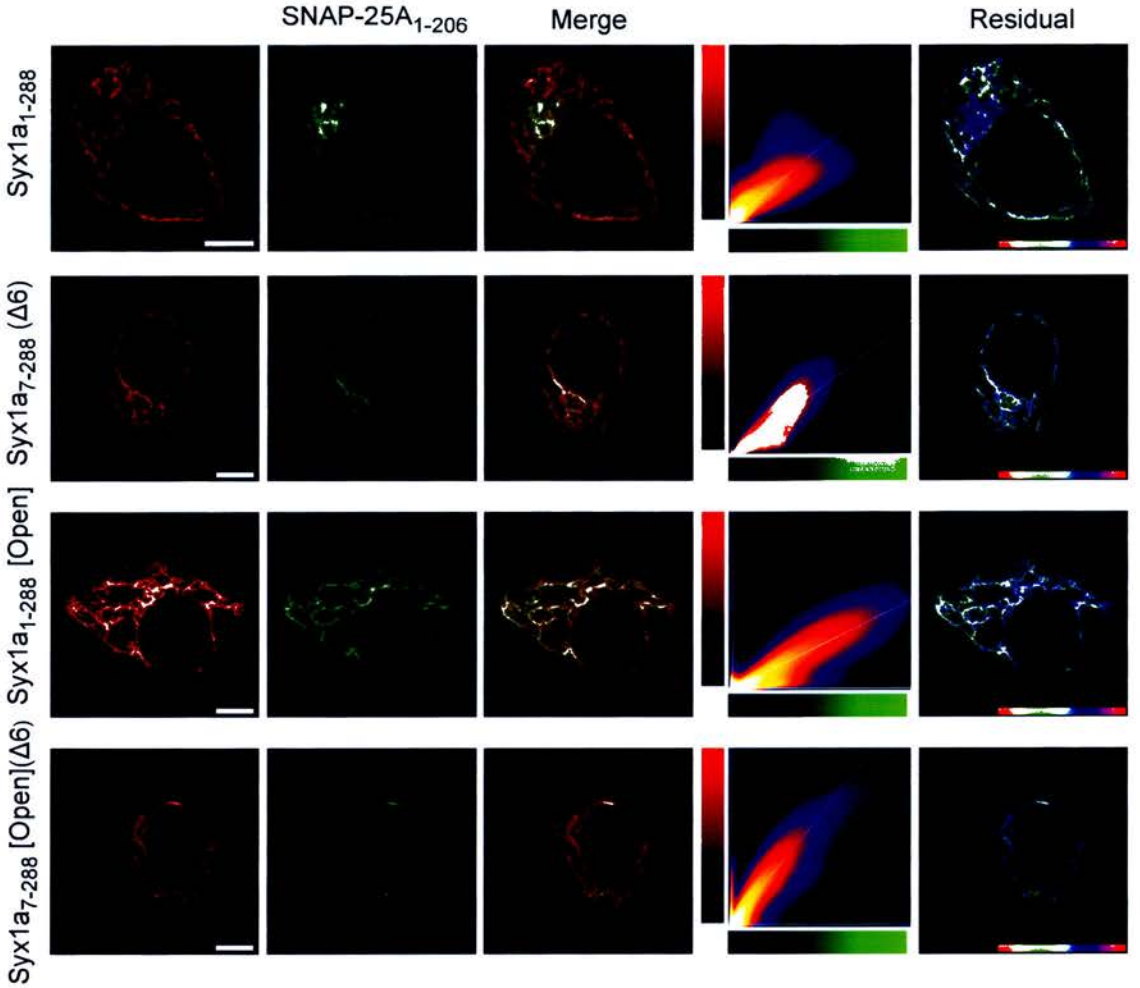

Figure 4.5 In the absence of munc18-1 the open and wild-type form of syntaxin 1a co-localise with SNAP-25 in intracellular membranes.

Wild-type or mutants of mCerulean-Syx1a$_{1-288}$ (red), EYFP-SNAP-25A (green) were co-expressed in HEK293 cells in the absence of munc18-1 and imaged by CLSM. The merged image shows areas of coincidence in yellow hues. The two dimensional histogram represents the intensity of each channel in each voxel, with a colour scale representing frequency. The residual map corresponds to weighted residuals from the line fit to the histogram, thus indicating fluorescent channel covariance. The hue is from -1 to 1, with cyan corresponding to a zero residual. Shown are representative equatorial sections from 10 experiments. Scale bar, 5 µm.

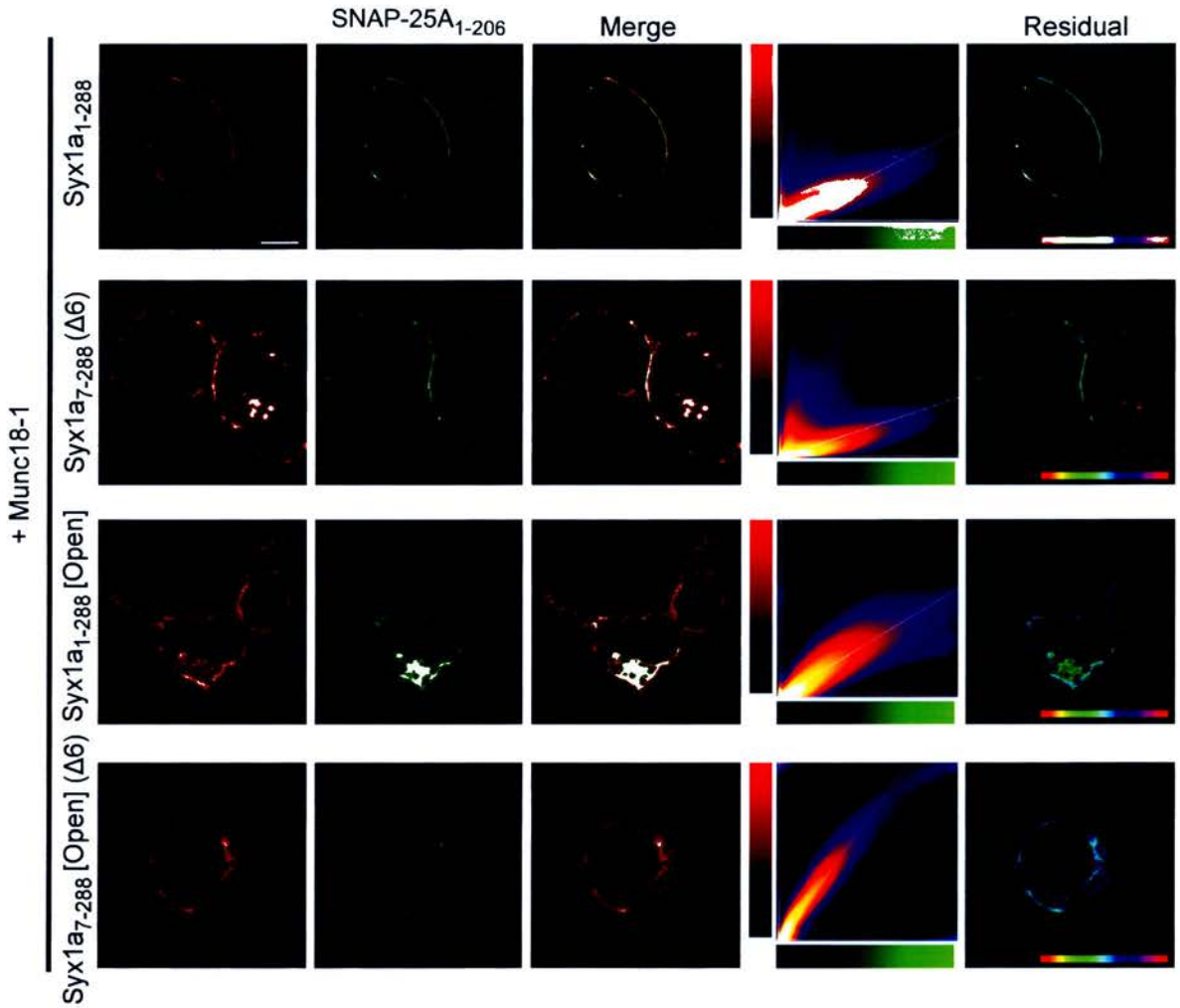

Figure 4.6 Syntaxin 1a in the closed form and SNAP-25 can traffic to the plasma membrane in the presence of munc18-1 .
In HEK293 cells, wild-type or mutants of mCerulean-Syx1a$_{1-288}$ (red) and EYFP-SNAP-25A$_{1-206}$ (green) were co-expressed in the presence of munc18-1 and imaged by CLSM. The merged image shows areas of coincidence in yellow hues. The two dimensional histogram represents the intensity of each channel in each voxel, with a colour scale representing frequency. The residual map corresponds to weighted residuals from the line fit to the histogram, thus indicating fluorescent channel covariance. The hue is from -1 to 1, with cyan corresponding to a zero residual. The covariance between the t-SNAREs is unaffected by the presence of munc18-1, but the location of the co-localisation is altered. Scale bar, 5 µm.

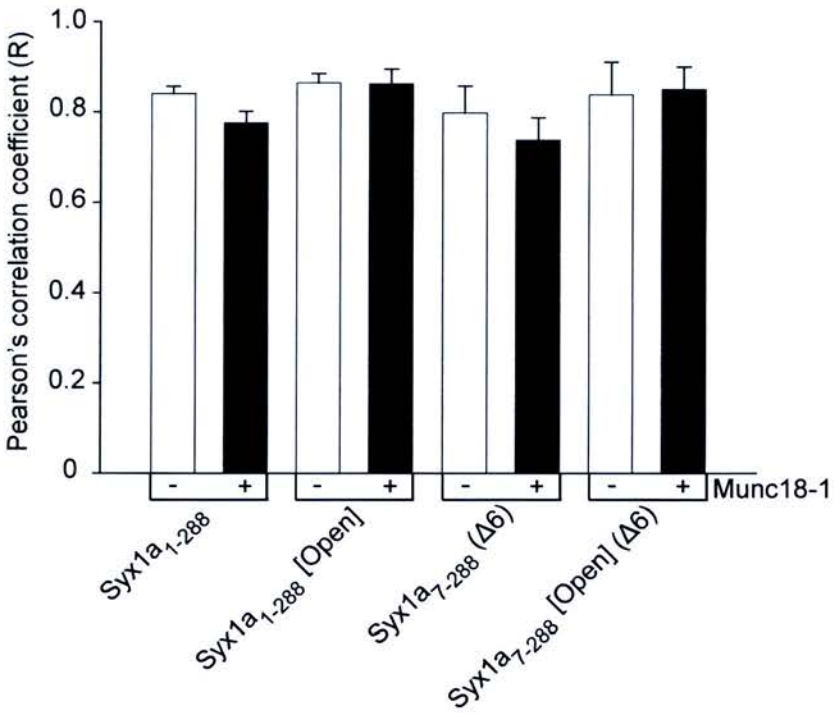

Figure 4.7 Syntaxin 1a and SNAP-25 co-localisation is unaffected by the presence of munc18-1.

The covariance data from HEK293 cells co-expressing wildtype or mutants of mCerulean-Syx1a$_{1-288}$ and SNAP-25A$_{1-206}$ in the absence (open bars) and the presence of munc18-1 (filled bars) were quantified and expressed as Pearson's correlation coefficient values (R). For each data set in the absence or presence of munc18-1 there is no significant difference in the co-localisation of the t-SNAREs. The t-SNAREs still co-localise in the presence of munc18-1, but the location of the co-localisation changes to the plasma membrane for wildtype Syx1a$_{1-288}$ and Syx1a$_{7-288}$ (Δ6) (see Figures 4.5 and 4.6). Data are expressed as the mean ± SEM., n ≥4, Mann Whitney Rank Sum test. Syntaxin 1a that can adopt closed form binding with munc18-1, permits the trafficking of both syntaxin 1a and SNAP-25 to the plasma membrane.

4.8 CONCLUSION

As a result of the diversity of SM protein-SNARE interactions, the function of SM proteins such as munc18-1 have remained controversial. I have demonstrated that munc18-1 bound to the closed conformation of syntaxin 1a has an essential regulatory role in the prevention of ectopic t-SNARE complexes, in addition to its role in trafficking syntaxin 1a to the plasma membrane. Therefore, the two distinct binding modes of munc18-1 with syntaxin 1a serve two very different functions in the SNARE protein life cycle.

The role of munc18-1 in trafficking syntaxin 1a through the secretory pathway relies on it being present in appropriate concentrations at the correct time and in the correct place. It would appear that if munc18-1 does not first inactivate syntaxin 1a by binding to and maintaining the closed conformation and the t-SNAREs encounter one another, then a misplaced intracellular SNARE complex can form. Co-localisation and FLIM studies using GRASP65 demonstrate that misplaced SNARE complexes become trapped in the Golgi complex, perhaps involving a fourth SNARE helix provided by an intracellular SNARE, trapping the complex (Figures 4.3 and 4.4). This is supported by observations that syntaxin can interact promiscuously with intracellular SNAREs (Fasshauer et al, 1999). For example, the open mutant of syntaxin 1a that can switch between the open and closed conformation remains trapped intracellularly even in the presence of munc18-1 (Figure 4.6). Therefore, if munc18-1 is present at the correct levels and at the correct location, syntaxin 1a in the closed conformation and SNAP-25 can both traffic to the plasma membrane (Figure 4.6). Once through the endoplasmic reticulum and the Golgi complex membrane systems, syntaxin 1a appears to remain inactive bound to munc18-1 while SNAP-25 can traffic efficiently and independently to the plasma membrane where it associates with the inner leaflet (Loranger & Linder, 2002). At the plasma membrane, the ternary SNARE complex, bound to munc18-1, cannot include the closed conformation of syntaxin 1a. Therefore, an as yet unknown specialised factor must facilitate a change in the conformation of syntaxin 1a to permit N-terminal binding with munc18-1, revealing the SNARE helix. In the presence of a cognate

SNARE at the plasma membrane this would result in SNARE complex formation, and it is therefore essential that N-terminal binding of munc18-1 comes into play at the cell surface (Dulubova et al, 2007; Rickman et al, 2007).

Taken together, the findings of this study indicate a specific regulatory function of munc18-1 upon the syntaxin 1a – SNAP-25 complex in neuroendocrine cells, as munc18-1 can remain associated with syntaxin 1a throughout the assembly of both the binary and ternary SNARE complexes. It is possible that munc18-1 can remain bound to syntaxin 1a for its entire life cycle, yet in different conformational forms. These observations also highlight the crucial role that munc18-1 plays in trafficking syntaxin 1a through the secretory pathway and provides important insights into the spatial mechanisms regulating the function of SNARE proteins.

CHAPTER FIVE:

t-SNARE CLUSTERS FORM AT THE PLASMA MEMBRANE

5.1 INTRODUCTION

Exocytosis is reliant on the coordinated actions of a wide range of cellular proteins and the targeting of these proteins to specific areas of the plasma membrane. It is proposed that exocytosis is restricted to spatially distinct areas of the plasma membrane demanding specific interactions and conformational status of the exocytotic proteins at these sites. In the previous chapters I have demonstrated that munc18-1 bound to the closed conformation of syntaxin 1a is vital to hold syntaxin 1a in an inactive form to permit the trafficking of both t-SNAREs to the cell surface. Upon delivery to the plasma membrane, munc18-1 can bind to the N-terminus of syntaxin, allowing syntaxin to adopt an open or reactive conformation capable of forming the binary and ternary SNARE complexes.

There has been considerable interest in the mechanisms which define t-SNARE micro-patterning at the plasma membrane and it has been widely reported that upon delivery to the plasma membrane the t-SNAREs localise in clusters that define sites of vesicle docking and exocytosis (Lang et al, 2001; Liu et al, 2005; Predescu et al, 2005; Sieber et al, 2007). These clusters have been shown to range from 60-750 nm in size, depending on the imaging approach employed (Lang et al, 2001; Predescu et al, 2005; Rickman et al, 2004; Sieber et al, 2007). One recent study, suggested that syntaxin 1 clusters were approximately 60 nm in diameter in fixed samples, using stimulated emission depletion (STED) microscopy (Sieber et al, 2007). Importantly, previous studies have focused primarily on syntaxin clusters and not on its cognate partner SNAP-25, thus the forces that govern SNAP-25 cluster formation and integrity are not defined. Upon delivery to the plasma membrane, it is still unclear how the t-SNAREs are distributed, and whether every cluster is competent for priming and docking.

Several studies have focused predominantly on endogenous syntaxin clusters in membrane sheets or fragments which involves sonication to un-roof the cells and subsequent fixation of the membrane sheets (Lang et al, 2001; Predescu et al, 2005). However, it must be noted that the sonication of the cells used to prepare these

membrane sheets could lead to the mixing of sub-cellular compartments and a redistribution of SNAREs on the plasma membrane sheets. To address these issues I have investigated how the endogenous and heterologous t-SNARE proteins, syntaxin 1a and SNAP-25 are spatially localised in intact biological membranes using confocal laser scanning microscopy (CLSM) and total internal reflection fluorescence microscopy (TIRFM). I have shown that both endogenous and heterologous syntaxin 1a and SNAP-25 form clusters on the plasma membrane and that these clusters show high levels of co-localisation. From these findings it may be likely that the syntaxin 1a and SNAP-25 clusters observed in neuroendocrine cells define fusion sites on the plasma membrane.

5.2 Endogenous syntaxin 1a and SNAP-25 form clusters at the plasma membrane

My working model is that SNAP-25 can traffic independently to the cell surface without the involvement of specialised factors, provided that closed syntaxin 1a is first stabilised by munc18-1 binding to prevent aberrant interactions (Chapters 3 and 4). The distribution of endogenous syntaxin 1a and SNAP-25 upon delivery to the plasma membrane in living cells was investigated using CLSM combined with TIRFM. To analyse SNARE cluster distribution at the plasma membrane of living cells in CLSM images, it was first vital to ensure that I was studying the plasma membrane. A consistent protocol to ascertain the base of the cell was developed. To remove human subjective input a plot was made of the Z-axis profile for each cell, presenting the Z slice number against intensity. The base of a cell was chosen by taking the Z slice at half the maximum intensity as shown in Figure 5.1A and this technique was applied consistently throughout the study.

Subsequently, it was necessary to check if syntaxin 1a and SNAP-25 clustering was visible with endogenous proteins in N2a cells. N2a cells were immunostained with syntaxin 1a monoclonal antibody (clone HPC-1) or SNAP-25 monoclonal antibody (clone SMI81) (Table 2.2) and subsequently labelled with Fab fragment secondary

fluorescent antibodies (see Chapter 2: Materials and Methods). N2a cells were imaged using CLSM and data deconvolution techniques (see Chapter 2: Materials and Methods). As shown in Figure 5.1B endogenous syntaxin 1a labelling was highly concentrated in numerous small spots scattered over the membrane surface, clearly visible in the cropped region of interest. This clustered distribution observed on the plasma membrane in N2a cells agrees with reports on syntaxin clusters in other cell types (Lang et al, 2001; Sieber et al, 2006; Sieber et al, 2007). To compare the clustering of both t-SNAREs, next I analysed the distribution of endogenous SNAP-25 clusters on the plasma membrane. SNAP-25 is anchored to the plasma membrane via a palmitoylated linker region and operates alongside syntaxin 1a in membrane fusion. As shown in Figure 5.1C, the spot staining pattern observed was very similar to that of syntaxin 1a clustering, with numerous brightly fluorescent dots distributed across the plasma membrane surface in N2a cells.

TIRFM was employed to confirm that endogenous t-SNAREs showed clustering at the cell membrane. TIRFM is ideally suited for looking at the plasma membrane as it selectively illuminates and excites fluorophores immediately adjacent to the glass-water interface. TIRFM penetrates to a depth of approximately 150 nm into the sample medium and thus ensures the selective visualisation of the plasma membrane to analyse SNARE clusters (Figure 5.2A). N2a cells were immunostained with syntaxin 1a mouse monoclonal antibody (clone HPC-1) or SNAP-25 mouse monoclonal antibody (clone SMI81) and subsequently labelled with Fab fragment secondary fluorescent antibodies. TIRFM confirmed that both endogenous syntaxin 1a and SNAP-25 displayed clustering across the surface of the plasma membrane (Figure 5.2B). This confirmed that in CLSM studies that to the best of our ability we are looking at the base of the cell. Furthermore, this ensured that future studies incorporating FLIM were viable to examine t-SNARE interactions within the SNARE clusters at the plasma membrane.

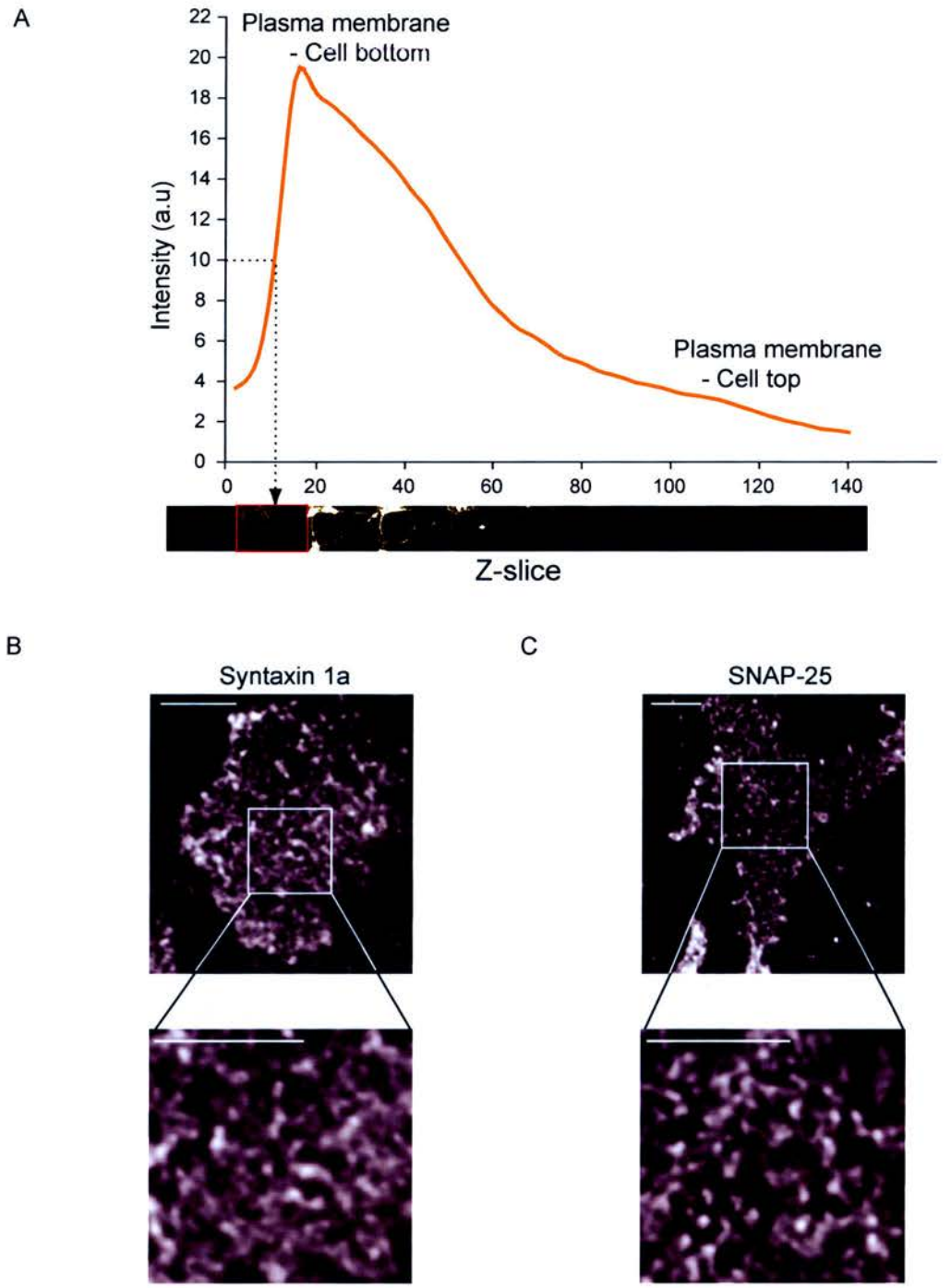

Figure 5.1 Defining the cell base and identifying t-SNARE clusters.
(A) A confocal Z stack plot profile of an N2a cell expressing syntaxin 1a to illustrate the technique used to identify a cell base in this study. A montage of the confocal Z-stack showing every 14th Z-slice is shown below the x axis. A plot of the confocal Z-stack profile was made showing the Z-slice number against intensity. The base of the cell was chosen by taking the slice number at half the maximum intensity and is highlighted by a red rectangle. **(B)** N2a cells were immunostained separately for the endogenous t-SNAREs, syntaxin 1a using a monoclonal antibody (clone HPC-1), and **(C)** SNAP-25 using a monoclonal antibody (clone SMI81), and imaged by CLSM. The boxed regions of interest are shown in the lower panels and illustrate syntaxin 1a and SNAP-25 clusters at the plasma membrane. Scale bars, 5 µm.

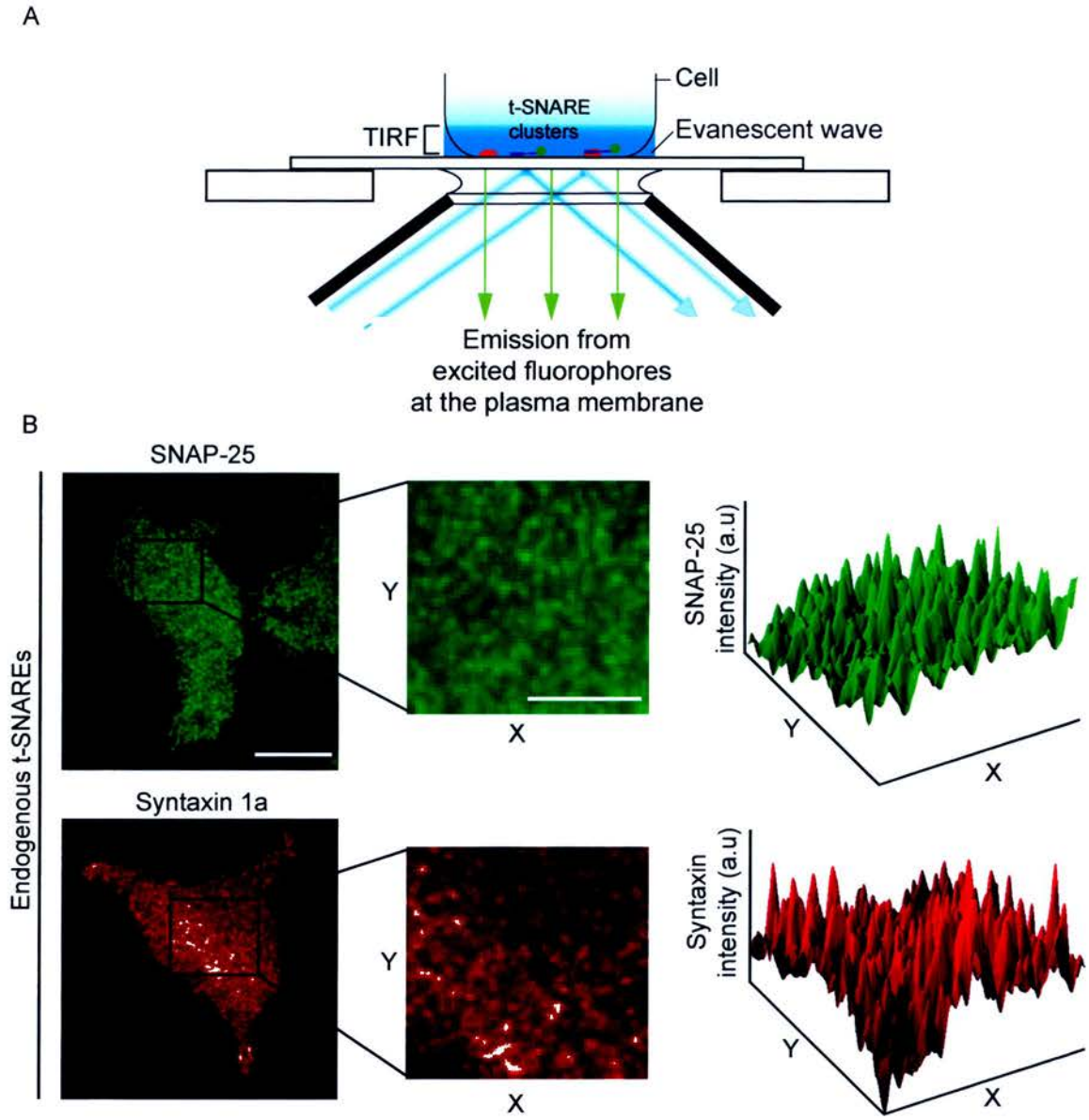

Figure 5.2 Syntaxin 1a and SNAP-25 clusters are visible at the plasma membrane after TIRF microscopy.

(A) Schematic diagram illustrating the visualisation of SNARE clusters using TIRF micrscopy. TIRF microscopy is a near-field imaging approach that selectively illuminates fluorophores immediately adjacent to the glass-water interface. TIRF penetrates to a depth of approximately 150 nm into the sample medium and thus ensures the selective visualisation of SNARE clusters at the plasma membrane. **(B)** N2a cells were immunostained for the endogenous t-SNAREs, syntaxin 1a using a monoclonal antibody (clone HPC-1) and SNAP-25 using a monoclonal antibody (clone SMI81), and imaged by TIRFM. Scale bar, 10 µm. The boxed regions of interest shown in the middle panel illustrate t-SNARE clusters at the plasma membrane. Scale bar, 5 µm. In the right panel the cropped regions of the plasma membrane were plotted as a 3D plot showing the varying intensities of the t-SNAREs at the plasma membrane. Shown are representative images from 10 experiments.

5.3 HETEROLOGOUS SYNTAXIN 1A AND SNAP-25 FORM CLUSTERS AT THE PLASMA MEMBRANE

All subsequent SNARE cluster analysis employed CLSM to permit the use of FLIM to determine SNARE interactions within the independent clusters. It was vital to investigate the expression of heterologous syntaxin 1a and SNAP-25 at the plasma membrane to answer the question of whether fluorescent fusions to the t-SNAREs still exhibit clustering at the cell surface as evident with endogenous t-SNAREs. To investigate this, N2a cells were transfected with mCerulean fused $Syx1a_{1-288}$ and unfused munc18-1 and/or EYFP fused $SNAP\text{-}25A_{1-206}$ and imaged by CLSM (Figure 5.3).

These studies using fluorescent fusions to the t-SNAREs are in agreement with the endogenous cluster studies described previously. Upon close inspection of regions on the plasma membrane, heterologous syntaxin 1a (in the presence of munc18-1) was found to be concentrated in clusters or spots that were similar in appearance to those observed for endogenous syntaxin 1a (Figure 5.3A). In addition, heterologous SNAP-25 also demonstrated a clustered distribution across the plasma membrane as noted previously for endogenous SNAP-25 (Figure 5.3B). If $Syx1a_{1-288}$ (in the presence of munc18-1) and $SNAP\text{-}25A_{1-206}$ were co-expressed in N2a cells, images from the base of the cell revealed that the clustered distribution is unaltered and both t-SNAREs still exist in fluorescent spots on the cell surface (Figure 5.3C). Comparison of endogenous and heterologous t-SNAREs shows that they both exhibit a clustered distribution across the surface of the plasma membrane.

5.4 SYNTAXIN 1A AND SNAP-25 CLUSTERS CO-LOCALISE ON THE PLASMA MEMBRANE

Considering that both endogenous and heterologous syntaxin 1a and SNAP-25 are concentrated in clusters at the plasma membrane as outline above, the next question was whether the t-SNAREs co-localised in these spots. It is thought that membrane fusion is restricted to spatially distinct zones or "hot spots" of the plasma membrane

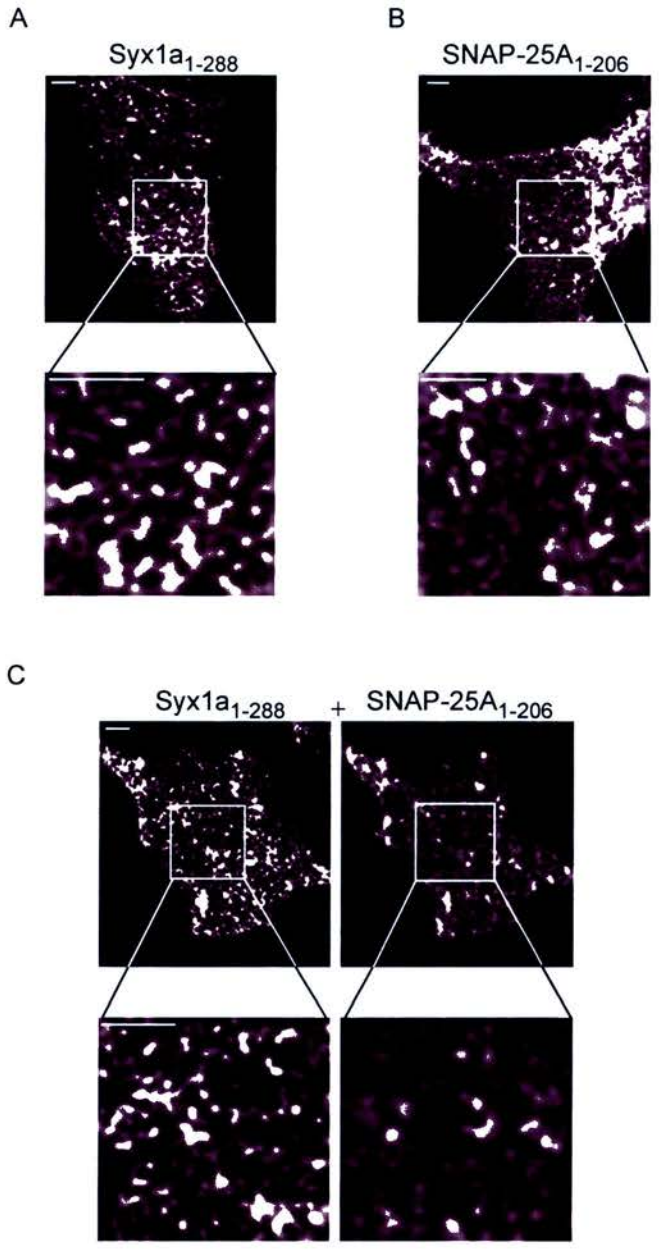

Figure 5.3 Heterologous t-SNAREs are concentrated in clusters at the plasma membrane.

mCerulean-Syx1a$_{1-288}$ (in the presence of munc18-1) and/or EYFP-SNAP-25A$_{1-206}$ were expressed in live N2a cells and imaged by CLSM. **(A)** mCerulean-Syx1a$_{1-288}$ (in the presence of munc18-1) forms clusters at the cell membrane. The boxed region of interest is shown in the lower panel and illustrates syntaxin1a clusters at the plasma membrane. **(B)** EYFP-SNAP-25A$_{1-206}$ forms clusters at the cell membrane. The boxed region of interest is shown in the lower panel and illustrates SNAP-25A clusters at the plasma membrane. **(C)** mCerulean-Syx1a$_{1-288}$ (in the presence of munc18-1) and EYFP-SNAP-25A$_{1-206}$ both form clusters at the cell membrane when co-expressed. Again the boxed regions of interest are shown in the lower panels and illustrate t-SNARE clusters at the plasma membrane. Shown are representative equatorial sections from 10 experiments. All scale bars, 2 µm.

(Bennett et al, 1992; Predescu et al, 2005). Therefore, the uneven clustered distribution of syntaxin 1a and SNAP-25 suggests that fusion sites are confined to those sites containing clusters. As proposed in previous studies, together these proteins form binary complexes at the cell surface (Lang et al, 2002; Rickman et al, 2004), so it seemed plausible that both the t-SNAREs would be distributed in a similar manner at the plasma membrane, providing a sufficient number of pre-assembled clusters at fusion sites. If the t-SNARE binary complexes are pre-assembled at high local concentrations, the subsequent arrival of synaptobrevin to form the ternary SNARE complex would enable rapid membrane fusion at these sites.

Next I examined whether syntaxin 1a and SNAP-25 clusters are co-localised on the plasma membrane in secretory cells. N2a cells were immunostained with syntaxin 1 rabbit polyclonal antibody, and SNAP-25 mouse monoclonal antibody (clone SMI81) and subsequent labelling with Fab fragment secondary fluorescent antibodies (see Chapter 2: Materials and Methods) and imaged by CLSM. Wild-type mCerulean-fused $Syx1a_{1\text{-}288}$ and EYFP-fused $SNAP\text{-}25A_{1\text{-}206}$ in the presence of munc18-1 were also co-expressed in live N2a cells and imaged by CLSM.

To quantify the co-localisation between syntaxin 1a and SNAP-25 I employed quantitative co-localisation analysis (see Chapter 2: Materials and Methods). Notably, there was a high degree of co-localisation and covariance observed between syntaxin 1a and SNAP-25 for endogenous and heterologous proteins (Figure 5.4A). Covariance data were quantified for endogenous and heterologous t-SNAREs in N2a cells and expressed as Pearson's correlation coefficient (R) and Mander's overlap coefficient (r) values (Figures 5.4B and 5.4C). Pearson's correlation coefficient was used as the intensities of the heterologous proteins would be expected to be dependent upon each other. In addition, Mander's overlap coefficient was employed as the relative intensities of the endogenous proteins would not be expected to be dependent upon each other due to concentration differences from antibody staining.

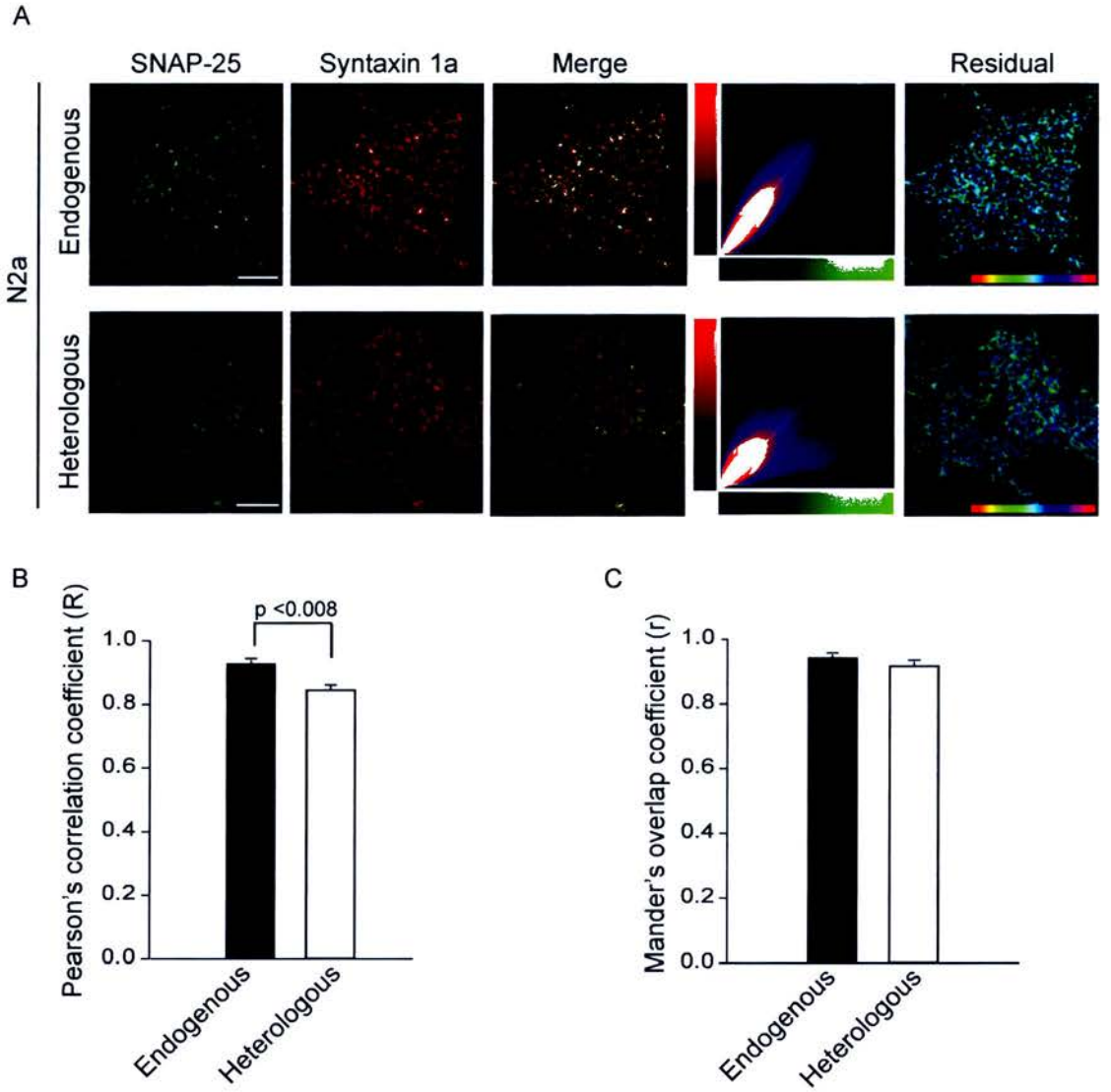

Figure 5.4 Endogenous and heterologous t-SNAREs co-localise on the plasma membrane.

(A) N2a cells were immunostained for the endogenous t-SNAREs, SNAP-25 (green) using a monoclonal antibody (clone SMI81) and syntaxin (red) using anti-syntaxin rabbit and imaged by CLSM. Scale bar, 5 µm. Wild-type EYFP-SNAP-25$A_{1\text{-}206}$ (green) and mCerulean-Syntaxin1$a_{1\text{-}288}$ (red) in the presence of munc18-1 were co-expressed in N2a cells and imaged by CLSM. Scale bar, 5 µm.The merged image shows areas of coincidence in yellow hues. The two dimensional histogram represents the intensity of each channel in each voxel, with a colour scale representing frequency. The residual map corresponds to weighted residuals from the linear regression of the histogram, thus indicating fluorescent channel covariance. The hue is from -1 to 1, with cyan corresponding to a zero residual and perfect covariance. Covariance data were quantified for endogenous and heterologous t-SNAREs in N2a cells and expressed as Pearson's correlation coefficient values (R), **(B)**, or Mander's overlap coefficient (r), **(C)**. These data show that both endogenous and heterologous t-SNARE clusters show high levels of co-localisation. There is a significant difference between the quantitative Pearson's correlation values (Mann Whitney Rank Sum test, $p < 0.008$), yet both show high levels of co-localisation. There is no significant difference between the quantitative Mander's co-localisation values for both (Mann Whitney Rank Sum test). Data shown as mean ± SEM, n ≥6 experiments.

Evidently, there were high levels of correlation and overlap between the t-SNAREs for both endogenous and heterologous proteins. Quantitative co-localisation analyses revealed a high degree of positive correlation between the endogenous syntaxin 1a and SNAP-25 ($R = 0.93 \pm 0.008$, mean ± SEM; $n = 6$) and heterologous syntaxin 1a and SNAP-25 ($R = 0.85 \pm 0.017$, mean ± SEM; $n = 7$) proteins. Although a significant difference was observed between the correlation values for endogenous and heterologous proteins (Mann Whitney Rank Sum test, $p < 0.008$), the most important point to note is that high levels of correlation were evident for both endogenous and heterologous t-SNAREs compared to the non co-localisation control shown in Figure 6.4. No significant difference was observed for Mander's overlap coefficient, with both endogenous ($r = 0.94 \pm 0.007$, mean ± SEM; $n = 6$) and heterologous ($r = 0.92 \pm 0.011$, mean ± SEM; $n = 7$) t-SNAREs revealing identical overlap coefficient values. The observations for endogenous t-SNAREs coincided with those for heterologous t-SNAREs, and there was no visible difference with both revealing high levels of co-localisation and covariance between syntaxin 1a and SNAP-25.

5.5 Syntaxin 1a and SNAP-25 cluster FWHM analysis in neuroendocrine cells

Having detected no apparent difference between endogenous and heterologous syntaxin 1a and SNAP-25 co-localisation, I next assessed whether there was a difference in the full width half maximum (FWHM) size (see Chapter 2: Materials and Methods) of the t-SNARE clusters at the plasma membrane. FWHM is a standard method for defining spot or cluster size as it does not require definition of the cluster edge. Previous studies have noted a varying assortment of t-SNARE cluster sizes, ranging from 60-750 nm in size, depending on the imaging approach employed (Lang et al, 2001; Predescu et al, 2005; Rickman et al, 2004; Sieber et al, 2007). The highest resolution light microscopy approach available, STED (lateral resolution 50 nm) has reported an average size of 60 nm FWHM (Sieber et al, 2007), yet immuno-electron microscopy has reported SNARE clusters of up to 400 nm

(Lang et al, 2001). Interestingly, many of these studies used inside-out sheets of lysed plasma membrane (Lang et al, 2001; Predescu et al, 2005; Taverna et al, 2007). Instead, I have applied my analysis to live N2a cells to investigate the size of endogenous and heterologous t-SNARE clusters.

N2a cells were immunostained with syntaxin 1 rabbit polyclonal antibody, and SNAP-25 mouse monoclonal antibody (clone SMI81) and labelled with fluorescent secondary antibodies or Fab fragment versions for imaging by CLSM. Wild-type mCerulean-fused $Syx_{1\text{-}288}$ and EYFP-fused $SNAP\text{-}25A_{1\text{-}206}$ in the presence of munc18-1 were also co-expressed in live N2a cells and imaged by CLSM. In order to examine the size of endogenous and heterologous syntaxin 1a and SNAP-25 clusters at the cell surface, the base of each cell was first selected as shown in Figure 5.1A. To assist in identifying individual clusters at the base of the cell, the image was converted into false colour, with colour representing intensity. Using Image J software, two perpendicular lines were drawn through the centre of a cluster ensuring that they bisect the brightest area of fluorescence as shown in Figure 5.5A and the profiles plotted. To quantify the FWHM (the distance at the half maximal point) of an individual cluster, the intensity profile along a row of pixels centred on the cluster was used. The pixel intensity along the line bisecting the brightest fluorescence of the cluster was plotted. Figure 5.5B illustrates the application of Gaussian statistics to calculate the FWHM as this is directly proportional to the standard deviation (σ). The FWHM for each cluster was calculated by multiplying the standard deviation of the individual cluster value (determined from the Gaussian fit of the line plot) by 2.35, thereby yielding a FWHM value per cluster. For both heterologous syntaxin 1a and SNAP-25 channels, cluster FWHM size was measured for 100 clusters, from 5 images, and 20 clusters per cell. For both endogenous syntaxin and SNAP-25 channels, cluster FWHM size was measured for 60 clusters, from 3 images, and 20 clusters per cell.

The FWHM measurements of endogenous and heterologous syntaxin 1a and SNAP-25 clusters are shown in Table 5.1. To exclude the possibility of cross linking between antibodies affecting the FWHM, a Fab fragment secondary fluorescent

antibody was employed in addition to the full secondary fluorescent antibody for immunofluorescence studies.

Table 5.1 FWHM sizes of endogenous and heterologous syntaxin 1a and SNAP-25 clusters.

	Endogenous clusters Mean FWHM (nm) ± SEM		Heterologous clusters Mean FWHM (nm) ± SEM
	anti*	anti (Fab)**	
Syntaxin	511 ± 8	313 ± 5	259 ± 5
SNAP-25	623 ± 11	322 ± 5	366 ± 9

* Secondary antibody
** Secondary antibody (Fab fragment)

In N2a cells, endogenous syntaxin clusters were ~313-511 nm in size and SNAP-25 clusters were ~322-623 nm in size. These conflicting data were observed for endogenous syntaxin 1a and SNAP-25 clusters in N2a cells based on the secondary antibody employed. Immunofluorescent staining using a full secondary antibody revealed significantly larger syntaxin 1a clusters (~511 nm) and SNAP-25 clusters (~623 nm) than those obtained for the Fab fragment secondary antibody (Mann Whitney Rank Sum test, $p < 0.001$). Cross-linking of the full secondary antibodies may explain why these FWHM sizes were approximately double those obtained for endogenous t-SNARE clusters using Fab fragment antibodies. For this reason, I chose to focus on the endogenous data obtained using Fab fragment antibodies. Statistical analysis revealed that heterologous syntaxin 1a cluster sizes were significantly smaller than endogenous (Fab fragment) syntaxin clusters (Mann Whitney Rank Sum test, $p < 0.001$). However, for SNAP-25 cluster FWHM sizes, heterologous SNAP-25 cluster sizes were significantly larger than endogenous (Fab fragment) SNAP-25 cluster sizes (Mann Whitney Rank Sum test, $p < 0.001$).

To further investigate the varying FWHM sizes obtained for each data set, the syntaxin 1a FWHM size from 100 clusters from 5 images of N2a cells expressing $Syx1a_{1\text{-}288}$ and $SNAP\text{-}25A_{1\text{-}206}$ were plotted as a histogram of cluster sizes. The FWHM sizes were fit with a single Gaussian distribution ($R^2 = 0.7713$) or the sum of two Gaussians ($R^2 = 0.8365$) (Figure 5.5C). The syntaxin 1a FWHM sizes were better fit to two populations suggesting that a wide distribution of t-SNARE clusters were measured. To investigate the possibility that the FWHM cluster size measured

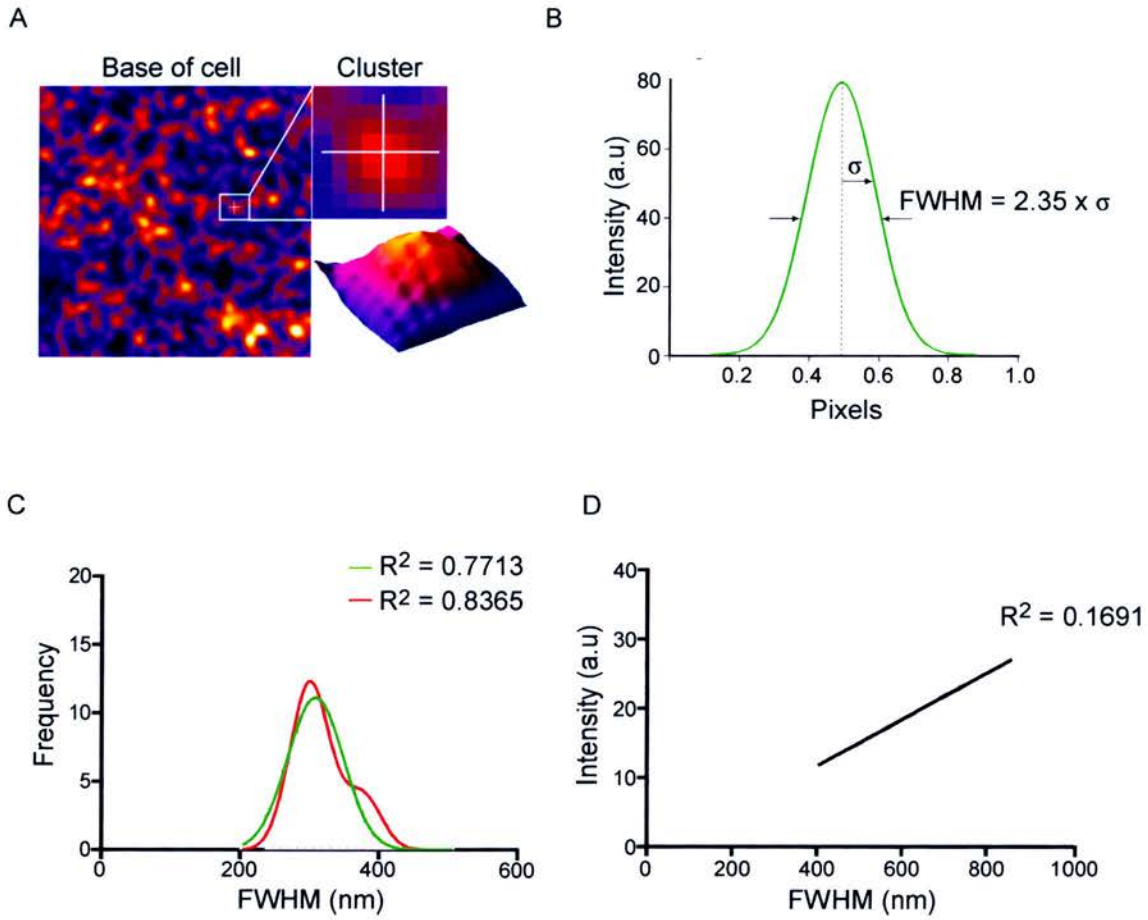

Figure 5.5 t-SNARE cluster FWHM analysis in neuroendocrine cells.
(A) The base of an N2a cell in false colour to illustrate FWHM measurements showing a cluster as a cropped region of interest. Two lines were drawn through the centre and brightest part of a cluster and the profiles plotted using Image J software. An interactive 3D plot of a cluster spot (bottom right panel). **(B)** To quantify the FWHM (the distance at the half maximum point), the intensity profile along a row of pixels centred on a cluster was used. The pixel intensity along a line bisecting the brightest fluorescence of the cluster was plotted using Image J software. Using Gaussian statistics, the FWHM can be calculated as it is directly proportional to the standard deviation (σ). **(C)** FWHM size was measured for 100 clusters from 5 images of N2a cells co-expressing $Syx1a_{1-288}$ and $SNAP\text{-}25A_{1-206}$ and a histogram was plotted for syntaxin 1a clusters. Histogram values were fit with a single Gaussian distribution or the sum of two gaussians. The FWHM distribution of syntaxin 1a cluster sizes is fit better to two populations. **(D)** SNAP-25 cluster FWHM size was plotted against intensity for 60 clusters from 3 images of N2a cells immunostained for SNAP-25 using a monoclonal antibody (clone SMI81) and syntaxin 1a using anti-syntaxin rabbit. These data were fit with a linear regression. There is a weak relationship between the FWHM size and the intensity of the clusters. There are discrepancies with these FWHM measurements as the cluster sizes are below the resolution of the microscope.

was related to the intensity of the cluster, I plotted SNAP-25 cluster FWHM size against intensity for 60 clusters from 3 images of N2a cells immunostained for SNAP-25 using a monoclonal antibody (clone SMI81) and syntaxin 1a using a syntaxin 1 rabbit antibody. These data were fit with a linear regression (Figure 5.5D). These findings indicated that there was a very weak relationship between the FWHM size and the intensity of the clusters ($R^2 = 0.1691$). Together, these findings confirm that numerous discrepancies may exist between the FWHM measurements for both endogenous and heterologous t-SNARE clusters. The FWHM measurements obtained are at the resolution of our microscope system (maximally 178 nm). However, what is clear from these results is that both endogenous and heterologous syntaxin 1a and SNAP-25 are organised in clusters at the cell surface and furthermore the t-SNARE clusters show high levels of co-localisation at the plasma membrane.

5.6 Conclusion

We know that once syntaxin 1a has trafficked through intracellular membrane systems it remains inactive bound to munc18-1 in its closed form, and SNAP-25 can traffic independently to the plasma membrane. The findings presented in this study demonstrate that upon delivery to the plasma membrane both syntaxin 1a and SNAP-25 reside in clusters at the cell surface in agreement with previous studies (Lang et al, 2001; Predescu et al, 2005; Rickman et al, 2004; Sieber et al, 2007). Standard CLSM and TIRFM confirmed that both endogenous and heterologous syntaxin and SNAP-25 proteins were distributed in clusters across the cell surface and no visible difference between the t-SNARE clusters was identified. Furthermore, quantitative co-localisation analysis indicated that both endogenous and heterologous syntaxin 1a and SNAP-25 clusters showed considerably high levels of co-localisation at the plasma membrane. Importantly, the similarities detected between endogenous and heterologous t-SNARE clusters confirmed that it was acceptable to proceed with heterologous studies to analyse FRET and FLIM within the individual t-SNARE clusters.

Other studies have reported cluster sizes ranging from 200-300 nm in PC12 cells and MIN6 cells or ~700 nm in chromaffin cells (Lang et al, 2001; Ohara-Imaizumi et al, 2004c; Rickman et al, 2004). These studies all determined the FWHM size from immunostained images; however, there does not seem to be good agreement between all these studies despite the use of similar protocols. Furthermore, the present study adds to the confusion over the exact size of t-SNARE clusters at the plasma membrane of live cells. It is evident that the FWHM cluster size is dependent upon the t-SNARE labelling protocol, the imaging approach applied, the intensity of the clusters and additionally the cluster identification technique. The t-SNARE FWHM cluster sizes presented in this study are at the resolution of our microscope system (maximally 178 nm), and therefore it is not possible to exclude the possibility that groups of clusters are being detected instead of individual clusters. These findings confirm that both endogenous and heterologous syntaxin 1a and SNAP-25 are distributed in overlapping clusters at the plasma membrane in agreement with previous studies.

Sieber and co-workers have provided comprehensive evidence for t-SNARE cluster size, reporting an average size of 60 nm FWHM for syntaxin 1 using STED microscopy of fixed membrane sheets (Sieber et al, 2007). Furthermore, syntaxin clusters were demonstrated to be dynamic, containing a modelled 75 "open" syntaxin molecules tightly packed in a bunch-like structure (Sieber et al, 2007). It is not possible to reach the resolution possible of STED microscopy using live cell imaging approaches, so I decided instead to examine the molecular interactions between the t-SNARE proteins within individual spots on the cell surface. I would expect that a distribution of t-SNARE clusters at these plasma membrane sites may potentially include a mixture of monomers, dimers and multimers. Given that syntaxin 1a and SNAP-25 have a high affinity for one another, and co-localise at the plasma membrane, it may be likely that the syntaxin 1a and SNAP-25 clusters observed in neuroendocrine cells are composed of pre-assembled t-SNARE dimers that remain inactive until required for membrane fusion.

CHAPTER SIX:

FACTORS AFFECTING t-SNARE CLUSTER ORGANISATION AT THE PLASMA MEMBRANE

6.1 INTRODUCTION

The cell surface is a crowded place where numerous biological activities occur simultaneously. For fast and efficient processing, it is envisaged that necessary factors are enriched in specialised "hot spots" on the plasma membrane. It is, therefore, not surprising that both syntaxin 1a and SNAP-25 show a clustered distribution at discrete areas across the cell surface. In recent years there has been considerable interest in the mechanisms which define t-SNARE micro-patterning at the plasma membrane (Lang et al., 2001; Ohara-Imaizumi et al., 2004b; Sieber et al., 2007). It has been well established that the t-SNAREs are concentrated in clusters in or on the plasma membrane and these clusters have been shown to define docking and fusion sites for secretory vesicles (Lang et al., 2001; Ohara-Imaizumi et al., 2004a; Predescu et al., 2005; Sieber et al., 2007).

In previous studies, it has been proposed that t-SNARE clusters are organised at the plasma membrane by cholesterol and thereby dependent on cholesterol for their integrity (Lang et al., 2001; Predescu et al., 2005). Using microscopic studies, varying degrees of t-SNARE distribution changes have been observed following cholesterol depletion, ranging from moderate (Lang et al., 2001; Predescu et al., 2005) to complete disintegration of t-SNARE domains (Chamberlain and Gould, 2002; Lang et al., 2001), leading to the suggestion that membrane lipids are essential for micro-domain formation and thus play an important role in t-SNARE cluster integrity. Cholesterol in part defines the lipid order of a membrane and this has strengthened the hypothesis that these clusters may be maintained in membrane "rafts" (Chamberlain et al., 2001) or cholesterol-rich micro-domains (Lang et al., 2001). However, in contrast, other *in vitro* assays have reported that the SNARE proteins syntaxin 1a and synaptobrevin have a preference for lipid disorder over ordered domains (Bacia et al., 2004), something at odds with biochemical data (Salaun et al., 2005a; Salaun et al., 2005b). However, together these observations do not necessarily mean that lipids alone are sufficient for SNARE protein membrane patterning as the lipid preference of palmitoylated SNAP-25 has not been assessed. For instance, the multitude of proteins at the cell surface may be inserted into

specific lipid micro-domains at the plasma membrane at the start of membrane patterning, yet protein-protein interactions may eventually refine this process.

In this study, I have investigated the spatial regulation of t-SNARE heterodimer interactions in intact biological membranes and how cholesterol depletion and lipid order affect the targeting or localisation of the t-SNARE proteins. It is also not clear if every t-SNARE cluster is fusion competent and if the t-SNAREs are active before fusion occurs. In this analysis I have concentrated on the t-SNAREs, syntaxin 1a and SNAP-25 that co-localise at the plasma membrane, and present evidence to show that t-SNARE cluster stability is regulated by two distinct factors: protein-protein interactions and membrane lipid order. I demonstrate that t-SNARE clusters are heterogeneous in their interaction status and that different heterodimer complexes co-exist within clusters in living cell membranes. Given that syntaxin and SNAP-25 have a high affinity for one another, and co-localise at the plasma membrane, these findings indicate that some syntaxin 1a and SNAP-25 clusters observed in neuroendocrine cells are composed of pre-assembled t-SNARE dimers, and furthermore that some clusters may support membrane fusion better than others.

6.2 METHYL-β-CYCLODEXTRIN AS AN EFFECTIVE TOOL FOR THE DEPLETION OF MEMBRANE CHOLESTEROL

To examine the role of cholesterol in SNARE cluster integrity in living cells, methyl-β-cyclodextrin (MβCD) was used throughout this study. Cyclodextrins possess an oligomeric ring of glucose that is able to sequester cholesterol within its hydrophobic core, forming an inclusion compound that is soluble in water (Kilsdonk et al., 1995; Pitha et al., 1988). Therefore, MβCD acts by pulling cholesterol out of the membrane and making it soluble in the surrounding aqueous environment. This reagent has been used extensively to study the role of membrane cholesterol in diverse cellular processes (Chamberlain et al., 2001; Kilsdonk et al., 1995; Lang et al., 2001). Several previous

studies have suggested that the clustering of syntaxin 1a is dependent on cholesterol and SNARE cluster dispersal is visible upon cholesterol depletion by MβCD (Lang et al., 2001; Ohara-Imaizumi et al., 2004a).

It was vital to confirm that MβCD did in fact effectively deplete cholesterol from the N2a cell membrane, and to ensure that the correct levels of MβCD were employed to prevent cell toxicity. It has been reported that 10 mM MβCD causes a reduction of ~21% in the mean intensity of staining of the cholesterol binding agent filipin in N2a cells (Brechin, 2007) and removed ~20% of the cholesterol from synaptosomes (Taverna et al., 2004). Yet, in PC12 cells 15 mM MβCD has been shown to deplete ~40% of cellular cholesterol (Lang et al., 2001). In this study N2a cells were plated on poly-D-lysine coated coverslips (Chapter 2: Materials and Methods) 24 hours prior to imaging by CLSM. N2a cells were treated with 10 or 20 mM MβCD (Chapter 2: Materials and Methods) for 30 minutes at 37 °C before being incubated for 5 minutes with fluorescent markers of cell viability, calcein and propidium iodide, each at a final concentration of 3 μM (Chapter 2: Materials and Methods).

Surprisingly, both $Syx1a_{1-288}$ and $SNAP\text{-}25A_{1-206}$ were punctate on the plasma membrane in the presence and absence of 10 mM MβCD indicating that MβCD appeared to have no effect on t-SNARE clustering at the cell surface (Figure 6.1A). However, previous studies, as discussed above, have shown that 10 mM or 15 mM MβCD was sufficient to significantly reduce cholesterol. To investigate the possibility of increasing MβCD levels, the effects of varying concentrations of MβCD on cell viability was examined by calculating the percentage of dead cells in a field of view ($n = 6$ fields of view and ~100 cells per field of view) using Volocity software (Figure 6.1B). The cell viability assay showed that whilst 10 mM MβCD did not significantly decrease cell viability, compared with the untreated control, 20 mM MβCD significantly reduced cell viability (t-test, $p < 0.001$, $n = 6$). In a field of view, 14.7 ± 3 % of cells were dead after a 30 minute treatment with 20 mM MβCD, compared with 1.1 ± 0.3 % in the absence of MβCD. Importantly, it must be noted that at concentrations higher than 10 mM MβCD

cell morphology was noticeably altered, and for this reason I employed MβCD at the sub-lethal concentration of 10 mM MβCD throughout this study.

6.3 CHOLESTEROL DEPLETION DISRUPTS MEMBRANE LIPID ORDER

As cholesterol is proposed to play a role in ordering the membrane lipid phase, the functional significance of cholesterol depletion on the plasma membrane of N2a cells was investigated. For this analysis, the fluorescent probe Laurdan was employed. In the context of this study, Laurdan's most important trait is that its emission spectrum depends on the polarity and the phase state of the phospholipid bilayer (Parasassi et al., 1994a; Parasassi et al., 1994b) and it can therefore be used to detect changes in lipid order in living membranes. The fluorescence emission reports changes in the packing of surrounding lipids as a spectral shift (Parasassi et al., 1997). These spectral shifts in the fluorescence emission of Laurdan can be quantified by calculating the generalised polarisation values (GP) (Gaus et al., 2003; Parasassi et al., 1990). It is known that the GP value decreases when water penetration into the lipid bilayer increases and thus the surrounding lipids are disordered (Parasassi et al., 1994a). Therefore, in this study, Laurdan proved a useful tool to monitor and report changes in the lipid order in living membranes and was used to observe the affect of 10 mM MβCD on the lipid order in live N2a cells.

To visualise lipid order, N2a cells were plated on poly-D-lysine coated coverslips (see Chapter 2: Materials and Methods) for 24 hours and incubated with 5 μM Laurdan for one hour prior to imaging to enable the Laurdan to spread throughout the entire cell (see Chapter 2: Materials and Methods). Before imaging, the cells were incubated at 37 °C in the presence or absence of 10 mM MβCD (see Chapter 2: Materials and Methods). Generalised polarisation (GP) values for each pixel in the image were calculated (see Chapter 2: Materials and Methods). Figure 6.1C shows that this approach revealed two different lipid populations in living N2a cells, with distinct GP values. The higher the

GP value is, the more ordered the surrounding lipids (Gaus et al., 2003). Figure 6.1C shows that for an untreated N2a cell, two distinct GP populations were identified. The plasma membrane, which is rich in cholesterol, was found to be more ordered than intracellular membranes, in agreement with previous studies of diverse cell types (Gaus et al., 2005; Gaus et al., 2003; Gaus et al., 2006; Vieira et al., 2006). Interestingly, the GP frequency histogram of N2a cells before and after treatment with MβCD demonstrated that in the presence of MβCD the ordered GP population previously detected in the plasma membrane was completely abolished (Figure 6.1C right panel), whilst maintaining cell viability. Therefore, Laurdan proved a useful tool to directly report changes in lipid order and cholesterol depletion demonstrating that relatively low levels of MβCD have a direct effect on the lipid order of a living membrane.

6.4 SNAP-25 [G43D] HAS A WEAKENED BINDING AFFINITY FOR SYNTAXIN 1A

Next I chose to examine if cholesterol depletion coupled with a disruption of the lipid order of the plasma membrane played a role in regulating syntaxin 1a and SNAP-25 clusters at the plasma membrane. To investigate the effect of cholesterol depletion and the possibility of disrupting the SNAP-25 and syntaxin 1a interaction on t-SNARE cluster integrity, I employed SNAP-25A $[G43D]_{1\text{-}206}$ alongside wild-type $SNAP\text{-}25A_{1\text{-}206}$. This mutation was originally identified at the homologous position in the yeast *sec*9 protein, resulting in a temperature-dependent loss of the functional phenotype (Brennwald et al., 1994). The N-terminus of SNAP-25 was also found not to enter into complexes with syntaxin 1a *in vitro* if this mutation was introduced (Fasshauer et al., 1997), and subsequently it was reported that SNAP-25 does not interact with syntaxin 1a in cells in the presence of this mutation (Loranger and Linder, 2002). Furthermore, this mutant has also been used previously to suggest the existence of alternative SNARE complex formations (An and Almers, 2004). This is a SNAP-25 SN1 point mutation in which a glycine amino acid at position 43 has been switched to an aspartic acid residue. The position of the SNAP-25 SN1 point mutation G43D on the ternary SNARE complex

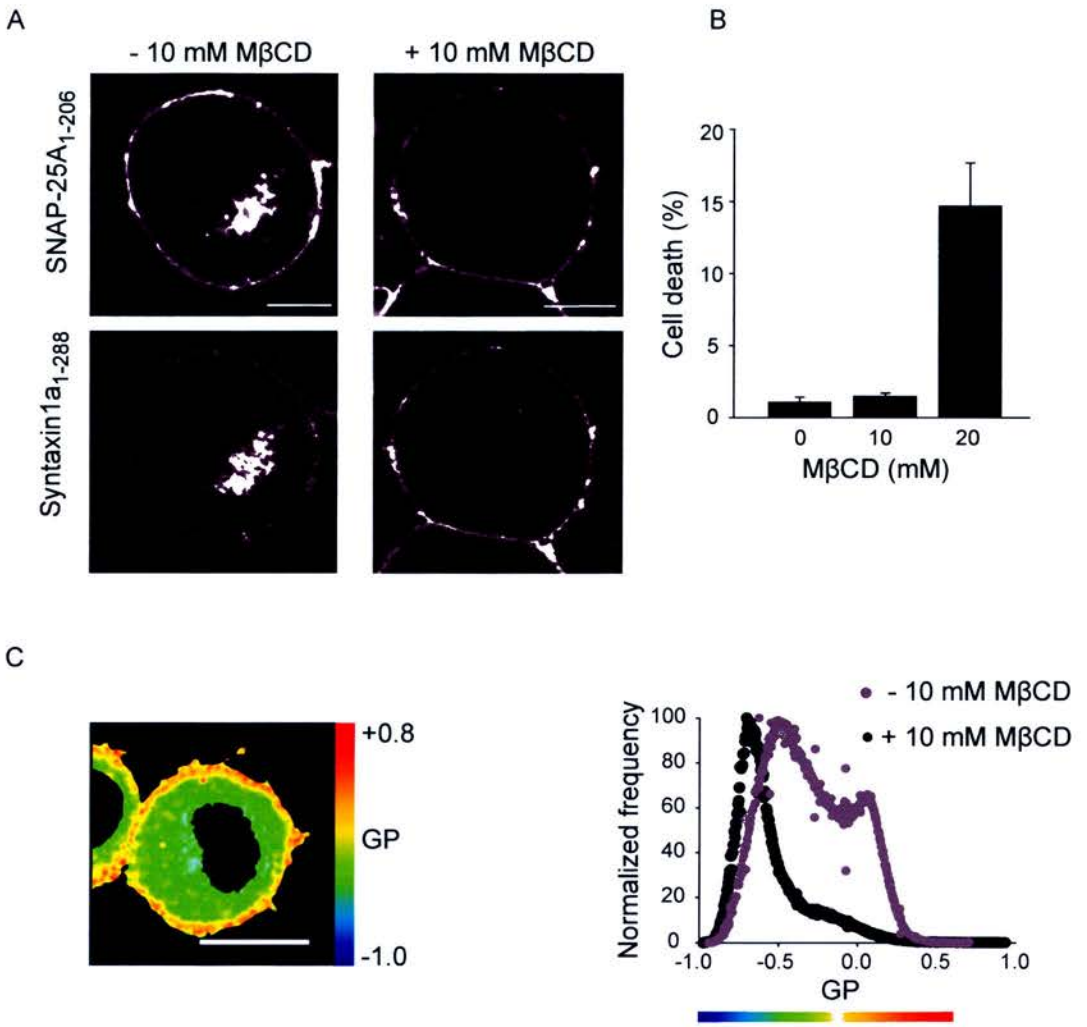

Figure 6.1 Methyl-β-cyclodextrin as a tool for cholesterol depletion.
(A) mCerulean-Syx1a$_{1-288}$, EYFP-SNAP-25A$_{1-206}$ and munc18-1 were co-expressed in live N2a cells and incubated in the presence or absence of 10 mM MβCD for 30 mins and imaged by CLSM. MβCD appears to have no effect on t-SNARE clustering as both Syx1a$_{1-288}$ and SNAP-25A$_{1-206}$ are punctate on the plasma membrane in the presence and absence of Mβ CD. Scale bar, 5 μm. **(B)** N2a cells were treated with varying concentrations of MβCD for 30 mins and then incubated with fluorescent markers of cell viability, calcein and propidium ioidide. The percentage of dead cells calculated in a field of view. Mean values ± SEM, n = 15 presented. **(C)** N2a cells incubated in the presence or absence of 10 mM MβCD for 30 mins after staining with laurdan. Generalised polarisation (GP) values were calculated for each pixel in the image. An untreated N2a cell coloured according to GP values, orange = high GP (more ordered), green = low GP (more disordered). GP values plotted as a frequency distribution histogram (• untreated, • MβCD treated). Scale bar, 5 μm.

is shown in Figure 6.2A. However, it must be noted that previous studies have used the isolated first helix of SNAP-25 (amino acids 1-90) containing the G43D mutation, thereby missing both the palmitoylated linker region and the second SNARE helix (Fasshauer et al., 1997). In our study, we have employed live N2a cells expressing full length SNAP-25A $[G43D]_{1\text{-}206}$.

The G43D mutation was generated by site-directed mutagenesis using a QuikChange II XL kit (see Chapter 2: Materials and Methods). Utilising pEYFP-C2-$SNAP25A_{1\text{-}206}$ the glycine amino acid at position 43 was switched to an aspartic acid residue (G43D) that is thought to change the overall interaction of SNAP-25 with its cognate partner syntaxin 1a. Standard PCR and molecular techniques were employed using the following primers (see Chapter 2: Materials and Methods): 5' –GAA GAG AGT AAA GAT GCT GAT ATC AGG ACT TTG GTT ATG- 3' and 5' –CAT AAC CAA AGT CCT GAT ATC AGC ATC TTT ACT CTC TTC- 3'. Throughout this study the naming system SNAP25A $[G43D]_{1\text{-}206}$ was adopted for this plasmid construct. The plasmid construct map is shown in Appendix 1.

To confirm that SNAP-25A $[G43D]_{1\text{-}206}$ was unable to interact with syntaxin 1a as previously reported (Fasshauer et al., 1997; Loranger and Linder, 2002), I performed saturation binding assays with syntaxin 1a and both the wild-type or mutant SNAP-25 (see Chapter 2: Materials and Methods). $Syx1a_{1\text{-}288}$ was immobilised on glutathione sepharose beads and incubated with purified His_6-tagged $SNAP\text{-}25A_{1\text{-}206}$ and SNAP-25A $[G43D]_{1\text{-}206}$ in a total volume of 50 µl of buffer A (see Chapter 2: Materials and Methods). Following standard washes of the beads to remove unbound protein (see Chapter 2: Materials and Methods), bound protein was eluted in SDS-containing sample buffer followed by SDS-PAGE and Coomassie Blue staining (see Chapter 2: Materials and Methods). Surprisingly, both $SNAP\text{-}25A_{1\text{-}206}$ and SNAP-25A $[G43D]_{1\text{-}206}$ proteins readily bound to the cytoplasmic domain of syntaxin 1a (Figure 6.2B). Importantly, the G43D mutation had no effect on the ability of SNAP-25 to bind to syntaxin 1a and demonstrated similar levels of binding to those observed for wild-type SNAP-25.

Saturation binding indicated no difference between the interaction of wild-type SNAP-25A$_{1\text{-}206}$ and SNAP-25A [G43D]$_{1\text{-}206}$ with syntaxin 1a. However, as binding reactions are largely dependent on the relative concentrations of the proteins involved, to further characterise the syntaxin 1a/SNAP-25A [G43D]$_{1\text{-}206}$ interaction, the equilibrium dissociation constant (K_d) was measured (Figure 6.2C). To calculate the binding affinities of SNAP-25A$_{1\text{-}206}$ or SNAP-25A [G43D]$_{1\text{-}206}$ for syntaxin 1a, the concentration of syntaxin 1a was kept constant while the concentration of the other partner, wild-type SNAP-25A$_{1\text{-}206}$ or SNAP-25A [G43D]$_{1\text{-}206}$ was varied. The approach taken was to use syntaxin 1a immobilised on glutathione sepharose beads and to incubate this in the presence of increasing concentrations of purified His$_6$-tagged SNAP-25A$_{1\text{-}206}$ or SNAP-25A [G43D]$_{1\text{-}206}$ for 2 hours at 21 °C (see Chapter 2: Materials and Methods). Following standard washes of the beads to remove unbound protein, bound material was analysed using SDS-PAGE, and subsequent western immunoblotting using a mouse monoclonal SNAP-25 antibody (clone SMI81) (Table 2.4) and enhanced chemiluminescence. Luminescence data was quantified using a cooled CCD camera and these data fit with a variable slope dose response relationship yielding a dissociation constant (K_d) for each set of data (Figure 6.2C). Measurement of the equilibrium dissociation constant for the syntaxin 1a-SNAP-25 complex revealed that SNAP-25A [G43D]$_{1\text{-}206}$ had an increased K_d for syntaxin 1a (K_d = 14.3 μM) when compared with SNAP25A$_{1\text{-}206}$ (K_d = 1 μM). This *in vitro* data shows SNAP-25A [G43D]$_{1\text{-}206}$ can indeed interact with syntaxin 1a but with a reduced affinity. Despite the presence of the G43D mutation, it is possible that the t-SNARE helix can still continue to form around the mutation yet a weakened interaction ensues.

Furthermore, I wanted to examine if SNAP25A [G43D]$_{1\text{-}206}$ was capable of binding to other proteins at similar levels as wild-type SNAP-25 in freshly prepared rat brain lysates. The next step was to determine the ability of SNAP-25A$_{1\text{-}206}$ and SNAP-25A [G43D]$_{1\text{-}206}$ to bind to syntaxin 1a, synaptobrevin and complexin (known to bind to the ternary SNARE complex) in rat brain lysates. Rat brain lysates were prepared as

described in Chapter 2: Materials and Methods. Both SNAP-25A$_{1-206}$ and SNAP-25A [G43D]$_{1-206}$ were immobilised on glutathione sepharose beads and incubated with 1 ml of rat brain lysate for 1 hour at 4 °C. As a control, glutathione sepharose beads alone were incubated with 1 ml of rat brain lysate. The beads were washed with buffer A (see Chapter 2: Materials and Methods) by low speed centrifugation and bound proteins were analysed by SDS-PAGE (see Chapter 2: Materials and Methods) and western immunoblotting (see Chapter 2: Materials and Methods) using a monoclonal syntaxin 1a antibody (clone HPC-1), a monoclonal synaptobrevin antibody (clone 69.1) or a rabbit complexin antibody (SySy) (Table 2.4). Figure 6.2D shows that both SNAP-25A$_{1-206}$ and SNAP-25A [G43D]$_{1-206}$ readily bound to syntaxin 1a, synaptobrevin and complexin from rat brain lysates. Quantification studies revealed that there was no significant difference between SNAP-25A$_{1-206}$ and SNAP-25A [G43D]$_{1-206}$ binding to syntaxin 1a and complexin. This suggests that syntaxin 1a and SNAP-25 can still form the binary complex even in the presence of the G43D mutation. However, quantification of wild-type SNAP-25A$_{1-206}$ and SNAP-25A [G43D]$_{1-206}$ binding to synaptobrevin revealed that SNAP25A [G43D]$_{1-206}$ was seen to bind to synaptobrevin at significantly lower levels (-71% ± 12.07%, mean ± SEM; n = 3, t-test, $p < 0.030$) when compared to wild-type SNAP-25A$_{1-206}$ (Figure 6.2D). It would appear that SNAP-25A [G43D]$_{1-206}$ is able to form the binary complex with syntaxin 1a, yet the formation of the ternary complex with synaptobrevin is significantly weakened by the presence of the G43D mutation.

6.5 SNAP-25 AND SYNTAXIN 1A CLUSTERS ARE NOT DISPERSED BY CHOLESTEROL DEPLETION

The next step was to determine whether cholesterol content and plasma membrane lipid order played a role in regulating the organisation of SNAP-25 and syntaxin 1a clusters at the cell surface and if a reduced binding affinity between SNAP-25 and syntaxin 1a enhanced this effect. Previous reports have suggested that the clustering of syntaxin 1a is

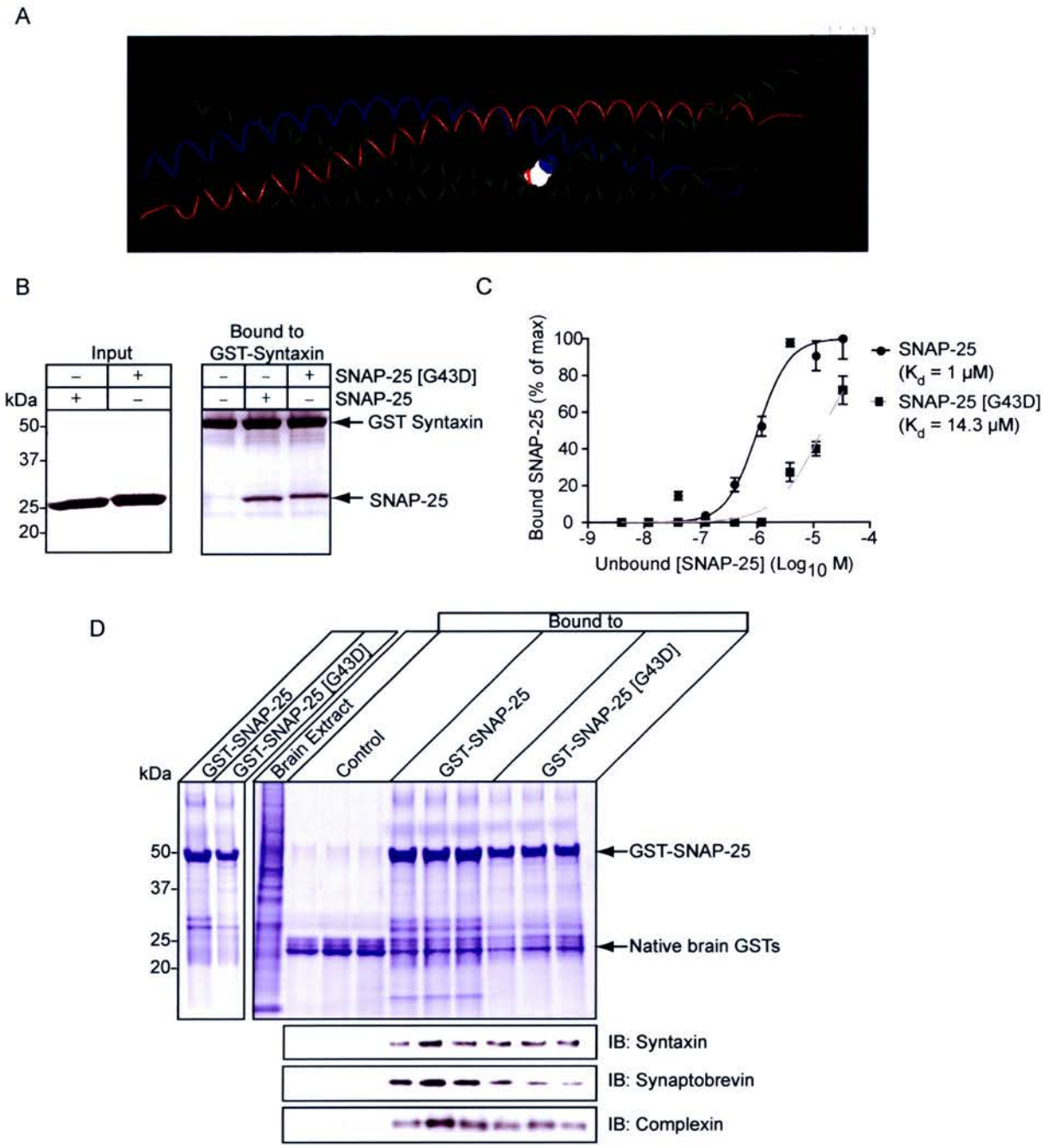

Figure 6.2 SNAP-25 [G43D] has a decreased binding affinity for syntaxin 1a.
(A) The ternary SNARE complex showing the position of the SNAP-25 SN1 point mutation G43D. **(B)** Purified His_6-tagged SNAP-25A_{1-206} or SNAP-25A $[G43D]_{1-206}$ incubated with GST-Syx1a_{1-288}. Both SNAP-25A_{1-206} and SNAP-25A $[G43D]_{1-206}$ proteins readily bound to the cytoplasmic domain of syntaxin1a. **(C)** GST-Syx1a_{1-288} was immobilised on Sepharose beads and incubated with varying concentrations of purified His_6-tagged SNAP-25A_{1-206} or SNAP-25A $[G43D]_{1-206}$. Bound material was analysed by western immunoblotting. Error bars represent SEM (n=3). Measurement of the equilibirum dissociation constant for the syntaxin-SNAP-25 complex revealed that SNAP-25A $[G43D]_{1-206}$ has a decreased affinity for Syx1a_{1-288}. **(D)** Both SNAP-25A_{1-206} and SNAP-25A_{1-206} [G43D] were immobilised on Sepharose beads and incubated with rat brain lysate. Bound proteins were analysed by western immunoblotting (IB). Both wildtype SNAP-25A_{1-206} and SNAP-25A $[G43D]_{1-206}$ readily bind syntaxin, synaptobrevin and complexin from rat brain lysates. Native brain GSTs bind directly to the sepharose resin.

dependent upon cholesterol (Lang et al., 2001; Ohara-Imaizumi et al., 2004a). However, a number of these studies have focused on inside-out sheets of lysed plasma membrane rather than intact cells. The cells are unroofed using a brief ultrasound pulse, leaving only the basal plasma membrane adhering to the coverslip and intact (Lang et al., 2001).

Immunostaining for syntaxin 1a showed complete dispersal of clusters after 30 minutes using 15 mM MβCD (Lang et al., 2001). This study also examined intact PC12 cells, yet it is difficult to ascertain if complete syntaxin 1a dispersal was achieved as only equatorial sections through the cells are shown rather than images of the basal plasma membrane (Lang et al., 2001). Ohara-Imaizumi and co-workers also showed that 10 mM MβCD treatment dispersed syntaxin 1a clusters in MIN6 insulinoma cells (Ohara-Imaizumi et al., 2004a) yet the representative images do not display a convincing dispersal and although the staining intensity is reduced clusters are still visible. Furthermore, recent studies have suggested that syntaxin 1a and SNAP-25 clustering requires an intact SNARE motif and disruption of the SNARE motif dispersed clusters (Rickman et al., 2004; Sieber et al., 2006). Both these recent studies indicated that localisation to cholesterol rich domains alone was not sufficient for the maintenance of SNARE clusters and that this may instead play a secondary role. Thus at present the effect of cholesterol depletion on SNARE protein clustering still remains ambiguous.

Live N2a cells were grown on glass coverslips coated with poly-D-lysine (see Chapter 2: Materials and Methods) for 24 hours and then transfected with mCerulean fused $Syx1a_{1-288}$ and EYFP fused $SNAP\text{-}25A_{1-206}$ or SNAP-25A $[G43D]_{1-206}$ in the presence of munc18-1 and imaged by CLSM and data deconvolution techniques (see Chapter 2: Materials and Methods). Immediately prior to imaging N2a cells were incubated in the presence or absence of 10 mM MβCD for 30 minutes at 37 °C (see Chapter 2: Materials and Methods). Co-localisation analyses (see Chapter 2: Materials and Methods) revealed a high degree of positive correlation between SNAP-25 or SNAP-25A $[G43D]_{1-206}$ and syntaxin 1a in live N2a cells (Figure 6.3). Notably, in both instances there was a high degree of co-localisation and covariance observed between syntaxin 1a and SNAP-25

even in the presence of the G43D mutation (Figure 6.3B). Interestingly, however, cholesterol depletion which abolishes the ordered GP population at the plasma membrane did not disperse syntaxin 1a or SNAP-25 clusters and it had no effect on the co-localisation of the SNAREs for both wild-type SNAP-25A_{1-206} or SNAP-25A $[G43D]_{1-206}$. Quantitative co-localisation analyses by means of Pearson's correlation coefficient (R) revealed a high degree of positive correlation throughout the cell (R = 0.86 ± 0.02, mean ± SEM; n = 7) and at the plasma membrane (R = 0.81 ± 0.03, mean ± SEM; n = 8), between SNAP-25A_{1-206} and Syx1a_{1-288}. Interestingly, in the presence of MβCD there was no significant difference in correlation throughout the cell (R = 0.88 ± 0.01, mean ± SEM; n = 7) or at the plasma membrane (R = 0.80 ± 0.03, mean ± SEM; n=7), with both t-SNAREs still exhibiting high levels of correlation after cholesterol depletion and lipid disorder (Figure 6.4). Despite SNAP-25A $[G43D]_{1-206}$ being shown previously to have a reduced binding affinity for syntaxin 1a, a high degree of positive correlation was also visible with syntaxin 1a throughout the cell (R = 0.85 ± 0.03, mean ± SEM; n = 4) and at the plasma membrane (R = 0.85 ± 0.02, mean ± SEM; n = 5) at similar levels to those observed for wild-type SNAP-25. Furthermore, the t-SNARE clusters still remained intact and showed no significant difference in correlation when a reduced binding affinity with syntaxin 1a was coupled with MβCD treatment (R = 0.88 ± 0.02, mean ± SEM; n = 8, throughout the cell and R = 0.82 ± 0.3, mean ± SEM; n = 7, at the plasma membrane) (Figure 6.4). Interestingly, these results indicate that disrupting the plasma membrane lipid order had no effect on the co-localisation of the t-SNAREs in the entire cell volume or on the plasma membrane, even in the presence of a weakened binding affinity between syntaxin 1a and SNAP-25 (Figure 6.4). Furthermore, the t-SNARE clusters remained intact after MβCD treatment and no cluster dispersal was visible.

The lack of effect of cholesterol depletion on SNAP-25 and syntaxin 1a clusters observed here is at odds with previous reports. However, we were able to confirm that under the conditions employed, 10 mM MβCD treatment resulted in both cholesterol

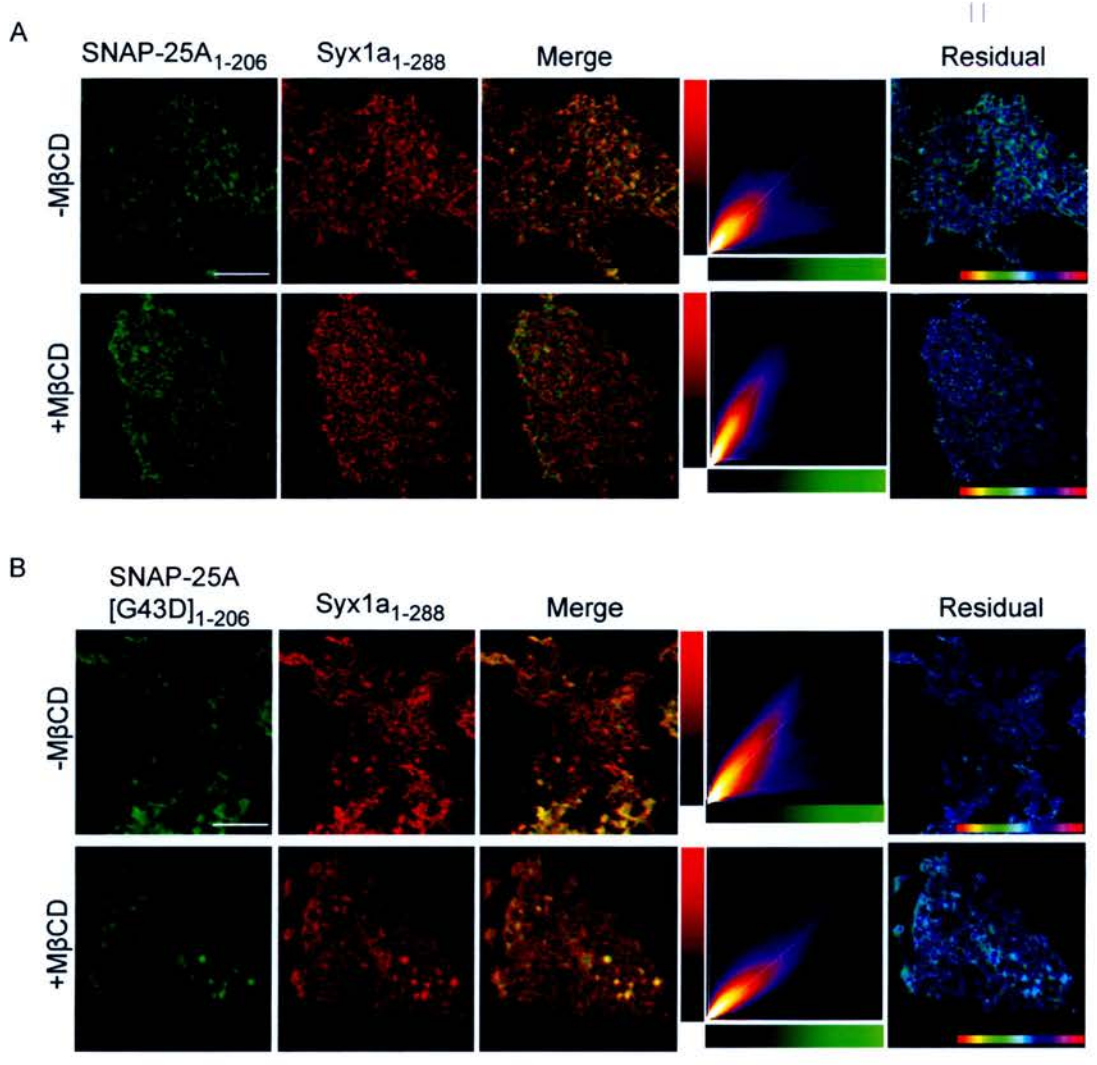

Figure 6.3 Syntaxin 1a and SNAP-25 clusters are not dispersed by cholesterol depletion.

(A) Wild-type EYFP-SNAP-25A$_{1-206}$ (green), mCerulean-Syx1a$_{1-288}$ (red) and munc18-1 were co-expressed in live N2a cells. Immediately prior to imaging by CLSM the cells were incubated at 37 °C in the presence or absence of 10 mM MβCD for 30 minutes. The merged image shows areas of coincidence in yellow hues. The two-dimensional histogram represents the intensity of each channel in each voxel, with a colour scale representing frequency. The residual map corresponds to weighted residuals from the linear regression of the histogram, thus indicating fluorescent channel covariance. The hue is from -1 to 1, with cyan corresponding to a zero residual and perfect covariance. **(B)** SNAP-25A[G43D]$_{1-206}$ (green), mCerulean-Syx1a$_{1-288}$ (red) and munc18-1 were co-expressed in live N2a cells. Immediately prior to imaging by CLSM the cells were incubated at 37 °C in the presence or absence of 10 mM MβCD for 30 minutes. Shown are representative equatorial sections from 10 experiments. Scale bar, 5 µm.

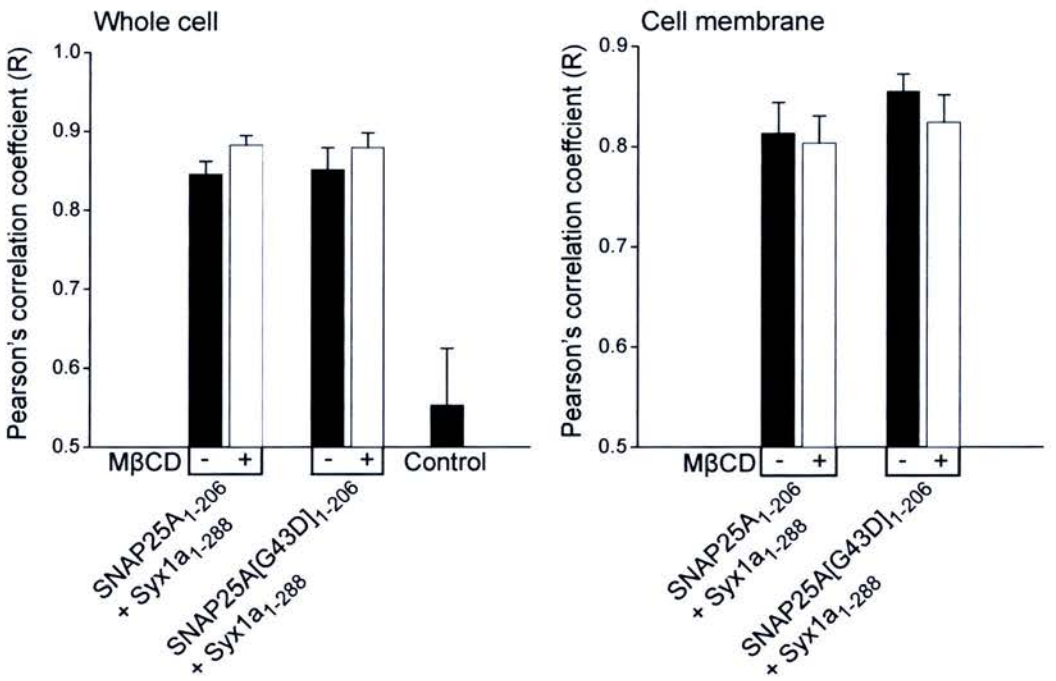

Figure 6.4 Cholesterol depletion does not affect t-SNARE co-localisation in living cells.

The covariance data from live N2a cells expressing $SNAP25A_{1-206}$ or SNAP25A $[G43D]_{1-206}$ and $Syx1a_{1-288}$ and munc18-1, in the absence (filled bars) or presence (open bars) of 10 mM MβCD are shown. Covariance data were quantified for the t-SNAREs in the whole cell and at the cell membrane and expressed as Pearson's correlation coefficient values (R). EYFP and unfused munc18-1 were used as a control. This data shows that there is no significant difference between t-SNARE co-localisation in the absence or presence of MβCD (t-test). After cholesterol depletion and alteration of the lipid order of the membrane, the t-SNAREs still co-localise. Data is expressed as the mean ± SEM., n ≥4.

depletion and a loss of plasma membrane order whilst maintaining cell viability. Furthermore, our studies were conducted on live cells, whereas other reports examining SNARE clusters have focused on plasma membrane sheets or fragments and have not reported on MβCD effects on cell viability or lipid order. The findings from this study indicate that cholesterol depletion, shown to quantitatively reduce lipid order on the plasma membrane, does not affect the clustering, targeting or co-localisation of the t-SNAREs in living cells.

6.6 ANALYSIS OF SNAP-25 AND SYNTAXIN 1A CLUSTER FWHM SIZE FOLLOWING CHOLESTEROL DEPLETION

To investigate whether a weakened binding affinity between the t-SNAREs or cholesterol depletion coupled with lipid disorder affected cluster size, the previous data describing untreated and MβCD-treated cells co-expressing mCerulean-fused $Syx1a_{1-288}$ and EYFP-fused $SNAP\text{-}25A_{1-206}$ or SNAP-25A $[G43D]_{1-206}$ in the presence of munc18-1 were analysed for the mean FWHM cluster size. In addition, N2a cells in the presence or absence of 10 mM MβCD were fixed and double immunostained for anti-syntaxin 1a and anti-SNAP-25 using fluorescent secondary Fab fragment antibodies (see Chapter 2: Materials and Methods) and the mean FWHM measured for both t-SNARE cluster sizes. The FWHM size of t-SNARE clusters was measured using standard procedures previously discussed in section 5.5 and these are reported in Table 6.1. For both heterologous syntaxin 1a and SNAP-25 channels, cluster FWHM size was measured for 100 clusters, from 5 images, and 20 clusters per cell. For both endogenous syntaxin and SNAP-25 channels, cluster FWHM size was measured for 60 clusters, from 3 images, and 20 clusters per cell.

An attempt was made to measure the FWHM size of t-SNARE clusters in the presence or absence of MβCD to investigate if there was a dramatic reduction in cluster size or even cluster dispersal following cholesterol depletion. Nonetheless, the problems

encountered in section 5.5 still stand in this instance and discrepancies existed between endogenous and heterologous t-SNARE cluster sizes. However, it must be noted that in N2a cells cholesterol depletion and lipid disorder did not disperse the syntaxin 1a or SNAP-25 clusters which is in conflict with previous studies. In addition SNAP25A $[G43D]_{1\text{-}206}$ clusters showed a large reduction in size after MβCD treatment (Table 6.1) which may suggest that the reduced binding affinity of the t-SNARE interaction coupled with lipid disorder may have a more dramatic effect on cluster stability.

Table 6.1 FWHM sizes of syntaxin 1a and SNAP-25 clusters in the presence or absence of MβCD in N2a cells.

		Untreated Mean FWHM (nm) ± SEM	+ 10 mM MβCD Mean FWHM (nm) ± SEM	Mann Whitney Rank Sum Test Untreated *versus* Treated
Syntaxin 1a	Heterologous	259 ± 5	222 ± 4	$p < 0.001$
	Endogenous	313 ± 5	331 ± 6	$p < 0.032$
SNAP-25	Heterologous	366 ± 9	294 ± 6	$p < 0.001$
	Endogenous	322 ± 5	321 ± 5	-
SNAP-25 [G43D]	Heterologous	364 ± 9	261 ± 6	$p < 0.001$
Syntaxin 1a	Heterologous	258 ± 6	213 ± 3	$p < 0.001$

Furthermore, the FWHM cluster sizes are very close to the resolution of our microscope (maximally about 178 nm) and further analysis using STED microscopy or electron microscopy would be necessary to provide reliable t-SNARE cluster sizes. Instead, I chose to investigate the molecular interactions of syntaxin 1a and SNAP-25 within individual clusters in ordered and disordered membranes. Nevertheless, it still remains clear neither syntaxin 1a or SNAP-25 clusters are dispersed after cholesterol depletion and we know at higher concentrations of MβCD, cell viability is directly affected. The results presented so far in this study may imply that the integrity of t-SNARE clusters does not depend solely on cholesterol content and may also be maintained by t-SNARE protein interactions.

6.7 SNARE CLUSTERS ARE HETEROGENEOUS IN THEIR INTERACTION STATUS

At the plasma membrane, it is unknown whether all of the t-SNARE clusters are non-reactive, or instead both reactive and non-reactive t-SNARE clusters are present. Having detected no clear role for cholesterol and lipid order in regulating syntaxin 1a and SNAP-25 clusters, next I investigated whether the t-SNAREs within clusters interact on the plasma membrane in the presence of munc18-1. As co-localisation data is limited by the resolution of the microscope (maximally 178 nm) and does not directly indicate interaction TCSPC-FLIM was employed.

Live N2a cells were grown on glass coverslips coated with poly-D-lysine (see Chapter 2: Materials and Methods) for 24 hours and then transfected with mCerulean fused Syx1a$_{1-288}$ and EYFP fused SNAP-25A$_{1-206}$ in the presence of munc18-1 and imaged by FLIM and two photon microscopy (see Chapter 2: Materials and Methods). In resting cells, mCerulean-Syx1a$_{1-288}$ exhibited a plasma membrane distribution and a significant donor lifetime quenching was not detected even in the presence of co-localised EYFP-SNAP-25A$_{1-206}$ (Figure 6.5A). This indicates that either the t-SNAREs do not interact at the cell surface before fusion occurs or the t-SNARE interaction adopts a conformation where the fluorophores are sufficiently distant, or of an orientation that precludes FRET. The next step was to try and force t-SNARE interaction at the plasma membrane to further our understanding of the factors regulating t-SNARE interactions. Depolarisation of the N2a cells with 55 mM KCl induced FRET in puncta on the cell surface (Figure 6.5B). Following this FLIM analysis at the base of the cell was conducted to obtain FLIM-FRET data for individual SNARE clusters before and after treatment with 55 mM KCl.

In the presence of KCl depolarisation, mCerulean-Syx1a$_{1-288}$ (donor) fluorescence in the presence of EYFP-SNAP-25A$_{1-206}$ (acceptor) and munc18-1 showed clusters at the base of the cell. The donor fluorescence lifetime was significantly shortened, indicative of FRET between the t-SNAREs. The proportion of FRET-positive t-SNARE clusters

increased compared with resting cells (Figure 6.5C). The donor fluorescence lifetime data for each sample were fit separately by a nonlinear regression (Figure 6.5D). The donor fluorescence lifetimes in the KCl treated samples were significantly reduced (least sum of squares F test, $p < 0.0001$) compared with those from resting cells. To further investigate this effect, ionomycin was employed, to elevate intracellular Ca^{2+} levels directly, avoiding any potential indirect effect of Ca^{2+} channels on t-SNARE interactions. In this instance, clusters were still visible at the base of the cell and in both resting cells and stimulated cells in a Ca^{2+} free, chelating medium heterogeneity in the SNARE cluster population was detected (Figure 6.6A). After ionomycin-induced Ca^{2+} influx, the situation was reversed, and almost every t-SNARE cluster (95 ± 4%) was seen to contain interacting t-SNAREs (Figure 6.6B). The mCerulan-Syx1a$_{1\text{-}288}$ (donor) fluorescence lifetime was quenched in the presence of EYFP-SNAP-25A$_{1\text{-}206}$ (acceptor) and munc18-1, indicating FRET between the t-SNAREs in the clusters. These data demonstrate heterogeneity in resting t-SNARE clusters not previously recognised, perhaps resulting from alternative SNARE complex conformational states or due to the sequestering of closed syntaxin by munc18-1 at the cell surface. Furthermore, these data suggest that the formation of suitable syntaxin-SNAP-25 dimeric binary complexes, which can act as acceptor sites for synaptobrevin containing vesicles, might be a regulatory step of SNARE function and thus some clusters may represent active fusion sites on the plasma membrane.

6.8 t-SNARE CLUSTER HETEROGENEITY IS THE RESULT OF TWO t-SNARE HETERODIMER COMPLEX CONFORMATIONS

To further examine the molecular interactions of the t-SNARE proteins within individual clusters in ordered and disordered membranes we again employed time correlated single photon counting (TCSPC)-FLIM. Live N2a cells were grown on glass coverslips coated with poly-D-lysine (see Chapter 2: Materials and Methods) for 24 hours and then transfected with mCerulean fused Syx1a$_{1\text{-}288}$ and EYFP fused SNAP-25A$_{1\text{-}206}$ in the

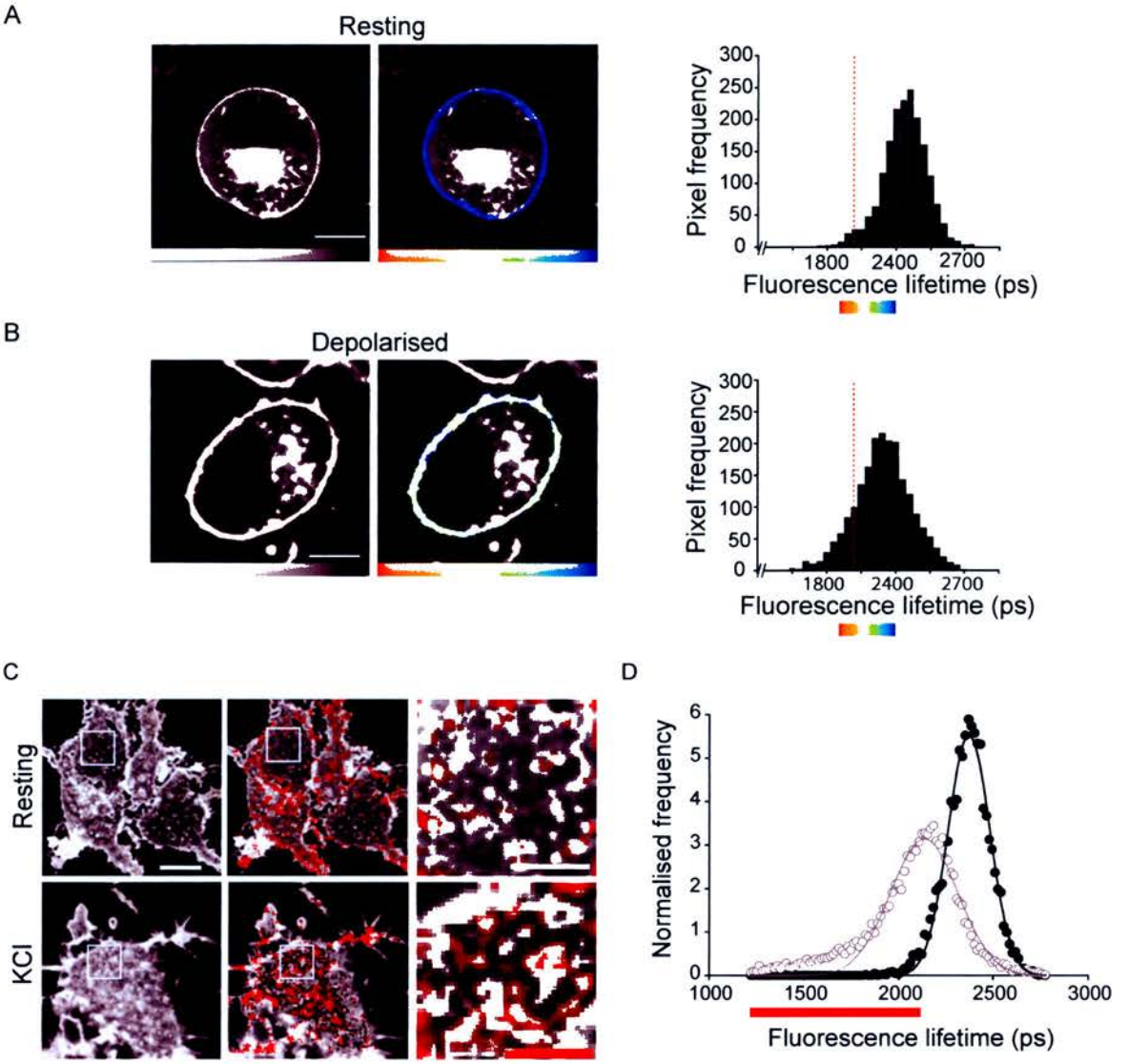

Figure 6.5 t-SNAREs interact on the plasma membrane in the presence of munc18-1.

Intensity images and FLIM maps showing mCerulean-Syx1a$_{1\text{-}288}$, in the presence of EYFP-SNAP-25A$_{1\text{-}206}$ and munc18-1 in live N2a cells, imaged by FLIM and two photon microscopy. **(A)** mCerulean-Syx1a$_{1\text{-}288}$ (donor) fluorescence exhibited a plasma membrane distribution. The colour scale [1900 (red) - 2400 pseconds (blue)] in the FLIM map represents the donor fluorescence lifetime in resting cells, and **(B)** after depolarisation with 55 mM KCl. These data were plotted as a frequency distribution histogram, showing the 99 % confidence interval of the donor lifetime distribution (red dashed line; bars are mean ± SEM., n = 5 experiments). Scale bar, 5 µm. **(C)** mCerulean-Syx1a$_{1\text{-}288}$ (donor) fluorescence in the presence of EYFP-SNAP-25A$_{1\text{-}206}$ (acceptor) and munc18-1 showed clusters at the base of the cell. The boxed regions of interest are shown in the right-hand panels as zoomed images and illustrates clusters at the plasma membrane in both resting and KCl depolarised cells. Pixels containing fluorescence lifetimes below the 99 % confidence interval of the non-FRET distributions in panels A and B are shown in red indicating that the proportion of FRET-positive t-SNARE clusters increased after KCl induced depolarisation. Scale bar, 1 µm. **(D)** The donor fluorescence lifetime data for each sample were plotted as a frequency distribution histogram. The fluorescence lifetimes in the KCl-treated samples (—○—) were significantly reduced compared with those from resting cells (—●—) (Least sum of squares F test).

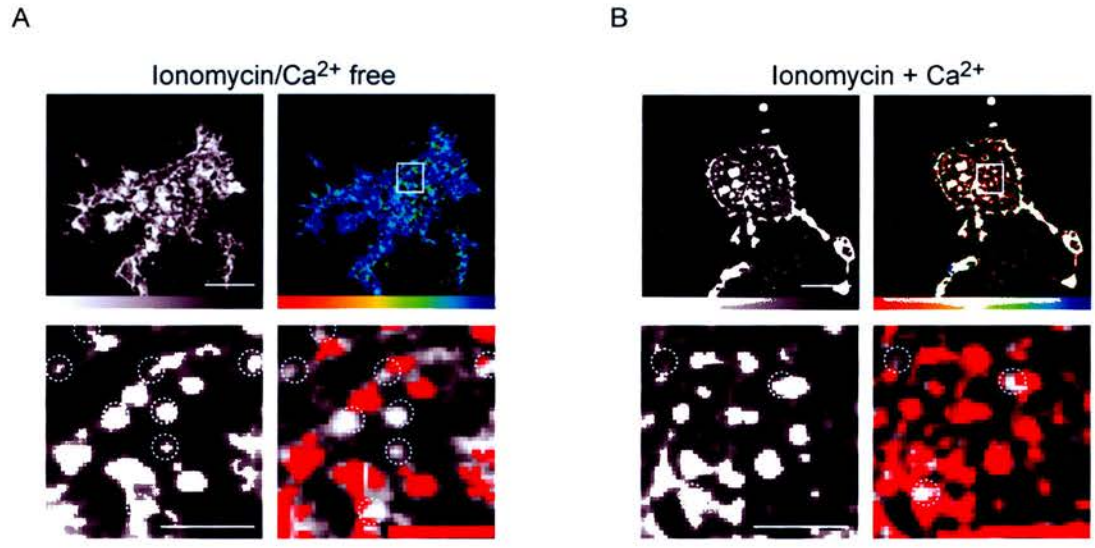

Figure 6.6 SNARE clusters are heterogenous in their interaction status.
Intensity images and FLIM maps showing mCerulean-Syx1a$_{1-288}$, in the presence of EYFP-SNAP-25A$_{1-206}$ and munc18-1 in live N2a cells, imaged by FLIM and two photon microscopy. **(A)** mCerulean-Syx$_{1-288}$ (donor) fluorescence. The colour scale [1500 (red) - 2000 pseconds (blue)] in the FLIM map represents the donor lifetime in the presence of ionomycin, but a Ca^{2+} free environment revealed clusters at the base of the cell. The boxed regions of interest are shown in the lower panels and illustrate the clusters at the plasma membrane. Scale bar, 5 µm. Pixels containing fluorescence lifetimes below the 99 % confidence interval of the non-FRET distribution in Figure 6.5 are shown in red. Scale bar, 1 µm. SNARE clusters where no FRET could be detected are highlighted with a dashed circle. **(B)** In the presence of ionomycin and Ca^{2+}, mCerulean-Syx1a$_{1-288}$ (donor) fluorescence in the presence of EYFP-SNAP-25A$_{1-206}$ (acceptor) and munc18-1 showed clusters at the base of the cell. The colour scale [1500 (red) - 2000 pseconds (blue)] in the FLIM map represents the donor lifetime in the presence of ionomycin and Ca^{2+}. The donor fluorescence lifetime was significantly shortened, indicative of FRET between the t-SNAREs. Scale bar, 5 µm. The boxed region of interest is shown in the lower panels and again illustrates clusters at the plasma membrane. Pixesl containing fluorescence lifetimes below the 99 % confidence interval of the non-FRET distribution in Figure 6.5A are shown in red. SNARE clusters where no FRET could be detected are again highlighted in dashed circles. Scale bar, 1 µm.

presence of munc18-1 and imaged by TCSPC-FLIM (see Chapter 2: Materials and Methods).

The TCSPC-FLIM approach confirmed an interaction between mCerulean-Syx1a$_{1-288}$ and EYFP-SNAP-25A$_{1-206}$ within individual clusters at the plasma membrane of live N2a cells (Figure 6.7). The fluorescence lifetime of the donor, mCerulean-Syx1a$_{1-288}$ in the presence of unfused EYFP and munc18-1 exhibited a mono-exponential decay function, with a single fluorescence lifetime detected throughout the entire cell of 2377 ± 65 ps (mean ± SEM; n = 6) (Figure 6.7A and B). In direct contrast, the fluorescence lifetime recorded for the same donor, mCerulean-Syx1a$_{1-288}$ in the presence of the acceptor, EYFP-SNAP-25A$_{1-206}$ no longer fit a mono-exponential decay function and was fit instead to a bi-exponential decay function revealing a dramatically shortened donor fluorescence lifetime (Figure 6.7A and C). As I reported previously the t-SNARE clusters show significant FRET heterogeneities between individual clusters at the plasma membrane. Improved FLIM detection and analysis of these data compared to that in Figure 6.5 revealed that all the SNARE clusters containing both donor and acceptor t-SNAREs (>85% of clusters) exhibited quenched donor fluorescence lifetimes significantly shorter than those observed for the control, donor alone, dataset (Figure 6.7A-C). This indicated that all these clusters contained t-SNARE heterodimers.

To gain further insights into the organisation of these t-SNARE cluster sites, we investigated whether conformational heterogeneities may exist between the t-SNARE clusters at the cell surface. Multiple FLIM datasets describing entire images of cells expressing both donor and acceptor t-SNARE proteins were analysed. By plotting the weighted mean of the two fluorescence lifetimes we demonstrated that the t-SNARE clusters populate two distinct FRET efficiency groups (Figure 6.7 C). If this same fluorescence lifetime data was plotted as two separate lifetimes, a long (non-FRET) and a short (FRET) fluorescence lifetime were evident in every pixel (Figure 6.7D). Importantly, this showed that the non-FRET component had a fluorescence lifetime identical to the donor alone fluorescence lifetime, yet surprisingly the FRET component

actually consisted of two FRET populations (Figure 6.7D), showing mean fluorescence lifetimes of 605 ± 50 ps (high FRET) and 1231 ± 56 ps (intermediate FRET; mean ± SEM, n = 589824 data points from 9 cells each). After further analysis the ratio of non-FRET versus FRET components per pixel were determined (Figure 6.7D) and demonstrated that the number of interacting molecules within heterogenous t-SNARE clusters in fact not different. Together this data suggests that the significant differences in FRET observed between the t-SNARE clusters is not due to stoichiometric variance, but is instead due to two conformational states of the syntaxin1a-SNAP-25 heterodimer complex. In addition, t-SNARE clusters are heterogenous in terms of their interaction status and they may possess at least two forms of SNARE heterodimer that are spatially organised into high or intermediate FRET predominant clusters at the cell surface.

6.9 LIPID ORDER REGULATES t-SNARE HETERODIMER ORGANISATION

The results so far have documented that t-SNARE clusters are heterogenous in their interaction status and that the plasma membrane contains a mixture of two conformational states of the t-SNARE heterodimer complex arranged in clusters. It may be possible that membrane lipid order plays a role in the organisation of these two t-SNARE heterodimer complexes. To clarify the functional implications of the separate FRET components described above, and the role of membrane lipid order in t-SNARE molecular organisation and cluster integrity, MβCD was employed. To disrupt lipid order at the plasma membrane, N2a cells co-expressing mCerulean-Syx1a$_{1\text{-}288}$ (in the presence of munc18-1) and EYFP-SNAP-25A$_{1\text{-}206}$ were treated with 10 mM MβCD (see Chapter 2: Materials and Methods) and imaged by TCSPC-FLIM. In previous studies I showed that cholesterol depletion and lipid disorder did not disperse t-SNARE clusters and the clusters still showed high levels of co-localisation at the plasma membrane (Figures 6.3 and 6.4).

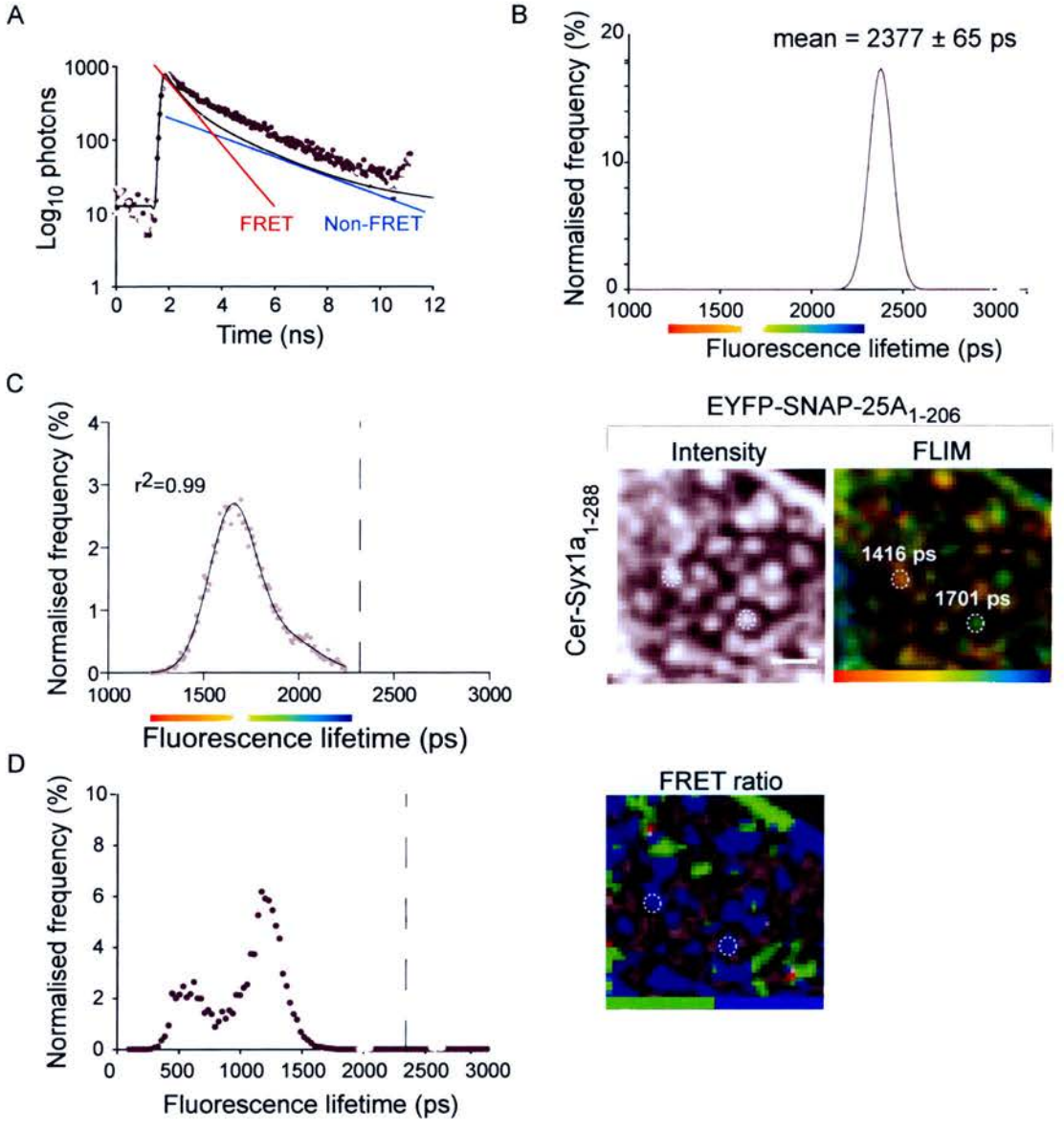

Figure 6.7 Two distinct t-SNARE heterodimer complex conformations exist causing t-SNARE cluster heterogeneity.

(A) In N2a cells, the excited state fluorescence lifetime of the donor mCerulean-Syx1a$_{1-288}$ alone follows a mono-exponential decay function (Rickman et al., 2007), yet in the presence of the acceptor EYFP-SNAP25A$_{1-206}$ this data is better fit to a bi-exponential decay function. Dark grey circles represent the control, donor mCerulean-Syx1a$_{1-288}$ alone, and light grey circles show data from the same donor in the presence of the acceptor EYFP-SNAP-25A$_{1-206}$. The short fluorescence decay time constant represents FRET and thus indicates an interaction between the t-SNARE proteins. The long fluorescence decay time constant indicates the non-FRET component in the same pixel. The contribution from each components adds up to 100%. **(B)** Frequency distribution histogram of all the fluorescence lifetime values from an entire dataset acquired from an N2a cell expressing mCerulean-Syx1a$_{1-288}$ alone. The donor alone has a single fluorescence lifetime of 2377 ± 65 ps. **(C)** Frequency distribution histogram showing the weighted mean fluorescence lifetimes from the plasma membrane of an N2a cell expressing mCerulean-Syx1a$_{1-288}$ and EYFP-SNAP-25A$_{1-206}$. In the presence an the acceptor the donor fluorescence lifetime is markedly reduced. These data are better fit to two Gaussian functions and the r^2 value relates to the 2 component fit demonstrating that 2 separate populations exist. These fluorescence lifetime values are displayed in false colour as a FLIM map (right panel). Individual SNARE clusters can be identified and show significant fluorescence lifetime heterogeneities. The colour scale shown is from 1250-2250 ps. **(D)** Deconvolution of the weighted mean fluorescence lifetime into the non-FRET long lifetime and the FRET short lifetime reveals two distinct FRET populations.. This indicates that two t-SNARE heterodimer complexes exist. A ratio of the FRET versus non-FRET components represents the proportion of interacting molecules in each pixel of an image (right panel). Colour scale shown is green, 0-2.5 and blue, 2.5-5. Scale bar, 1 µm.

TCSPC-FLIM analyses revealed that as expected the t-SNARE clusters appeared to remain intact as reported by co-localisation studies, but after lipid order disruption the overall fluorescence lifetime of the donor, mCerulean-Syx1a$_{1-288}$ was lengthened (Figure 6.8A and B). Using multiple data sets and analysing the high and intermediate FRET components, I confirmed that two t-SNARE heterodimer conformations exist and are concentrated into clusters of distinct fractional proportions. However, upon lipid order disruption, the intermediate FRET component was increased and visible as an increase in the frequency of the longer lifetime FRET component (Figure 6.8B). In this instance, the high FRET population was almost abolished (Figure 6.8B) and the combined data was best fit by the sum of two Gaussian distributions. In control cells, the high FRET population fraction was 30.7% of the total FRET, whereas after disruption of lipid order it was reduced to 17.5%. In comparison, the intermediate FRET population increased slightly in mean values from 69.3% to 82.5% of the total FRET contribution. Together these data support the existence of two heterodimer complexes, and more importantly that the organisation within each cluster, is affected by lipid disorder.

To test the role of both lipid order and t-SNARE protein interactions in the organisation and stability of the heterodimer complexes within t-SNARE clusters, the mutant EYFP-SNAP25A [G43D]$_{1-206}$ was employed. This mutation was used to see what effect the reduced affinity of SNAP-25 to syntaxin had on t-SNARE interactions in a living cell. To analyse this, live N2a cells co-expressing mCerulean-Syx1a$_{1-288}$ (in the presence of munc18-1) and EYFP-SNAP-25A [G43D]$_{1-206}$ were incubated in the presence or absence of 10 mM MβCD (see Chapter 2: Materials and Methods) to disrupt lipid order and imaged by TCSPC-FLIM as before. As with wild-type SNAP-25A$_{1-206}$, SNAP-25A [G43D]$_{1-206}$ was seen to traffic to the plasma membrane. Interestingly, in the presence of a reduced binding affinity and lipid disorder, cluster integrity was still maintained. Furthermore, despite the reduced binding affinity between syntaxin 1a and this mutant, both proteins could interact on the plasma membrane in living N2a cells. There were no differences between the wild-type complex and the mutant complex with SNARE cluster heterodimer heterogeneity on the plasma membrane still detected (Figure 6.8A and C).

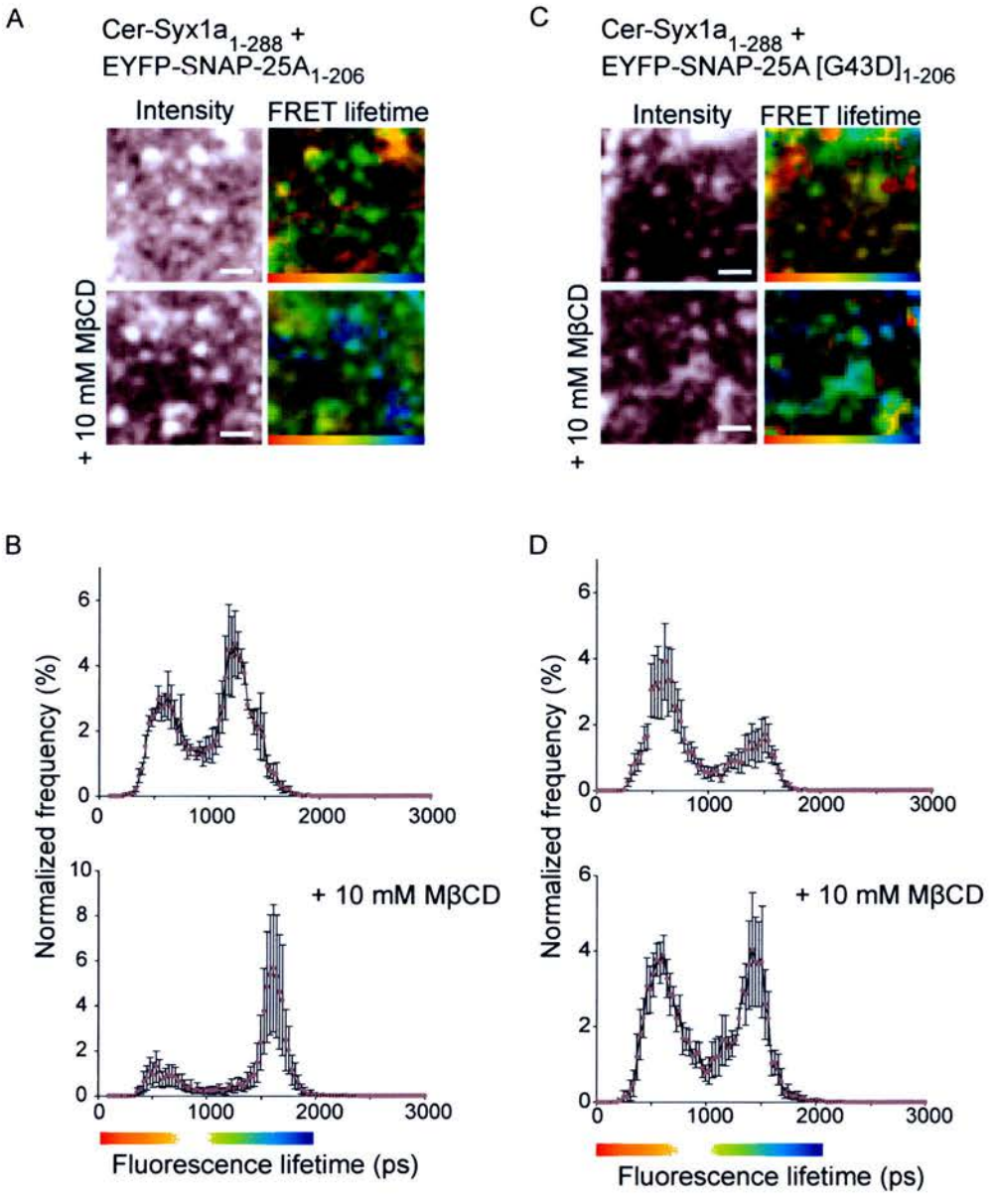

Figure 6.8 t-SNARE heterodimer organisation is regulated by lipid order.
(A) Quantifying data from multiple cells confirms that t-SNARE clusters are heterogeneous and two distinct conformational states exist. FLIM images show representative fluorescence intensity images, and FRET (short) lifetime images. The colour scale shown is from 0 (red) to 2000 ps (blue). MβCD treatment to disrupt lipid order results in the lengthening of the overall donor fluorescence lifetime, yet the maintenance of both t-SNARE interaction and cluster integrity. **(B)** TCSPC-FLIM analysis for N2a cells expressing mCerulean-Syx1a$_{1-288}$ and EYFP-SNAP-25A$_{1-206}$, and in the presence or absence of 10 mM MβCD. Plotting the FRET lifetime data combined from multiple experiments confirms two FRET populations . Cholesterol depletion enhances the intermediate FRET conformation at the expense of the high FRET values. **(C)** Similar experiments using SNAP25A [G43D]$_{1-206}$ as the acceptor also demonstrates similar SNARE cluster heterodimer heterogeneity on the plasma membrane. **(D)** Plotting the FRET values as before demonstrates a movement of the data towards the shorter lifetime population, compared to wild-type SNAP-25A$_{1-206}$. MβCD treatment to induce lipid disorder on the plasma membrane has a similar, yet less pronounced effect on the heterodimer conformation distribution compared to wild-type SNAP-25A$_{1-206}$. Scale bar, 1 μm.

Multiple data set analysis of the high and intermediate FRET components also confirmed that two t-SNARE heterodimer conformations exist (Figure 6.8D). Disruption of plasma membrane lipid order had a similar effect to that observed for wild-type SNAP-25A$_{1\text{-}206}$, and a reduction of the high FRET population was observed. This was visible as an increase in the intermediate FRET component in the presence of lipid disorder, yet this effect was less pronounced than that observed in the wild-type complex. These findings also support the presence of two heterodimer complexes, yet more importantly they confirm that t-SNARE cluster integrity and organisation is dependent upon both t-SNARE protein-protein interactions and lipid order at the plasma membrane.

6.10 Conclusion

In recent years, the membrane micro-patterning of plasma membrane SNARE proteins has been the subject of several studies. Microscopic analysis has shown that syntaxin and SNAP-25 reside in clusters at the plasma membrane and that these sites represent sites of vesicle docking and exocytosis (Lang et al., 2001; Ohara-Imaizumi et al., 2004b; Predescu et al., 2005; Sieber et al., 2007). The mechanisms underlying SNARE cluster organisation are not yet adequately understood, largely due to a limited knowledge about the size, composition, and dynamics of the clusters.

I have presented evidence to show that upon delivery to the plasma membrane t-SNARE organisation is regulated by two distinct factors: heterodimer interaction which is in turn modulated directly by lipid order. In neuroendocrine cells, the t-SNAREs, syntaxin 1a and SNAP-25 co-exist, co-localise and interact on the plasma membrane even in the presence of the greatly reduced binding affinity of the SNAP25A [G43D]$_{1\text{-}206}$ mutant for syntaxin 1a *in vitro* coupled with disruption of lipid order of the plasma membrane (Figures 6.3 and 6.4). In neuroendocrine cells, syntaxin 1a and SNAP-25 have been shown to interact in heterodimeric clusters at the plasma membrane with at least two spatially distinct complex conformations evident (Figure 6.7D). Upon partial cholesterol

depletion and disruption of plasma membrane lipid order in neuroendocrine cells, a significant change in the relative proportion of the two heterodimer complexes ensues. This results in the reduction of the high FRET conformation resulting in a dramatic increase in the intermediate FRET conformation (Figure 6.8B). In this regard, disruption of the lipid order leads to a re-arrangement of t-SNARE cluster organisation at the plasma membrane with one heterodimer conformation becoming dominant at the expense of the other, resulting in heterogeneities in cluster interaction status.

These observations demonstrate that t-SNARE clusters on the plasma membrane are heterogeneous in their interaction status, containing two distinct t-SNARE heterodimer complexes. The heterogeneities that exist between the t-SNARE clusters are due to the organisation of each heterodimer conformation into membrane areas where one complex form predominates over the other. At the plasma membrane t-SNARE organisation may be regulated by both t-SNARE protein interactions and a favourable lipid environment. These findings substantiate the theory that the t-SNARE clusters may support membrane fusion at the cell surface to varying degrees, depending on the local lipid environment. Further experiments will be required to provide data to describe the structural reasons for the different FRET populations at the cell membrane.

CHAPTER SEVEN:

DISCUSSION

7.1 SUMMARY OF FINDINGS

The aim of this investigation was to determine the molecular mechanisms that modulate the conformational states of syntaxin 1a, including the spatial and temporal regulation of its interactions with munc18-1 and SNAP-25 in living cells. To date, the role of munc18-1 in SNARE protein regulation has been difficult to define. In contrast with the consensus on SNARE protein function, the analysis of SM proteins in different systems has produced conflicting findings regarding their precise role, site of action and relationship with SNARE proteins. At the inception of this study the munc18-1-syntaxin interaction was in sharp contrast with that observed for other species such as yeast. Despite exhibiting high structural homology, mammalian munc18-1 and yeast Sly1p appeared to interact with their cognate syntaxins through independent sites. As SM proteins show a high degree of structural conservation throughout evolution this would suggest a common binding mechanism and function, indicating that mammalian munc18-1 may also be capable of dual mechanisms of binding to its cognate syntaxin as seen with yeast counterparts. If munc18-1 is indeed capable of two modes of binding with syntaxin, then SM proteins may have evolved multiple binding modes which represent different functional roles within a cellular context.

The findings from this thesis fall into three main categories: 1) Munc18-1 can adopt two distinct modes of binding with syntaxin 1a; 2) Munc18-1 prevents the formation of ectopic SNARE complexes in living cells; and 3) t-SNARE clusters are heterogeneous in their interaction status at the plasma membrane. In this investigation I have demonstrated that munc18-1 has two distinct modes of binding with syntaxin 1a that are spatially segregated within living cells. Munc18-1 binds to a closed conformation of syntaxin 1a, which is essential to keep syntaxin 1a inactive, and permit its trafficking to the plasma membrane. I demonstrate that in the absence of munc18-1, syntaxin 1a and SNAP-25 can interact in the Golgi complex, forming reactive SNARE complexes that fail to traffic to the plasma membrane. Therefore, munc18-1 has the vital regulatory function of binding to syntaxin 1a, essentially inactivating it, to permit its trafficking through the secretory pathway and preventing

ectopic interactions between the t-SNARE proteins before they reach the plasma membrane. Upon delivery to the plasma membrane, both syntaxin 1a and SNAP-25 are concentrated in clusters of high local concentration that co-localise in living cells. At the cell surface an unknown factor allows syntaxin 1a to switch to an open conformation, bound to munc18-1 via its N-terminus, initiating assembly of the binary and ternary SNARE complexes. Furthermore, the t-SNAREs form interaction-heterogeneous clusters that represent a mechanism of membrane patterning that is dependent upon t-SNARE protein interactions and the local membrane lipid environment.

7.2 INTERPRETATION OF FINDINGS

7.2.1 MODES OF MUNC18-1-SYNTAXIN 1A INTERACTION

It is clear that munc18-1 can interact with syntaxin 1a through two distinct modes of binding that are spatially distinct within living cells (Chapter 3). The closed conformation of syntaxin 1a, with the Habc domain interacting with the SNARE helix, bound to munc18-1, is structurally constrained and has properties similar to those observed in previous studies (Misura et al, 2000a; Pevsner et al, 1994b). This investigation showed that munc18-1 has a high affinity for this closed conformation (K_d = 5 nM) (Figure 3.3B) which has subsequently been confirmed (Burkhardt et al, 2008). In addition to this closed conformation of interaction, it is now clear that munc18-1 can also bind to the N-terminus of syntaxin 1a, in a similar way to the yeast homologues Sly1p and Sed5p (Bracher & Weissenhorn, 2002). The additional N-terminal binding of mammalian munc18-1 to syntaxin (Rickman et al, 2007) is in agreement with other studies which have been published during the completion of this thesis (Burkhardt et al, 2008; Dulubova et al, 2007; Shen et al, 2007). Interestingly, the N-terminus of syntaxin 4 has been shown to bind to the outer surface of munc18-3 in a similar manner to that observed for the Sly1p-Sed5p complex (Hu et al, 2007; Latham et al, 2006). Munc18-3 and syntaxin 4 are closely related to munc18-1 and syntaxin 1a. Furthermore, munc18-1 has been shown to bind to assembled SNARE complexes containing syntaxin 1a, thereby supporting a

general function of SM proteins in executing membrane fusion (Dulubova et al, 2007; Shen et al, 2007). Munc18-1 interaction with the N-terminus of syntaxin 1a has also been suggested to control the accessibility of syntaxin 1a to its cognate partners, thereby directly regulating SNARE complex formation (Burkhardt et al, 2008). These experiments involved the removal of the first 25 amino acid residues of the N-terminus of syntaxin 1a, resulting in the assembly of the SNARE complex. However, this N-terminal truncation would most likely have perturbed the first helix of the Habc domain, resulting in the disruption of both N-terminal and the closed (known to be inhibitory) modes of munc18-1 binding to syntaxin 1a.

In contrast to a previous report (Dulubova et al, 1999), our rat brain lysate pull downs showed that munc18-1 readily binds to the "open" conformation of syntaxin 1a, exhibiting no reduction in binding affinity with munc18-1 when compared to wild-type syntaxin 1a (Figure 3.3). It is unclear from the previous study (Dulubova et al, 1999) what the recombinant syntaxin proteins were. It must be noted that in contrast with their previous findings, the same group have recently reported that munc18-1 can bind directly to the SNARE complex via N-terminal binding (Dulubova et al, 2007). Furthermore, in this thesis it was shown that N-terminal truncation of the open mutation still allowed munc18-1 binding yet with reduced affinity (K_d = 44 nM) (Figure 3.3B). The discrepancies remain unexplained.

SM proteins have evolved different binding modes with their cognate syntaxins, which suggests that the separate modes of binding have functional significance within a cellular context. The intracellular locations of SM-syntaxin interactions have not been extensively reported. The yeast SM homologue Vps45p can interact *in vitro* with its cognate syntaxin through an undefined second mode of binding in addition to its N-terminal interaction (Carpp et al, 2006). Furthermore, it has been shown that munc18-3 binds to syntaxin 4, through an N-terminal interaction *in vitro* (Hu et al, 2007; Latham et al, 2006). However, previous studies have not reported on the spatial organisation of the two distinct modes of interaction between munc18-1 and syntaxin 1a in living cells. I demonstrate using TCSPC-FLIM that the two modes of munc18-1 binding to syntaxin 1a are spatially distinct within a cellular context

(Figure 3.7). Abolition of syntaxin 1a closed conformation binding directly affected intracellular syntaxin 1a-munc18-1 complexes. In contrast, N-terminal deletion affected plasma membrane interactions between munc18-1 and syntaxin 1a. This indicates that the interaction between munc18-1 and the closed conformation of syntaxin 1a occurs predominantly in intracellular membranes, while syntaxin 1a N-terminal binding to munc18-1 is adopted at the plasma membrane. This being the case, it may be possible that syntaxin 1a in the open conformation can bind munc18-1 and the other SNARE proteins simultaneously at the plasma membrane.

Protein biochemistry studies confirmed that the closed conformation of syntaxin, bound to munc18-1, is structurally constrained preventing the formation of the binary and ternary SNARE complexes (Figure 3.8A), which is in agreement with previous reports (Dulubova et al, 1999; Misura et al, 2000b; Rowe et al, 1999). In direct comparison, the open conformation of syntaxin 1a, bound via its N-terminus to munc18-1, was able to progress through binary and ternary SNARE complex formation while remaining associated with munc18-1 (Figure 3.8C). Therefore, I propose that at the plasma membrane syntaxin 1a adopts N-terminal binding with munc18-1 to free up the SNARE helix, thereby allowing the binary and ternary SNARE complexes to form so that membrane fusion can proceed. This is supported by observations in a reconstituted system, in which munc18-1 is in direct contact with the SNARE complex, and strongly accelerates neuronal exocytosis (Shen et al, 2007). A direct role for munc18-1 on the fusion step was proposed previously (Fisher & Burgoyne, 1999), however, it should be noted that this study used an N-terminally truncated form of syntaxin 1a. These findings place munc18-1 at the late steps of membrane fusion, and suggest that the N-terminal mode of interaction of munc18-1 and syntaxin 1a may be vital at the plasma membrane for this reason.

7.2.2 A CHAPERONE ROLE FOR MUNC18-1

The findings of this thesis have demonstrated that the two distinct binding modes of munc18-1 to syntaxin have important functional significance in the SNARE trafficking life cycle within living cells (Chapter 4). As SNARE proteins drive

membrane fusion in all the trafficking steps of the secretory pathway, it is vital that they are strictly regulated both temporally and spatially. A number of regulatory steps must be in place to ensure that the plasma membrane SNARE proteins are transported through the ER and Golgi complex in an inactive state until delivery to their target destination. I have shown that munc18-1 has an important role in preventing the formation of ectopic SNARE complexes during the trafficking of syntaxin 1a in neuroendocrine cells, and that the closed conformation of syntaxin 1a is vital for this function.

In neuroendocrine cells, the closed conformation of syntaxin 1a becomes trapped within intracellular membranes in the absence of munc18-1 (Figure 3.9). However, if munc18-1 is present at the correct levels, it plays a vital role in trafficking syntaxin 1a to the plasma membrane, as shown in this study (Figures 3.9 and 3.10). This supports previous studies in non-specialised cells that have reported a chaperone role for SM proteins (Rowe et al, 1999). It is possible that a small percentage of syntaxin 1a can reach the plasma membrane independent of munc18-1 (Figure 3.10). This would agree with a report that total cellular syntaxin is severely depleted, but still present at low levels, in organisms where a specific SM protein has been ablated (Toonen et al, 2005). However, I have shown that the level of syntaxin 1a trafficking is significantly enhanced when bound to munc18-1 (Figure 3.10). The close interrelationship that SM proteins share with their cognate syntaxin has been highlighted by numerous studies. The direct knockdown of expression of syntaxin 1 (de Wit et al, 2006) has been shown to result in a phenocopy of that observed in the munc18-1 knockout mouse (de Wit et al, 2006; Voets et al, 2001). Furthermore, the down-regulation of munc18-1 results in reductions in the secretion capability, as well as the docking of dense core vesicles, and more importantly, the expression levels of syntaxin 1 in PC12 cells (Arunachalam et al, 2008). Together these observations provide clarification of the exceptionally close interrelationship that SM proteins share with their cognate syntaxin throughout their life cycle. The data presented in this investigation supports the hypothesis that syntaxin 1a and munc18-1 may remain bound to one another throughout the syntaxin 1a and SM protein life cycles. This

conclusion would be in compliance with yeast homologous pairs such as Sly1p and Sed5p (Bracher & Weissenhorn, 2002).

The role of munc18-1 in trafficking syntaxin 1a through the secretory pathway appears to rely on it being present in the correct location. SNAP-25 in comparison can traffic to the plasma membrane without any specialised factors (Figure 4.1), which is in agreement with previous studies (Loranger & Linder, 2002). However, if the t-SNAREs encounter one another before munc18-1 has first inactivated syntaxin 1a by binding to the closed conformation, then a misplaced SNARE complex can form in intracellular membranes. In this thesis I have shown with quantitative co-localisation and TCPSC-FLIM/FRET studies that these misplaced SNARE complexes can form in the Golgi complex where they become trapped (Figures 4.3 and 4.4 respectively), perhaps involving a fourth SNARE helix provided by an intracellular SNARE protein. In the absence of munc18-1, the trapping of the t-SNAREs in the Golgi complex supports the observations that syntaxin can interact promiscuously with intracellular SNARE proteins (Fasshauer et al, 1999). This data is also in agreement with studies in which SNARE complexes can assemble in munc18-1 null mutant mice (Toonen et al, 2005), yet based on the complete blocking of neurotransmitter release in the munc18-1 null mutant mice (Verhage et al, 2000) these SNARE complexes may be non-functional. In contrast, when munc18-1 is present at the correct levels and the correct location, the t-SNAREs can traffic through the intracellular membrane system provided that syntaxin 1a is in the closed conformation bound to munc18-1 (Figure 4.6). Syntaxin 1a can remain inactive bound to munc18-1 in its closed conformation at the plasma membrane (Figure 3.6), while SNAP-25 can proceed via a syntaxin independent mechanism to the plasma membrane (Figure 4.1) and associate with the inner leaflet in agreement with a previous report (Loranger & Linder, 2002). I propose that at the plasma membrane, syntaxin 1a can remain bound to munc18-1 in its closed form until an as yet undefined factor or mechanism switches it to the open conformation to initiate binary and ternary SNARE complex assembly.

7.2.3 SYNTAXIN 1A AND SNAP-25 FORM HETEROGENOUS CLUSTERS AT THE PLASMA MEMBRANE

Upon delivery to the plasma membrane both endogenous and heterologous t-SNARE proteins can form clusters (Chapter 5). This is in agreement with previous studies in which a variety of imaging approaches have been applied to investigate SNARE clusters in various cell types (Lang et al, 2001; Lang et al, 2002; Ohara-Imaizumi et al, 2002; Rickman et al, 2004; Sieber et al, 2007). There has been significant interest in syntaxin micro-patterning at the plasma membrane, and using STED microscopy, this was recently advanced by the finding that syntaxin 1 clusters are smaller than previously thought at 60 nm (Sieber et al, 2007). These clusters were also suggested to contain approximately 75 densely packed syntaxin 1 molecules that dynamically exchange with freely diffusing molecules in the plasma membrane (Sieber et al, 2007). Based on the observations of this thesis, the data supports this model, whereby syntaxin traffics to the plasma membrane and dynamic syntaxin clusters can form by virtue of self association. While syntaxin is in the closed conformation bound to munc18-1, SNAP-25 is permitted to traffic independently of syntaxin, and subsequent targeting to lipid ordered membrane domains is possible due to palmitoylation via its cysteine rich linker region (Loranger & Linder, 2002). I have shown that both endogenous and heterologous syntaxin 1a and SNAP-25 clusters form at the cell surface in neuroendocrine cells (Figures 5.1 to 5.3), and furthermore that these t-SNARE clusters co-localise on the plasma membrane (Figure 5.4).

These clusters are thought to define sites of vesicle docking and exocytosis (Lang et al, 2001; Lang et al, 2002). However, it was never shown whether every cluster was fusion competent, or whether the t-SNAREs contained within each cluster interact before final fusion occurs. These experiments focused on inside-out plasma membrane sheets and showed that heterologous VAMP or syntaxin (yet not SNAP-25) interacted with pre-existing endogenous SNAREs in clusters (Lang et al, 2002). However, this phenomenon relied on "aged" membrane preparations instead of freshly prepared membrane sheets (Lang et al, 2002). These studies led to the present hypothesis that SNAREs are constitutively reactive and that no additional factor was required to prevent SNARE protein interactions (Lang et al, 2002). The data

presented in this thesis agrees with these findings, but it supports a different conclusion. I propose that syntaxin 1a is held in an inactive closed state by munc18-1, and it is therefore possible that the run-down of "aged" membrane sheet preparations is due to the loss of soluble munc18-1 and other cytoplasmic material. Additionally, the failure of additional SNAP-25 to enter into complexes (Lang et al, 2002) also supports our conclusion that some syntaxin is kept in an inactive state at the cell surface. The t-SNARE clusters are heterogeneous in their interaction status, with interactions modulated by elevations of intracellular Ca^{2+} levels (Figures 6.5 and 6.6). The t-SNAREs can interact at the plasma membrane even in the presence of a reduced binding affinity of SNAP-25 [G43D] mutant for syntaxin 1a (Figures 5.2, 6.7 and 6.8). However, one can not exclude the possibility that these interacting clusters may represent a conformational change due to the binding of synaptobrevin.

Numerous studies have implied that upon delivery to the plasma membrane, SNARE clusters are dependent upon cholesterol for their integrity, as cholesterol in part defines the lipid order of a membrane. This has led to the hypothesis that SNARE clusters are maintained in cholesterol rich micro-domains or membrane lipid "rafts" (Chamberlain et al, 2001). However, the raft hypothesis is controversial as much of this work has focused on detergent resistant membrane (DRM) techniques. Recent studies have suggested that DRMs are not the same as pre-existing rafts and that the detergent isolation technique may even induce the formation of artificial domains that are mistaken for rafts (Lichtenberg et al, 2005; van Rheenen et al, 2005). Detergent treatment is also carried out at 4 °C, which would alter the lipid phase of the membrane bilayer. In addition the composition of DRM fractions has also been found to depend on both the temperature and the concentration of detergent applied (Heerklotz, 2002) and thus a great deal of controversy currently exists over this approach. The marker Laurdan proves a useful tool in directly visualising and quantifying changes in the lipid phase in model living membranes as shown in this study (Chapter 6). The importance of cholesterol in ordered domain formation was supported in this study by a decrease in lipid order of the plasma membrane after cholesterol depletion in living cells (Figure 6.1). The biological relevance of lipid rafts remains controversial, yet it is evident that the localisation of the t-SNAREs

relative to lipid micro-domains has no effect on cluster integrity, yet it could have implications for their function.

I have presented evidence to show that t-SNARE organisation on the plasma membrane is regulated by two distinct factors: heterodimer interaction which is in turn regulated by lipid order. TCSPC-FLIM analysis of syntaxin 1a and SNAP-25, expressed in neuroendocrine cells, revealed that two spatially distinct populations of clusters containing different FRET efficiencies exist (Figure 6.7). I propose that the variance observed between different clusters is a result of different conformational states of the interaction of syntaxin 1a and SNAP-25 at the plasma membrane, spatially organised so that a t-SNARE cluster belongs to one of two distinct populations. This may suggest that some clusters are active while others are not, owing to alternative SNARE complex conformational states. The two distinct populations may represent two different syntaxin 1a and SNAP-25 complexes.

As the plasma membrane contains a mixture of two heterodimer complexes, arranged into distinct clusters, it was investigated if a change in the membrane environment, in particular depletion of cholesterol and disruption of lipid order, played a role in this organisation. Although cholesterol depletion had no effect on cluster stability at a microscopic level (Figures 6.3 and 6.4), it had a dramatic effect at the molecular level. Importantly, upon depletion of cholesterol and disruption of lipid order, a bimodal distribution was still evident, but the high FRET population was significantly reduced and the two t-SNARE heterodimer conformational states showed a shift towards a single conformational state (Figure 6.8A and B). When lipid order was coupled with a reduction in the binding affinity of SNAP-25 for syntaxin 1a a similar outcome was observed (Figure 6.8C and D). The high FRET population was reduced and this was evident as an increase in the intermediate FRET component, however, this effect was less pronounced than that observed in the wild-type complex. These data therefore indicate that lipid order results in a re-arrangement of t-SNARE cluster organisation at the plasma membrane.

Taken together, these data demonstrate that t-SNARE clusters on the plasma membrane are heterogeneous in their interaction status and that two distinct heterodimer complexes exist within individual clusters. The formation of suitable syntaxin 1a-SNAP-25 binary complexes may act as acceptor sites for synaptobrevin, and this may be an important regulatory step of SNARE protein function at the plasma membrane. Additionally, the lipid environment within which the t-SNARE clusters reside may influence the conformational states that they adopt. Therefore, I can conclude that t-SNARE protein organisation at the plasma membrane is influenced by both protein-protein interactions and the local lipid environment of the plasma membrane.

7.2.4 Significance of these findings in understanding the role syntaxin 1a conformations play in SNARE protein regulation

Previous studies reporting the role of munc18-1, in trafficking syntaxin 1a and its ability to interact with both the binary and ternary SNARE complexes, have produced conflicting data, so here I present a model based primarily on the simplest interpretation of munc18-1 function (Figure 7.1). It is clear that munc18-1 plays an essential role in trafficking syntaxin 1a to the plasma membrane, and it appears that the closed form of interaction is necessary for this function. I propose that the closed conformation of syntaxin 1a, in which the N-terminal Habc domain folds back over and interacts with the SNARE helix, maintains syntaxin 1a in an inactive state for sufficient trafficking to the plasma membrane by munc18-1. This enables syntaxin 1a to traffic through the ER and Golgi complex preventing any interactions with cognate SNARE proteins. After delivery to the plasma membrane an, at present, undefined factor or mechanism changes the conformation of syntaxin 1a from a closed state to an open state. In this open conformation, munc18-1 interacts with open syntaxin through an alternative N-terminal binding site. This allows open syntaxin 1a, bound to munc18-1 via its N-terminus, to interact with SNAP-25 and synaptobrevin simultaneously at the cell surface, forming the binary and ternary SNARE complexes and may exert a positive influence. Munc18-1 N-terminal binding may act in the same manner as yeast Sly1p by supporting the formation of

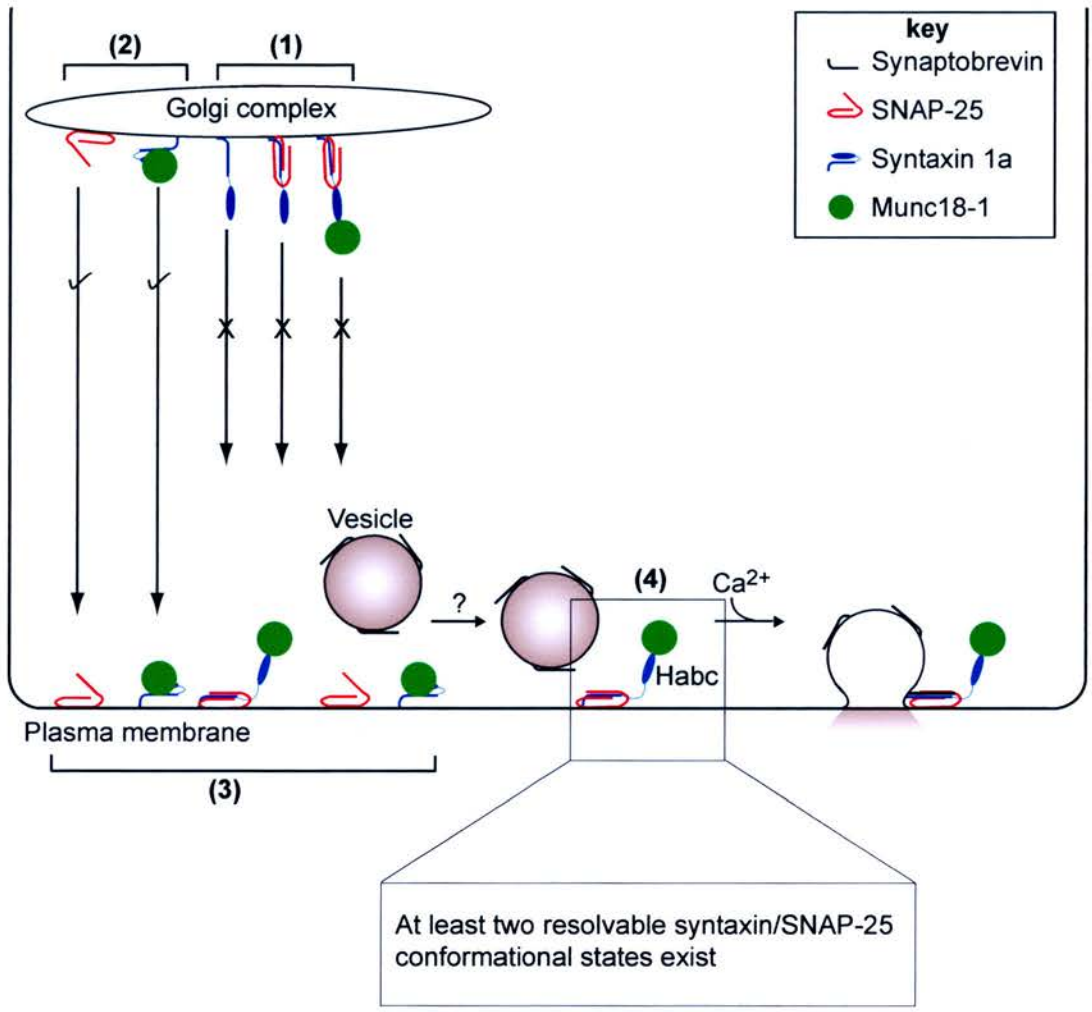

Figure 7.1 Proposed role of syntaxin 1a conformations and the targeting and regulation of t-SNAREs at the plasma membrane.

The open conformation of syntaxin 1a fails to traffic to the plasma membrane and can interact with SNAP-25 to form misplaced SNARE complexes that become trapped in the Golgi complex of living cells **(1)**. The closed conformation of syntaxin 1a bound to munc18-1 permits the trafficking of syntaxin 1a and the independent trafficking of SNAP-25 to the plasma membrane **(2)**. Once at the plasma membrane, an unknown factor switches syntaxin 1a to the open conformation in which munc18-1 adopts N-terminal binding **(3)**. In this open conformation syntaxin 1a can interact with SNAP-25 and synaptobrevin to form the binary and ternary SNARE complexes **(4)**. At the plasma membrane, the t-SNARE clusters are heterogeneous in their interaction status, with at least two resolvable syntaxin/SNAP-25 conformational states existing.

the binary and ternary SNARE complexes, but still maintaining an interaction with its cognate syntaxin. As munc18-1 can remain bound to syntaxin 1a throughout the formation of the binary and ternary SNARE complexes then it may remain bound to syntaxin 1a for its entire life cycle. Once at the plasma membrane, the t-SNARE clusters are heterogeneous in their interaction status. These heterogeneities between the t-SNARE clusters are due to heterodimer complexes between syntaxin 1a and SNAP-25 which exist in two different forms, and at the plasma membrane one or other become predominant in individual clusters. These t-SNARE clusters contain different functional conformations at the molecular level, organised by the protein-protein interactions and the local lipid environment of the plasma membrane.

7.3 CONCLUDING REMARKS

The findings presented here contribute to a greater understanding of the role that syntaxin 1a conformational states play in trafficking and regulating SNARE protein function, providing important insights into the spatially regulated molecular mechanisms regulating the biogenesis and function of SNARE complexes. Additionally, this investigation highlights the importance of combining *in vitro* biochemical data with quantitative imaging approaches to resolve protein function and molecular dynamics within living cells. Together, these approaches will be paramount in unravelling the molecular mechanisms which permit syntaxin 1a to switch from a closed to an open conformation at the plasma membrane to initiate final membrane fusion. As previously discussed (section 1.4.4), this may be due to a single protein, multiple proteins or an environmental factor such as the fatty acid composition of the plasma membrane. By understanding the molecular conformations adopted by proteins, and their spatial organisation within cells, this will ultimately lead to a fuller understanding of the molecular machinery of SNARE driven membrane fusion. Further work and development of the current technologies will ultimately lead to the ability to quantify protein dynamics in living cells to expose protein dynamics immediately before, during and after membrane fusion.

BIBLIOGRAPHY

Amos WB, White JG (2003) How the confocal laser scanning microscope entered biological research. *Biol Cell* **95**(6): 335-342

Amsterdam A, Lin S, Moss LG, Hopkins N (1996) Requirements for green fluorescent protein detection in transgenic zebrafish embryos. *Gene* **173**(1 Spec No)**:** 99-103

An SJ, Almers W (2004) Tracking SNARE complex formation in live endocrine cells. *Science* **306**(5698)**:** 1042-1046

Arunachalam L, Han L, Tassew NG, He Y, Wang L, Xie L, Fujita Y, Kwan E, Davletov B, Monnier PP, Gaisano HY, Sugita S (2008) Munc18-1 Is Critical for Plasma Membrane Localization of Syntaxin1 but Not of SNAP-25 in PC12 Cells. *Mol Biol Cell* **19**(2)**:** 722-734

Ashery U, Varoqueaux F, Voets T, Betz A, Thakur P, Koch H, Neher E, Brose N, Rettig J (2000) Munc13-1 acts as a priming factor for large dense-core vesicles in bovine chromaffin cells. *Embo J* **19**(14)**:** 3586-3596

Bacia K, Schuette CG, Kahya N, Jahn R, Schwille P (2004) SNAREs prefer liquid-disordered over "raft" (liquid-ordered) domains when reconstituted into giant unilamellar vesicles. *J Biol Chem* **279**(36)**:** 37951-37955

Balch WE, Dunphy WG, Braell WA, Rothman JE (1984) Reconstitution of the transport of protein between successive compartments of the Golgi measured by the coupled incorporation of N-acetylglucosamine. *Cell* **39**(2 Pt 1)**:** 405-416

Barclay JW, Craig TJ, Fisher RJ, Ciufo LF, Evans GJ, Morgan A, Burgoyne RD (2003) Phosphorylation of Munc18 by protein kinase C regulates the kinetics of exocytosis. *J Biol Chem* **278**(12)**:** 10538-10545

Barnstable CJ, Hofstein R, Akagawa K (1985) A marker of early amacrine cell development in rat retina. *Brain Res* **352**(2)**:** 286-290

Barr FA, Puype M, Vandekerckhove J, Warren G (1997) GRASP65, a protein involved in the stacking of Golgi cisternae. *Cell* **91**(2)**:** 253-262

Barr FA, Nakamura N, Warren G (1998) Mapping the interaction between GRASP65 and GM130, components of a protein complex involved in the stacking of Golgi cisternae. *Embo J* **17**(12)**:** 3258-3268

Bastiaens PI, Squire A (1999) Fluorescence lifetime imaging microscopy: spatial resolution of biochemical processes in the cell. *Trends Cell Biol* **9**(2)**:** 48-52

Baumert M, Maycox PR, Navone F, De Camilli P, Jahn R (1989) Synaptobrevin: an integral membrane protein of 18,000 daltons present in small synaptic vesicles of rat brain. *Embo J* **8**(2)**:** 379-384

Becker W, Bergmann A, Konig U, Tirlapur U (2001) Picosecond fluorescence lifetime microscopy by TCSPC imaging. *Proc SPIE* **4262:** 414-419

Becker W, Bergmann A, Biskup C, Zimmer T, Klocker N, Benndorf K (2002) Multi-wavelength TCSPC lifetime imaging. *Proc SPIE* **4620:** 79-84

Becker W, Bergmann A, Biscotti G, Ruck A (2004) Advanced time-correlated single photon counting technique for spectroscopy and imaging in biomedical systems *Proc SPIE* **5340:** 104-112

Becker W (2005) *Advanced Time-Correlated Single Photon Counting Techniques*, Berlin, Germany: Springer-Verlag Berlin Heidelberg.

Bellen HJ (ed) (1999) *Neurotransmitter Release*. New York: Oxford University Press

Bennett MK, Calakos N, Scheller RH (1992) Syntaxin: a synaptic protein implicated in docking of synaptic vesicles at presynaptic active zones. *Science* **257**(5067)**:** 255-259

Bennett MK, Garcia-Arraras JE, Elferink LA, Peterson K, Fleming AM, Hazuka CD, Scheller RH (1993) The syntaxin family of vesicular transport receptors. *Cell* **74**(5)**:** 863-873

Bennett MK, Scheller RH (1993) The molecular machinery for secretion is conserved from yeast to neurons. *Proc Natl Acad Sci U S A* **90**(7)**:** 2559-2563

Berns MW (1976) A possible two-photon effect in vitro using a focused laser beam. *Biophys J* **16**(8)**:** 973-977

Betz A, Okamoto M, Benseler F, Brose N (1997) Direct interaction of the rat unc-13 homologue Munc13-1 with the N terminus of syntaxin. *J Biol Chem* **272**(4)**:** 2520-2526

Betz A, Thakur P, Junge HJ, Ashery U, Rhee JS, Scheuss V, Rosenmund C, Rettig J, Brose N (2001) Functional interaction of the active zone proteins Munc13-1 and RIM1 in synaptic vesicle priming. *Neuron* **30**(1)**:** 183-196

Betz WJ, Bewick GS (1992) Optical analysis of synaptic vesicle recycling at the frog neuromuscular junction. *Science* **255**(5041)**:** 200-203

Bolte S, Cordelieres FP (2006) A guided tour into subcellular colocalization analysis in light microscopy. *J Microsc* **224**(Pt 3)**:** 213-232

Bousso P, Robey EA (2004) Dynamic behavior of T cells and thymocytes in lymphoid organs as revealed by two-photon microscopy. *Immunity* **21**(3)**:** 349-355

Bracher A, Weissenhorn W (2002) Structural basis for the Golgi membrane recruitment of Sly1p by Sed5p. *Embo J* **21**(22)**:** 6114-6124

Bracher A, Weissenhorn W (2004) Crystal structure of the Habc domain of neuronal syntaxin from the squid Loligo pealei reveals conformational plasticity at its C-terminus. *BMC Struct Biol* **4:** 6

Brechin C (2007) SNAREs, 14-3-3 proteins and cholesterol dependent membrane domains. PhD Thesis, Centre for Integrative Physiology, The University of Edinburgh, Edinburgh, UK

Brenner S (1974) The genetics of Caenorhabditis elegans. *Genetics* **77**(1): 71-94

Brennwald P, Kearns B, Champion K, Keranen S, Bankaitis V, Novick P (1994) Sec9 is a SNAP-25-like component of a yeast SNARE complex that may be the effector of Sec4 function in exocytosis. *Cell* **79**(2): 245-258

Bryant NJ, James DE (2001) Vps45p stabilizes the syntaxin homologue Tlg2p and positively regulates SNARE complex formation. *Embo J* **20**(13): 3380-3388

Burgess TL, Kelly RB (1987) Constitutive and regulated secretion of proteins. *Annu Rev Cell Biol* **3**: 243-293

Burgoyne RD, Morgan A (2003) Secretory granule exocytosis. *Physiol Rev* **83**(2): 581-632

Burkhardt P, Hattendorf DA, Weis WI, Fasshauer D (2008) Munc18a controls SNARE assembly through its interaction with the syntaxin N-peptide. *Embo J* **27**(7): 923-933

Cahalan MD, Parker I, Wei SH, Miller MJ (2003) Real-time imaging of lymphocytes in vivo. *Curr Opin Immunol* **15**(4): 372-377

Calakos N, Bennett MK, Peterson KE, Scheller RH (1994) Protein-protein interactions contributing to the specificity of intracellular vesicular trafficking. *Science* **263**(5150): 1146-1149

Callis PR (1997) Two-photon-induced fluorescence. *Annu Rev Phys Chem* **48**: 271-297

Campbell RE, Tour O, Palmer AE, Steinbach PA, Baird GS, Zacharias DA, Tsien RY (2002) A monomeric red fluorescent protein. *Proc Natl Acad Sci U S A* **99**(12): 7877-7882

Carpp LN, Ciufo LF, Shanks SG, Boyd A, Bryant NJ (2006) The Sec1p/Munc18 protein Vps45p binds its cognate SNARE proteins via two distinct modes. *J Cell Biol* **173**(6): 927-936

Carr CM, Grote E, Munson M, Hughson FM, Novick PJ (1999) Sec1p binds to SNARE complexes and concentrates at sites of secretion. *J Cell Biol* **146**(2): 333-344

Casper SJ, Holt CA (1996) Expression of the green fluorescent protein-encoding gene from a tobacco mosaic virus-based vector. *Gene* **173**(1 Spec No): 69-73

Centonze VE, White JG (1998) Multiphoton excitation provides optical sections from deeper within scattering specimens than confocal imaging. *Biophys J* **75**(4)**:** 2015-2024

Centonze VE, Sun M, Masuda A, Gerritsen H, Herman B (2003) Fluorescence resonance energy transfer imaging microscopy. *Methods Enzymol* **360:** 542-560

Chalfie M, Tu Y, Euskirchen G, Ward WW, Prasher DC (1994) Green fluorescent protein as a marker for gene expression. *Science* **263**(5148)**:** 802-805

Chalfie M (1995) Green fluorescent protein. *Photochem Photobiol* **62**(4)**:** 651-656

Chamberlain LH, Burgoyne RD, Gould GW (2001) SNARE proteins are highly enriched in lipid rafts in PC12 cells: implications for the spatial control of exocytosis. *Proc Natl Acad Sci U S A* **98**(10)**:** 5619-5624

Chamberlain LH, Gould GW (2002) The vesicle- and target-SNARE proteins that mediate Glut4 vesicle fusion are localized in detergent-insoluble lipid rafts present on distinct intracellular membranes. *J Biol Chem* **277**(51)**:** 49750-49754

Chapman ER, An S, Barton N, Jahn R (1994) SNAP-25, a t-SNARE which binds to both syntaxin and synaptobrevin via domains that may form coiled coils. *J Biol Chem* **269**(44)**:** 27427-27432

Chen Y, Mills JD, Periasamy A (2003) Protein localization in living cells and tissues using FRET and FLIM. *Differentiation* **71**(9-10)**:** 528-541

Chen YA, Scheller RH (2001) SNARE-mediated membrane fusion. *Nat Rev Mol Cell Biol* **2**(2)**:** 98-106

Clary DO, Griff IC, Rothman JE (1990) SNAPs, a family of NSF attachment proteins involved in intracellular membrane fusion in animals and yeast. *Cell* **61**(4)**:** 709-721

Clary DO, Rothman JE (1990) Purification of three related peripheral membrane proteins needed for vesicular transport. *J Biol Chem* **265**(17)**:** 10109-10117

Clayton EL, Cousin MA (2008) Differential labelling of bulk endocytosis in nerve terminals by FM dyes. *Neurochem Int* **53**(3-4)**:** 51-55

Cochilla AJ, Angleson JK, Betz WJ (1999) Monitoring secretory membrane with FM1-43 fluorescence. *Annu Rev Neurosci* **22:** 1-10

Cody CW, Prasher DC, Westler WM, Prendergast FG, Ward WW (1993) Chemical structure of the hexapeptide chromophore of the Aequorea green-fluorescent protein. *Biochemistry* **32**(5)**:** 1212-1218

Cole MJ, Siegel J, Webb SE, Jones R, Dowling K, Dayel MJ, Parsons-Karavassilis D, French PM, Lever MJ, Sucharov LO, Neil MA, Juskaitis R, Wilson T (2001)

Time-domain whole-field fluorescence lifetime imaging with optical sectioning. *J Microsc* **203**(Pt 3)**:** 246-257

Connell E, Darios F, Broersen K, Gatsby N, Peak-Chew SY, Rickman C, Davletov B (2007) Mechanism of arachidonic acid action on syntaxin-Munc18. *EMBO Rep* **8**(4)**:** 414-419

Cormack BP, Valdivia RH, Falkow S (1996) FACS-optimized mutants of the green fluorescent protein (GFP). *Gene* **173**(1 Spec No)**:** 33-38

Cousin MA, Robinson PJ (1999) Mechanisms of synaptic vesicle recycling illuminated by fluorescent dyes. *J Neurochem* **73**(6)**:** 2227-2239

Craig TJ, Evans GJ, Morgan A (2003) Physiological regulation of Munc18/nSec1 phosphorylation on serine-313. *J Neurochem* **86**(6)**:** 1450-1457

Darios F, Davletov B (2006) Omega-3 and omega-6 fatty acids stimulate cell membrane expansion by acting on syntaxin 3. *Nature* **440**(7085)**:** 813-817

Day RN, Piston DW (1999) Spying on the hidden lives of proteins. *Nat Biotechnol* **17**(5)**:** 425-426

Day RN, Schaufele F (2005) Imaging molecular interactions in living cells. *Mol Endocrinol* **19**(7)**:** 1675-1686

de Wit H, Cornelisse LN, Toonen RF, Verhage M (2006) Docking of secretory vesicles is syntaxin dependent. *PLoS ONE* **1:** e126

Denk W, Strickler JH, Webb WW (1990) Two-photon laser scanning fluorescence microscopy. *Science* **248**(4951)**:** 73-76

Denk W, Svoboda K (1997) Photon upmanship: why multiphoton imaging is more than a gimmick. *Neuron* **18**(3)**:** 351-357

Diaspro A (2002) *Confocal and Two-Photon Microscopy: Foundations, Applications and Advances*, New York: Wiley-Liss.

Diaspro A, Bianchini P, Vicidomini G, Faretta M, Ramoino P, Usai C (2006) Multi-photon excitation microscopy. *Biomed Eng Online* **5:** 36

Dodson G, Steiner D (1998) The role of assembly in insulin's biosynthesis. *Curr Opin Struct Biol* **8**(2)**:** 189-194

Dulubova I, Sugita S, Hill S, Hosaka M, Fernandez I, Sudhof TC, Rizo J (1999) A conformational switch in syntaxin during exocytosis: role of munc18. *Embo J* **18**(16)**:** 4372-4382

Dulubova I, Yamaguchi T, Arac D, Li H, Huryeva I, Min SW, Rizo J, Sudhof TC (2003) Convergence and divergence in the mechanism of SNARE binding by Sec1/Munc18-like proteins. *Proc Natl Acad Sci U S A* **100**(1)**:** 32-37

Dulubova I, Khvotchev M, Liu S, Huryeva I, Sudhof TC, Rizo J (2007) Munc18-1 binds directly to the neuronal SNARE complex. *Proc Natl Acad Sci U S A* **104**(8): 2697-2702

Dumas D, Gaborit N, Grossin L, Riquelme B, Gigant-Huselstein C, De Isla N, Gillet P, Netter P, Stoltz JF (2004) Spectral and lifetime fluorescence imaging microscopies: new modalities of multiphoton microscopy applied to tissue or cell engineering. *Biorheology* **41**(3-4): 459-467

Duncan RR, Greaves J, Wiegand UK, Matskevich I, Bodammer G, Apps DK, Shipston MJ, Chow RH (2003) Functional and spatial segregation of secretory vesicle pools according to vesicle age. *Nature* **422**(6928): 176-180

Duncan RR, Bergmann A, Cousin MA, Apps DK, Shipston MJ (2004) Multi-dimensional time-correlated single photon counting (TCSPC) fluorescence lifetime imaging microscopy (FLIM) to detect FRET in cells. *J Microsc* **215**(Pt 1): 1-12

Eftink MR (1991) Fluorescence quenching: Theory and application. *In: JR Lakowicz, Topics in fluorescence spectroscopy* **2:** 53-126

Elangovan M, Day RN, Periasamy A (2002) Nanosecond fluorescence resonance energy transfer-fluorescence lifetime imaging microscopy to localize the protein interactions in a single living cell. *J Microsc* **205**(Pt 1): 3-14

Epel BL, Padgett HS, Heinlein M, Beachy RN (1996) Plant virus movement protein dynamics probed with a GFP-protein fusion. *Gene* **173**(1 Spec No): 75-79

Esposito A, Federici F, Usai C, Cannone F, Chirico G, Collini M, Diaspro A (2004) Notes on theory and experimental conditions behind two-photon excitation microscopy. *Microsc Res Tech* **63**(1): 12-17

Fasshauer D, Bruns D, Shen B, Jahn R, Brunger AT (1997) A structural change occurs upon binding of syntaxin to SNAP-25. *J Biol Chem* **272**(7): 4582-4590

Fasshauer D, Sutton RB, Brunger AT, Jahn R (1998) Conserved structural features of the synaptic fusion complex: SNARE proteins reclassified as Q- and R-SNAREs. *Proc Natl Acad Sci U S A* **95**(26): 15781-15786

Fasshauer D, Antonin W, Margittai M, Pabst S, Jahn R (1999) Mixed and non-cognate SNARE complexes. Characterization of assembly and biophysical properties. *J Biol Chem* **274**(22): 15440-15446

Fasshauer D (2003) Structural insights into the SNARE mechanism. *Biochim Biophys Acta* **1641**(2-3): 87-97

Fasshauer D, Margittai M (2004) A transient N-terminal interaction of SNAP-25 and syntaxin nucleates SNARE assembly. *J Biol Chem* **279**(9): 7613-7621

Fernandez I, Ubach J, Dulubova I, Zhang X, Sudhof TC, Rizo J (1998) Three-dimensional structure of an evolutionarily conserved N-terminal domain of syntaxin 1A. *Cell* **94**(6): 841-849

Ferro-Novick S, Jahn R (1994) Vesicle fusion from yeast to man. *Nature* **370**(6486): 191-193

Fischer von Mollard G, Stahl B, Li C, Sudhof TC, Jahn R (1994) Rab proteins in regulated exocytosis. *Trends Biochem Sci* **19**(4): 164-168

Fisher RJ, Burgoyne RD (1999) The effect of transfection with Botulinum neurotoxin C1 light chain on exocytosis measured in cell populations and by single-cell amperometry in PC12 cells. *Pflugers Arch* **437**(5): 754-762

Fix M, Melia TJ, Jaiswal JK, Rappoport JZ, You D, Sollner TH, Rothman JE, Simon SM (2004) Imaging single membrane fusion events mediated by SNARE proteins. *Proc Natl Acad Sci U S A* **101**(19): 7311-7316

Fletcher AI, Shuang R, Giovannucci DR, Zhang L, Bittner MA, Stuenkel EL (1999) Regulation of exocytosis by cyclin-dependent kinase 5 via phosphorylation of Munc18. *J Biol Chem* **274**(7): 4027-4035

Förster T (1946) Energiewanderung und Fluoreszenz *Naturwissenschaften* **6:** 166-175

Förster T (1965) Delocalized excitation and excitation transfer. *In Sinanoglu, O (ed) Modern quantum chemistry* **3:** 93-137

Fries E, Rothman JE (1980) Transport of vesicular stomatitis virus glycoprotein in a cell-free extract. *Proc Natl Acad Sci U S A* **77**(7): 3870-3874

Fujita Y, Sasaki T, Fukui K, Kotani H, Kimura T, Hata Y, Sudhof TC, Scheller RH, Takai Y (1996) Phosphorylation of Munc-18/n-Sec1/rbSec1 by protein kinase C: its implication in regulating the interaction of Munc-18/n-Sec1/rbSec1 with syntaxin. *J Biol Chem* **271**(13): 7265-7268

Gaisano HY, Ostenson CG, Sheu L, Wheeler MB, Efendic S (2002) Abnormal expression of pancreatic islet exocytotic soluble N-ethylmaleimide-sensitive factor attachment protein receptors in Goto-Kakizaki rats is partially restored by phlorizin treatment and accentuated by high glucose treatment. *Endocrinology* **143**(11): 4218-4226

Garcia EP, Gatti E, Butler M, Burton J, De Camilli P (1994) A rat brain Sec1 homologue related to Rop and UNC18 interacts with syntaxin. *Proc Natl Acad Sci U S A* **91**(6): 2003-2007

Gaus K, Gratton E, Kable EP, Jones AS, Gelissen I, Kritharides L, Jessup W (2003) Visualizing lipid structure and raft domains in living cells with two-photon microscopy. *Proc Natl Acad Sci U S A* **100**(26): 15554-15559

Gaus K, Chklovskaia E, Fazekas de St Groth B, Jessup W, Harder T (2005) Condensation of the plasma membrane at the site of T lymphocyte activation. *J Cell Biol* **171**(1)**:** 121-131

Gaus K, Zech T, Harder T (2006) Visualizing membrane microdomains by Laurdan 2-photon microscopy. *Mol Membr Biol* **23**(1)**:** 41-48

Gerber SH, Rah JC, Min SW, Liu X, de Wit H, Dulubova I, Meyer AC, Rizo J, Arancillo M, Hammer RE, Verhage M, Rosenmund C, Sudhof TC (2008) Conformational Switch of Syntaxin-1 Controls Synaptic Vesicle Fusion. *Science* **321**(5895)**:** 1507-1510

Gerst JE (1999) SNAREs and SNARE regulators in membrane fusion and exocytosis. *Cell Mol Life Sci* **55**(5)**:** 707-734

Gerst JE (2003) SNARE regulators: matchmakers and matchbreakers. *Biochim Biophys Acta* **1641**(2-3)**:** 99-110

Gillis KD, Mossner R, Neher E (1996) Protein kinase C enhances exocytosis from chromaffin cells by increasing the size of the readily releasable pool of secretory granules. *Neuron* **16**(6)**:** 1209-1220

Glick BS, Rothman JE (1987) Possible role for fatty acyl-coenzyme A in intracellular protein transport. *Nature* **326**(6110)**:** 309-312

Gonzalo S, Greentree WK, Linder ME (1999) SNAP-25 is targeted to the plasma membrane through a novel membrane-binding domain. *J Biol Chem* **274**(30)**:** 21313-21318

Göppert-Mayer M (1931) Über Elementarakte mit zwei Quantensprüngen (On elementary processes with two quantum steps). *Ann Phys* **9**

Gordon GW, Berry G, Liang XH, Levine B, Herman B (1998) Quantitative fluorescence resonance energy transfer measurements using fluorescence microscopy. *Biophys J* **74**(5)**:** 2702-2713

Granseth B, Odermatt B, Royle SJ, Lagnado L (2007) Clathrin-mediated endocytosis: the physiological mechanism of vesicle retrieval at hippocampal synapses. *J Physiol* **585**(Pt 3)**:** 681-686

Griffiths G, Simons K (1986) The trans Golgi network: sorting at the exit site of the Golgi complex. *Science* **234**(4775)**:** 438-443

Gu Y, Di WL, Kelsell DP, Zicha D (2004) Quantitative fluorescence resonance energy transfer (FRET) measurement with acceptor photobleaching and spectral unmixing. *J Microsc* **215**(Pt 2)**:** 162-173

Guan KL, Dixon JE (1991) Eukaryotic proteins expressed in Escherichia coli: an improved thrombin cleavage and purification procedure of fusion proteins with glutathione S-transferase. *Anal Biochem* 192(2): 262-267

Gundelfinger ED, Kessels MM, Qualmann B (2003) Temporal and spatial coordination of exocytosis and endocytosis. *Nat Rev Mol Cell Biol* **4**(2)**:** 127-139

Hanson PI, Otto H, Barton N, Jahn R (1995) The N-ethylmaleimide-sensitive fusion protein and alpha-SNAP induce a conformational change in syntaxin. *J Biol Chem* **270**(28)**:** 16955-16961

Harrison SD, Broadie K, van de Goor J, Rubin GM (1994) Mutations in the Drosophila Rop gene suggest a function in general secretion and synaptic transmission. *Neuron* **13**(3)**:** 555-566

Hata Y, Slaughter CA, Sudhof TC (1993) Synaptic vesicle fusion complex contains unc-18 homologue bound to syntaxin. *Nature* **366**(6453)**:** 347-351

Hayashi T, McMahon H, Yamasaki S, Binz T, Hata Y, Sudhof TC, Niemann H (1994) Synaptic vesicle membrane fusion complex: action of clostridial neurotoxins on assembly. *Embo J* **13**(21)**:** 5051-5061

Heerklotz H (2002) Triton promotes domain formation in lipid raft mixtures. *Biophys J* **83**(5)**:** 2693-2701

Heim R, Prasher DC, Tsien RY (1994) Wavelength mutations and posttranslational autoxidation of green fluorescent protein. *Proc Natl Acad Sci U S A* **91**(26)**:** 12501-12504

Heim R, Cubitt AB, Tsien RY (1995) Improved green fluorescence. *Nature* **373**(6516)**:** 663-664

Helmchen F, Denk W (2002) New developments in multiphoton microscopy. *Curr Opin Neurobiol* **12**(5)**:** 593-601

Helmchen F, Denk W (2005) Deep tissue two-photon microscopy. *Nat Methods* **2**(12)**:** 932-940

Hess DT, Slater TM, Wilson MC, Skene JH (1992) The 25 kDa synaptosomal-associated protein SNAP-25 is the major methionine-rich polypeptide in rapid axonal transport and a major substrate for palmitoylation in adult CNS. *J Neurosci* **12**(12)**:** 4634-4641

Hille B, Billiard J, Babcock DF, Nguyen T, Koh DS (1999) Stimulation of exocytosis without a calcium signal. *J Physiol* **520 Pt 1:** 23-31

Hink MA, Bisselin T, Visser AJ (2002) Imaging protein-protein interactions in living cells. *Plant Mol Biol* **50**(6)**:** 871-883

Hinz B, Becher A, Mitter D, Schulze K, Heinemann U, Draguhn A, Ahnert-Hilger G (2001) Activity-dependent changes of the presynaptic synaptophysin-synaptobrevin complex in adult rat brain. *Eur J Cell Biol* **80**(10)**:** 615-619

Hu K, Carroll J, Fedorovich S, Rickman C, Sukhodub A, Davletov B (2002) Vesicular restriction of synaptobrevin suggests a role for calcium in membrane fusion. *Nature* **415**(6872)**:** 646-650

Hu SH, Latham CF, Gee CL, James DE, Martin JL (2007) Structure of the Munc18c/Syntaxin4 N-peptide complex defines universal features of the N-peptide binding mode of Sec1/Munc18 proteins. *Proc Natl Acad Sci U S A* **104**(21)**:** 8773-8778

Inoue A, Akagawa K (1992) Neuron-specific antigen HPC-1 from bovine brain reveals strong homology to epimorphin, an essential factor involved in epithelial morphogenesis: identification of a novel protein family. *Biochem Biophys Res Commun* **187**(2)**:** 1144-1150

Inoué S (1995) *Foundations of Confocal Scanned Imaging in Light Microscopy*. New York: Plenum Press.

Jacobsson G, Bean AJ, Scheller RH, Juntti-Berggren L, Deeney JT, Berggren PO, Meister B (1994) Identification of synaptic proteins and their isoform mRNAs in compartments of pancreatic endocrine cells. *Proc Natl Acad Sci U S A* **91**(26)**:** 12487-12491

Jahn R, Sudhof TC (1999) Membrane fusion and exocytosis. *Annu Rev Biochem* **68:** 863-911

Jahn R, Lang T, Sudhof TC (2003) Membrane fusion. *Cell* **112**(4)**:** 519-533

Jahn R (2004) Principles of exocytosis and membrane fusion. *Ann N Y Acad Sci* **1014:** 170-178

Jamieson JD, Palade GE (1967) Intracellular transport of secretory proteins in the pancreatic exocrine cell. I. Role of the peripheral elements of the Golgi complex. *J Cell Biol* **34**(2)**:** 577-596

Kaether C, Gerdes HH (1995) Visualization of protein transport along the secretory pathway using green fluorescent protein. *FEBS Lett* **369**(2-3)**:** 267-271

Kahana JA, Schnapp BJ, Silver PA (1995) Kinetics of spindle pole body separation in budding yeast. *Proc Natl Acad Sci U S A* **92**(21)**:** 9707-9711

Kaiser W, Garrett CBG (1961) Two-photon excitation in CaF_2:Eu^{2+} *Physiol Rev Lett* **7:** 229-231

Kamphuis W, Smirnova T, Hicks A, Hendriksen H, Mallet J, Lopes da Silva FH (1995) The expression of syntaxin1B/GR33 mRNA is enhanced in the hippocampal kindling model of epileptogenesis. *J Neurochem* **65**(5)**:** 1974-1980

Kee Y, Lin RC, Hsu SC, Scheller RH (1995) Distinct domains of syntaxin are required for synaptic vesicle fusion complex formation and dissociation. *Neuron* **14**(5)**:** 991-998

Kilsdonk EP, Yancey PG, Stoudt GW, Bangerter FW, Johnson WJ, Phillips MC, Rothblat GH (1995) Cellular cholesterol efflux mediated by cyclodextrins. *J Biol Chem* **270**(29): 17250-17256

Kuliawat R, Kalinina E, Bock J, Fricker L, McGraw TE, Kim SR, Zhong J, Scheller R, Arvan P (2004) Syntaxin-6 SNARE involvement in secretory and endocytic pathways of cultured pancreatic beta-cells. *Mol Biol Cell* **15**(4): 1690-1701

Lagnado L, Gomis A, Job C (1996) Continuous vesicle cycling in the synaptic terminal of retinal bipolar cells. *Neuron* **17**(5): 957-967

Laiho LH, Pelet S, Hancewicz TM, Kaplan PD, So PT (2005) Two-photon 3-D mapping of ex vivo human skin endogenous fluorescence species based on fluorescence emission spectra. *J Biomed Opt* **10**(2): 024016

Lakowicz JR, Szmacinski H, Nowaczyk K, Berndt KW, Johnson M (1992) Fluorescence lifetime imaging. *Anal Biochem* **202**(2): 316-330

Lakowicz JR (2006) *Principles of Fluorescence Spectroscopy*, 3rd edn. New York: Springer.

Lam PP, Leung YM, Sheu L, Ellis J, Tsushima RG, Osborne LR, Gaisano HY (2005) Transgenic mouse overexpressing syntaxin-1A as a diabetes model. *Diabetes* **54**(9): 2744-2754

Lang T, Wacker I, Steyer J, Kaether C, Wunderlich I, Soldati T, Gerdes HH, Almers W (1997) Ca2+-triggered peptide secretion in single cells imaged with green fluorescent protein and evanescent-wave microscopy. *Neuron* **18**(6): 857-863

Lang T, Bruns D, Wenzel D, Riedel D, Holroyd P, Thiele C, Jahn R (2001) SNAREs are concentrated in cholesterol-dependent clusters that define docking and fusion sites for exocytosis. *Embo J* **20**(9): 2202-2213

Lang T, Margittai M, Holzler H, Jahn R (2002) SNAREs in native plasma membranes are active and readily form core complexes with endogenous and exogenous SNAREs. *J Cell Biol* **158**(4): 751-760

Latham CF, Lopez JA, Hu SH, Gee CL, Westbury E, Blair DH, Armishaw CJ, Alewood PF, Bryant NJ, James DE, Martin JL (2006) Molecular dissection of the Munc18c/syntaxin4 interaction: implications for regulation of membrane trafficking. *Traffic* **7**(10): 1408-1419

Lerman JC, Robblee J, Fairman R, Hughson FM (2000) Structural analysis of the neuronal SNARE protein syntaxin-1A. *Biochemistry* **39**(29): 8470-8479

Lichtenberg D, Goni FM, Heerklotz H (2005) Detergent-resistant membranes should not be identified with membrane rafts. *Trends Biochem Sci* **30**(8): 430-436

Littleton JT, Barnard RJ, Titus SA, Slind J, Chapman ER, Ganetzky B (2001) SNARE-complex disassembly by NSF follows synaptic-vesicle fusion. *Proc Natl Acad Sci U S A* **98**(21): 12233-12238

Liu J, Ernst SA, Gladycheva SE, Lee YY, Lentz SI, Ho CS, Li Q, Stuenkel EL (2004) Fluorescence resonance energy transfer reports properties of syntaxin1a interaction with Munc18-1 in vivo. *J Biol Chem* **279**(53): 55924-55936

Liu T, Tucker WC, Bhalla A, Chapman ER, Weisshaar JC (2005) SNARE-driven, 25-millisecond vesicle fusion in vitro. *Biophys J* **89**(4): 2458-2472

Loranger SS, Linder ME (2002) SNAP-25 traffics to the plasma membrane by a syntaxin-independent mechanism. *J Biol Chem* **277**(37): 34303-34309

Ludin B, Doll T, Meili R, Kaech S, Matus A (1996) Application of novel vectors for GFP-tagging of proteins to study microtubule-associated proteins. *Gene* **173**(1 Spec No): 107-111

Ma L, Bindokas VP, Kuznetsov A, Rhodes C, Hays L, Edwardson JM, Ueda K, Steiner DF, Philipson LH (2004) Direct imaging shows that insulin granule exocytosis occurs by complete vesicle fusion. *Proc Natl Acad Sci U S A* **101**(25): 9266-9271

Majewski H, Iannazzo L (1998) Protein kinase C: a physiological mediator of enhanced transmitter output. *Prog Neurobiol* **55**(5): 463-475

Manders EEM, Verbeek FJ, Aten JA (1993) Measurement of co-localisation of objects in dual-colour confocal images. *Journal of Microscopy* **169**: 375-382

Martinez-Arca S, Rudge R, Vacca M, Raposo G, Camonis J, Proux-Gillardeaux V, Daviet L, Formstecher E, Hamburger A, Filippini F, D'Esposito M, Galli T (2003) A dual mechanism controlling the localization and function of exocytic v-SNAREs. *Proc Natl Acad Sci U S A* **100**(15): 9011-9016

McNally JG, Karpova T, Cooper J, Conchello JA (1999) Three-dimensional imaging by deconvolution microscopy. *Methods* **19**(3): 373-385

Medine CN, McDonald A, Bergmann A, Duncan RR (2007a) Time-correlated single photon counting FLIM: some considerations for physiologists. *Microsc Res Tech* **70**(5): 420-425

Medine CN, Rickman C, Chamberlain LH, Duncan RR (2007b) Munc18-1 prevents the formation of ectopic SNARE complexes in living cells. *J Cell Sci* **120**(Pt 24): 4407-4415

Misura KM, May AP, Weis WI (2000a) Protein-protein interactions in intracellular membrane fusion. *Curr Opin Struct Biol* **10**(6): 662-671

Misura KM, Scheller RH, Weis WI (2000b) Three-dimensional structure of the neuronal-Sec1-syntaxin 1a complex. *Nature* **404**(6776): 355-362

Molitoris BA, Sandoval RM (2005) Intravital multiphoton microscopy of dynamic renal processes. *Am J Physiol Renal Physiol* **288**(6): F1084-1089

Morin JG, Hastings JW (1971) Biochemistry of the bioluminescence of colonial hydroids and other coelenterates. *J Cell Physiol* **77**(3): 305-312

Morise H, Shimomura O, Johnson FH, Winant J (1974) Intermolecular energy transfer in the bioluminescent system of Aequorea. *Biochemistry* **13**(12): 2656-2662

Müller M (2002) *Introduction to Confocal Fluorescence Microscopy*, Maastricht, Netherlands: Shaker.

Munson M, Hughson FM (2002) Conformational regulation of SNARE assembly and disassembly in vivo. *J Biol Chem* **277**(11): 9375-9381

Nagamatsu S, Nakamichi Y, Yamamura C, Matsushima S, Watanabe T, Ozawa S, Furukawa H, Ishida H (1999) Decreased expression of t-SNARE, syntaxin 1, and SNAP-25 in pancreatic beta-cells is involved in impaired insulin secretion from diabetic GK rat islets: restoration of decreased t-SNARE proteins improves impaired insulin secretion. *Diabetes* **48**(12): 2367-2373

Nichols BJ, Ungermann C, Pelham HR, Wickner WT, Haas A (1997) Homotypic vacuolar fusion mediated by t- and v-SNAREs. *Nature* **387**(6629): 199-202

Nicholson KL, Munson M, Miller RB, Filip TJ, Fairman R, Hughson FM (1998) Regulation of SNARE complex assembly by an N-terminal domain of the t-SNARE Sso1p. *Nat Struct Biol* **5**(9): 793-802

Novick P, Schekman R (1979) Secretion and cell-surface growth are blocked in a temperature-sensitive mutant of Saccharomyces cerevisiae. *Proc Natl Acad Sci U S A* **76**(4): 1858-1862

Novick P, Field C, Schekman R (1980) Identification of 23 complementation groups required for post-translational events in the yeast secretory pathway. *Cell* **21**(1): 205-215

Novick P, Ferro S, Schekman R (1981) Order of events in the yeast secretory pathway. *Cell* **25**(2): 461-469

Ohara-Imaizumi M, Nakamichi Y, Nishiwaki C, Nagamatsu S (2002) Transduction of MIN6 beta cells with TAT-syntaxin SNARE motif inhibits insulin exocytosis in biphasic insulin release in a distinct mechanism analyzed by evanescent wave microscopy. *J Biol Chem* **277**(52): 50805-50811

Ohara-Imaizumi M, Nishiwaki C, Kikuta T, Kumakura K, Nakamichi Y, Nagamatsu S (2004a) Site of docking and fusion of insulin secretory granules in live MIN6 beta cells analyzed by TAT-conjugated anti-syntaxin 1 antibody and total internal reflection fluorescence microscopy. *J Biol Chem* **279**(9): 8403-8408

Ohara-Imaizumi M, Nishiwaki C, Kikuta T, Nagai S, Nakamichi Y, Nagamatsu S (2004b) TIRF imaging of docking and fusion of single insulin granule motion in primary rat pancreatic beta-cells: different behaviour of granule motion between normal and Goto-Kakizaki diabetic rat beta-cells. *Biochem J* **381**(Pt 1)**:** 13-18

Ohara-Imaizumi M, Nishiwaki C, Nakamichi Y, Kikuta T, Nagai S, Nagamatsu S (2004c) Correlation of syntaxin-1 and SNAP-25 clusters with docking and fusion of insulin granules analysed by total internal reflection fluorescence microscopy. *Diabetologia* **47**(12)**:** 2200-2207

Oheim M, Beaurepaire E, Chaigneau E, Mertz J, Charpak S (2001) Two-photon microscopy in brain tissue: parameters influencing the imaging depth. *J Neurosci Methods* **111**(1)**:** 29-37

Ormo M, Cubitt AB, Kallio K, Gross LA, Tsien RY, Remington SJ (1996) Crystal structure of the Aequorea victoria green fluorescent protein. *Science* **273**(5280)**:** 1392-1395

Oyler GA, Higgins GA, Hart RA, Battenberg E, Billingsley M, Bloom FE, Wilson MC (1989) The identification of a novel synaptosomal-associated protein, SNAP-25, differentially expressed by neuronal subpopulations. *J Cell Biol* **109**(6 Pt 1)**:** 3039-3052

Palade G (1975) Intracellular Aspects of the Process of Protein Synthesis. *Science* **189**(4206)**:** 867

Parasassi T, De Stasio G, d'Ubaldo A, Gratton E (1990) Phase fluctuation in phospholipid membranes revealed by Laurdan fluorescence. *Biophys J* **57**(6)**:** 1179-1186

Parasassi T, Di Stefano M, Loiero M, Ravagnan G, Gratton E (1994a) Cholesterol modifies water concentration and dynamics in phospholipid bilayers: a fluorescence study using Laurdan probe. *Biophys J* **66**(3 Pt 1)**:** 763-768

Parasassi T, Di Stefano M, Loiero M, Ravagnan G, Gratton E (1994b) Influence of cholesterol on phospholipid bilayers phase domains as detected by Laurdan fluorescence. *Biophys J* **66**(1)**:** 120-132

Parasassi T, Gratton E, Yu WM, Wilson P, Levi M (1997) Two-photon fluorescence microscopy of laurdan generalized polarization domains in model and natural membranes. *Biophys J* **72**(6)**:** 2413-2429

Parlati F, Weber T, McNew JA, Westermann B, Sollner TH, Rothman JE (1999) Rapid and efficient fusion of phospholipid vesicles by the alpha-helical core of a SNARE complex in the absence of an N-terminal regulatory domain. *Proc Natl Acad Sci U S A* **96**(22)**:** 12565-12570

Pawley JB (ed) (1995) Handbook of Biological Confocal Microscopy. New York: Plenum Press

Pawley JB (ed) (2006) Handbook of Biological Confocal Microscopy. 2nd ed. New York: Springer

Periasamy A, Elangovan M, Elliott E, Brautigan DL (2002) Fluorescence lifetime imaging (FLIM) of green fluorescent fusion proteins in living cells. *Methods Mol Biol* **183:** 89-100

Pevsner J, Hsu SC, Braun JE, Calakos N, Ting AE, Bennett MK, Scheller RH (1994a) Specificity and regulation of a synaptic vesicle docking complex. *Neuron* **13**(2)**:** 353-361

Pevsner J, Hsu SC, Scheller RH (1994b) n-Sec1: a neural-specific syntaxin-binding protein. *Proc Natl Acad Sci U S A* **91**(4)**:** 1445-1449

Pitha J, Irie T, Sklar PB, Nye JS (1988) Drug solubilizers to aid pharmacologists: amorphous cyclodextrin derivatives. *Life Sci* **43**(6)**:** 493-502

Prasher DC, Eckenrode VK, Ward WW, Prendergast FG, Cormier MJ (1992) Primary structure of the Aequorea victoria green-fluorescent protein. *Gene* **111**(2)**:** 229-233

Predescu SA, Predescu DN, Shimizu K, Klein IK, Malik AB (2005) Cholesterol-dependent syntaxin-4 and SNAP-23 clustering regulates caveolar fusion with the endothelial plasma membrane. *J Biol Chem* **280**(44)**:** 37130-37138

Rickman C, Meunier FA, Binz T, Davletov B (2004) High affinity interaction of syntaxin and SNAP-25 on the plasma membrane is abolished by botulinum toxin E. *J Biol Chem* **279**(1)**:** 644-651

Rickman C, Davletov B (2005) Arachidonic acid allows SNARE complex formation in the presence of Munc18. *Chem Biol* **12**(5)**:** 545-553

Rickman C, Medine CN, Bergmann A, Duncan RR (2007) Functionally and spatially distinct modes of munc18-syntaxin 1 interaction. *J Biol Chem* **282**(16)**:** 12097-12103

Rizzo MA, Springer GH, Granada B, Piston DW (2004) An improved cyan fluorescent protein variant useful for FRET. *Nat Biotechnol* **22**(4)**:** 445-449

Rizzo MA, Springer G, Segawa K, Zipfel WR, Piston DW (2006) Optimization of pairings and detection conditions for measurement of FRET between cyan and yellow fluorescent proteins. *Microsc Microanal* **12**(3)**:** 238-254

Rizzoli SO, Betz WJ (2004) The structural organization of the readily releasable pool of synaptic vesicles. *Science* **303**(5666)**:** 2037-2039

Rorsman P, Renstrom E (2003) Insulin granule dynamics in pancreatic beta cells. *Diabetologia* **46**(8)**:** 1029-1045

Rothman JE, Fries E (1981) Transport of newly synthesized vesicular stomatitis viral glycoprotein to purified Golgi membranes. *J Cell Biol* **89**(1)**:** 162-168

Rothman JE (1994a) Intracellular membrane fusion. *Adv Second Messenger Phosphoprotein Res* **29:** 81-96

Rothman JE (1994b) Mechanisms of intracellular protein transport. *Nature* **372**(6501)**:** 55-63

Rowe J, Corradi N, Malosio ML, Taverna E, Halban P, Meldolesi J, Rosa P (1999) Blockade of membrane transport and disassembly of the Golgi complex by expression of syntaxin 1A in neurosecretion-incompetent cells: prevention by rbSEC1. *J Cell Sci* **112 (Pt 12):** 1865-1877

Rowe J, Calegari F, Taverna E, Longhi R, Rosa P (2001) Syntaxin 1A is delivered to the apical and basolateral domains of epithelial cells: the role of munc-18 proteins. *J Cell Sci* **114**(Pt 18)**:** 3323-3332

Rubart M (2004) Two-photon microscopy of cells and tissue. *Circ Res* **95**(12)**:** 1154-1166

Salaun C, James DJ, Greaves J, Chamberlain LH (2004) Plasma membrane targeting of exocytic SNARE proteins. *Biochim Biophys Acta* **1693**(2)**:** 81-89

Salaun C, Gould GW, Chamberlain LH (2005a) The SNARE proteins SNAP-25 and SNAP-23 display different affinities for lipid rafts in PC12 cells. Regulation by distinct cysteine-rich domains. *J Biol Chem* **280**(2)**:** 1236-1240

Salaun C, Gould GW, Chamberlain LH (2005b) Lipid raft association of SNARE proteins regulates exocytosis in PC12 cells. *J Biol Chem* **280**(20)**:** 19449-19453

Salzberg A, Cohen N, Halachmi N, Kimchie Z, Lev Z (1993) The Drosophila Ras2 and Rop gene pair: a dual homology with a yeast Ras-like gene and a suppressor of its loss-of-function phenotype. *Development* **117**(4)**:** 1309-1319

Schatten G, Pawley JB (1988) Advances in optical, confocal, and electron microscopic imaging for biomedical researchers. *Science* **239**(4841 Pt 2)**:** G164,G148

Schutz D, Zilly F, Lang T, Jahn R, Bruns D (2005) A dual function for Munc-18 in exocytosis of PC12 cells. *Eur J Neurosci* **21**(9)**:** 2419-2432

Sekar RB, Periasamy A (2003) Fluorescence resonance energy transfer (FRET) microscopy imaging of live cell protein localizations. *J Cell Biol* **160**(5)**:** 629-633

Shen N, Guryev O, Rizo J (2005) Intramolecular occlusion of the diacylglycerol-binding site in the C1 domain of munc13-1. *Biochemistry* **44**(4)**:** 1089-1096

Shen J, Tareste DC, Paumet F, Rothman JE, Melia TJ (2007) Selective activation of cognate SNAREpins by Sec1/Munc18 proteins. *Cell* **128**(1)**:** 183-195

Sheu L, Pasyk EA, Ji J, Huang X, Gao X, Varoqueaux F, Brose N, Gaisano HY (2003) Regulation of insulin exocytosis by Munc13-1. *J Biol Chem* **278**(30)**:** 27556-27563

Shimohama S, Kamiya S, Taniguchi T, Akagawa K, Kimura J (1997) Differential involvement of synaptic vesicle and presynaptic plasma membrane proteins in Alzheimer's disease. *Biochem Biophys Res Commun* **236**(2)**:** 239-242

Shimomura O, Johnson FH, Saiga Y (1962) Extraction, purification and properties of aequorin, a bioluminescent protein from the luminous hydromedusan, Aequorea. *J Cell Comp Physiol* **59:** 223-239

Shimomura O (1979) Structure of the chromophore of Aequorea green fluorescent protein. *FEBS Letters* **104**: 220-22.

Sibarita JB (2005) Deconvolution microscopy. *Adv Biochem Eng Biotechnol* **95:** 201-243

Sieber JJ, Willig KI, Heintzmann R, Hell SW, Lang T (2006) The SNARE motif is essential for the formation of syntaxin clusters in the plasma membrane. *Biophys J* **90**(8)**:** 2843-2851

Sieber JJ, Willig KI, Kutzner C, Gerding-Reimers C, Harke B, Donnert G, Rammner B, Eggeling C, Hell SW, Grubmuller H, Lang T (2007) Anatomy and dynamics of a supramolecular membrane protein cluster. *Science* **317**(5841)**:** 1072-1076

Sogaard M, Tani K, Ye RR, Geromanos S, Tempst P, Kirchhausen T, Rothman JE, Sollner T (1994) A rab protein is required for the assembly of SNARE complexes in the docking of transport vesicles. *Cell* **78**(6)**:** 937-948

Sollner T, Bennett MK, Whiteheart SW, Scheller RH, Rothman JE (1993a) A protein assembly-disassembly pathway in vitro that may correspond to sequential steps of synaptic vesicle docking, activation, and fusion. *Cell* **75**(3)**:** 409-418

Sollner T, Whiteheart SW, Brunner M, Erdjument-Bromage H, Geromanos S, Tempst P, Rothman JE (1993b) SNAP receptors implicated in vesicle targeting and fusion. *Nature* **362**(6418)**:** 318-324

Stevens DR, Wu ZX, Matti U, Junge HJ, Schirra C, Becherer U, Wojcik SM, Brose N, Rettig J (2005) Identification of the minimal protein domain required for priming activity of Munc13-1. *Curr Biol* **15**(24)**:** 2243-2248

Straub M, Lodemann P, Holroyd P, Jahn R, Hell SW (2000) Live cell imaging by multifocal multiphoton microscopy. *Eur J Cell Biol* **79**(10)**:** 726-734

Stryer L, Haugland RP (1967) Energy transfer: a spectroscopic ruler. *Proc Natl Acad Sci U S A* **58**(2)**:** 719-726

Stryer L (1978) Fluorescence energy transfer as a spectroscopic ruler. *Annu Rev Biochem* **47:** 819-846

Sudhof TC, Baumert M, Perin MS, Jahn R (1989) A synaptic vesicle membrane protein is conserved from mammals to Drosophila. *Neuron* **2**(5)**:** 1475-1481

Sudhof TC (2004) The synaptic vesicle cycle. *Annu Rev Neurosci* **27:** 509-547

Sutton RB, Fasshauer D, Jahn R, Brunger AT (1998) Crystal structure of a SNARE complex involved in synaptic exocytosis at 2.4 A resolution. *Nature* **395**(6700)**:** 347-353

Sze CI, Bi H, Kleinschmidt-DeMasters BK, Filley CM, Martin LJ (2000) Selective regional loss of exocytotic presynaptic vesicle proteins in Alzheimer's disease brains. *J Neurol Sci* **175**(2)**:** 81-90

Takahashi N, Kishimoto T, Nemoto T, Kadowaki T, Kasai H (2002) Fusion pore dynamics and insulin granule exocytosis in the pancreatic islet. *Science* **297**(5585)**:** 1349-1352

Taverna E, Saba E, Rowe J, Francolini M, Clementi F, Rosa P (2004) Role of lipid microdomains in P/Q-type calcium channel (Cav2.1) clustering and function in presynaptic membranes. *J Biol Chem* **279**(7)**:** 5127-5134

Taverna E, Saba E, Linetti A, Longhi R, Jeromin A, Righi M, Clementi F, Rosa P (2007) Localization of synaptic proteins involved in neurosecretion in different membrane microdomains. *J Neurochem* **100**(3)**:** 664-677

Teng FY, Wang Y, Tang BL (2001) The syntaxins. *Genome Biol* **2**(11)**:** REVIEWS3012

Theer P, Hasan MT, Denk W (2003) Two-photon imaging to a depth of 1000 microm in living brains by use of a Ti:Al2O3 regenerative amplifier. *Opt Lett* **28**(12)**:** 1022-1024

Toonen RF (2003) Role of Munc18-1 in synaptic vesicle and large dense-core vesicle secretion. *Biochem Soc Trans* **31**(Pt 4)**:** 848-850

Toonen RF, de Vries KJ, Zalm R, Sudhof TC, Verhage M (2005) Munc18-1 stabilizes syntaxin 1, but is not essential for syntaxin 1 targeting and SNARE complex formation. *J Neurochem* **93**(6)**:** 1393-1400

Toonen RF, Verhage M (2007) Munc18-1 in secretion: lonely Munc joins SNARE team and takes control. *Trends Neurosci* **30**(11)**:** 564-572

Trimble WS, Cowan DM, Scheller RH (1988) VAMP-1: a synaptic vesicle-associated integral membrane protein. *Proc Natl Acad Sci U S A* **85**(12)**:** 4538-4542

Tsien RY (1998) The green fluorescent protein. *Annu Rev Biochem* **67:** 509-544

Tsien RY, Miyawaki A (1998) Seeing the machinery of live cells. *Science* **280**(5371): 1954-1955

Ungermann C, Nichols BJ, Pelham HR, Wickner W (1998) A vacuolar v-t-SNARE complex, the predominant form in vivo and on isolated vacuoles, is disassembled and activated for docking and fusion. *J Cell Biol* **140**(1): 61-69

van Rheenen J, Achame EM, Janssen H, Calafat J, Jalink K (2005) PIP2 signaling in lipid domains: a critical re-evaluation. *Embo J* **24**(9): 1664-1673

van Roessel P, Brand AH (2002) Imaging into the future: visualizing gene expression and protein interactions with fluorescent proteins. *Nat Cell Biol* **4**(1): E15-20

Veit M, Sollner TH, Rothman JE (1996) Multiple palmitoylation of synaptotagmin and the t-SNARE SNAP-25. *FEBS Lett* **385**(1-2): 119-123

Verhage M, Maia AS, Plomp JJ, Brussaard AB, Heeroma JH, Vermeer H, Toonen RF, Hammer RE, van den Berg TK, Missler M, Geuze HJ, Sudhof TC (2000) Synaptic assembly of the brain in the absence of neurotransmitter secretion. *Science* **287**(5454): 864-869

Verkhusha VV, Lukyanov KA (2004) The molecular properties and applications of Anthozoa fluorescent proteins and chromoproteins. *Nat Biotechnol* **22**(3): 289-296

Verveer PJ, Squire A, Bastiaens PI (2001) Improved spatial discrimination of protein reaction states in cells by global analysis and deconvolution of fluorescence lifetime imaging microscopy data. *J Microsc* **202**(Pt 3): 451-456

Vieira OV, Gaus K, Verkade P, Fullekrug J, Vaz WL, Simons K (2006) FAPP2, cilium formation, and compartmentalization of the apical membrane in polarized Madin-Darby canine kidney (MDCK) cells. *Proc Natl Acad Sci U S A* **103**(49): 18556-18561

Voets T, Toonen RF, Brian EC, de Wit H, Moser T, Rettig J, Sudhof TC, Neher E, Verhage M (2001) Munc18-1 promotes large dense-core vesicle docking. *Neuron* **31**(4): 581-591

Voss TC, Demarco IA, Day RN (2005) Quantitative imaging of protein interactions in the cell nucleus. *Biotechniques* **38**(3): 413-424

Wallace W, Schaefer LH, Swedlow JR (2001) A workingperson's guide to deconvolution in light microscopy. *Biotechniques* **31**(5): 1076-1078, 1080, 1082 passim

Wang S, Hazelrigg T (1994) Implications for bcd mRNA localization from spatial distribution of exu protein in Drosophila oogenesis. *Nature* **369**(6479): 400-403

Ward WW, Cormier MJ (1979) An energy transfer protein in coelenterate bioluminescence. Characterization of the Renilla green-fluorescent protein. *J Biol Chem* **254**(3): 781-788

Weber T, Zemelman BV, McNew JA, Westermann B, Gmachl M, Parlati F, Sollner TH, Rothman JE (1998) SNAREpins: minimal machinery for membrane fusion. *Cell* **92**(6): 759-772

Weimbs T, Low SH, Chapin SJ, Mostov KE, Bucher P, Hofmann K (1997) A conserved domain is present in different families of vesicular fusion proteins: a new superfamily. *Proc Natl Acad Sci U S A* **94**(7): 3046-3051

Weninger K, Bowen ME, Choi UB, Chu S, Brunger AT (2008) Accessory proteins stabilize the acceptor complex for synaptobrevin, the 1:1 syntaxin/SNAP-25 complex. *Structure* **16**(2): 308-320

Wheeler MB, Sheu L, Ghai M, Bouquillon A, Grondin G, Weller U, Beaudoin AR, Bennett MK, Trimble WS, Gaisano HY (1996) Characterization of SNARE protein expression in beta cell lines and pancreatic islets. *Endocrinology* **137**(4): 1340-1348

Wilson DW, Wilcox CA, Flynn GC, Chen E, Kuang WJ, Henzel WJ, Block MR, Ullrich A, Rothman JE (1989) A fusion protein required for vesicle-mediated transport in both mammalian cells and yeast. *Nature* **339**(6223): 355-359

Wouters FS, Verveer PJ, Bastiaens PI (2001) Imaging biochemistry inside cells. *Trends Cell Biol* **11**(5): 203-211

Wu P, Brand L (1994) Resonance energy transfer: methods and applications. *Anal Biochem* **218**(1): 1-13

Xia Z, Liu Y (2001) Reliable and global measurement of fluorescence resonance energy transfer using fluorescence microscopes. *Biophys J* **81**(4): 2395-2402

Xia Z, Zhou Q, Lin J, Liu Y (2001) Stable SNARE complex prior to evoked synaptic vesicle fusion revealed by fluorescence resonance energy transfer. *J Biol Chem* **276**(3): 1766-1771

Yang B, Steegmaier M, Gonzalez LC, Jr., Scheller RH (2000) nSec1 binds a closed conformation of syntaxin1A. *J Cell Biol* **148**(2): 247-252

Yang F, Moss LG, Phillips GN, Jr. (1996) The molecular structure of green fluorescent protein. *Nat Biotechnol* **14**(10): 1246-1251

Yerrapureddy A, Korte T, Hollmann S, Nordhoff M, Ahnert-Hilger G, Herrmann A, Veit M (2005) Intracellular interaction between syntaxin and Munc 18-1 revealed by fluorescence resonance energy transfer. *Mol Membr Biol* **22**(5): 401-410

Zacharias DA, Violin JD, Newton AC, Tsien RY (2002) Partitioning of lipid-modified monomeric GFPs into membrane microdomains of live cells. *Science* **296**(5569)**:** 913-916

Zhang W, Khan A, Ostenson CG, Berggren PO, Efendic S, Meister B (2002) Down-regulated expression of exocytotic proteins in pancreatic islets of diabetic GK rats. *Biochem Biophys Res Commun* **291**(4)**:** 1038-1044

Zhang Y, Su Z, Zhang F, Chen Y, Shin YK (2005) A partially zipped SNARE complex stabilized by the membrane. *J Biol Chem* **280**(16)**:** 15595-15600

APPENDIX 1

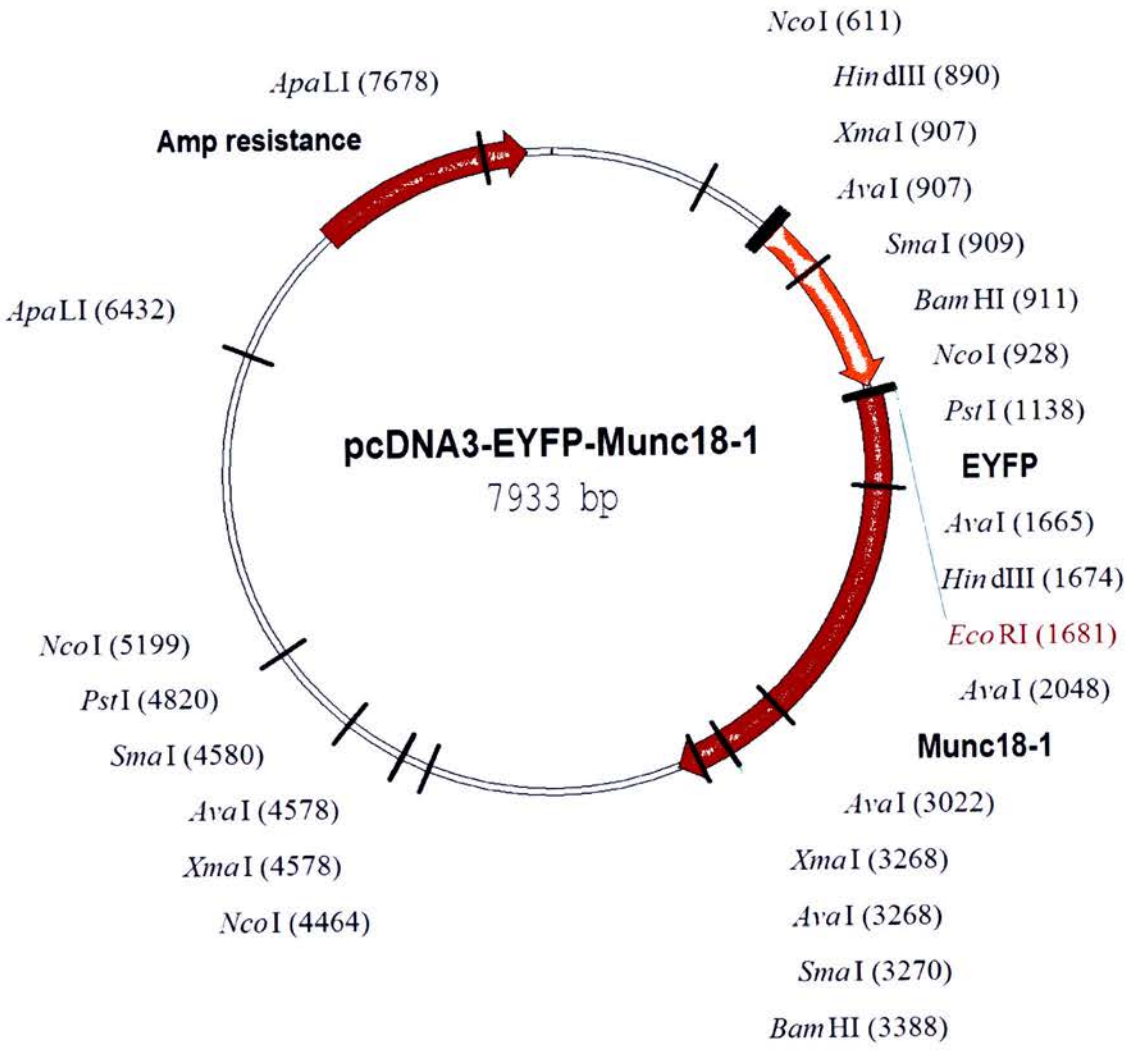
NcoI (611)
HindIII (890)
XmaI (907)
AvaI (907)
SmaI (909)
BamHI (911)
NcoI (928)
PstI (1138)
EYFP
AvaI (1665)
HindIII (1674)
EcoRI (1681)
AvaI (2048)
Munc18-1
AvaI (3022)
XmaI (3268)
AvaI (3268)
SmaI (3270)
BamHI (3388)
NcoI (4464)
XmaI (4578)
AvaI (4578)
SmaI (4580)
PstI (4820)
NcoI (5199)
ApaLI (6432)
Amp resistance
ApaLI (7678)
pcDNA3-EYFP-Munc18-1
7933 bp

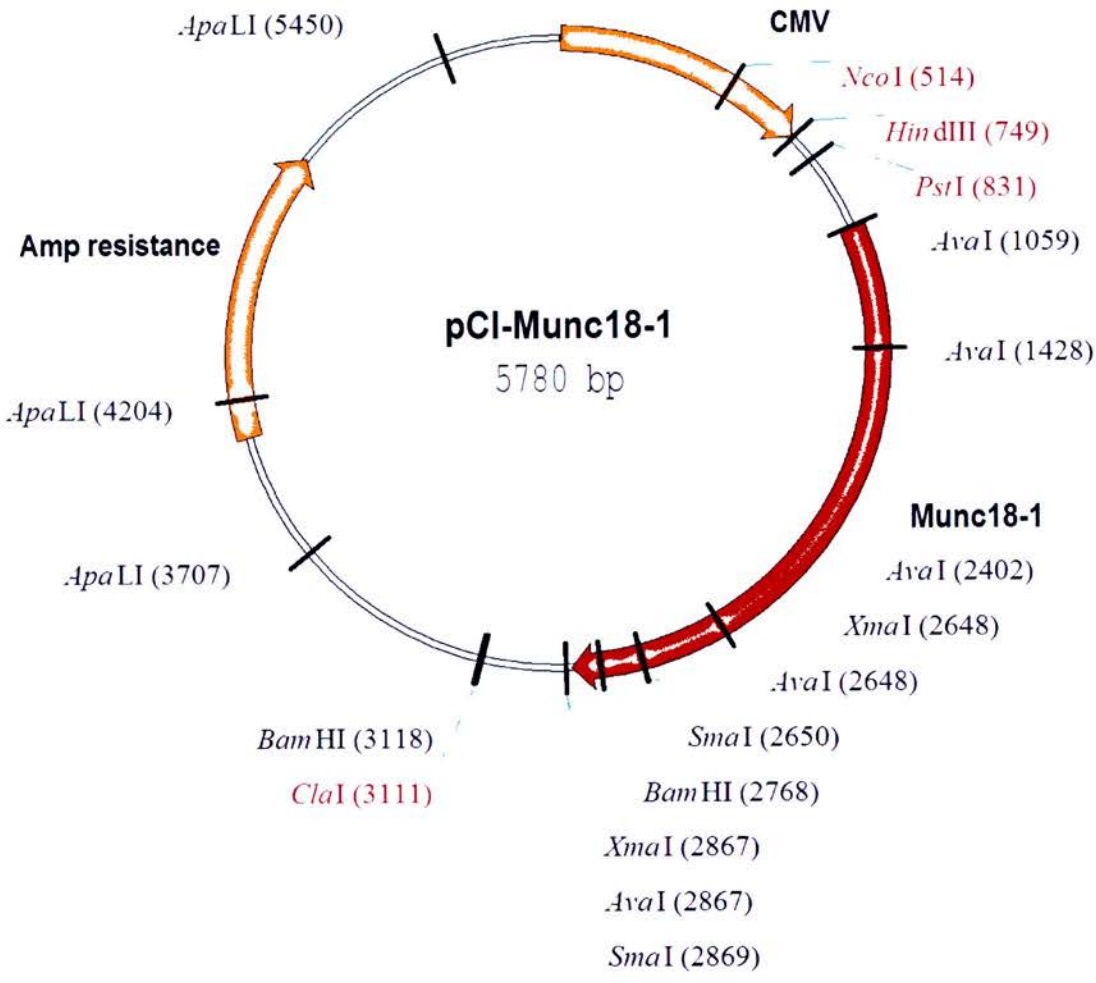
ApaLI (5450)
CMV
NcoI (514)
HindIII (749)
PstI (831)
AvaI (1059)
AvaI (1428)
Munc18-1
AvaI (2402)
XmaI (2648)
AvaI (2648)
SmaI (2650)
BamHI (2768)
XmaI (2867)
AvaI (2867)
SmaI (2869)
BamHI (3118)
ClaI (3111)
ApaLI (3707)
ApaLI (4204)
Amp resistance
pCI-Munc18-1
5780 bp

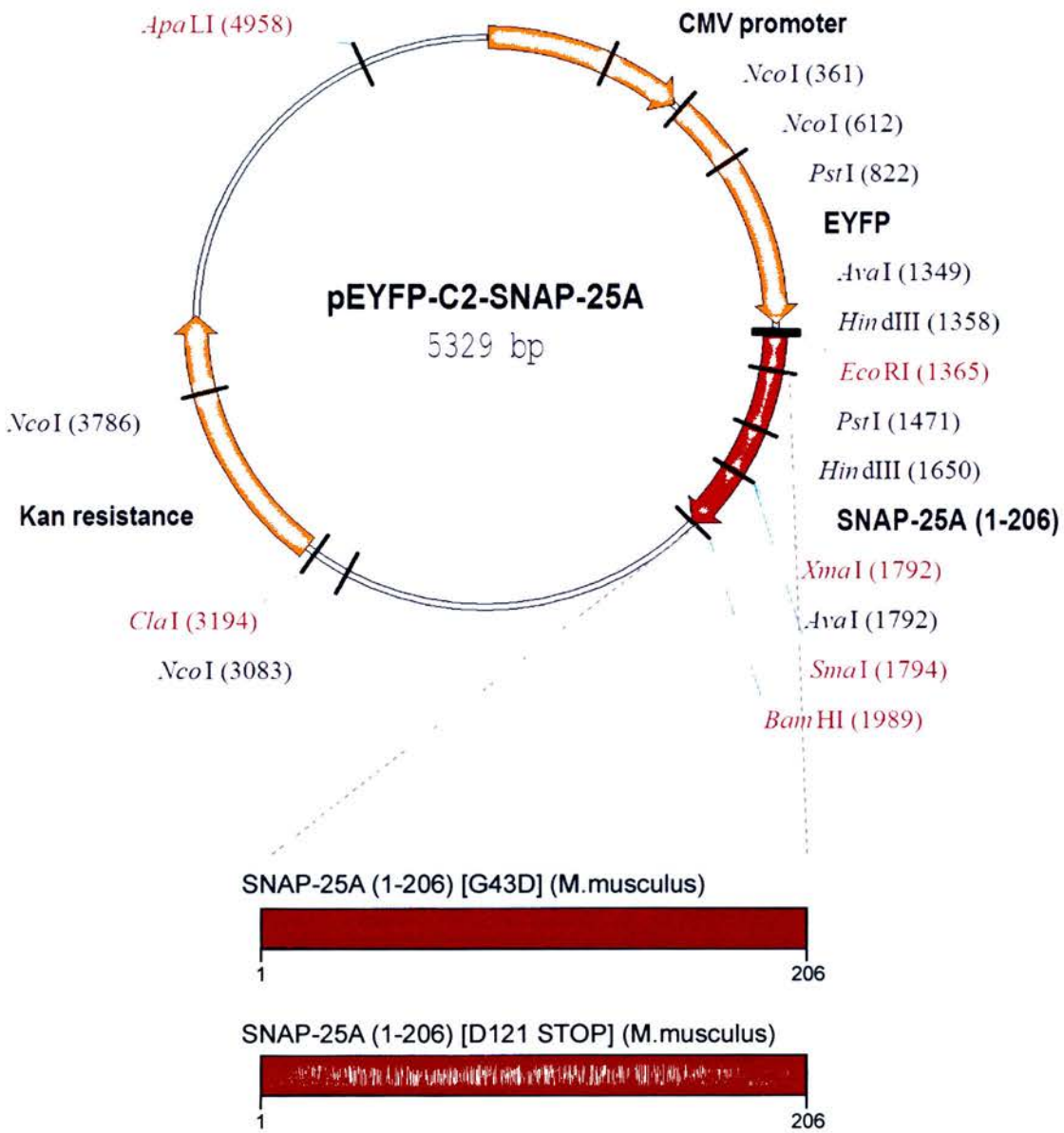
ApaLI (4958)
CMV promoter
NcoI (361)
NcoI (612)
PstI (822)
EYFP
AvaI (1349)
HindIII (1358)
EcoRI (1365)
PstI (1471)
HindIII (1650)
SNAP-25A (1-206)
XmaI (1792)
AvaI (1792)
SmaI (1794)
BamHI (1989)
pEYFP-C2-SNAP-25A
5329 bp
NcoI (3786)
Kan resistance
ClaI (3194)
NcoI (3083)
SNAP-25A (1-206) [G43D] (M.musculus)
1
206
SNAP-25A (1-206) [D121 STOP] (M.musculus)
1
206

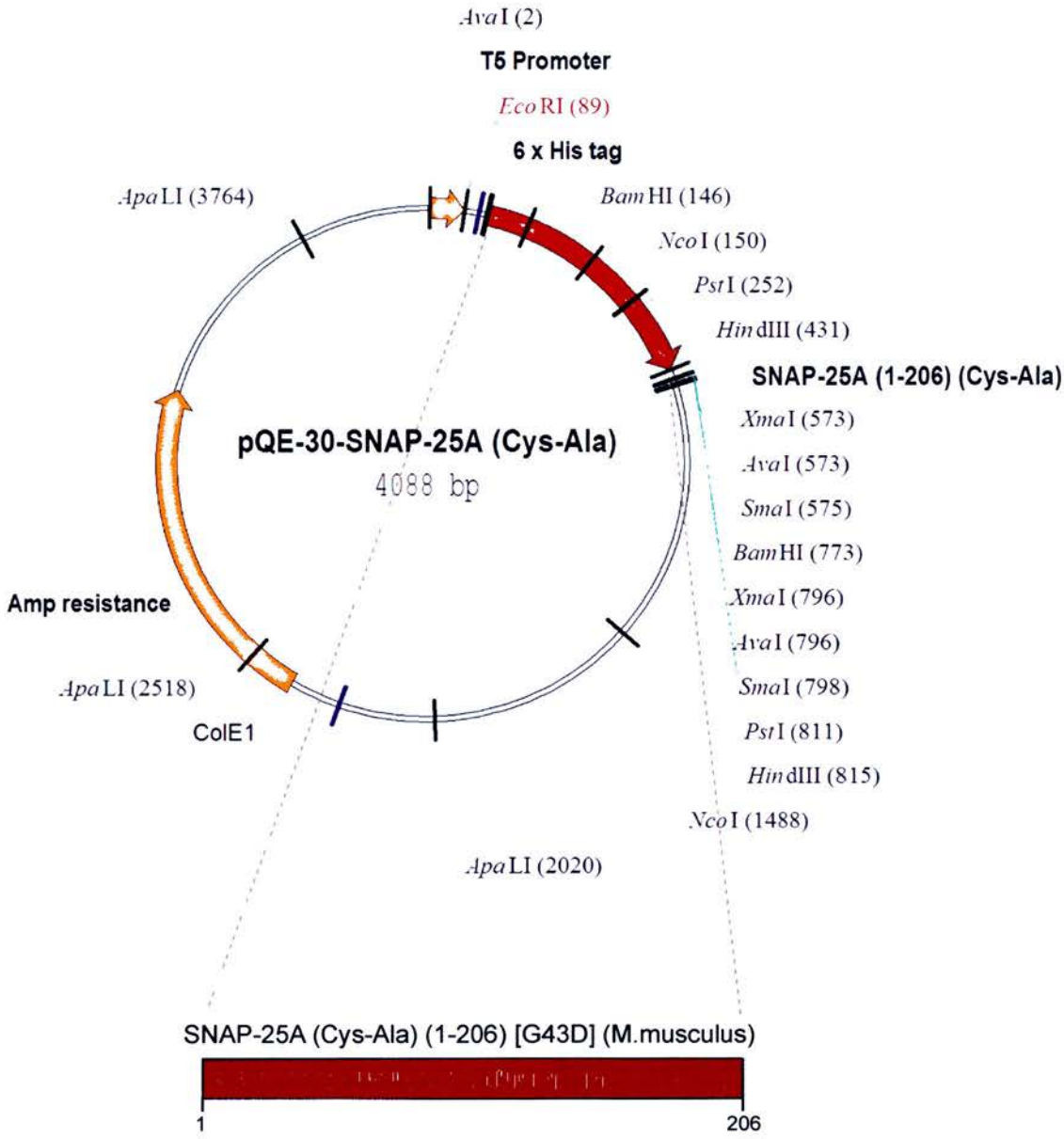
AvaI (2)
T5 Promoter
EcoRI (89)
6 x His tag
ApaLI (3764)
BamHI (146)
NcoI (150)
PstI (252)
HindIII (431)
SNAP-25A (1-206) (Cys-Ala)
XmaI (573)
AvaI (573)
SmaI (575)
BamHI (773)
XmaI (796)
AvaI (796)
SmaI (798)
PstI (811)
HindIII (815)
NcoI (1488)
pQE-30-SNAP-25A (Cys-Ala)
4088 bp
Amp resistance
ApaLI (2518)
ColE1
ApaLI (2020)
SNAP-25A (Cys-Ala) (1-206) [G43D] (M.musculus)
1
206

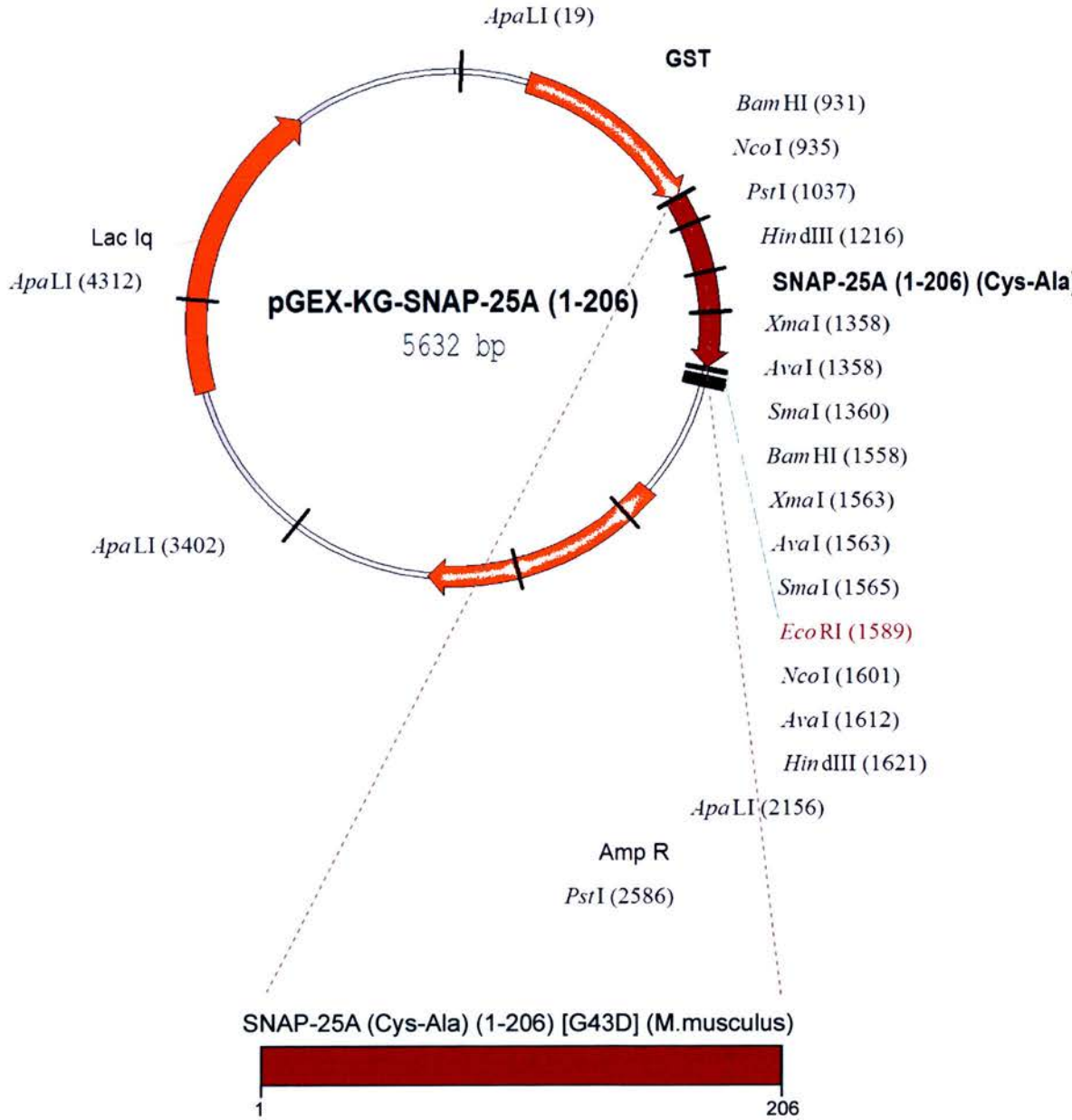
ApaLI (19)
GST
BamHI (931)
NcoI (935)
PstI (1037)
HindIII (1216)
SNAP-25A (1-206) (Cys-Ala)
XmaI (1358)
AvaI (1358)
SmaI (1360)
BamHI (1558)
XmaI (1563)
AvaI (1563)
SmaI (1565)
EcoRI (1589)
NcoI (1601)
AvaI (1612)
HindIII (1621)
ApaLI (2156)
Amp R
PstI (2586)
ApaLI (3402)
Lac Iq
ApaLI (4312)
pGEX-KG-SNAP-25A (1-206)
5632 bp
SNAP-25A (Cys-Ala) (1-206) [G43D] (M.musculus)
1
206

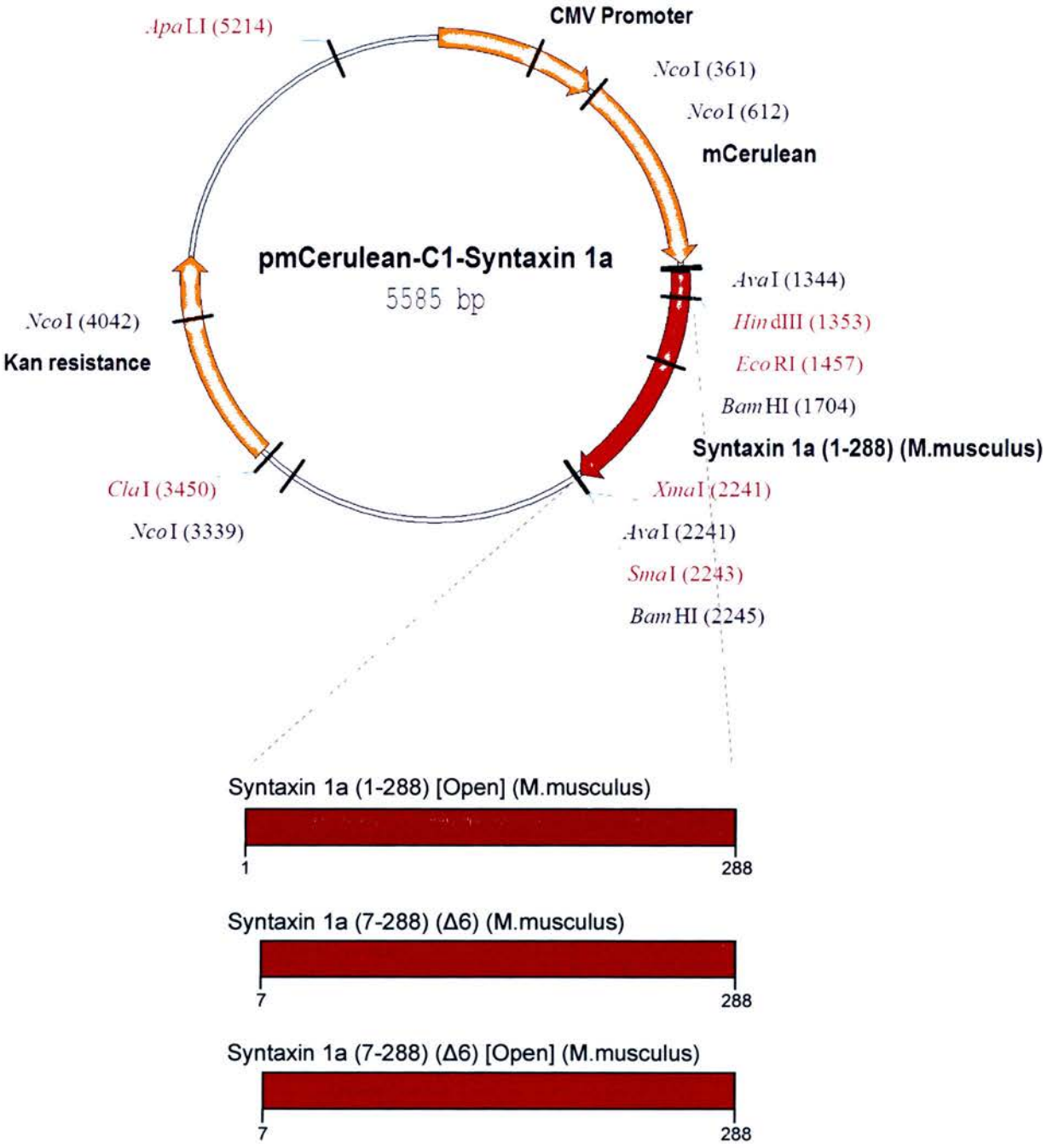
ApaLI (5214)
CMV Promoter
NcoI (361)
NcoI (612)
mCerulean
pmCerulean-C1-Syntaxin 1a
5585 bp
AvaI (1344)
HindIII (1353)
EcoRI (1457)
BamHI (1704)
Syntaxin 1a (1-288) (M.musculus)
NcoI (4042)
Kan resistance
ClaI (3450)
NcoI (3339)
XmaI (2241)
AvaI (2241)
SmaI (2243)
BamHI (2245)
Syntaxin 1a (1-288) [Open] (M.musculus)
1
288
Syntaxin 1a (7-288) (Δ6) (M.musculus)
7
288
Syntaxin 1a (7-288) (Δ6) [Open] (M.musculus)
7
288

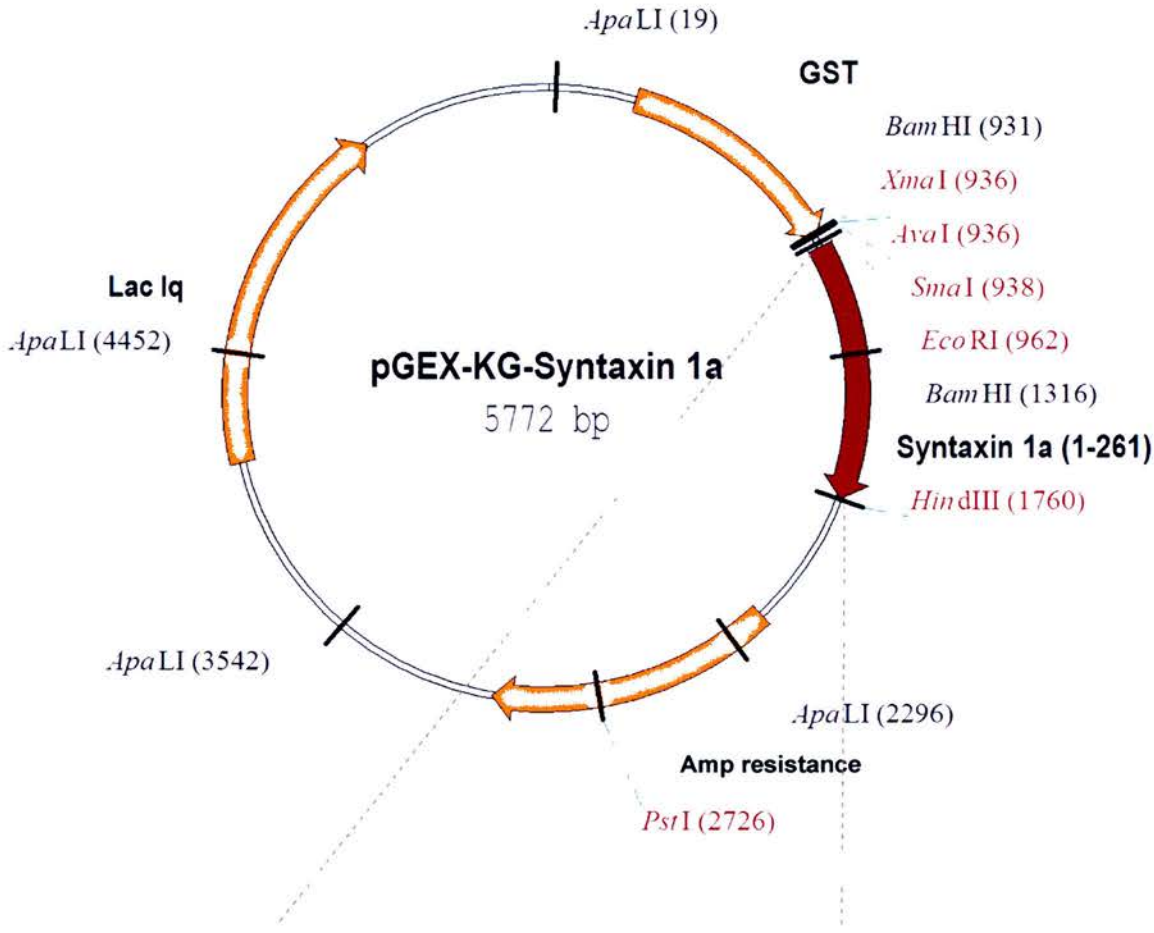
ApaLI (19)
GST
BamHI (931)
XmaI (936)
AvaI (936)
SmaI (938)
EcoRI (962)
BamHI (1316)
Syntaxin 1a (1-261)
HindIII (1760)
Lac Iq
ApaLI (4452)
pGEX-KG-Syntaxin 1a
5772 bp
ApaLI (3542)
ApaLI (2296)
Amp resistance
PstI (2726)

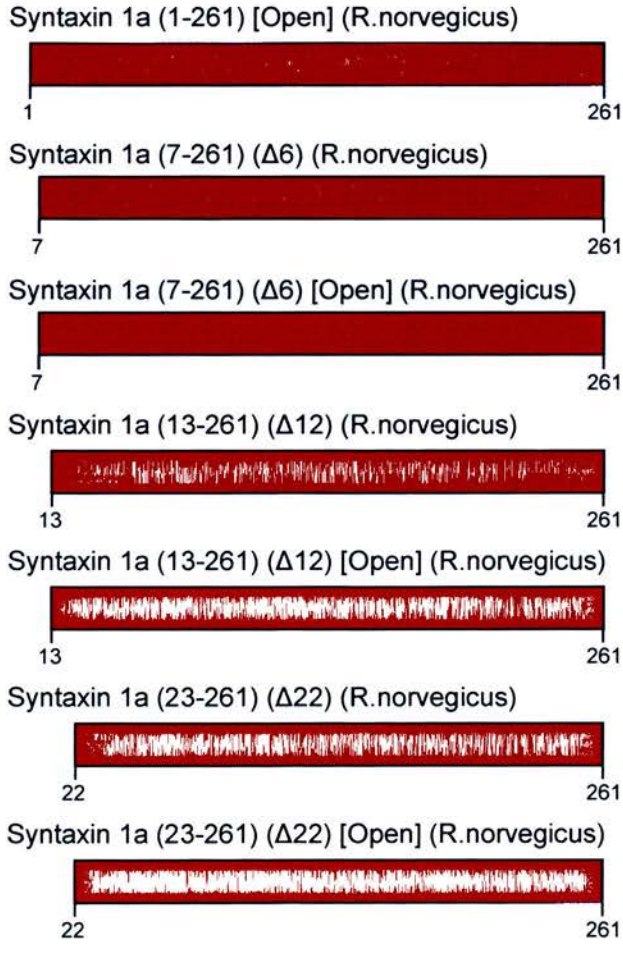
Syntaxin 1a (1-261) [Open] (R.norvegicus)
1
261
Syntaxin 1a (7-261) (Δ6) (R.norvegicus)
7
261
Syntaxin 1a (7-261) (Δ6) [Open] (R.norvegicus)
7
261
Syntaxin 1a (13-261) (Δ12) (R.norvegicus)
13
261
Syntaxin 1a (13-261) (Δ12) [Open] (R.norvegicus)
13
261
Syntaxin 1a (23-261) (Δ22) (R.norvegicus)
22
261
Syntaxin 1a (23-261) (Δ22) [Open] (R.norvegicus)
22
261